A Study of Compact Objects: Stellar Evolution Models and X-Ray Binaries.

Lise du Buisson

Christ Church
University of Oxford

A thesis submitted for the degree of
Doctor of Philosophy

Trinity 2021

Abstract

Compact and double compact binary systems are excellent natural laboratories for the study of a variety of physical phenomena. In this Thesis I study black hole binary systems and neutron star low-mass X-ray binaries in order to investigate binary stellar evolution pathways and accretion mechanisms.

Estimating the binary black hole merger rate and comparing it with predictions from gravitational-wave observatories is an important method to constrain binary stellar evolution channels. I investigate the chemically homogeneous evolution of close binary systems consisting of rapidly rotating, massive stars at low metallicities, by combining, for the first time, realistic binary models with detailed cosmological calculations of the chemical and star-formation history of the Universe. By constraining the population properties and determining the cosmological and detection rates of binary black hole mergers more precisely than before, I find that the chemically homogeneous evolution pathway can be an important source of aLIGO events.

Probing accretion processes in neutron star low-mass X-ray binaries offers unique tests of general relativity and helps to constrain the elusive equation of state of neutron stars. In the next part of the Thesis, I explore one of the most promising models to explain the accreting quasi-periodic oscillations observable in the power density spectra of neutron stars and black holes in binary systems: the relativistic precession model. I analyse the RXTE data of the neutron star X-ray binary 4U1608-52, presenting the first case study where more than one usable set of the necessary three quasi-periodic oscillations (a so-called triplet) are found for one single source, and for which multiple tests of the relativistic precession model can be carried out. I find that the mass and spin values resulting from such triplets cluster around physically realistic values, which can be considered reliable estimates of the neutron star fundamental parameters. If confirmed, my results indicate that 4U1608-52 would be one of the heaviest neutron stars known to date.

Finally, I analyse the RXTE data of the 11 Hz accreting pulsar IGR J17480-2446. Previous studies failed to find in this source the very low-frequency quasi-periodic oscillation associated with frame-dragging in the relativistic precession model, thus casting doubt on the validity of the model itself. In this study I find previously undetected very low-frequency quasi-periodic oscillations and show that these are consistent with being produced via frame-dragging, thus re-establishing the validity of the relativistic precession model.

A Study of Compact Objects: Stellar Evolution Models and X-Ray Binaries.

Lise du Buisson

Christ Church

University of Oxford

A thesis submitted for the degree of

Doctor of Philosophy

Trinity 2021

To S and J.
Friendship and uncorruptedness.

Abstract

Compact and double compact binary systems are excellent natural laboratories for the study of a variety of physical phenomena. In this Thesis I study black hole binary systems and neutron star low-mass X-ray binaries in order to investigate binary stellar evolution pathways and accretion mechanisms.

Estimating the binary black hole merger rate and comparing it with predictions from gravitational-wave observatories is an important method to constrain binary stellar evolution channels. I investigate the chemically homogeneous evolution of close binary systems consisting of rapidly rotating, massive stars at low metallicities, by combining, for the first time, realistic binary models with detailed cosmological calculations of the chemical and star-formation history of the Universe. By constraining the population properties and determining the cosmological and detection rates of binary black hole mergers more precisely than before, I find that the chemically homogeneous evolution pathway can be an important source of aLIGO events.

Probing accretion processes in neutron star low-mass X-ray binaries offers unique tests of general relativity and helps to constrain the elusive equation of state of neutron stars. In the next part of the Thesis, I explore one of the most promising models to explain the accreting quasi-periodic oscillations observable in the power density spectra of neutron stars and black holes in binary systems: the relativistic precession model. I analyse the RXTE data of the neutron star X-ray binary 4U1608-52, presenting the first case study where more than one usable set of the necessary three quasi-periodic oscillations (a so-called triplet) are found for one single source, and for which multiple tests of the relativistic precession model can be carried out. I find that the mass and spin values resulting from such triplets cluster around physically realistic values, which can be considered reliable estimates of the neutron star fundamental parameters. If confirmed, my results indicate that 4U1608-52 would be one of the heaviest neutron stars known to date.

Finally, I analyse the RXTE data of the 11 Hz accreting pulsar IGR J17480-2446. Previous studies failed to find in this source the very low-frequency quasi-periodic oscillation associated with frame-dragging in the relativistic precession model, thus casting doubt on the validity of the model itself. In this study I find previously undetected very low-frequency quasi-periodic oscillations and show that these are consistent with being produced via frame-dragging, thus re-establishing the validity of the relativistic precession model.

Acknowledgements

First and foremost, my thanks to Sara and Rob, who took me on after my first year and supervised me for most of the ride.

I've been fortunate enough to be graced by the company of friends without whom I probably would not have completed this long and arduous degree. Sanja, you've been an absolute joy in my life. I'll always be thankful we met and took an instant liking to one another: years later and we've conquered Oxford, won Henley, and are about to get a cat. Crazy. Johan, words will always fall short of what you mean to me. You keep reminding me of what is and should be important in life. Kumeren, what a delight you've been - broken fingers, cèilidh dances, balls, formals and sunsets - may we have many adventures yet.

Rhodes House offered a safe haven and a place of rest in times of trouble, and a celebration of life, friendship and reason in times of peace. Mary, thanks for standing up for me, and for offering a kind ear and sincere help when I needed it most.

I had the privilege of spending a season in the ranks of OUWBC, and to have raced the Boat Race. The experience changed me in many ways, and altogether gave me a feeling of strength and freedom I hope will last a lifetime. Gavin, thanks for laying the groundwork for what would become a pretty decent rower, and thanks for always believing in me and encouraging me.

Christ Church was home during my time at Oxford, and its boat club shaped many of my most cherished memories during my first year. A special thanks to Mike - you were my second rowing dad, and an amazing coach. Your kindness and sense of humour is with me still.

Lastly, to my mother and father. I've been away for a long time now, and it's hard seeing small flashes of you once a year. I love you and miss you incredibly much, and am eternally grateful for what you sacrificed so that I could be here today.

And Anne - quarantine and the Victorian era left me waking up, swept aside by something that remained. On the right shore.

Declaration

The body of this Thesis consists of three chapters (Chapters 2, 3 and 4) that have been reproduced from three papers of which I am the principal author (see below for a list of first-author peer-reviewed publications). Some of the passages in these papers have been moved to the introductory and concluding chapters (Chapters 1 and 5).

In Chapter 2, the binary calculations used are based on the chemically homogeneous evolution scenario as described by Marchant et al. (2016), but extended and covering a much larger range of initial conditions. These simulations, the results of which serve as inputs to my binary population synthesis simulations, were carried out by Pablo Marchant, one of the collaborators on the paper. My simulations further make use of the hydrodynamical simulations and resulting metallicity-dependent star formation history of Taylor and Kobayashi (2015b).

All work and papers contained in this Thesis were written by me, unless otherwise indicated in the text.

First-author peer-reviewed publications

1. *Mass and spin measurements for the neutron star 4U1608-52 through the relativistic precession model.* **Lise du Buisson**, Sara Motta, Rob Fender. 2019. Monthly Notices of the Royal Astronomical Society, Volume 486, Issue 4, p.4485-4497. doi: 10.1093/mnras/stz1160. This is reproduced in this Thesis as Chapter 3, and is referred to where otherwise relevant as du Buisson et al. (2019).

2. *Cosmic Rates of Black Hole Mergers and Pair-Instability Supernovae from Chemically Homogeneous Binary Evolution.* **Lise du Buisson**, Pablo Marchant, Philipp Podsiadlowski, Chiaki Kobayashi, Filipe Abdalla, Philipp Taylor, Ilya Mandel, Selma de Mink, Takashi Moriya, Norbert Langer. 2020. Monthly Notices of the Royal Astronomical Society, Volume 499, Issue 4, p.5941-5959. doi: 10.1093/mnras/staa3225. This is reproduced in this Thesis as Chapter 2, and is referred to where otherwise relevant as du Buisson et al. (2020).

3. *Very low-frequency oscillations from the 11 Hz pulsar in Terzan 5: frame-dragging back on the table.* **Lise du Buisson**, Sara Motta, Rob Fender. 2021. Monthly Notices of the Royal Astronomical Society, Volume 502, Issue 4, p.5472–5479. doi: 10.1093/mnras/stab422. This is reproduced in this Thesis as Chapter 4, and is referred to where otherwise relevant as du Buisson et al. (2021).

Contents

List of Abbreviations

AGN . . . . . Active Galactic Nuclei

AdV . . . . . Advanced Virgo

aLIGO . . . . . Advanced Laser Interferometer Gravitational-Wave Observatory

ASM . . . . . All Sky Monitor

BH . . . . . Black Hole

BHBH . . . . . Black Hole Binary

CCSN . . . . . Core-Collapse Supernova

CE . . . . . Common Envelope

CHE . . . . . Chemically Homogeneous Evolution

CCD . . . . . Colour-Colour Diagram

CNO . . . . . Carbon-Nitrogen-Oxygen

DES . . . . . Dark Energy Survey

EoS . . . . . Equation of State

ET . . . . . Einstein Telescope

EXOSAT . . . European X-ray Observatory Satellite

FBO . . . . . Flaring Branch Oscillation

FWHM . . . . Full Width at Half Maximum

GR . . . . . General Relativity

HBO . . . . . Horizontal Branch Oscillation

HEXTE . . . . High Energy X-ray Timing Experiment

HF . . . . . High-Frequency

HID . . . . . Hardness-Intensity Diagram

HMXB . . . . High-mass X-ray Binary

HRD . . . . . Hardness-Rms Diagram

HSC . . . . . Hyper Suprime-Cam

IMF . . . . . Initial Mass Function
ISCO . . . . . Innermost Stable Circular Orbit
KAGRA . . . Kamioka Gravitational Wave Detector
LF . . . . . Low-Frequency
LISA . . . . . Laser Interferometer Space Antenna
LMXB . . . . . Low-Mass X-ray Binary
LSST . . . . . Large Synoptic Survey Telescope
LT . . . . . Lense-Thirring
MHD . . . . . Magnetohydrodynamic
MJD . . . . . Modified Julian Day
MOB . . . . . Massive Overcontact Binaries
MWEQ . . . . Milky Way Equivalent Galaxy
NASA . . . . . National Aeronautics and Space Administration
NBO . . . . . Normal Branch Oscillation
NS . . . . . Neutron Star
Pan-STARRS Panoramic Survey Telescope And Rapid Response System
PCA . . . . . Proportional Counter Array
PCU . . . . . Proportional Counter Unit
PDS . . . . . Power Density Spectrum
PISN . . . . . Pair-Instability Supernova
PPISN . . . . Pulsational Pair-Instability Supernova
PTF . . . . . Palomar Transient Factory
QPO . . . . . Quasi-Periodic Oscillation
RID . . . . . Rms-Intensity Diagram
RLOF . . . . . Roche-Lobe Overflow
RPM . . . . . Relativistic Precession Model
RXTE . . . . . Rossi X-ray Timing Explorer
SDSS . . . . . Sloan Digital Sky Survey
SFR . . . . . Star Formation Rate
SNR . . . . . Signal to Noise Ratio
VLF . . . . . Very Low-Frequency
ZAMS . . . . . Zero Age Main Sequence
ZTF . . . . . Zwicky Transient Facility

List of Figures

List of Tables

"When you're a kid, they tell you it's all... Grow up, get a job, get married, get a house, have a kid, and that's it. But the truth is, the world is so much stranger than that. It's so much darker. And so much madder. And so much better."

Elton Pope, Doctor Who

1 Introduction

1.1 Motivation

Of the many, many stars in our Universe, a large percentage are found interacting with one or more other stars through their gravitational pull. This interaction between two orbiting stars in a binary system could influence the evolution and eventual fate of its individual counterparts in a way very different to how solitary stars, existing without the influence of a companion, would live and die. The study of these systems is therefore an important one, as most observed stars would have companions playing a direct role in the traits and characteristics they exhibit - a lack of understanding of binary systems would have as consequence the diminished ability to understand what we observe.

Amongst binary systems, compact and double compact binaries are of particular interest. These are exotic systems where either one or both of the stellar components have collapsed to form a compact object - be that a black hole (BH), a neutron star (NS) or a white dwarf. Compact binaries provide us with an array of interesting avenues through which to investigate stars, their evolution and the physical phenomena involved.

The first of these avenues is that of general relativity. Compact objects are extremely dense, and studying the environments close to them can enable us to test

strong-field gravity and its effects. Compact binaries in which a stellar component transfers mass onto a NS or BH companion via an accretion disc are among the most powerful X-ray sources in our Galaxy - the X-ray emission originates from the innermost parts of the disc closest to the compact object, where the effects of gravity are strongest, and careful analysis of X-ray spectra using models such as relativistic precession can lead to knowledge regarding the mass and spin of the compact companion. Furthermore, where the constituents of double compact binaries are close enough together that they can spiral in and merge in our current epoch, the resulting gravitational waves can be detected by ground-based observatories and used to test and refine current models of gravity.

Compact binaries further give us insight into the different fates of stars, and the evolution they were subject to in order to arrive at these particular fates. The recent detection of gravitational waves emitted from merging double BH and double NS systems raise some interesting questions as to close binary evolution: is it possible and feasible for stars to spend their lives in such extreme close proximity to one another without merging during the traditional expansion phase of their evolution? If so, what would this alternative evolution look like?

Lastly, low-mass X-ray binaries (LMXBs) provide us with valuable insight as to the accretion and ejection mechanisms at play in systems such as these, which in turn helps us to understand similar phenomena on larger scales elsewhere in the Universe. Their outbursts occur on timescales accessible to humans, and so it is possible for us to follow their cycles of outburst evolutions and analyse the resulting observed X-ray spectral-timing properties in order to better understand the associated complex phenomenology. Understanding accretion in turn leads to a better understanding of high-energy astrophysics, which in turn helps us to understand the rate of change in these systems, the binary evolution processes involved and the gravitational effects in these environments (spectral lines in the X-ray originating from the accretion disc can be used to probe strong-field gravity).

It is evident that compact and double compact binaries are invaluable exotic laboratories worthy of studying in depth. They can be used to test and probe

the theory of general relativity, understand and study stellar and binary evolution and to investigate the accretion-ejection mechanisms at play in accreting systems. The aim of this thesis is to investigate these facets by looking at stellar-mass double BH binaries for a study of binary evolution, and NS LMXBs for probing general relativity and to study accretion.

In order to lay a background enabling us to proceed effectively with the above, the next four sections will be dedicated to the necessary general relativistic knowledge, stellar evolution, and X-ray binary systems. The experimental background will then be discussed, followed by a summary of the main aims of the thesis and an outline of the chapters it comprises of.

1.2 General Relativity: Relevant Background

The general theory of relativity is a geometric theory of gravitation first published by Albert Einstein in 1915, and it is currently the accepted description of gravitation in modern physics. This section provides the reader with the necessary basic background in specific general relativistic topics so that material in later chapters and sections can be better understood. Sections 1.2.1 – 1.2.3 introduce the Einstein field equations and two of their exact solutions, namely the Schwarzschild and Kerr metrics, adapted from Hobson et al. (2006). Section 1.2.4 describes the effect of orbital precession using the basic model of a planet orbiting a star, and Section 1.2.5 discusses gravitational waves. As the focus of this thesis is not general relativity in itself, material here is kept as simple as possible, and the reader will be directed to other sources for more in-depth treatments.

1.2.1 Basic Background

According to general relativity, mass and energy affects the geometry of spacetime, which can account for a large number of commonly observed effects, such as the gravitational pull between two massive objects resulting in an orbit, as well as somewhat unexpected effects, such as the slowing of time for an object in a gravitational field as seen by an observer sitting at infinity with respect to the source

of said gravitational field. Given that the speed of light is invariant for inertial observers, we find that the transformations relating different inertial frames of reference mix time and space coordinates, prompting the introduction of spacetime as a unified structure combining space and time. In this sense, an *event* in spacetime requires four coordinates to be properly specified: the three-dimensional location in space, and the position in time. This might, for example, be chosen as a four-vector, taking the form (x^0, x^1, x^2, x^3) which can be defined as the (t, x, y, z) that we use here (where the speed of light, c, is set equal to 1).

The simplest spacetime is flat Minkowski space, and it combines 3D Euclidean space and time in the absence of gravity. This is the regime in which special relativity operates, and in this spacetime we can define small incremental distances (or the line element) in Euclidian coordinates as

$$ds^2 = \eta_{\mu\nu} dx^\mu dx^\nu = -dt^2 + dx^2 + dy^2 + dz^2, \tag{1.1}$$

where Greek indices run from 0 to 3 and $\eta_{\mu\nu}$ is the Minkowski metric tensor. In the tensor-notation used for relativity, using the coordinates above, $\eta_{\mu\nu}$ is defined as

$$\eta_{\mu\nu} = \begin{pmatrix} -1 & 0 & 0 & 0 \\ 0 & 1 & 0 & 0 \\ 0 & 0 & 1 & 0 \\ 0 & 0 & 0 & 1 \end{pmatrix}. \tag{1.2}$$

The Minkowski tensor describes flat space only and therefore, in order to be able to incorporate gravitational fields, we need a metric that can operate in arbitrary coordinates and geometries. We introduce such a metric $g_{\mu\nu}$ that can accommodate curvature, such that the line element in some arbitrary coordinate system x^μ now takes the general form

$$ds^2 = g_{\mu\nu} dx^\mu dx^\nu. \tag{1.3}$$

While we can always choose our coordinates such that at a given point, the first derivatives of the metric will be zero (such that the space will look locally "flat"), in

the presence of curvature, we find that second derivatives of the metric tensor are necessarily non-zero.

The information about the curvature of a given metric is contained in another tensor known as the Riemann curvature tensor, which incorporates derivatives of the metric tensor through "connection" coefficients or "Christoffel coefficients". We define Christoffel symbols $\Gamma^{\sigma}_{\mu\nu}$ as

$$\Gamma^{\sigma}_{\mu\nu} = \frac{1}{2} g^{\sigma\rho}(\partial_{\mu} g_{\nu\rho} + \partial_{\nu} g_{\rho\mu} - \partial_{\rho} g_{\mu\nu}), \tag{1.4}$$

and further define the Riemann curvature tensor $R^{\sigma}_{\mu\alpha\beta}$ as

$$R^{\sigma}_{\mu\alpha\beta} = \partial_{\alpha}\Gamma_{\mu\beta} - \partial_{\beta}\Gamma^{\alpha}_{\mu\alpha} + \Gamma^{\sigma}_{\alpha\lambda}\Gamma^{\lambda}_{\mu\beta} - \Gamma^{\sigma}_{\beta\lambda}\Gamma^{\lambda}_{\mu\alpha}. \tag{1.5}$$

The Riemann curvature tensor is an extremely important tensor that incorporates all the information about the curvature of the spacetime. For flat space, in which all components of the metric are constant in Euclidian coordinates, all the components of the curvature tensor would vanish. This tensor also gives rise, by contraction[1] of its indices, to two other important objects, the Ricci scalar and the Ricci tensor. The Ricci tensor $R_{\alpha\beta}$ is obtained by contracting over one index in the manner

$$R_{\alpha\beta} = R^{\lambda}_{\alpha\lambda\beta}, \tag{1.6}$$

and the Ricci scalar is the trace of the Ricci tensor, defined as

$$R = R^{\Lambda}_{\Lambda} = g^{\mu\nu} R_{\mu\nu}, \tag{1.7}$$

with $g^{\mu\nu}$ being the inverse metric of the metric tensor. This description of curvature enables us to set up the Einstein equations, which relates the curvature of spacetime to the distribution of matter and energy. The Einstein field equations are given by

$$R_{\mu\nu} - \frac{1}{2} g_{\mu\nu} R = -\frac{8\pi G}{c^4} T_{\mu\nu}. \tag{1.8}$$

[1]The Einstein summation convention is used here - repeated indices are summer over.

The left side of Equation 1.8 is also known as the Einstein tensor, denoted by $G_{\mu\nu}$, and $R_{\alpha\beta}$ and R are the Ricci tensor and the Ricci scalar, respectively, defined above. $T_{\mu\nu}$ is the energy-momentum tensor which describes the distribution of energy and momentum in spacetime, and several of its components have a direct physical interpretation (Hobson et al., 2006). The time-time component T^{00}, for instance, gives the energy density of the spacetime, and the other 0-index terms, T^{0i}, give the "mass flux" or the linear momentum in the i^{th} direction. The diagonal components give the pressure or normal stress on the i^{th} surface, while more generally, the cross-terms T^{ij} are defined as the flux of the i^{th} component of momentum in the j^{th} direction, also known as the shear stress.

Equation 1.8 forms the mathematical basis of the theory of general relativity. These gravitational field equations are non-linear in $g_{\mu\nu}$, and therefore involve numerous non-linear differential equations. One can solve the above field equations to obtain spacetime metrics for various mass and energy distributions. Two of these solutions, the Schwarzschild and Kerr metrics – some of the most-used metrics in astrophysics – are discussed next in Section 1.2.2 and 1.2.3, followed by their applications in precession and gravitational waves.

1.2.2 Schwarzschild Solution

In 1916, little after a month from Einstein first publishing his theory of general relativity, Karl Schwarzschild became the first to discover an exact solution to his field equations[2], a solution which described the rather simplistic case of spacetime around a spherically symmetric matter distribution. The solution makes the assumption that the spherical mass has no electric charge and no angular momentum, and is a useful approximation when dealing with slowly-rotating spherical astronomical objects like planets and stars. A Schwarzschild black hole, for example, is a black hole that has neither charge nor angular momentum, and can therefore be described by the Schwarzschild metric. Being spherically symmetric,

[2]Notably, while he was in the trenches on the Eastern Front while fighting in the First World War.

such black holes can only be distinguished by their mass, which is effectively the only parameter that characterises them.

In Schwarzschild spherical polar coordinates (t, r, θ, ϕ), t is the time coordinate measured by a stationary clock infinitely far from the spherical mass, r is the radial coordinate of a sphere centred on the massive body, so that

$$x = r\sin\theta\cos\phi, \quad y = r\sin\theta\sin\phi, \quad z = r\cos\theta. \tag{1.9}$$

Solving the Einstein field equations given in Equation 1.8 assuming $\Lambda = 0$ and a spherically symmetric, static, and vacuum spacetime (implying that the energy-momentum tensor $T_{\mu\nu}$ is zero everywhere outside the spherically symmetric massive object), the Schwarzschild metric line element ds^2 for the area surrounding a spherical body with mass M is given, from Hobson et al. (2006), by

$$ds^2 = -c^2\left(1 - \frac{r_s}{r}\right)dt^2 + \left(1 - \frac{r_s}{r}\right)^{-1}dr^2 + r^2 d\theta^2 + r^2\sin^2\theta\, d\phi^2. \tag{1.10}$$

Here c is the speed of light (where, as before, it can be set equal to 1), G is the gravitational constant and r_s is the Schwarzschild radius given by

$$r_s = \frac{2GM}{c^2}. \tag{1.11}$$

Seeing as the Schwarzschild metric is a solution of the Einstein field equations in empty space, it is only valid outside the spherical mass - for a mass with radius R, therefore, Equation 1.10 is valid only for $r > R$. The surface at $r = r_s$ is called the *event horizon*. It represents the point past which light can no longer escape the gravitational field of an object - any object with a radius smaller than or equal to r_s will undergo gravitational collapse and form a black hole. Additionally, as this surface is approached in the case of a black hole, time dilation becomes increasingly significant. An observer, in fact, would never see an object cross the event horizon, but merely see the object approach it more and more slowly. The above implies that there cannot be a cause-effect relation between events happening on different sides of the event horizon.

1.2.3 Kerr Solution

While Schwarzschild's solution presents a physically meaningful case, most real astrophysical objects, unlike those described in Section 1.2.2, are rotating. This means that a spherically symmetric solution (such as the Schwarzschild metric) is inadequate, due to the object's rotation axis defining a special direction and destroying the isotropy of the solution.

It is not possible to find a coordinate system that reduces the spacetime geometry outside a rotating, uncharged object to that of the Schwarzschild geometry. Furthermore, a rotating body is characterised both by its mass M and by its angular momentum J, and so the corresponding spacetime metric should depend on these parameters.

Due to its difficulty, the first exact solution of the empty-space Einstein field equations for an uncharged, rotating mass had remained elusive, until it was finally obtained in 1963 by Roy Kerr (Kerr, 1963). As was the case for the Schwarzschild solution, the Kerr metric is valid only outside the massive rotating object. In *Boyer-Lindquist coordinates* (t, r, θ, ϕ), related to Cartesian coordinates through

$$x = \sqrt{r^2 + a^2}\sin\theta\cos\phi, \quad y = \sqrt{r^2 + a^2}\sin\theta\sin\phi, \quad z = r\cos\theta, \tag{1.12}$$

the Kerr metric line element ds^2 can be written as

$$ds^2 = -\frac{\rho^2\Delta}{\Sigma^2}c^2dt^2 + \frac{\Sigma^2\sin^2\theta}{\rho^2}(d\phi - \omega dt)^2 + \frac{\rho^2}{\Delta}dr^2 + \rho^2 d\theta^2, \tag{1.13}$$

where, ρ, Δ and Σ are defined by

$$\begin{aligned} \rho^2 &= r^2 + a^2\cos^2\theta \\ \Delta &= r^2 - 2\mu r + a^2 \\ \Sigma^2 &= (r^2 + a^2)^2 - a^2\Delta\sin^2\theta. \end{aligned} \tag{1.14}$$

In the above relations, μ and a are constants, with $\mu = GM/c^2$ and a related to the angular momentum of the body such that $J = Mac$. Further, the physically meaningful function ω is defined by $\omega = 2\mu cra/\Sigma^2$, and is thought of as a "twist",

which relates to the way in which the rotating black hole affects the space time surrounding it. This can be seen to arise from the cross term of $d\phi$ and dt, indicating that this twisting, or "frame-dragging" occurs in the ϕ-plane. Also known as Lense-Thirring precession, frame-dragging predicts that objects getting close to a rotating mass will be 'dragged' just by the influence of gravity such that they will acquire an angular velocity similar to that of the rotating mass.

1.2.4 Simple Precession Models

This section describes a simple model of precession, in the weak-field limit and in terms of the Schwarzschild geometry, of a planet orbiting a star. The purpose is to provide the reader with a basic intuition as to the principle of precession, so as to form a basis from which to understand more complex models of precession encountered later in the thesis. The discussion here is based on the text by Hobson et al. (2006).

We start by considering a general non-circular Newtonian orbit, for which the equation of motion is

$$\frac{d^2u}{d\phi^2} + u = \frac{GM}{j^2}. \tag{1.15}$$

Here, $u \equiv 1/r$ and j is the angular momentum per unit mass of the orbiting particle. Considering a bound orbit, it follows that u can be written as

$$u = \frac{GM}{j^2}(1 + e\cos\phi). \tag{1.16}$$

Equation 1.16 describes an elliptical orbit, with e being the ellipticity and ϕ being the orbital evolution over time. The distance of closest approach (the perihelion, r_1) and the distance of furthest approach (the aphelion, r_2), can be expressed as

$$\begin{aligned} r_1 &= a(1-e) \\ r_2 &= a(1+e), \end{aligned} \tag{1.17}$$

where a is the semi-major axis of the ellipse. From this, the equation of motion requires the semi-major axis to be

$$a = \frac{j^2}{GM(1-e^2)}. \tag{1.18}$$

Next, the general-relativistic equation of motion can be written as

$$\frac{d^2u}{d\phi^2} + u = \frac{GM}{j^2} + \frac{3GM}{c^2}u^2. \tag{1.19}$$

In systems with relatively small masses at large distances, we can assume that Newtonian gravity is a reliable approximation of the general relativistic motion. By using the Newtonian solution to Equation 1.19, we can write the general-relativistic solution as

$$u = \frac{GM}{j^2}(1 + e\cos\phi) + \Delta u, \tag{1.20}$$

with Δu a perturbation. Substituting Equation 1.20 into Equation 1.19, we find that, to first order in Δu,

$$\frac{d^2\Delta u}{d\phi^2} + \Delta u = A(1 + e^2\cos^2\phi + 2e\cos\phi). \tag{1.21}$$

Here, the constant A, expressed as

$$A = \frac{3(GM)^3}{c^2 j^4}, \tag{1.22}$$

is very small. Next, it can be shown that the perturbation Δu satisfies

$$\Delta u = A\left[1 + e^2(\frac{1}{2} - \frac{1}{6}\cos 2\phi) + e\phi\sin\phi\right]. \tag{1.23}$$

A is very small, and so the first two terms above can be ignored. The third term, however, will grow with time due to the evolution of ϕ over time. Keeping only the third term, we can therefore substitute Equation 1.23 into Equation 1.20 to obtain

$$u = \frac{GM}{j^2}[1 + e(\cos\phi + \alpha\phi\sin\phi)], \tag{1.24}$$

where α is just

$$\alpha = \frac{3(GM)^2}{j^2c^2} \ll 1. \tag{1.25}$$

Next, using the relation

$$\begin{aligned} \cos[\phi(1-\alpha)] &= \cos\phi\cos\alpha\phi + \sin\phi\sin\alpha\phi \\ &\approx \cos\phi + \alpha\phi\sin\phi \quad \text{for} \quad \alpha \ll 1, \end{aligned} \tag{1.26}$$

we can write Equation 1.24 as

$$u \approx \frac{GM}{j^2}\{1 + e\cos[\phi(1-\alpha)]\}. \tag{1.27}$$

Equation 1.27 shows that the orbit is periodic with a period $2\pi/(1-\alpha)$, meaning that r-values will repeat on cycles larger than 2π - the ellipse therefore precesses, as is illustrated in Figure 1.1. For every revolution, the ellipse rotates around the focus by $\Delta\phi$, expressed as

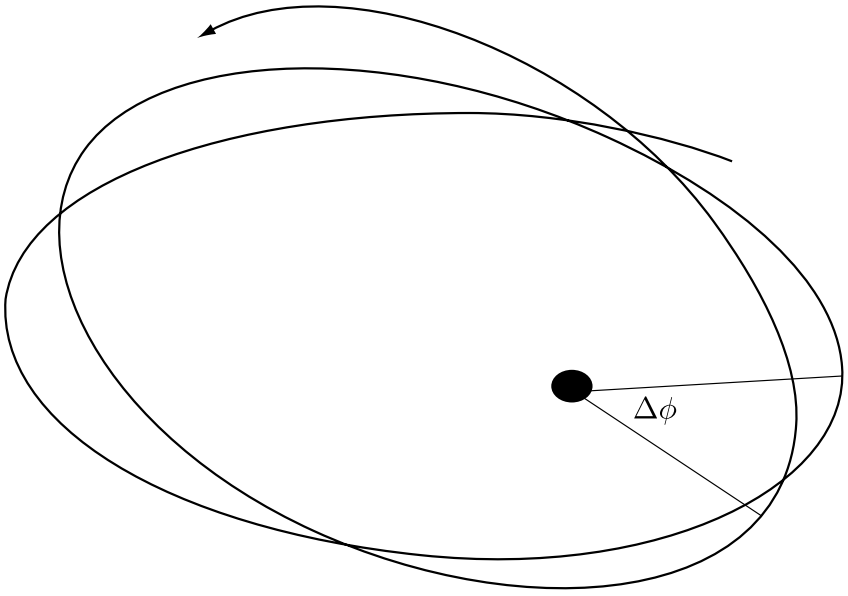

Figure 1.1: The precession of the elliptical orbit of a planet around a star, with $\Delta\phi$ being the amount that the orbit precesses with every revolution. The figure has been taken from Hobson et al. (2006).

$$\Delta\phi = \frac{2\pi}{1-\alpha} - 2\pi \approx 2\pi\alpha = \frac{6\pi(GM)^2}{j^2c^2}, \tag{1.28}$$

and substituting for j from Equation 1.18, we can at last write $\Delta\phi$ as

$$\Delta\phi = \frac{6\pi GM}{a(1-e^2)c^2}. \tag{1.29}$$

1.2.5 Gravitational Waves

One of the predictions of the theory of general relativity is the existence of gravitational waves - Einstein realised this in 1916, merely a year after first publishing the theory. Gravitational waves are small perturbations of the geometry of spacetime, travelling at the speed of light, generated by accelerating masses. We can write the spacetime metric $g_{\mu\nu}$ as

$$g_{\mu\nu} = \eta_{\mu\nu} + h_{\mu\nu}, \tag{1.30}$$

where $\eta_{\mu\nu}$ is the Minkowski metric tensor given in Equation 1.2, and $h_{\mu\nu}$ is the perturbation.

Similar to electromagnetic waves, gravitational waves are transverse to the direction of propagation and admit two polarisations. To illustrate this, consider a gravitational wave travelling along the z-axis in flat spacetime. Its polarisation state is referred to as the 'plus polarisation' if it is linearly polarised along the x-axis, and the 'cross polarisation' if it is linearly polarised along the direction oriented $45^{\odot}$ from the x-axis, in the $x-y$ plane. The gravitational wave's plus polarisation increases the proper length along the x-direction while decreasing it along the y-direction during the first half-cycle, and does the opposite for the second half-cycle. The cross polarisation has a similar effect, only rotated $45^{\odot}$ in the $x-y$ plane. Denoting the plus polarisation as h_+ and the cross polarisation as $h_\times$, the two polarisations of gravitational waves are illustrated in Figure 1.2.

There are various sources of gravitational waves, but the strongest waves reaching Earth are generated by collapsing stars, the formation of BHs, matter falling into BHs, supernova explosions, young pulsars and inspiralling or merging BH or NS binaries (Misner et al., 1973). For the work in this thesis, the interest primarily falls on gravitational waves generated by inspiralling BH binaries.

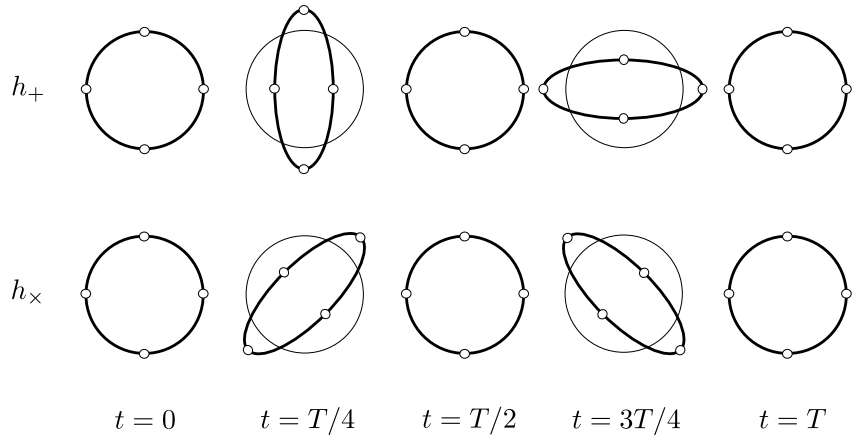

Figure 1.2: The effect of a linearly polarised gravitational wave on a ring of particles lying orthogonal to the direction of propagation of the wave is shown in this figure. The circle of particles can be seen to stretch in one direction and shrink in the orthogonal one during the first half-cycle of the wave, and to do the opposite during the second half-cycle. T is here used to denote the period of the wave. For the plus and cross polarisations (denoted by h_+ and $h_\times$ in the figure, respectively), the effect occurs in directions angled at $45^\odot$ from one another. This figure was adapted from Antelis and Moreno (2017) and Królak and Patil (2017).

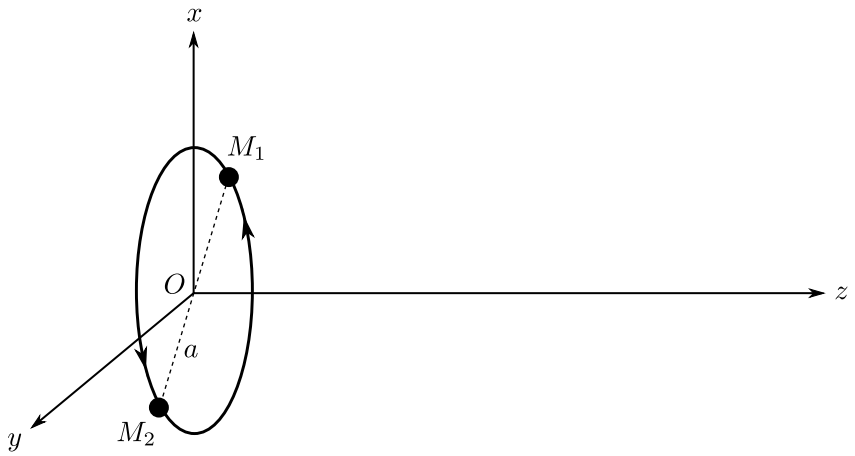

Figure 1.3: Two black holes, denoted by M_1 and M_2, rotating at angular speed ω about their common centre of mass, marked as O in the figure. The black holes are rotating in the $x - y$ plane, and have a separation a between them. This figure was adapted from Hobson et al. (2006).

For gravitational waves travelling to and arriving at an observer from a system in the early stages of inspiral, we start off by considering a binary BH system consisting of non-spinning BHs with masses denoted by M_1 and M_2, respectively. The BHs rotate around their common centre of mass O with a circular orbit and a separation a between them, and their angular rate is denoted by ω. This

configuration can be seen in Figure 1.3.

In the centre-of-mass frame, under the assumption that the binary exhibits Newtonian motion, we have through Kepler's third law that a and ω are related through

$$\omega^2 a^3 = GM, \tag{1.31}$$

where $M = M_1 + M_2$ and G denotes the gravitational constant. Solving the linearised vacuum Einstein equations using Equation 1.30, we can find the quadrupole perturbation $h_{\mu\nu}$, in transverse-traceless (TT) gauge, as

$$h_{\mu\nu} = \begin{pmatrix} 0 & 0 & 0 & 0 \\ 0 & h_+ & h_\times & 0 \\ 0 & h_\times & -h_+ & 0 \\ 0 & 0 & 0 & 0 \end{pmatrix}, \tag{1.32}$$

where h_+ and $h_\times$ are the two polarisations. It is beyond the scope of this Thesis to derive h_+ and $h_\times$, but the interested reader can consult the texts by Maggiore (2008), Misner et al. (1973), Hobson et al. (2006), Peters and Mathews (1963) and the dissertation by Curtis (2019) in which most of the derivation for early-stage inspiralling systems is set out. For late-stage inspirals and mergers, a more complex GR model is required - this can be found in Maggiore (2008).

To find an expression for the chirp mass M_{chirp} of the system, we consider the rate of energy loss in the BH binary system due to gravitational waves. The orbital energy E_{orb} of the system can be written as

$$E_{orb} = -\frac{GM_1M_2}{2a} = -\frac{GM\mu}{2a}, \tag{1.33}$$

were μ is the reduced mass given by $\mu = (M_1M_2)/(M_1 + M_2)$. From Misner et al. (1973) we have that the rate of energy loss due to gravitational waves, E_{gw}, can be expressed as

$$\frac{dE_{gw}}{dt} = \frac{32}{5}\frac{G}{c^5}\mu^2 a^4 \omega^6. \tag{1.34}$$

Taking the time derivative of E_{orb} in Equation 1.33, we have that

$$\frac{dE_{gw}}{dt} = \frac{32}{5}\frac{G}{c^5}\mu^2 a^4 \omega^6 = -\frac{dE_{orb}}{dt} = -\frac{GM\mu\dot{a}}{2a^2}. \tag{1.35}$$

Taking the time derivative of Kepler's third law given in Equation 1.31, using it and Equation 1.31 to substitute for a and $\dot{a}$ in Equation 1.35, and integrating with respect to t, gives

$$\omega(t) = \left(\frac{c^3}{G}\right)^{5/8} \frac{1}{M_{\text{chirp}}} \left(\frac{5}{256}\frac{M_{\text{chirp}}}{T-t}\right)^{3/8}. \tag{1.36}$$

Here, T represents the time of coalescence of the BHs, and M_{chirp} is the chirp mass of the BHs, defined as

$$M_{\text{chirp}} = (\mu^3 M^2)^{1/5}. \tag{1.37}$$

The chirp mass M_{chirp} of a system therefore determines the leading-order orbital evolution as a consequence of gravitational-wave energy loss. As the gravitational wave frequency is determined by the orbital frequency (it is twice the rotation frequency of the BH binary), the chirp mass also determines the frequency evolution of the gravitational wave signal emitted during a binary's inspiral phase. Ignoring higher order relativistic effects, Figure 1.4 shows the shapes of the inspiral waveforms h_+ and $h_\times$. It can be seen that the waveform increases in amplitude and sweeps upwards in frequency (called a "chirp") as the binary components spiral closer together. The shape of the individual waves (i.e. their harmonic content) is determined by the eccentricity of the binary's orbit, among other quantities. For circular orbits (with $e = 0$, as is the case for Figure 1.4), the rate of frequency change df/dt (or equivalently the number of cycles near a given frequency $n = f^2(df/dt)^{-1}$) is solely determined by the chirp mass, given by $M_{\text{chirp}} = (M_1 M_2)^{3/5}/(M_1 + M_2)^{1/5}$, where M_1 and M_2 are the component masses of the binary (Thorne, 1995). Higher order terms in the post-Newtonian expansion then needs to be measured in order to disentangle individual component masses from the chirp mass. The amplitudes of the two waveforms are dependent on M_{chirp}, the distance to the source, and the orbital inclination, such that if one measures the amplitude of the waveforms,

the frequency sweep and the harmonic content of the waveforms, it is possible to calculate the chirp mass, the distance to the source, the eccentricity, and the inclination of the binary's orbit (Schutz, 1986).

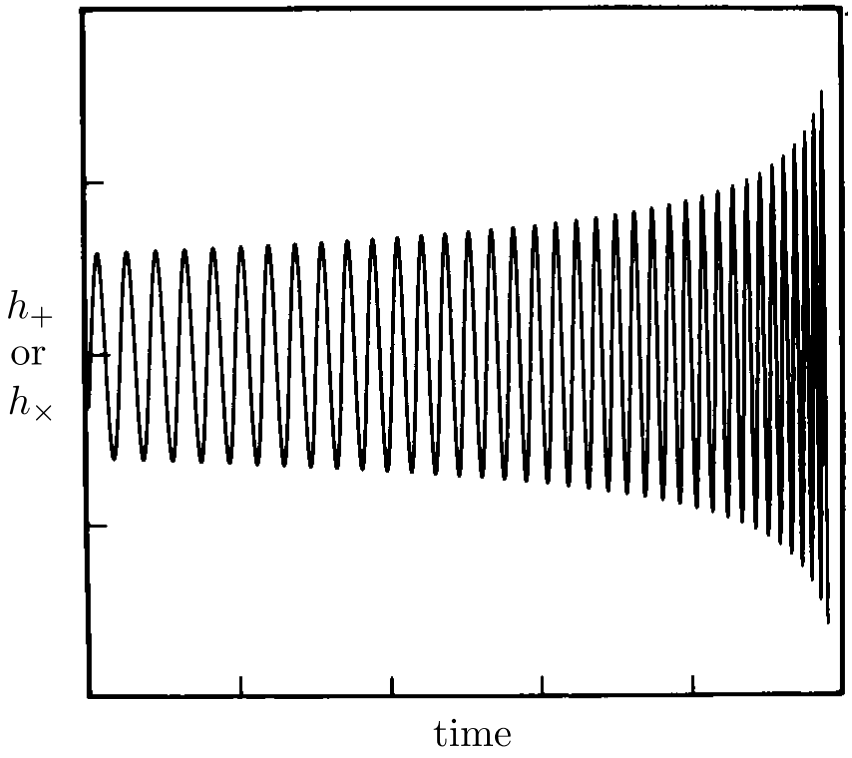

Figure 1.4: The waveform of an inspiralling compact binary (ignoring relativistic effects) for a circular orbit. Figure adapted from Abramovici et al. (1992).

1.3 Single-star Evolution

Stellar evolution details the processes by which stars change over time, typically including the evolutionary phases from protostar up to stellar death. It is largely studied with the help of numerical simulations that solve the set of first-order differential evolution equations commonly formulated in terms of the dependent variables $\{r, P, L, T, X_{\rm H}\}$, where r is the radial distance from the centre of the star, P is the pressure, L is the luminosity, T is the temperature and $X_{\rm H}$ is the hydrogen abundance (Christensen-Dalsgaard, 2008). P, T, X and the density ρ of a star are related through the equations of state (EoS).

The ultimate test of stellar-evolution theory lies in understanding the Hertzsprung-Russell diagram (H-R diagram, see Figure 1.5). The two most fundamental properties inferable when observing a star is its luminosity L and effective temperature T_{eff}, and a correlation between closely related quantities was first investigated by Ejnar Hertzsprung in 1911 and Henry Russell in 1913[3]. This gave eventual rise to a diagram with axes of luminosity (or related properties) and decreasing temperature (or related properties), on which every data point represents an observed star. Stellar evolution models aim at accurately predicting the locations of stars in the diagram. (Prialnik, 2010)

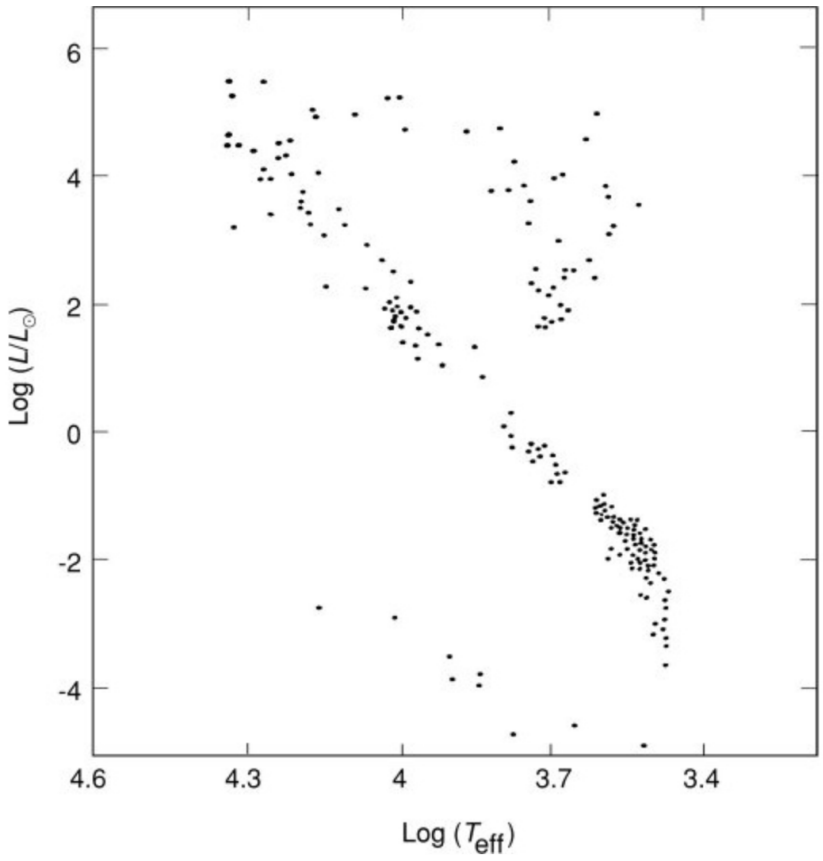

Figure 1.5: An H-R diagram of stars in the solar neighbourhood, showing luminosity $L/L_\odot$ versus effective temperature T_{eff}, where $L_\odot$ is the solar luminosity. This figure was taken from Prialnik (2010).

From Figure 1.5 it can be seen that most stars lie along a thin diagonal strip - this is referred to as the *main-sequence*, and stars along it are called *main-sequence*

[3]The original H-R diagram had axes of absolute magnitude and spectral type instead.

stars. The location of a star on the H-R diagram is a function of both its age and its initial mass - stars spend most of their lives on the main sequence, after which they move off the diagonal strip to their respective eventual fates.

This section discusses classical single-star evolution in the pre-main-sequence-, main-sequence- and post-main-sequence phases, with emphasis being placed on massive stellar evolution during the post-main-sequence phase as background to Chapter 2. The work by Christensen-Dalsgaard (2008) and Prialnik (2010) were used as sources for this background.

1.3.1 Pre-main-sequence evolution

Stars are formed through the phenomenon of fragmentation of interstellar gas clouds that become unstable to gravitational collapse. This fragmentation process can continue until fragments eventually reach stellar mass scales - the first to suggest such a model was Hoyle (1953). Once such a gas cloud fragment, bound by self-gravity, has formed, it can be regarded as the nucleus of a future star.

This nucleus continues to grow by accreting gas from its surroundings, converting the gravitational energy released in the process into thermal energy. The rise in temperature and density increases the opacity of the gas - when the contracting gas becomes opaque to its own radiation, the discernible boundary of the star in the making is referred to as the photosphere.

At first, the gas is too cold to oppose the gravitational pull, and contraction continues on the dynamical timescale. As the gas temperature increases, it eventually gets high enough to dissociate hydrogen molecules and ionise hydrogen and helium atoms, after which the temperature keeps rising again due to the ongoing release of gravitational energy. Eventually, the pressure of the gas becomes high enough to oppose the gravitational pull, and hydrostatic equilibrium[4] is achieved.

Stars in the pre-main-sequence phase are hard to detect due to both their scarcity (stars spend only roughly 1% of their lives here) and the fact that they are still enveloped in the remains of the cloud from which they were formed. After they

[4]Hydrostatic equilibrium is achieved when the gravitational force is balanced with outward pressure.

blow this envelope away, it becomes optically visible on the H-R diagram. The more massive a stellar object, the higher along the diagonal main sequence it will start its life as a fully-fledged star burning hydrogen.

1.3.2 Main-sequence evolution

Once stars first reach temperatures sufficient to start burning hydrogen in their cores, their location on the H-R diagram is referred to as the *zero-age main sequence* (ZAMS). Stars spend roughly 80% of their lives burning hydrogen on the main sequence (compared with roughly 1% spent in the pre-main sequence phase), and so the ZAMS is commonly regarded as the starting point of stellar evolution.

The nuclear energy generated through hydrogen-burning in stellar cores is transported outwards by either convection or radiation. In less massive stars with radiative cores, hydrogen-burning occurs mostly through the proton–proton chain (pp-chain) reaction[5] (Bethe, 1939a,b), whereas more massive stars with convective cores burn hydrogen predominantly through the temperature-sensitive carbon–nitrogen–oxygen (CNO) cycle[6] (von Weizsäcker, 1937, 1938; Bethe, 1939a,b).

As hydrogen is converted to helium in the core, the hydrogen abundance $X_{\rm H}$ decreases, causing the mean molecular weight to increase. It follows from the ideal gas law[7] that ρT needs to increase in response - the core therefore contracts, increasing ρ, and in turn raising the internal energy of the gas. This leads to the general trend for stars of all masses on the main sequence to have increasing luminosities during core hydrogen-burning - this can be seen in Figure 1.6, with the main-sequence designated as $1-2$. The same is not true for the effective temperature $T_{\rm eff}$. As the core of stars contract, their surface radii expands - but at

[5]The pp-chain reaction is a nuclear fusion reaction by which stars fuse hydrogen into helium. It starts at temperatures of $\sim 4 \times 10^6$ K (Reid and Hawley, 2005), making it the dominant source of energy in smaller stars. During the chain reaction, six protons are converted to a helium nucleus and two residual protons. The process releases energy in the form of gamma rays.

[6]The CNO cycle is a fusion reaction starting at temperatures of $\sim 15 \times 10^6$ K (Salaris and Cassisi, 2005) requiring carbon, nitrogen and oxygen isotopes as catalysts. It becomes the dominant source of energy at $\sim 17 \times 10^6$ K (Schuler et al., 2009). During the reaction four hydrogen nuclei are in effect converted into a He nucleus, releasing energy in the form of gamma rays.

[7]The ideal gas law states that $P = \rho k_{\rm B} T/\mu m_u$, where $k_{\rm B}$ is the Boltzman constant, μ is the mean molecular weight and m_u is the atomic mass constant.

very different rates. For low-mass stars the expansion is modest, and the increase in luminosity goes along with an increase in $T_{\rm eff}$. For more massive stars, however, the expansion is rapid, and the luminosity increase leads to a decrease in $T_{\rm eff}$.

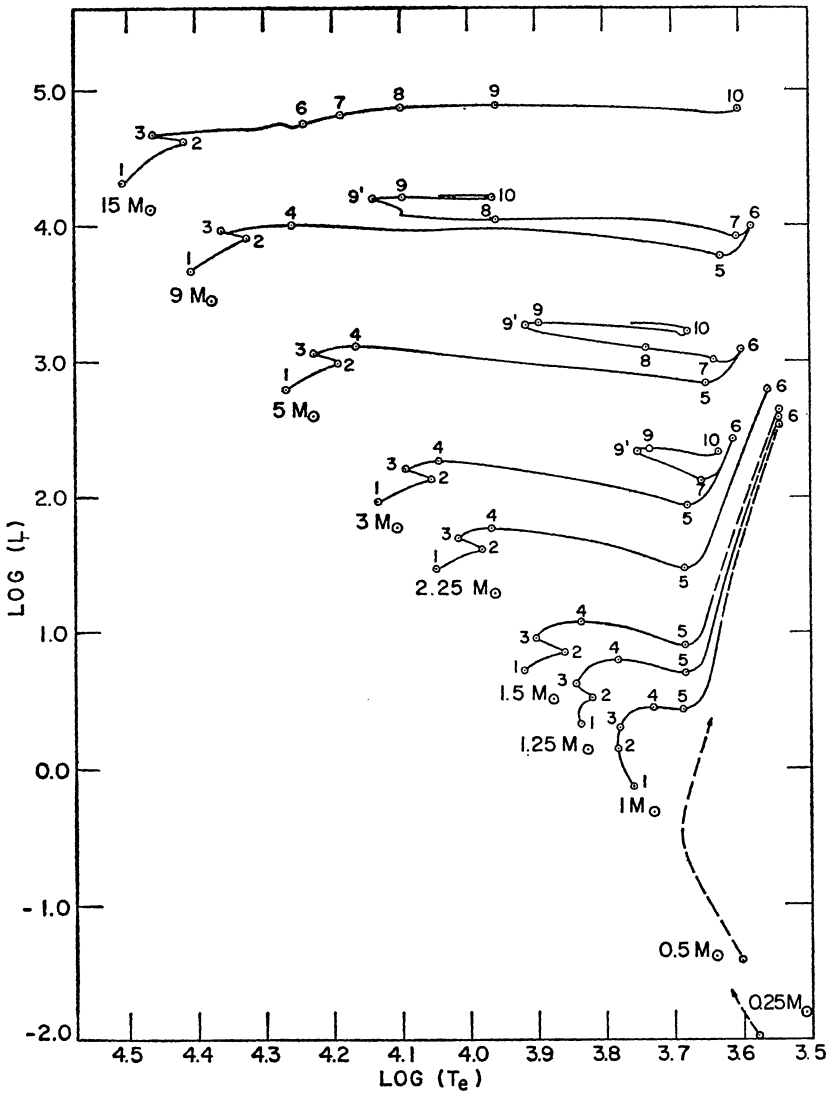

Figure 1.6: The H-R diagram for stars of different masses, from the ZAMS (the left side of the tracks). Luminosity L is in units of solar luminosity here, and $T_{\rm e}$ is the effective temperature. Phases are as follows: $1-2$, main sequence; $2-3$, overall contraction; $3-5$, hydrogen burning in thick shell; $5-6$, shell narrowing; $6-7$, red giant branch; $7-10$, core-helium burning; $8-9$, envelope contraction. This figure was taken from Iben (1967).

The method by which hydrogen is burned in the core have substantial effect on the later evolution of a star. Hydrogen is fused into helium most rapidly in the center of a star due to the temperature sensitivity of the nuclear reactions. For low-mass stars with mostly radiative cores, it is usually assumed that there

is no core mixing. More massive stars, on the other hand, have convective cores mixed on timescales much shorter than the evolutionary timescale, and so chemical composition is assumed to remain uniform. As a result hydrogen-burning, while still occurring mostly in the center due to the higher temperature, leads to a uniform reduction in X_{H} in the core.

It is important to note that stellar winds[8] cause mass loss at all stages of stellar evolution. On the main sequence, the rate of mass loss varies over a large range: for low-mass stars on the lower main sequence the mass-loss rate is low enough as to have barely any discernible effect on stellar mass whatsoever, while for massive stars, the winds are more intense and can remove a large fraction of the stellar mass. As stellar mass plays a role in determining the rate of evolution of stars (with more massive stars evolving faster while less massive stars evolve more slowly) as well as the eventual fate of stars, mass-loss has important consequences for the subsequent evolution of stars.

While stars of all masses partake in the main-sequence phase, subsequent evolution differs for stars of different masses. The evolutionary aspects of this thesis (see Chapter 2) are concerned with the evolution of *massive stars*, defined as stars with masses $M \gtrsim 10\,\mathrm{M}_{\odot}$. The next section is therefore only focused on the post-main-sequence evolution of these massive stars.

1.3.3 Post-main-sequence evolution of massive stars

Once hydrogen is exhausted near the center, the star has a core of helium and trace amounts of heavier elements. Due to the temperature of the helium core initially being far below the 10^8 K required for helium ignition, there is no nuclear energy generation in the core, its luminosity is generally very low and the temperature gradient is therefore small - the core can therefore be considered isothermal.

The hydrogen-containing region surrounding the core, called the *hydrogen shell source*, still has temperatures high enough for hydrogen-burning, and serves as the energy source from which the star's luminosity is derived. As hydrogen is

[8]Stellar winds are gas outflows ejected from the upper atmospheres of stars.

fused to helium in the shell and the mass of the helium core increases, the core starts contracting. The changes in the core causes a response in the observable properties of the star, largely explained by the *shell-burning law*: when the core inside a burning shell contracts, the envelope expands, and vice versa. As mentioned before, the general trend is for T_{eff} to increase with a decrease in effective radius R, and to decrease with an increase in R.

The massive expansion at the end of the main sequence, caused by the contracting helium core, results in the star moving to the right on an H-R diagram, onto the red giant or supergiant branch (see Figure 1.6). This transition is of short duration and is therefore rarely observed, causing a gap between the main sequence and the giant/supergiant branch on observational H-R diagrams termed the *Hertzsprung gap*.

The contracting helium core releases gravitational energy that is partly converted to thermal energy in the core. If the core is not degenerate (and in massive stars it won't be yet), the temperature in the core will increase until it is sufficiently high for helium-burning to start. The process is then roughly repeated. Helium-burning in the core continues until helium is exhausted (while the hydrogen shell source is maintained). The core, then consisting of carbon and oxygen and surrounded by both a helium- and hydrogen shell source, again starts contracting - if the contraction proceeds to the point where the core temperature is sufficiently high, carbon will start burning.

At this point, the core temperature is so high that there are significant energy losses due to neutrino emission - the nuclear energy source therefore has to compensate for these losses, along with supplying the high luminosity radiated at the surface of the star. Fusion of heavier elements releases far less energy per unit mass of burnt material than fusion processes for lighter elements, and so nuclear resources are consumed more rapidly for heavier cores. After core carbon burning, the rest of the nuclear burning stages pass rapidly, until finally an iron core is left, surrounded by shells of different compositions (silicon, oxygen, neon, carbon, helium, and a hydrogen envelope). Figure 1.7 shows a schematic of a massive star once it arrives at an iron core.

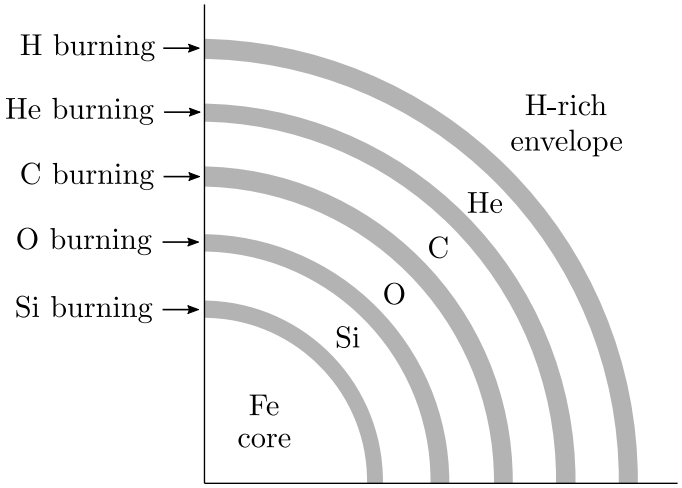

Figure 1.7: The layers and shell-burning layers of a massive star after it finished burning silicon and is left with an iron core. This figure was adapted from Prialnik (2010).

A characteristic of massive stellar evolution is that, throughout the various expansions, contractions and internal changes associated with the transitions between the burning of different elements and the fusion processes in the core, the luminosity (which is already near the Eddington critical limit[9] on the main sequence) remains almost constant (see Figure 1.6). The evolutionary track on the H-R diagram is therefore horizontal, moving back and forth between higher and lower effective temperatures.

During the final burning stages, when the star's core consists of iron, the electrons in the core become degenerate, and core contraction does not lead to an increase in core temperature anymore. Having no energy from nuclear fusion to oppose the gravitational pull, the star's core collapses in a supernova (SN) explosion (here called a Type II, or core-collapse supernova[10] (CCSN)). For progenitor stars above $8M_{\odot}$ and below $20M_{\odot}$, the CCSN leaves a neutron star (NS) remnant, whereas for progenitors more massive than this, a black hole (BH) is left.

[9]The Eddington limit, or Eddington luminosity L_{Edd}, is the maximum luminosity of a body such that hydrostatic equilibrium is maintained between the inward gravitational force and the outward radiation pressure.

[10]Core-collapse supernovae (CCSNe) are SNe in which the rapid gravitational collapse of a massive star's iron core leads to a violent explosion, leaving either a NS or BH remnant behind.

Wolf-Rayet stars and metallicity in massive stars

Classic Wolf-Rayet (WR) stars are massive, very hot (and therefore very luminous — thousands to a million times the solar bolometric luminosity), evolved stars fusing helium or heavier elements in their cores, that have lost their hydrogen envelope due to strong stellar winds — their spectra show prominent broad emission lines of ionised helium and highly ionised nitrogen (nitrogen sequence WR stars, or WN stars) or carbon (carbon sequence WR stars, or WC stars). As a result of the strong mass-loss they undergo during their earlier evolution, WR stars are more common at higher metallicities (Crowther, 2006). The lower limit to their progenitor star masses lie at $\sim 25\,\mathrm{M}_\odot$ for He-burning WN stars, $40\,\mathrm{M}_\odot$ for WC stars, and $75\,\mathrm{M}_\odot$ for H-burning WN stars, with typical masses of WR stars falling between $10 - 25\,\mathrm{M}_\odot$, and extending up to $80\,\mathrm{M}_\odot$ for H-burning WN stars (Crowther, 2007).

Meynet and Maeder (2005) found that the rotational velocities of the most massive O-type stars is dependent on the mass loss rates, a quantity that is, in turn, dependent on the initial metallicity value of the star. They find that rotation lowers the minimum initial mass for a star for entering the WR phase and that, regardless of metallicity, rotating stars enter the WR phase at an earlier stage of evolution. WR stars are, in general, believed to have relatively low rotational velocities on the order of $< 50\,\mathrm{kms}^{-1}$ (Meynet and Maeder, 2005).

The metallicity of high mass stars is paramount in order to understand their evolution; we will see in Chapter 2 that binary evolution, coupled with the metallicity of these same stars, will ultimately determine the fate of such high mass stars. The same is true for stars that evolve alone, without mass transfer. (Limongi and Chieffi, 2018) found that for massive non-rotating stars ($13 - 120\,\mathrm{M}_\odot$) at solar metallicity, the maximum mass at which red supergiant stars explode is $\sim 17\,\mathrm{M}_\odot$, with more massive stars instead entering a WR phase and exploding as WR stars. For rotating massive stars, however, they find that all of them explode as WR stars. Rotation-induced instabilities trigger the interaction between the He- and H-burning shells that causes the synthesis of a large primary amount of CNO products, and it has been shown that non-rotating to moderately rotating massive stars of all

metallicities produce remnant masses on the order of those inferred by the first few gravitational wave detections (Limongi and Chieffi, 2018). The modeling of such massive stars still has many theoretical uncertainties, including specifically, but not exclusively, how they lose mass via winds.

Pair-instability supernovae

For progenitor stars of low to moderate metallicity (in high-metallicity stars stellar wind carries away too much mass) with masses between roughly $130 - 250\,\mathrm{M}_\odot$, the end fate of evolution is a pair-instability supernova (PISN, see e.g. Woosley et al. 2002; Woosley 2017, 2019; Belczynski et al. 2016; Spera and Mapelli 2017). In large, hot stars with temperatures above $\sim 3 \times 10^8\,\mathrm{K}$, gamma rays are the predominant form of photon production in the core - the radiation pressure they supply supports the star against gravitational collapse. Sufficiently energetic gamma rays (with energies above 1.022 MeV) can interact with atomic nuclei to achieve pair production, in which the energy of the photon is converted into an electron-positron pair. These pairs can also annihilate each other to again produce gamma rays. At the very high densities found in large stellar cores, pair production and electron-positron annihilation happens rapidly, and the core remains stable.

As the temperature, and therefore the gamma ray energies, increases, an increasing amount of gamma ray energy is absorbed in pair-production. The energy density reduction leads to a decrease in radiation pressure, in turn causing the star to contract. The subsequent compression and heating of the core leads to further increases in gamma ray energies, making their interactions with atomic nuclei more likely and increasing the rate at which pair-production occurs. This runaway process therefore sees gamma rays created at an ever-increasing rate, with more and more of them absorbed in pair-production, and with electron-positron annihilation insufficient to halt further contraction of the core - this runaway process ends in a supernova blowing the star completely apart, and leaving no stellar remnant behind.

For progenitor stars with masses in the range $\sim 130-250\,\mathrm{M}_\odot$ that develop helium core masses between roughly $60 < M_{\mathrm{He}}/\mathrm{M}_\odot < 130$ (Heger et al., 2003), a runaway

process starts as soon as conditions support pair-instability the first time. Stellar collapse compresses the core, and the overpressure is sufficient to cause runaway nuclear fusion, resulting in a thermonuclear explosion. The thermal energy released being larger than the gravitational binding energy, the star is completely disrupted and no remnant is left behind. This leads to a mass gap, referred to as the 'PISN gap', in the mass distribution of stellar black holes, found between roughly $60 - 130\,\mathrm{M}_\odot$.

For progenitor stars between roughly $100 - 130\,\mathrm{M}_\odot$ that develop smaller helium cores between roughly $30 < M_{\mathrm{He}}/\mathrm{M}_\odot < 60$ (Woosley et al., 2007), although pair-production occurs, the resulting decrease in radiation pressure is insufficient to cause the overpressure necessary for a runaway reaction and a supernova. The contraction instead increases thermonuclear activity, which supplies the energy to withstand the gravitational pressure and returns the star to equilibrium. These events present as pulses, and through a series of such pulses stars in this mass range will shed mass until their cores eventually leave the pair-instability mass range, and collapse into black holes after a supernova explosion. Due to pulsational PISNe (PPISNe) and the details of stellar evolution and rotational effects (see e.g. Mapelli et al. 2020), the lower edge of the PISN gap can be as low as $\sim 40\,\mathrm{M}_\odot$ (see Di Carlo et al. 2020, and references therein).

Progenitor stars above $250\,\mathrm{M}_\odot$, on the other hand, instead undergo photodisintegration[11] after the initial pair-instability collapse (Bond et al., 1984; Fryer et al., 2001). This endothermic process absorbs the excess energy from earlier stages, reducing the pressure and temperature in the star's core before the runaway nuclear fusion can result in an explosion. Instead, the lack of energy to oppose gravitational collapse leads to the formation of a black hole, giving rise to the upper edge of the PISN mass gap around $130\,\mathrm{M}_\odot$.

Data from the first and second aLIGO/Virgo runs are consistent with a maximum black hole mass of $\sim 45\,\mathrm{M}_\odot$, in good agreement with the prediction of a PISN gap (Abbott et al., 2019a). A black hole merger with either one or both components in the PISN gap has, however, been found in the third aLIGO/Virgo run: components

[11] Photodisintegration is an endothermic nuclear reaction whereby an atomic nucleus absorbs a high-energy gamma ray and immediately decays by emitting a subatomic particle.

of masses $85^{+21}_{-14}\,M_\odot$ and $66^{+17}_{-18}\,M_\odot$ merged to form a black hole of mass $142^{+28}_{-16}\,M_\odot$ (Abbott et al., 2020d). Black holes in the PISN gap may be due to a number of exotic channels: primordial black holes might have masses in the PISN gap (Carr and Hawking, 1974; Carr et al., 2016); black holes born from the merger of two smaller black holes ('second'- or 'third-generation' black holes, see e.g. Gerosa and Berti 2017) could end up with masses in the PISN gap; the merger of a massive star having a well-developed helium core with a non-evolved companion might give birth to an evolved star with an oversized hydrogen envelope - if the helium core remains below $\sim 32\,M_\odot$ and the star collapses before losing much of its envelope, the resulting black hole could be in the PISN gap (Spera et al., 2019; Di Carlo et al., 2019); if an energy source, in addition to nuclear fusion, is added throughout a star, it is possible for a black hole remnant to be left behind after the PISN Ziegler and Freese (2020) - an example of such an energy source could be dark matter annihilation within the star.

PISNe are again discussed in Chapter 2, and the above serves as background to some of the work contained there. Other evolutionary outcomes to stellar fates are not relevant to Chapter 2, and is therefore not discussed here.

1.4 Binary Evolution

Most stars in the Universe are not single, but form part of binary (or multi-) star systems in which orbital periods P can range all the way up to $\sim 10^6$ yr (Podsiadlowski, 2014). In most cases, the components of binary systems are far enough apart that their individual courses of evolution are barely affected. A large fraction of binaries, however, are close enough ($P < 10$ yr) for mass to be transferred from one star to the other, changing the stellar structure and subsequent evolution of both stars (Podsiadlowski, 2014). Although the numbers are somewhat uncertain, binary surveys suggest that $30\% - 50\%$ of binary systems contain interacting components (with a higher binary fraction for more massive stars - see e.g. Duquennoy and Mayor 1991 and Kobulnicky and Fryer 2007). Understanding

binary systems and their interactions is therefore crucial for the understanding of the wealth of phenomena they can bring about.

Although this thesis contains chapters on both neutron star low-mass X-ray binary (NS LMXB) and black hole binary (BHBH) systems, we are only concerned with the evolutionary pathways involved in obtaining the latter. After discussing the Roche Lobe and mass transfer in binary systems (making use of Prialnik 2010 and Podsiadlowski 2014), the possible evolutionary pathways that could produce BHBH systems close enough to merge in our current epoch is therefore investigated.

1.4.1 The Roche lobe

A single star (viewed as a point mass) generates a spherically symmetric gravitational field that can be described by spherical equipotential surfaces centred on it. A test particle can move freely on such a surface without requiring or releasing energy. When moving from one surface to another, however, it either has to gain energy to reach a higher potential value (moving further away from the star) or lose energy to drop to a lower potential value (moving closer to the star).

For a binary system these equipotential surfaces have more complicated geometrical shapes, however. Approximating the two stars as point masses denoted by M_1 and M_2, respectively, where $M_1 > M_2$, having circular orbits around their common centre of mass with constant angular velocity ω. The angular velocity can be expressed as

$$\omega^2 = \frac{G(M_1 + M_2)}{a^3}, \tag{1.38}$$

where $\omega = 2\pi/P$ with P the rotation period, and a is the constant distance between the stars. Equation 1.38 expresses Kepler's third law, stating that $P^2 \propto a^3$. In a co-rotating Cartesian coordinate system (x, y, z) with its origin fixed at $M1$, the masses M_1 and M_2 are located at $(0, 0, 0)$ and $(a, 0, 0)$, respectively. The centre of mass is at $(x_{\rm CM}, 0, 0)$, where $x_{\rm CM} = aM_2/(M_1 + M_2)$. At any point in space, a test particle will then experience a gravitational potential Φ given by

$$\Phi = -\frac{GM_1}{(x^2+y^2+z^2)^{1/2}} - \frac{GM_2}{[(x-a)^2+y^2+z^2]^{1/2}} - \frac{1}{2}\omega^2\left[\left(x - \frac{M_2 a}{M_1+M_2}\right)^2 + y^2\right]. \tag{1.39}$$

Here, the first two terms are the gravitational potentials of M_1 and M_2, and the third term is the rotational potential resulting from the fictitious centrifugal force of the rotating system. Defining the mass ratio as $q \equiv M_2/M_1$ and measuring distances in units of a, the potential can be normalised such that

$$\Phi' = \frac{2}{(1+q)(x^2+y^2+z^2)^{1/2}} + \frac{2q}{(1+q)[(x-1)^2+y^2+z^2]^{1/2}} + \left[\left(x - \frac{q}{1+q}\right)^2 + y^2\right], \tag{1.40}$$

where

$$\Phi' = \left[-\frac{G(M_1+M_2)}{2a}\right]^{-1}\Phi. \tag{1.41}$$

Equipotential surfaces obtained by setting $\Phi' = C$, with C a constant, are called *Roche equipotentials*, after Édouard Albert Roche who first studied this problem in the nineteenth century. For large values of C, the surfaces will form separate, closed, elongated spheroids around each point mass - the larger C, the more spherical the surfaces will be. As the value of C decreases, surfaces become more distorted, especially close to the centre of mass along the line of centres, until eventually, for a critical value of C, the surfaces surrounding the point masses will touch one another along the line of centres. This figure-eight configuration, known as the *Roche limit* surface, can be seen in Figure 1.8, with the point of contact known as the *inner Lagrangian point*, denoted by L_1. This is one of five so-called Lagrangian points where the gradient of the potential is zero (i.e. where the force in the co-rotating frame is zero). Apart from L_1, the other two Lagrangian points of interest here are L_2 and L_3, both also located along the line of centres - L_2 to the right of the less massive star, and L_3 to the left of the more massive star, as indicated in Figure 1.8.

The volumes enclosed by the Roche limit surface are called *Roche lobes*, and they delimit the volume within which material is gravitationally bound to only one star. When one star fills its Roche lobe, matter can flow through the L_1 point into the Roche lobe of the other star - this mass transfer is called *Roche-lobe overflow* (RLOF). For $q = 1$, the lobes are identical, but as q decreases the lobe around the more massive star will expand while the lobe around the less massive star will shrink.

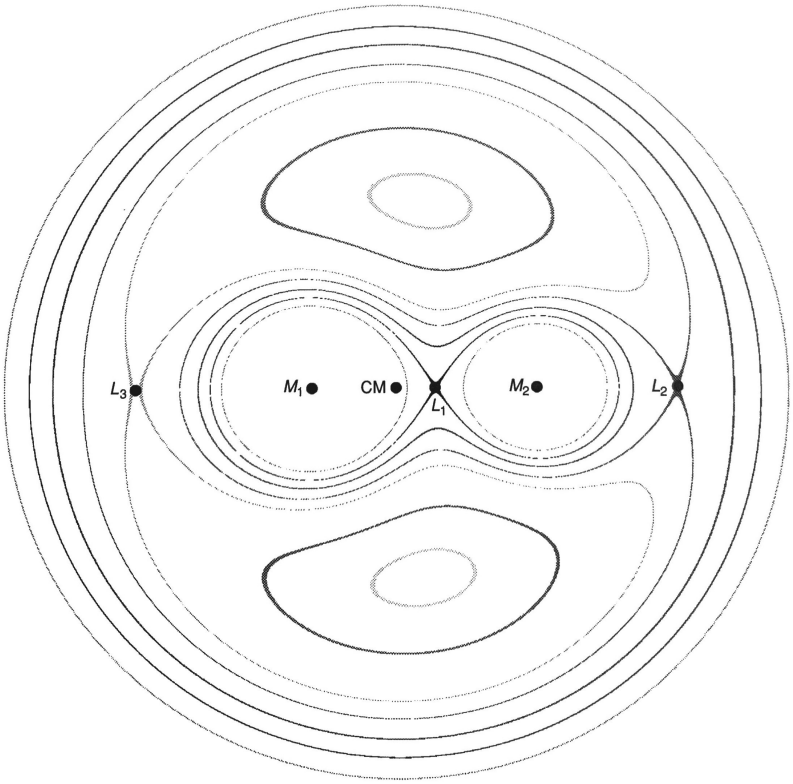

Figure 1.8: The projection of Roche equipotentials for two masses (M_1 and M_2, with $M_1 > M_2$) with a mass ratio of $q = 0.6$ on the orbital plane ($z = 0$). The Lagrangian points L_1, L_2 and L_3 and the centre of mass (CM) are also indicated. This figure was taken from Prialnik (2010).

The *Roche radius* r_{L} of a star is defined as the radius of a sphere having the same volume as the star's Roche lobe. It is well approximated by Eggleton (1983), and can be written as

$$\frac{r_{\mathrm{L}}}{a} = \frac{0.49\, q^{2/3}}{0.6\, q^{2/3} + \ln\left(1 + q^{1/3}\right)}, \tag{1.42}$$

corresponding to the lobe of M_2. For the lobe of M_1, q should be replaced by q^{-1}. We next discuss examples of three binary evolution mechanisms that could lead to the production of BH binary systems close enough to merge in our current epoch. Dynamical formation and Classical CE evolution are discussed briefly, whereafter chemically homogeneous evolution (CHE), the focus of Chapter 2, is investigated.

1.4.2 Dynamical formation

Regions of high stellar density, such as those found in globular clusters or galactic nuclei, could serve as sites of dynamical formation of stellar BHBH binaries. These environments harbour an overdensity of compact stellar remnants (such as NSs and BHs, produced by stellar evolution of the most massive stars in the cluster) close to their centre by virtue of mass segregation[12]. (Banerjee et al., 2010)

BHs will segregate to the core of the cluster, where they will form a dynamically isolated sub-cluster of BHs (Mackey et al., 2007). Here, the BH density is large enough for BH binary formation through three-body encounters (Heggie and Hut, 2003) to become important. These dynamically-formed BH binaries then harden[13] through encounters with BHs or other BH binaries in the surrounding area (this is known as the Heggie-Hills law[14]; see Heggie 1975.), whereafter the released binding energy is carried away by the single BHs and BH binaries involved in the encounters. This results in their ejection from the cluster's core to larger radii, where they transfer energy to cluster stars and gradually sink back to the BH core. As BH binaries harden in this way, the encounter-driven recoil becomes stronger, until it is eventually strong enough to eject the encountering single BHs or BH

[12]During a close encounter of two members of a cluster, the kinetic energy of the two members tend to equalise due to equipartition. This requires less massive objects to move faster than more massive objects, resulting in more massive members sinking to lower orbits (closer to the center of the cluster) while less massive members will rise to higher orbits (further away from the center). This phenomenon is called mass segregation.

[13]'Hard' binaries have smaller orbits, whereas 'soft' binaries have larger orbits.

[14]The Heggie-Hills law states that, given some distinction between small (hard) and large (soft) orbits, encounters with third objects tend to, on average, make large orbits larger and small orbits smaller. Consider a cluster with a velocity dispersion σ containing objects all having mass M, with some stars in binaries having binding energies ε. Using the equipartition principle, encounters between single BHs and hard binaries, where $\varepsilon > M\sigma^2$ will tend to transfer energy from the binary to the single BH and so increase the binary's binding energy, making it even harder. The opposite applies for interactions between single BHs and soft binaries.

binaries from the cluster - this process can result in BH binaries both outside the cluster and in the cluster core hard enough to merge in our current epoch via gravitational radiation (Banerjee et al., 2010).

Using detailed fits to dynamical models of binary BH formation in dense stellar clusters in combination with a cosmological model of cluster formation over cosmic time, Rodriguez and Loeb (2018) found the resulting BH merger rate from dynamical formation in globular clusters to fall in the range $4 - 18$ Gpc^{-3}yr^{-1} in the local Universe, with a typical rate of 14 Gyr^{-3}yr^{-1}. Their results are in good agreement with other studies of the same nature (see Fragione and Kocsis 2018, Hong et al. 2018 and Choksi et al. 2019). A further study by Antonini and Rasio (2016) found the BHBH merger rate resulting from dynamical formation in galactic nuclei in the local Universe to be ≈ 1.5 Gyr^{-3}yr^{-1}.

Rodriguez and Loeb (2018) further compare BHBH merger rates resulting from dynamical formation, triple origin evolution (see Section 1.4.4) and isolated binary evolution (common envelope evolution, discussed in Section 1.4.3, together with chemically homogeneous evolution, discussed in Section 1.4.5) to show possible ways in which these channels can constitute the full merger rate observed by aLIGO/Virgo. Considering both a uniform logarithmic BH mass distribution and a power-law BH mass distribution (as local rates are highly sensitive to the assumed BH mass distribution), they find that globular clusters contribute roughly half of all mergers in the local Universe when one assumes the former, and roughly one out of every seven BHBH mergers when assuming the latter distribution (with triple origin evolution contributing one out of nine).

1.4.3 Common envelope evolution

Common envelope (CE) evolution is one of the least understood binary interactions (see e.g. Iben and Livio 1993; Taam and Sandquist 2000; Podsiadlowski 2001), but it is also one of the main mechanisms thought to be responsible for dramatically decreasing the orbital period of initially wide binaries, possibly from many years down to several hours or days (Paczynski, 1976).

For the eventual formation of close BHBH systems able to merge in a Hubble time[15], CE typically occurs when a more massive O-type donor star with a compact companion (in this case a BH) becomes a red supergiant (Kruckow et al., 2016). As the donor overfills its Roche Lobe and transfers mass to its companion, the Roche radius shrinks as the donor keeps expanding, causing the donor to overfill its Roche lobe by an ever larger amount. This results in a runaway mass transfer, with components eventually overfilling their Roche lobes with the mass forming a common photosphere engulfing both components. This is called a common envelope.

Once the CE has formed, friction between the immersed binary and the envelope causes the binary to lose orbital energy, resulting in the two components spiralling towards each other until enough orbital energy has been released for the envelope to be ejected (Paczynski, 1976). Once the envelope is ejected, the spiral-in phase ends, leaving a much closer binary (consisting of the core of the giant and a BH secondary) having an orbital period typically in the range $0.1 < P/\mathrm{day} < 10$ (Podsiadlowski, 2014).

The core will eventually collapse into a BH, the result being a close BHBH system. In the case where the orbital energy released is not sufficient for envelope ejection, the spiral-in will continue until the core of the donor star has merged with the BH companion (Podsiadlowski, 2014).

Using a Monte Carlo binary population synthesis code to explore various different models of the above channel, Belczynski et al. (2020) found the predicted BHBH merger rate density to vary between $1.24 - 1368\ \mathrm{Gyr}^{-3}\mathrm{yr}^{-1}$ in the local Universe.

1.4.4 Triple origin evolution

BHBH systems close enough to merge in a Hubble time can also form through the secular interaction of a binary BH with a distant third companion in the field of a galaxy (Silsbee and Tremaine, 2017; Antonini et al., 2017). At an appropriate distance and inclination, the third companion can perturb the inner binary by

[15]Hubble time is defined as $1/H_0$, where H_0 is the Hubble constant with a value of about 70 (km/s)/Mpc. It is the time required for the Universe to have expanded to its current size. When it is said that a binary 'merges in a Hubble time', it is meant that said binary will merge in our current epoch.

inducing highly eccentric oscillations in it, in turn causing the orbit of the inner binary to become nearly radial (this is known as the Lidov-Kozai effect - see the review by Naoz 2016). Energy loss due to gravitational wave radiation will then cause the rapid merger of the inner binary.

Using a population synthesis approach, Rodriguez and Antonini (2018) modelled field stellar-mass BH triple systems across a range of different stellar metallicities and initial conditions, and found a resulting BH merger rate in the range $2 - 25$ Gpc^{-3}yr^{-1} in the local Universe. They further found that the channel naturally yields heavy binary BHs with near-zero effective spins, similar to most of the mergers observed to date.

1.4.5 Chemically homogeneous evolution

The CHE scenario requires binary systems that are in near contact at the onset of hydrogen burning. Such close binaries likely develop during star formation, where fragmentation of the molecular cloud can explain the formation of close binaries or multiple-star systems (Boss, 1992). On the main sequence, the tidal interactions between the components of one such binary system can cause rapid stellar rotation leading to the deformation and deviation from spherical symmetry, which for massive stars (where the effects of radiation are important) have been shown to keep the stars chemically mixed and homogeneous throughout core hydrogen burning (Eddington, 1924; Maeder, 1987; Langer, 1992; Heger and Langer, 2000).

Maeder (1987) showed that, due to the high radiative viscosity $\nu_{\rm rad}$ of massive stars ($\nu_{\rm rad}$ is dependent on temperature, and therefore also on stellar mass), the diffusion coefficient $D = {\rm Re}^*\nu$ (with Re* the Reynolds number and viscosity $\nu = \nu_{\rm mol} + \nu_{\rm rad}$) would be large enough to effectively mix the stellar interior during the main sequence lifetime. This would happen as long as the star was rotating above some critical velocity below which turbulent diffusive mixing (due to either rotation or tides in binaries) would be halted by the stabilising effects of the μ-gradient (the molecular weight gradient). The higher the rotation velocity, the larger Re* and D, and the larger the critical μ-gradient above which mixing is inhibited. Maeder

(1987) estimated that, without taking the inhibiting effects of the μ-gradient into account, stars initially more massive than about $25\,M_\odot$ with a low rotational velocity of about $\nu_{\rm rot} = 30\,{\rm km\,s^{-1}}$ (corresponding to $\alpha = -d\ln\Omega/d\ln r = 0.3$, with Ω the angular velocity) would get fully mixed - for higher rotation velocities the threshold mass for full mixing would be even lower than $25\,M_\odot$. Taking the μ-gradient into account, however, their numerical models show that only at rotational velocities corresponding to an α near or lower than 0.1 does the μ-barrier not succeed in preventing turbulent diffusion for fully homogeneous evolution to occur.

For single stars, low metallicity is required to ensure that mass loss from stellar winds is low to avoid the associated spin-down, so that the stars can essentially remain chemically homogeneous up to core hydrogen exhaustion (Yoon and Langer, 2005; Woosley and Heger, 2006; Brott et al., 2011a; Köhler et al., 2015; Szécsi et al., 2015). Due to their lack of composition gradients, these stars do not maintain a hydrogen-rich envelope and as such avoid the normal dramatic expansion during the post-main sequence phase. This motivated de Mink et al. (2009) to propose that close binary systems consisting of rapidly rotating, massive stars at low metallicities undergoing chemically homogeneous evolution could avoid merging during their early evolution and evolve without ever undergoing a contact or mass-transfer phase (see also de Mink and Mandel 2016a,b; Song et al. 2016).

In contrast, through detailed binary evolution models where the efficiency of rotational mixing processes had been calibrated to match the range of nitrogen abundances observed in early type stars (Brott et al., 2011b), Marchant et al. (2016) found that contact-free evolution in these close binaries is very rare, and that many systems undergo contact (referred to as 'overcontact') but still avoided merging during the core hydrogen burning phase. During overcontact, both stellar components overfill their Roche volumes. The evolution during the overcontact phase differs from the standard evolution during a more classical CE phase as co-rotation is maintained as long as material stays inside the L2 point. The binary system can therefore avoid a spiral-in phase due to viscous drag, giving rise to a stable system that evolves on a nuclear timescale. If both stars overflow the L2

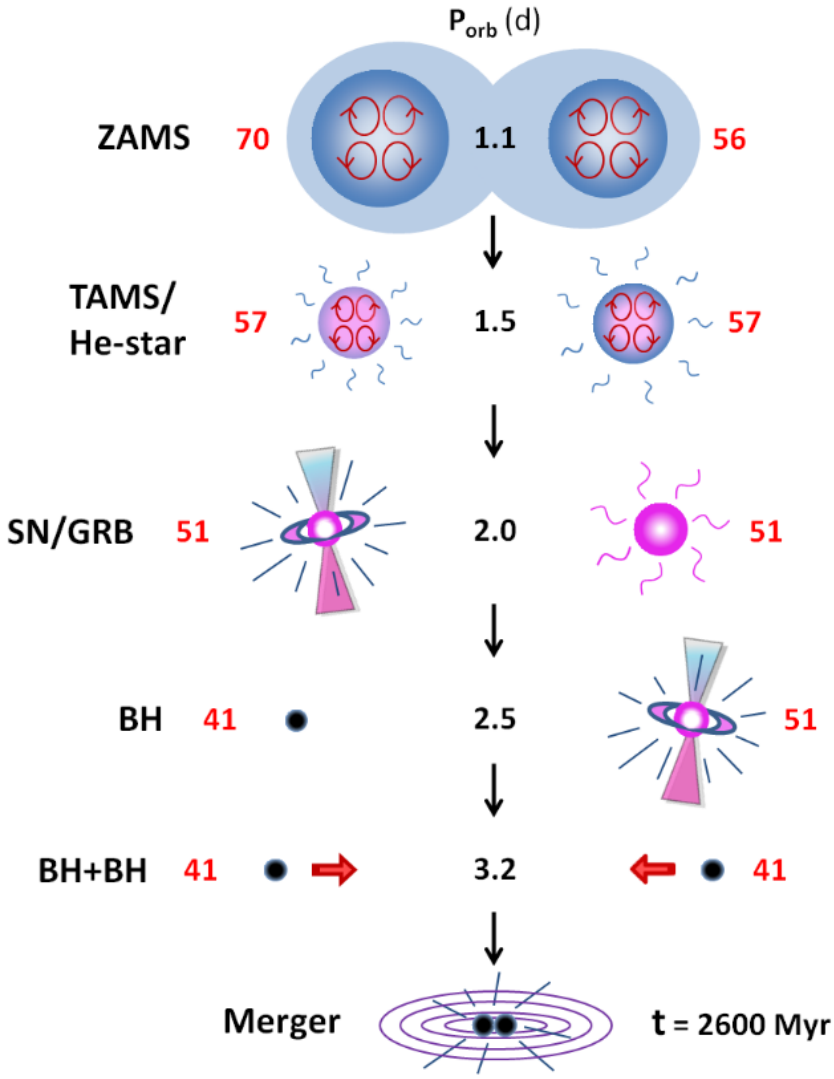

Figure 1.9: Binary evolution from the ZAMS to the BH merger stage (providing a merger after 2.6 Gyr) incorporating the CHE mechanism. Masses of binary components (in solar masses) are indicated in red, orbital periods (in days) are indicated in black, and the initial metallicity is $Z = Z_{\odot}/50$, where $Z_{\odot}$ is the solar metallicity. A contact phase near the ZAMS results in an eventual mass ratio of one, whereafter stellar wind mass loss causes the orbit to widen. This figure was taken from Marchant et al. (2016), with undeclared acronyms as follows: TAMS: termination of hydrogen burning; He-star: helium star; GRB: gamma-ray burst.

point, however, the system is expected to rapidly merge either due to the resulting angular momentum losses or due to an inspiral caused by a loss of co-rotation.

A system will typically enter an overcontact phase at the early stages of core hydrogen burning. Mass will be transferred back and forth between the binary components until their masses are roughly equal. During the main sequence and

post-core-hydrogen-burning phase where both stars are compact detached helium stars (see Figure 1.9), stellar wind mass loss is expected to result in a widening of the orbit, driving the system out of contact. As these winds are metallicity dependent (Vink et al., 2001; Vink and de Koter, 2005; Mokiem et al., 2007), more metal-rich systems evolve to longer orbital periods, and as the system remains tidally locked its rotational velocity can be lowered to the point where chemically homogeneous evolution is no longer effective. Even if the system remains chemically homogeneous, the orbit may be too wide for the resulting BHBH system to merge in a Hubble time. This is the reason why the CHE scenario, at least in its simplest version, requires low metallicity. Figure 1.9 illustrates the role of the CHE mechanism in binary evolution from the ZAMS to the BH merger stage, as laid out in Marchant et al. (2016).

This channel forms the basis of the investigation in Chapter 2, where we determine the predicted BHBH merger rate it gives rise to.

1.5 X-ray Binary Systems

An X-ray binary is a system in which one of the binary components is a compact object (either a BH or a NS), and where the binary is close enough to allow accretion, causing the system to become very bright in the X-ray. X-ray binaries can be divided into either high-mass or low-mass X-ray binaries (HMXBs or LMXBs); in HMXBs, the companion to the compact object has a mass typically larger than $10M_{\odot}$, whereas in LMXBs the companion star is faint and typically of a mass lower than $1M_{\odot}$. There are two main ways in which mass is transferred from the companion to the compact object in these systems: RLOF and wind accretion[16]. The X-ray binaries focused on in this thesis are low-mass systems, where mass transfer happens via RLOF.

The onset of RLOF requires either the companion star to expand past its Roche radius $r_{\rm L}$ (see Equation 1.42) during the course of its evolution, or the orbital separation to shrink (as a result of angular momentum losses). The transferred matter cannot fall directly onto the compact object due to the conservation of

[16]Wind accretion happens when the companion star has strong, outward flowing stellar winds. As the compact object moves through the ejected material while the binary components orbit one another, it will accumulate a fraction of the material.

angular momentum - instead of matter falling radially towards the compact object, it therefore orbits circularly at a certain radius from it. If the time needed for redistribution of angular momentum in the ring is longer than the timescale of energy loss, viscous dissipation will result in energy losses that will force matter to arrange itself into a sequence of circular concentric annuli with decreasing radius. This is called an accretion disc.

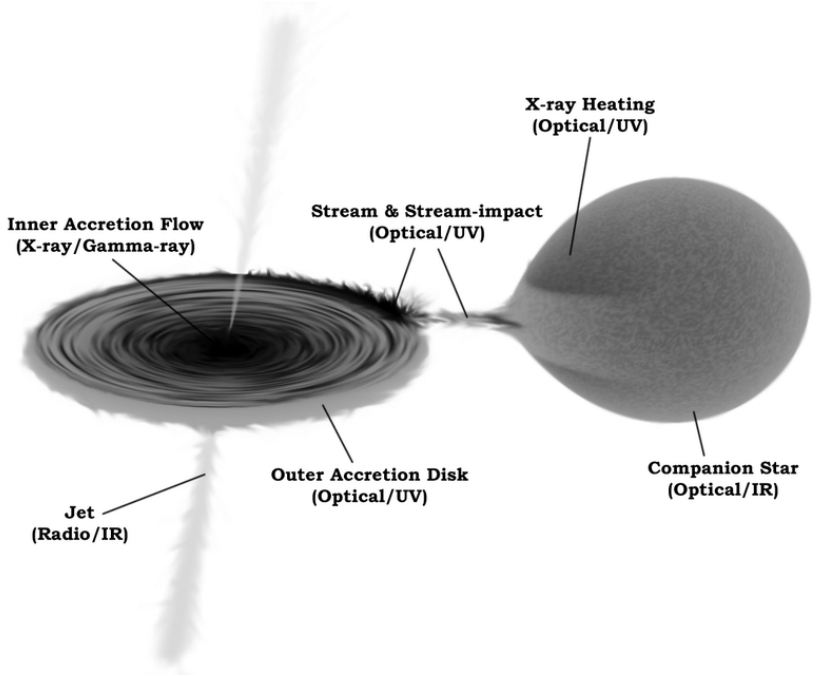

Figure 1.10: An artist's impression of a low-mass X-ray binary system, taken from Hynes (2010). Brightest areas appear darkest. Acronyms: UV: ultraviolet; IR: infrared.

At large disc radii, the accretion disc is relatively cold and will emit in the optical spectrum, whereas for the innermost regions of the disc, close to the compact object, the accretion flow can reach temperatures higher than $\sim 10^7$ K, allowing for X-ray radiation (Shakura and Sunyaev, 1973). For a Shakura-Sunyaev accretion disc (Shakura and Sunyaev, 1973), it is assumed that viscous stresses in an optically thick, geometrically thin Keplerian disc will transform gravitational potential energy to heat, which will be radiated away locally at a given radius (winds, jet cooling and advection are neglected). Each disc element is expected to radiate roughly as a blackbody, and if in thermal equilibrium, the temperature profile of the disc can be given by

$$\sigma T^4 = \frac{3GM\dot{M}}{8\pi r^3}\left[1 - \left(\frac{r_i}{r}\right)^{1/2}\right], \tag{1.43}$$

where G is the gravitational constant, σ is the Stefan-Boltzmann constant, M is the mass of the compact object and $\dot{M}$ the accretion rate onto the object. The innermost radius of the accretion disc is denoted by r_i, and r is the radial distance from the compact object, with $r \geq r_i$ (see Bhattacharyya (2002) or Lasota (2016) for a derivation). The assumption of thermal equilibrium leads to the temperature being independent of viscosity, and for $r >> r_i$, we have that

$$T(r) \sim r^{-3/4}. \tag{1.44}$$

The bulk of the gravitational potential energy is released at smaller radii, and so more luminosity is generated in this region. This is dissipated over a smaller area, and so the temperature increases inwards, radiating in the X-ray.

Due to the above, X-ray binaries are good natural laboratories with which to test general relativity in the strong field with, and they additionally allow for the study of extremely dense matter. In the case of NS LMXB systems, they can be used to investigate the equations of state of collapsed stars, where densities are thought to exceed those in atomic nuclei. A comprehensive study of X-ray binaries, however, needs to also take into account the phenomenon of relativistic jets[17]. On larger scales, e.g. in active galactic nuclei[18] (AGN), these jets are among the most powerful events in the Universe - and they are also commonly found in X-ray binaries. Jets are launched from regions very close to the compact object, and seem to be strictly related to the accretion mechanisms. The study of X-ray binaries and the proper understanding of their accretion processes is therefore fundamental to understanding relativistic jets - on large scales, like that for AGN, understanding

[17]Relativistic jets are collimated anti-parallel outflows of matter launched at relativistic velocities from regions very close to the central compact object.

[18]An active galactic nuclei (AGN) is a dense region at the center of a galaxy with a much higher than normal luminosity. The non-stellar radiation detected from AGN is thought to be due to the accretion of matter by a supermassive BH at the galaxy center.

the accretion-ejection picture can lead to the eventual better understanding of the formation and evolution of galaxies and large-scale structures in the Universe.

In this thesis, the focus is on NS LMXBs, and reference to BH LMXBs will only be made when useful - Section 1.5.1 will discuss the origin of persistent and transient behaviour, Section 1.5.2 will discuss the difference between NS and BH spectral evolution, and Section 1.5.3 will describe the relation between NS LMXB spectra and their colour-colour diagrams. Section 1.5.4 will investigate the differences between atoll and Z-sources, Section 1.5.5 will look at power density spectra and fast-time variability, and Section 1.5.6 depicts the outburst evolution of a NS LMXB system along an rms-intensity diagram. Finally, Section 1.5.7 will cover proposed models for the existence of quasi-periodic oscillations (QPOs) in the power density spectra of LMXB systems, and Section 1.5.8 will discuss the relativistic precession model (RPM) on which Chapters 3 and 4 is based.

1.5.1 The origin of persistent and transient behaviour

Two broad categories of LMXBs exist: *persistent* systems are those that are always active, with typical X-ray luminosities above $L_X \sim 10^{36}$ erg/s, while *transient* systems reside in a quiescent state ($L_X \sim 10^{30} - 10^{34}$ erg/s) for most of their lives, with occasional outbursts lasting from weeks to years, and recurring on timescales of months to decades. The majority of BH LMXBs are classified as transient systems, while the persistent population consists mostly of NS LMXBs (Done et al., 2007). This long term outburst behaviour of accreting sources stems from a disc instability, namely the hydrogen ionisation instability.

Shakura-Sunyaev discs that are accreting at low rates are unstable (thermally and viscously) at temperatures around $10^4 - 10^5$ K, where hydrogen get ionised. At low accretion rates the temperature in the disc is low, so that material is neutral and the opacity is low. A thermal instability is triggered when there is a small temperature increase in the disc, enabling the highest-energy photons to ionise some of the hydrogen, thereby leading to a drastic increase in opacity. The photons are absorbed in the process, increasing the disc temperature, so that even more

photons are able to ionise hydrogen (which keeps increasing the opacity), even more photons are trapped, and the temperature keeps increasing in a runaway fashion as a result. This process comes to a halt when most of the hydrogen is ionised (Frank et al., 2002; Done et al., 2007; Kato et al., 2008).

The increased temperature at a given radius in the disc means an increase in mass accretion rate through the local annulus, triggering the viscous instability — as the accretion rate is now higher than the input accretion rate, the disc is eaten away at this radius. The pressure falls, the temperature decreases, and hydrogen starts to recombine, triggering the thermal instability again, but in reverse this time. Cooling ensues in a runaway fashion until the temperature is below 10^4 K again, and hydrogen is once more neutral. This decreased temperature means that the accretion rate through the annulus is now lower than the input accretion rate, and material starts to heap up again (Frank et al., 2002; Done et al., 2007; Kato et al., 2008).

The above depicts a local instability happening at a specific radius in the accretion disc. However, the jump in temperature and mass accretion rate in the H-ionized annulus caused by the instability will have an effect on H-neutral annuli next to it, and if the mass accretion rate difference between such annuli is large enough, the instability can result in a global disc effect. In such a case, the entire disc will then cycle between having a mass accretion rate larger than the mass transfer rate of the companion star (an outburst), so that the disc is eaten away and eventually cooled down again to the point where H is mostly neutral again (quiescence) (Done et al., 2007).

The basic mechanism behind states of outburst and quiescence is therefore as follows: the quiescent disc will accrete mass steadily from the companion star, until the temperature is high enough for the hydrogen ionisation instability to be triggered at a certain radius in the disc. This leads to an increase in accretion rate in the annulus associated to that radius, which will in turn lead to an increase in accretion rate through the next annulus, increasing the temperature and triggering the hydrogen instability there as well, and in this fashion a heating wave of mass accretion will propagate through the entire disc. When the outer disc gets eaten

away enough for the temperature to decrease to a point where hydrogen recombines again, a cooling wave will in turn ripple through the disc, returning it to a quiescent state. The above can then be repeated to result in alternating states of outburst and quiescence (Lasota, 2001; Frank et al., 2002; Done et al., 2007; Kato et al., 2008).

While the above scenario is well-observed for cataclysmic variables, the disk instability is more complicated for NS and BH LMXB systems. While these systems show the expected fast rise to outburst, they show instead an exponential, and then a linear, decay into quiescence. This is due to their very luminous inner discs irradiating and heating up the rest of the disc (van Paradijs, 1996). If the irradiation is strong enough to keep temperatures above that which is needed for hydrogen recombination, the disc will retain a mass accretion rate higher than what is supplied by the companion, and the disc will be eaten away. This will lower the disc temperature, and likewise the mass accretion rate, which will in turn lessen the irradiation of the disc, resulting in exponential decay. Eventually the outer disc temperature gets cool enough for hydrogen to recombine, but inwards propagation (at the viscous timescale) of the cold wave is hampered by the remaining (and receding) extent of the irradiated region, resulting in linear decay (King and Ritter, 1998; Lasota, 2001; Done et al., 2007).

The difference in the long-term outburst behaviour of NS and BH LMXBs lies in the difference in their primary masses - NSs have lower masses than BHs. For a companion star (with a given mass) to overflow its Roche Lobe, NSs therefore require tighter binary orbits than BHs. A tighter binary orbit means a smaller disc, with the outer edge of the disc therefore not extending as far away from the NS, and its temperature therefore not reaching as low. With temperatures more likely to be above the hydrogen ionization temperature, NS LMXB discs are therefore more likely to be stable, and to remain in outburst as *persistent* sources, while BH LMXBs are *transients* (Done et al., 2007).

4U 1608-52 (the subject of Chapter 3) is an example of a *transient* NS LMXB. In this case, the orbital separation is known to be larger, and so therefore the accretion disc is as well, allowing for instabilities on the outer edges. The companion star is

most likely in a stage of evolution allowing for its expansion, so that it fills its Roche lobe and transfers material to the NS primary (King et al., 1997; Done et al., 2007).

1.5.2 Spectral differences between BHs and NSs

Whereas the hydrogen ionisation instability can explain a lot of the long-term behaviour of NSs and BHs, it does not fully account for their observed spectra. Disc spectra change in luminosity and temperature while mostly retaining their quasi-thermal shape, whereas the shape of observed spectra vary greatly. The below sections will discuss the general picture of BH and NS LMXB spectra, with the aim of outlining the differences in the spectral evolution of the two groups.

BH LMXB spectra

Figure 1.11 shows different spectral states of the BH LMXB Cyg-X1. The soft state, indicated in red, consists of a thermally dominant soft component peaking around ~ 1 keV, with a non-thermal tail stretching out to very high energies (Gierliński et al., 1999; McConnell et al., 2000). The soft component is ascribed to the thermal emission from a Shakura-Sunyaev type accretion disc (Dotani et al., 1997; Mitsuda et al., 1984), but the tail is not explained by this. The hard state, indicated in blue in the figure, shows a harder spectrum peaking at ~ 100 keV, and a low temperature disc component. Both the soft and the hard state therefore require two emission components from the accretion flow - an optically thick disc (accounting for the soft thermal spectral component), and a higher-energy component from an optically thin environment not thermalizing to the disc temperature. (Done et al., 2007)

One of the main assumptions for the optically thick, geometrically thin accretion disc is that of thermal equilibrium, requiring a sufficient number of collisions between particles for the energy to thermalize. However, in environments with a low mass accretion flow, the number of collisions are not necessarily sufficient to uphold such an assumption. Hot flows can become optically thin to collisions between photons and electrons, and between electrons and protons. Protons have most of the gravitational energy, and will therefore lose very little of that energy to

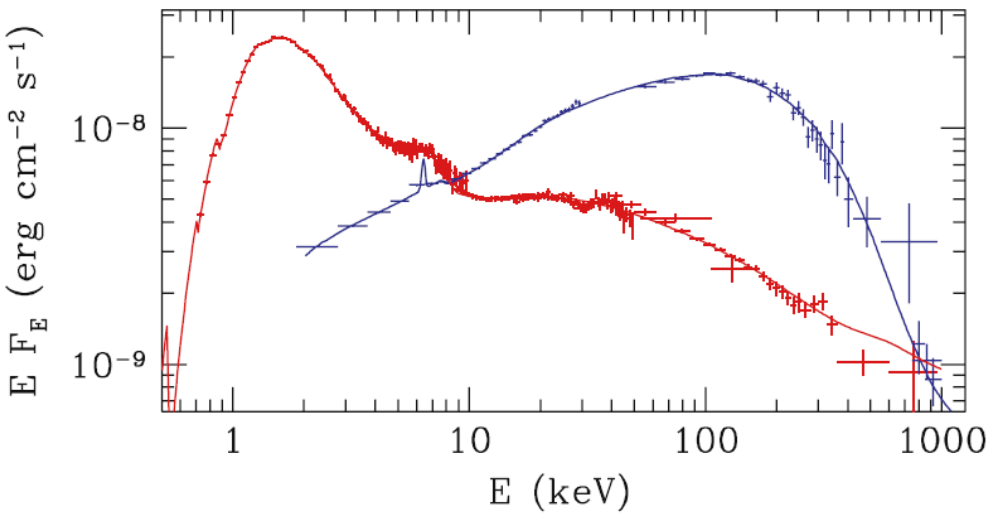

Figure 1.11: The soft (in red) and hard (in blue) spectral states of Cyg-X1, taken from Done et al. (2007), who adopted it from Gierliński et al. (1999).

electrons; as electrons will radiate most of the energy they do gain away, this leads to a two-temperature plasma. In this optically thin flow, electron radiation is in the form of inverse Compton scattering, instead of blackbody radiation. The high temperature of the protons give the accretion flow a large scale height, making the inner accretion flow geometrically thick, with the end result being a hot, two-temperature, geometrically thick and optically thin accretion flow with a Comptonization spectrum. (Done et al., 2007)

The hot inner flow and the cool accretion disc can explain the hard and soft spectra seen in Figure 1.11 using the truncated disc model: at low luminosities, the inner parts of the cool disc is replaced by the hot inner flow. Due to the cool disc being truncated, there is little overlap between it and the hot coronal flow, and so there is a low number of seed photons from the disc illuminating the flow. Coronal electron cooling via inverse Compton scattering is therefore not very efficient compared to the heating they undergo through collisions with protons. The ratio of power in the electrons to that in the seed photons (L_h/L_s, important in determining the shape of the Comptonized spectrum (Haardt and Maraschi, 1993)) is therefore $\gg 1$ in the hard state, resulting in a hard thermal Comptonized spectrum. As the accretion rate increases, the truncated disc moves progressively

inwards, increasingly overlapping with the hot flow so that more seed photons illuminate it, and leading to a decreasing L_h/L_s. Eventually, the source transitions to the soft state (via the intermediate state) — the range of luminosities where this happens (a single source often having different transition luminosities), is not very well understood, and is an example of hysteresis in these systems: one value of luminosity connected to a variation of spectra. (Done et al., 2007)

With the inward movement of the truncated disc, the hot inner flow becomes optically thick and geometrically thin once more — the associated increase in luminosity marks the transition from the hard to the soft state, as mentioned above. A larger amount of seed photons available now mean that any remaining electrons will undergo stronger Compton cooling ($L_h/L_s \leq 1$), resulting in much softer Comptonized spectra. The soft state therefore shows a strong soft disc component and a soft tail. (Done et al., 2007)

Spectral differences between BH and NS LMXBs

Due to the very similar gravitational potentials of BHs and NSs, and NS radii being roughly similar to the last stable orbit around BHs, the accretion flow around these systems give rise to many similarities in their spectral, timing and multi-wavelength properties (van der Klis, 2006; Motta et al., 2017; Muñoz-Darias et al., 2014), making the classification between BH and NS LMXB systems sometimes difficult (van der Klis, 2006). There is one fundamental and important difference between NS and BH systems, however, in that NSs have a solid *surface* that will influence accretion close to the NS, while BHs do not. This difference allows for clear identification of NSs in some cases: the presence of persistent pulsations (due to magnetic fields) and of Type-I X-ray bursts (from the nuclear burning of accreted material on the surface of NSs) are both evidence of a surface, and in such cases it is clear that the system in question does not contain a BH. But although the presence of these phenomena guarantees the presence of a surface, they are not present in all NS systems (van der Klis, 2006).

There is one NS effect that is always present due to the presence of a surface, however: a boundary layer between the NS surface and the accretion flow, at which a large amount of the gravitational potential energy of the infalling matter is radiated away. In Newtonian gravity, an accretion disc can radiate away half of the gravitational potential energy of the infalling matter, with the remaining half transformed into kinetic energy which gets radiated away at the boundary layer of the NS. This is different for a BH, where the energy would have disappeared over the event horizon. In General Relativity, the boundary layer of a NS can radiate up to twice as much energy as the accretion disc (Syunyaev and Shakura, 1986; Sibgatullin and Sunyaev, 2000), and even in the case of a NS spinning at half the Keplerian period, the boundary layer would still be roughly equally as energetic as the accretion disc (Sibgatullin and Sunyaev, 2000). Due to the similarities between BH and NS systems, it is expected that NS LMXBs would show similar accretion-related processes and states to that of BHs at similar L/L_{Edd}, with the addition of the effects of a boundary layer. (Done et al., 2007)

NS LMXBs are classified into two main groups: atolls and Z-sources. Z sources accrete at $> 0.5L_{Edd}$ and have magnetic fields of $B > 10^9$ G, while atolls accrete at lower rates (from less than $10^{-3}L_{Edd}$ to $\sim L_{Edd}$) and have magnetic fields of $B \sim 10^8$ G (Hasinger and van der Klis, 1989) — as atolls have similar luminosities to that of BH LMXB systems, they are used here for the spectral comparison to BHs. Z-sources, and the differences between them and atolls, are discussed in Section 1.5.4.

Like BH LMXBs, atolls switch between two distinct spectral states. These are called the soft 'banana' and the hard 'island' state (Mitsuda et al., 1989; Gierliński and Done, 2002a; Maccarone and Coppi, 2003), distinguishable in colour-colour diagrams (CCD, see Figure 1.14 for an example). Figure 1.12 shows the spectra for the island and banana states, respectively, so that similarities between the BH spectra in Figure 1.11 and the ones here can be seen – the island state corresponds to the hard state in BHs, and the banana state corresponds to the soft state. (Done et al., 2007)

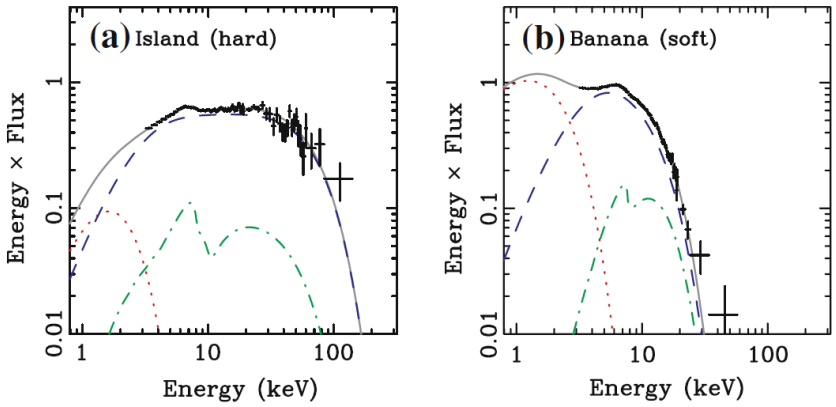

Figure 1.12: Spectra corresponding to the island and the lower banana states in the atoll system 4U1705-44, taken from Done et al. (2007) — the X-ray spectra is shown along with the best-fitting models extrapolated to soft energies. These spectra were fitted with blackbody spectra (red curve), thermal Comptonization spectra (blue curve), and a reflection component (green curve).

Even though atolls and BHs share the same approximate range of L/L_{Edd} and have similar gravitational potentials influencing their accretion flows, they have different spectral evolutions. This is illustrated in Figure 1.13, where a CCD is used to show the spectral evolution of atolls (in red), and BHs (in black). The difference between the spectral evolutions of these two groups can be explained using the truncated disc geometry, and taking into account a surface with a boundary layer for NS systems.

According to the truncated disc geometry at the lowest mass accretion rates for BH systems, the optically thick accretion disc is truncated at a large radius, with very few seed photons to illuminate the inner optically thin coronal flow. The result is a weak disc emission from the truncated disc, and a hard Comptonized spectrum from the hot inner flow. In NS systems the accretion disc is also truncated, and the hot inner flow joins into an optically thin boundary layer (Medvedev and Narayan, 2001; Medvedev, 2004). Due to the presence of the boundary layer, the inner hot flow is at least twice as luminous as it would have been without a boundary layer, leading to the expectation that the Comptonized emission from the coronal flow might be harder than that for BH systems. In NS systems, however, the NS surface is heated by irradiation, and the resulting thermal emission provides a source of seed photons additional to those provided by the truncated disc. As the surface

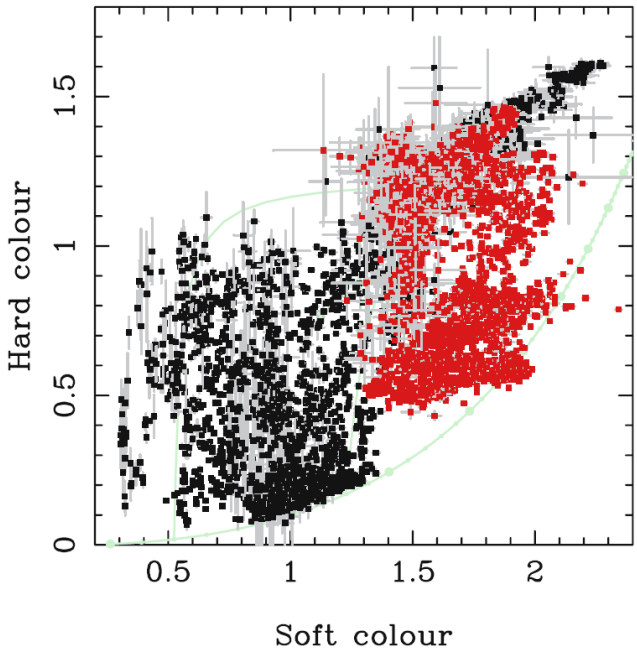

Figure 1.13: A CCD showing the spectral evolution of BHs (in black) and NSs (in red), making it clear that there are significant differences in the spectral evolution of the two groups. Figure from (Done et al., 2007).

emission is at the centre of the hot inner flow, it becomes the dominant source of seed photons, of which only a fraction is seen uncomptonized (and therefore at softer energies). This fraction is large enough to account for the soft component in the island state (Gierliński and Done, 2002b). The additional source of seed photons from the surface thermal emission is the reason why NS spectra are, in general, never as hard as their BH counterparts (Done and Gierliński, 2003); it further lies behind the difference in NS and BH spectral evolution. Done et al. (2007)

As the luminosity increases, NS systems move horizontally to the right on a CCD (Gierliński and Done, 2002a; Muno et al., 2002), unlike BH systems that move diagonally. This can be explained as follows: as the mass accretion rate and the optical depth of the hot inner flow increases, the temperature of the NS surface increases, leading to a rise in surface seed photon temperature. This causes the cut-off towards lower energies of the Comptonized spectrum to increase. The soft part of the X-ray spectrum becomes harder, and the soft colour therefore increases. As the majority of seed photons influencing the Comptonized spectrum comes from the surface of the NS, the truncation radius of the accretion disc has little

influence on the spectrum. The ratio of seed photon luminosity to hot electron luminosity does not change (as the seed photon luminosity is tied to that of the hot inner flow), and so the Comptonized spectrum stays the same at higher energies, and the hard colour remains roughly constant. The above, all together, is what causes the horizontal movement of a NS system on a CCD (Gierliński and Done, 2002a,b; Done and Gierliński, 2003).

As the accretion rate keeps increasing, the truncated disc moves inward, and the hot inner flow collapses into a thin, optically thick disc. The boundary layer becomes optically thick to electron scattering (although not thick enough for complete thermalization yet; see Popham and Sunyaev 2001), and its spectrum changes from hot, optically thin Comptonization to cooler, optically thick Comptonization. This change causes a large drop in hard colour, moving the system from the island branch onto the banana branch (see Figure 1.14 for reference). Done et al. (2007)

Unambiguously decomposing the soft banana branch into a disc and boundary layer component is difficult. Variability studies showed that the variable component has a hard spectrum, and as the boundary layer (rather than the disc) should be associated with the most rapid variability, this served as evidence for what was historically called the 'Eastern model' (Mitsuda et al., 1989): a cool disc component along with a hotter, Comptonized boundary layer component (Gilfanov et al., 2003; Revnivtsev and Gilfanov, 2006).

The disc becomes hotter and more luminous as the source moves along the banana branch, and the Comptonization component approaches a blackbody as the boundary layer becomes more optically thick with increasing accretion rate. Better thermalization of the boundary layer leads to a cooler temperature, opposed to the expected increase in temperature due to the increased luminosity. This is the reason why the boundary layer's temperature can remain fairly constant as accretion rate increases, leading to a relatively constant hard colour, while the disc's increasing luminosity leads to an increase in soft colour along the banana branch. (Gierliński and Done, 2002b; Revnivtsev and Gilfanov, 2006; Done et al., 2007)

Done and Gierliński (2003) showed that adding the boundary layer to BH LMXB accretion flow models reproduces the colour evolution along the banana branch seen in NS LMXB systems. It is therefore clear that the accretion flow models of NS LMXBs are similar to those of BH LMXBs, where the major spectral evolution can be explained by the truncated disc model and the movement of the inner truncation radius along an outburst, with the addition of a boundary layer and a surface. The fact that BH and NS LMXB systems have different spectral evolutions means that unknown transient systems could be classified simply based on their colour evolution as a function of flux. (Done and Gierliński, 2003; Done et al., 2007)

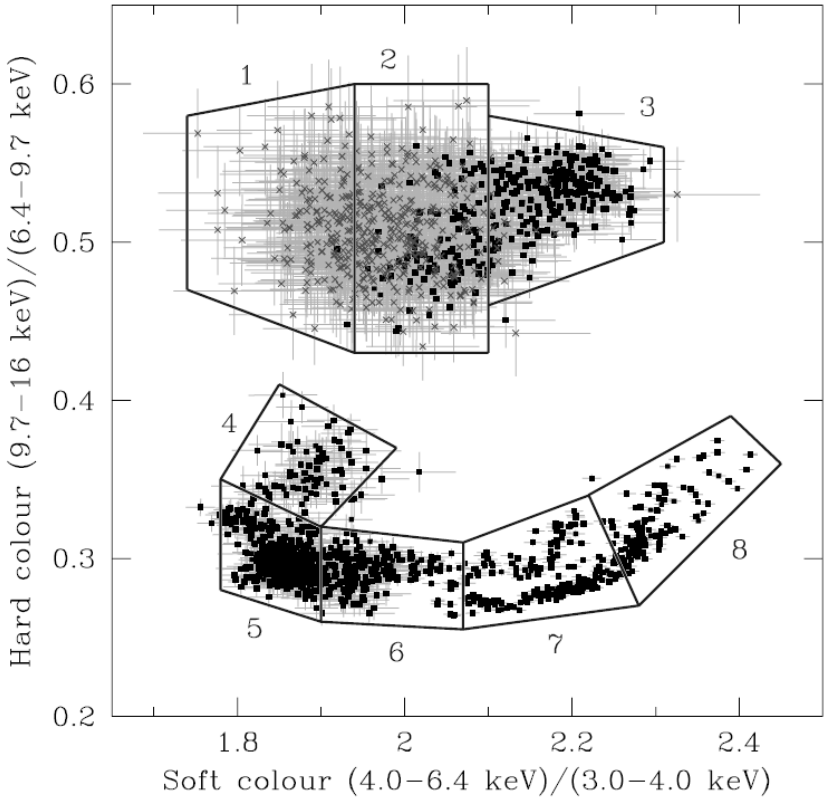

Figure 1.14: The CCD of 4U1608-52, taken from Gierliński and Done (2002b), showing observations from December 1996 when the source was at a low luminosity (crosses) and from its 1998 outburst (squares). The observations are divided into different spectral groups (numbered from 1 to 8), going along the Z-track that the source trace out during its outburst evolution. Number 1-3 corresponds to the island state, and 5-8 to the banana state.

1.5.3 NS LMXB evolution: relation between spectra and CCDs

As described above, NS spectral evolution can be traced on a colour-colour diagram (CCD). For atolls, the source moves along a Z-shaped track as accretion rate increases, from a low-luminosity hard island state lying in a horizontal branch towards the top of the CCD, to a high-luminosity soft banana branch at the bottom of the CCD (Gierliński and Done, 2002a) - this characteristic Z-track can be seen in Figure 1.14, which shows the CCD of the atoll 4U1608-52 (the subject of Chapter 3). The numbered sections shows the route that a source would trace out during its spectral evolution as a function of increasing accretion rate (Gierliński and Done, 2002b).

As the CCD is a tracer of the spectral evolution of the source, different locations on the CCD relates to different spectral shapes and states. To make the relation between the CCD location and its corresponding spectral characteristics clear, Gierliński and Done (2002b) selected spectra from each of the numbered sections in Figure 1.14 in order to show how the spectra evolves along the track. The spectra, along with their identifying numbers, can be seen in Figure 1.15 — section 1-3 corresponds to the hard island state, and section 5-8 to the soft banana state. The movement along the Z-track, and the corresponding spectral changes, have already been discussed in Section 1.5.2, and the descriptions there can be used to view the spectral components and the way in which they change in Figure 1.15.

1.5.4 Differences between atolls and Z-sources

Different to atoll sources, which switch between the hard island state and the soft banana state, Z-sources, with their higher luminosity ($L > 0.5L_{\rm Edd}$), are always soft. This means that, whereas atolls make a transition to the hard state at low luminosities, no such transitions are observed in Z-sources as their high luminosities mean they are always in a soft state. Their spectra are fit by a soft cool disc and an optically thick Comptonization with surface seed photons at higher energies. Z-sources occupy an area in the CCD similar to that of the atoll banana branch (Done and Gierliński, 2003), where they have a Z-shaped

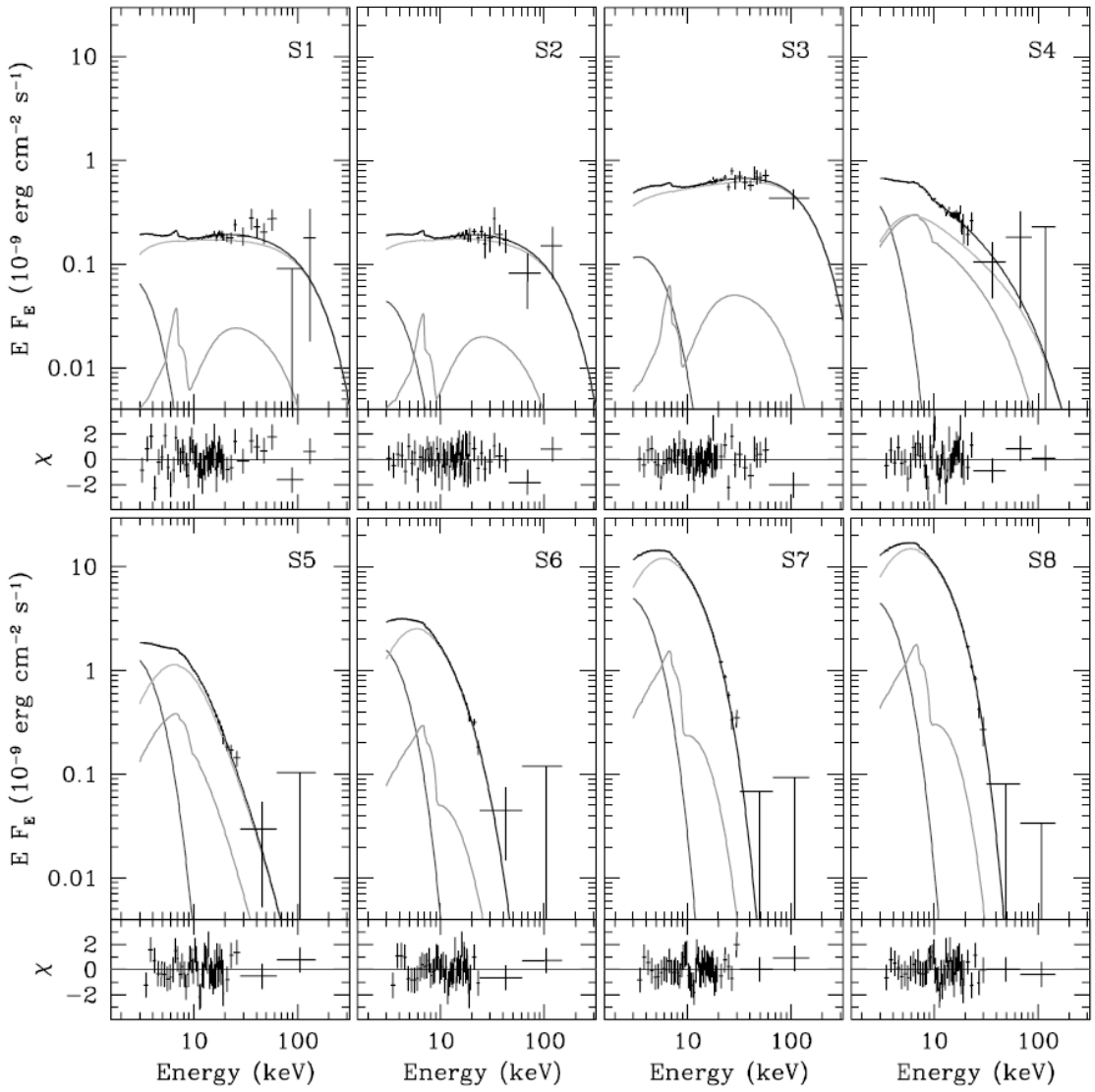

Figure 1.15: Selected PCA/HEXTE spectra of 4U1608-52 showing the number of the spectral group in Figure 1.14 that they were selected from. Panels show the data, model (consisting of the soft disc blackbody component, the hard Comptonization component, and its reflection), and residuals (at the bottom of every panel). Figure taken from Gierliński and Done (2002b).

track with three branches called, respectively, the horizontal branch (HB), normal branch (NB), and flaring branch (FB), the latter of which is the site of rapid and complex variability (Hasinger and van der Klis, 1989). See Figure 1.16 for an example of a Z-source CCD. (Done et al., 2007)

Assuming again the truncated disc model, another difference is that for the high luminosity of Z-sources, the accretion flow close to the NS cannot be optically thin. This means that the accretion disc cannot be truncated by its inner parts

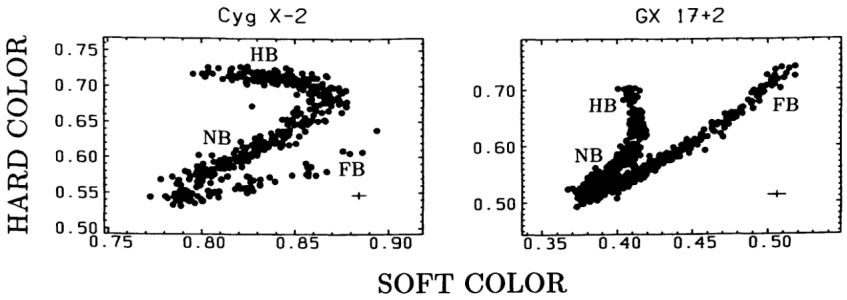

Figure 1.16: Example CCDs of Z sources Cyg X-2 and GX 17+2 taken from van der Klis (1989b) showing the Z-shaped pattern and the location of the horizontal branch (HB), normal branch (NB) and flaring branch (FB). Adopted from Hasinger and van der Klis (1989).

evaporating to be replaced by a hot inner flow, as is the case for atolls. Instead, the disc could possibly be truncated by a magnetic field, which is eventually overcome by the ram pressure of the increasing accretion flow (Gierliński and Done, 2002a), and the horizontal to flaring branch transition can then be caused by the accretion disc reaching the NS surface. Z-sources have been shown to show an additional Z-track from the flaring branch downwards (Gilfanov et al., 2003), however, in which case a better model for what happens at very high luminosities might be that the accretion disc is truncated by mass loss processes instead. Some evidence for this comes from the observation that the boundary layer component decreases from a contribution that is roughly equal to that of the disc at the top of the normal branch, to being non-existent by the time the source reaches the flaring branch (Revnivtsev and Gilfanov, 2006). (Done et al., 2007)

By studying XTE J1701-462, one of the only two sources found to transition from Z-source to atoll, Homan et al. (2010) found that the atoll upper banana state can equivalently be described as the final stage of a weakening Z-source's flaring branch. Their findings suggests that the different behaviours seen in NS LMXBs of different luminosities can be explained by the changes of a single parameter — that of the accretion rate.

1.5.5 Power density spectra and fast-time variability

The rapid variability in the X-ray emission of X-ray binaries is mainly analysed by studying the Fourier spectra of their X-ray flux times series. For the work contained in Chapters 3 and 4, the required X-ray observations were obtained from the *Rossi X-ray Timing Explorer* (RXTE) - the instrument is discussed in Section 1.6.4.

By taking the Fourier transform of the X-ray light curves, one can obtain an estimate of the variance (in terms of power density) as a function of Fourier frequency ν (see van der Klis 1989a). We therefore study X-ray variability in the frequency domain using power density spectra[19] (PDS) - as the Fourier power is proportional to the variance in the light curve, a power density spectrum shows any specific preferred frequencies present in the light curve. Using Parseval's theorem, the power density spectrum can be normalised such that the integral over all positive frequencies is equal to the square of the fractional root mean square deviation (or rms) of the corresponding time series (Lewin et al., 1988; Belloni and Hasinger, 1990) - the PDS used in the analysis contained in Chapters 3 and 4 are all rms normalised.

For both NS and BH LMXBs, the source signal contains valuable information - red noise, flat-top noise and quasi-periodic oscillations (QPOs) are examples, distinct from background noise (e.g. counting statistics). Whereas red noise and flat-top noise are seen in a PDS as a rise towards lower frequencies, QPOs are oscillations associated with certain frequencies and are observed as narrow peaks in the PDS.

In both NS and BH systems QPOs have been divided into high- and low-frequency QPOs. Low-frequency QPOs (LF QPOs) in NS LMXBs have centroid frequencies ranging between ~ 0.1 Hz and ~ 60 Hz. For Z sources, LF QPOs are divided into normal branch oscillations (NBOs, Middleditch and Priedhorsky 1986), horizontal branch oscillations (HBOs, van der Klis et al. 1985) and flaring branch oscillations (FBOs, van der Klis 1989b) based on their location on a CCD. Although LF QPO classification is less obvious for Atoll sources (van Straaten et al., 2001), they have also been divided into groups (Di Salvo et al., 2003), further studied

[19]The power density spectrum (PDS) is the modulus squared of the Fourier transform of the light curve (van der Klis, 1989a)

and named by Motta et al. (2017): HBO-like QPOs in the range from mHz to ~ 40 Hz, and FBO-like QPOs. NS high-frequency QPOs (HF QPOs, Strohmayer 2001; Belloni et al. 2012) are called kHz QPOs (divided into upper and lower kHz QPOs) with centroid frequencies in the range ~ 400 Hz to above 1 kHz - they often occur in a pair, are regularly observed and usually have very high amplitudes (Motta et al., 2017; van der Klis et al., 1996).

In BH LMXBs, on the other hand, LF QPOs range from ~ 0.1 Hz to ~ 30 Hz and are classified as either Type-A, -B or C QPOs (see Wijnands and van der Klis 1999; Casella et al. 2005; Motta et al. 2012), while QPOs with centre frequencies $\gtrsim 100$ Hz and up to ~ 500 Hz are referred to as upper or lower HF QPOs. An association between Type A, -B and -C QPOs in BHs with FBOs, NBOs and HBOs in NSs, respectively, has been proposed by Casella et al. (2005). An example of these LF QPOs observed in the PDS of BH LMXB systems, and their associated QPOs in NS systems, can be seen in Figure 1.17.

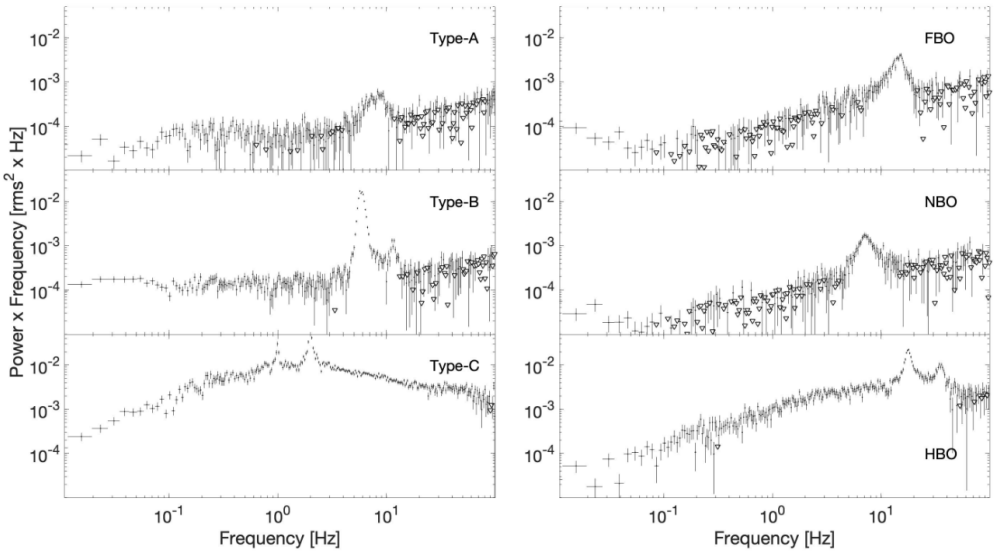

Figure 1.17: *Left:* LF QPOs from BH LMXBs. The top panel is an example from XTE J1859+226 whereas the two bottom panels are QPOs from GX 339-4. *Right:* LF QPOs from NS LMXBs. The top two panels are from GX17+2, and the bottom panel is from Cyg X-2. The power spectra here have been rms normalised, and the Poisson noise contribution has been subtracted. Arrows indicate $3\,\sigma$ limits. This figure has been taken from Ingram and Motta (2020).

QPOs can provide insight as to the variability nature of the source (van der

Klis, 2000) and can be used as powerful X-ray state trackers (Muñoz-Darias et al., 2011). As mentioned before, HBOs, NBOs and FBOs in Z-sources are so named due to the CCD branches they are found on, and their kHz QPOs are mostly found in the horizontal branch. In atolls, however, HBO QPOs are found in the hard to soft transitions, while FBOs are mostly found in the upper banana state. Atolls furthermore show kHz QPOs in all states, resulting in CCDs that can have kHz QPOs and HBOs present in many states (Motta et al., 2017). As an example of this, Figure 1.18 shows the CCD of the atoll 4U1608-52 (the subject of Chapter 3), with kHz QPOs and HBO QPOs marked with crosses and stars, respectively.

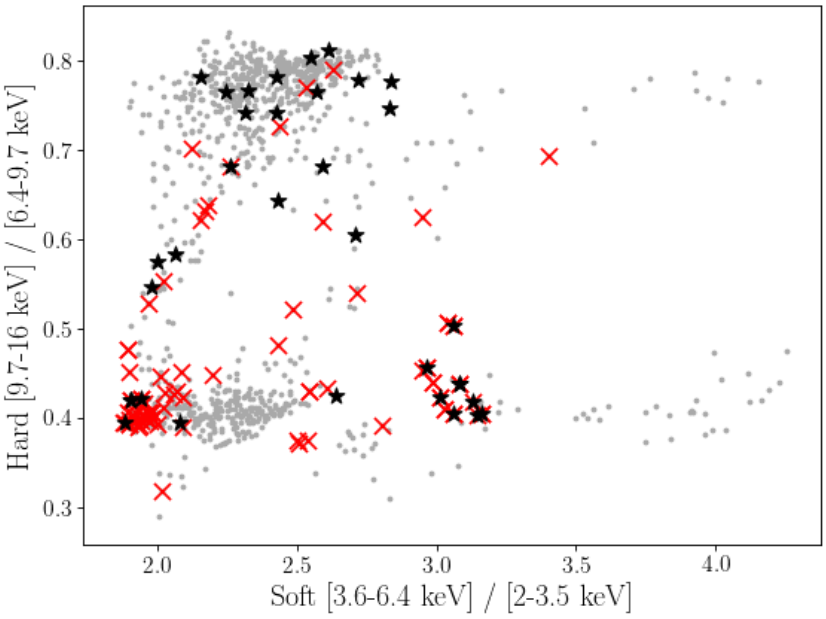

Figure 1.18: The CCD of 4U1608-52, produced via the analysis described in Chapter 3, showing the characteristic Z-track. Observations containing kHz QPOs are marked with red crosses, and those containing HBO QPOs are marked with black stars.

The origin of QPOs is still disputed, although many models have been proposed to explain their existence. I discuss these, and in particular the relativistic precession model (RPM) used in Chapters 3 and 4, later in this section.

1.5.6 NS LMXB outburst evolution along an RID

Apart from with CCDs, the outburst evolution of BH and NS LMXB systems are often described through the use of rms-intensity diagrams (RIDs, Muñoz-Darias et al. 2011), hardness-intensity diagrams (HIDs, Homan et al. 2001) and hardness-rms diagrams (HRDs). Hardness is defined as the ratio of counts in a harder X-ray band to that in a lower X-ray band, where a typical hard band would be $\sim 6-10$ keV and a typical soft band would be $\sim 4-6$ keV (Belloni et al., 2005). These energy ranges vary across different studies and different instruments. This section describes NS LMXB evolution using an RID and the findings presented by Muñoz-Darias et al. (2014). The idea is to describe the variability evolution along an outburst in relation to the contribution of thermal and Comptonization processes to the X-ray emission.

Fig. 1.19, taken from Muñoz-Darias et al. (2014), diagrammatically shows the behaviour of NS systems in the RID. Two main regions can be seen: a soft state having low variability (rms $< 5\%$) and a hard state with high variability (rms $> 20\%$). The soft state is dominated by a thermal component peaking at ~ 1 keV, while the hard state is dominated by a hard power-law with a high energy cut-off of ~ 100 keV. The thermal component originates from a geometrically thin, optically thick accretion disc, as well as from the NS surface (Shakura and Sunyaev, 1973; Novikov and Thorne, 1973; Lin et al., 2007). The optically thick disc locally emits a blackbody spectrum, with the blackbody temperature increasing with proximity to the NS (Ingram and Motta, 2020). The power-law component, as previously discussed, is the result of Compton up-scattering of soft photons from the disc by a cloud of hot electrons close to the NS (Thorne and Price, 1975; Sunyaev and Truemper, 1979), the high energy cut-off being determined by the characteristic electron temperature.

As with CCDs, the area traversed by a NS LMXB on an RID is strongly dependent on its luminosity (related to the accretion rate), which can be used to distinguish three regimes. The first of these is the hysteresis regime, found between $\sim 0.01 - 0.3\, L_{\rm Edd}$ as indicated in Fig. 1.19. This luminosity range is characteristic of atoll sources, and their hysteresis pattern and brightness are very

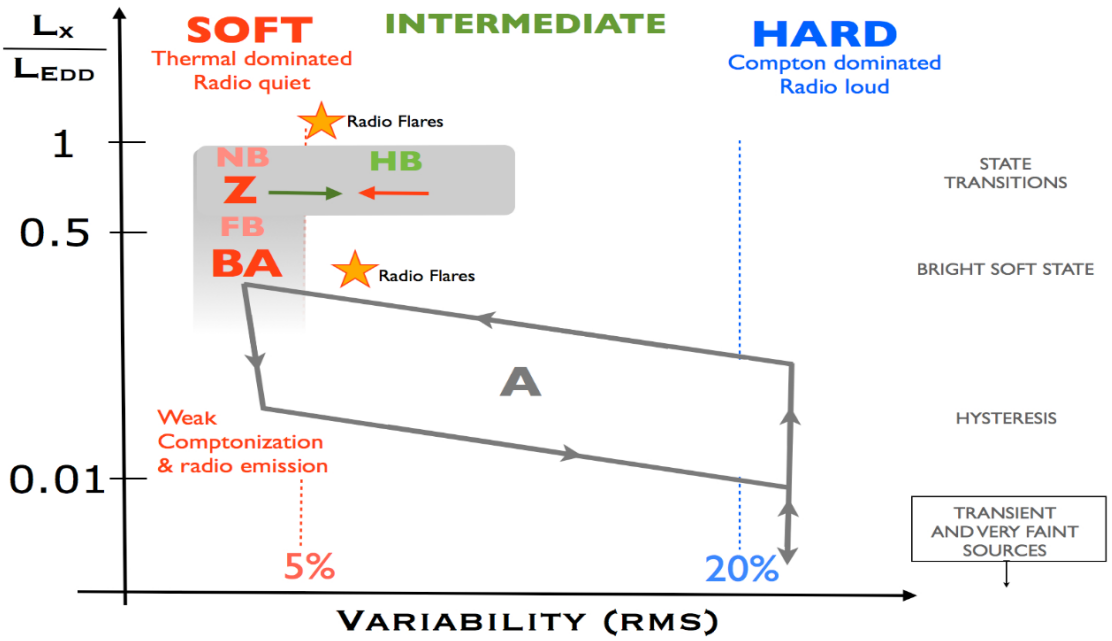

Figure 1.19: An explanatory RID describing the behaviour and location of zeta (Z), bright atoll (BA) and atoll (A) sources. FB, NB and HB denote the flaring, normal and horizontal branches, respectively, and the luminosity is given in units of the Eddington luminosity $L_{\rm edd}$. This figure was taken from Muñoz-Darias et al. (2014).

similar to that observed for BH systems (Dunn et al. 2010). The count rate for these sources increase during the hard-to-soft transition and decrease during the reverse transition, resulting in diagonal state transitions. In this regime there is a clear correlation between fast variability (i.e. rms) and the Comptonization fraction (i.e. hardness). The counter-clockwise hysteresis observed is as follows: during the rise of an outburst sources are found to be spectrally hard and variable (Comptonization processes are dominant) after which they will transition to a soft, less variable state (thermal disc dominated). Once here, the luminosity will gradually decrease until a reverse transition to the hard state is made. Hysteresis loops can last from days to months, while the transition times themselves are of the order of a few days.

The next regime falls between $\sim 0.3 - 0.6\ L_{\rm Edd}$ and is referred to in the figure as the "bright soft state"; it corresponds to bright atoll and faint Z-sources. Here, the spectrum is dominated by the thermal component, variability is very low and flaring (observed in the source emission) is present. The hardness-rms correlation mentioned above breaks down in this regime - hardness still varies but variability

stays at a constant low. This phenomenon is found essentially in NS systems and can be seen in an HRD as a flat rms-hardness relation towards lower luminosities. This regime covers both the flaring branch (FB) and part of the normal branch (NB), explained by Lin et al. (2009) as the inner disc radius moving inwards and outwards from the atoll soft-state value, causing instabilities (flaring branch) and as changes in the radius of the blackbody emission from the NS surface (normal branch). It is also suggested that the flaring could be the result of unstable nuclear burning on the NS surface (Church et al. 2006).

The last regime falls in the luminosity range $L_{\rm X} > 0.6\,L_{\rm Edd}$ and is characterised by fast horizontal transitions, as indicated in the figure. This regime corresponds to bright Z-source phases where the spectrum is soft and variability is low. Excursions to the intermediate states are also seen, however, and with that an increase in hardness and variability, corresponding to an increase in the fractional contribution from the Comptonization component Lin et al. (2009); hardness and rms are therefore correlated anew. These horizontal transitions constitute the horizontal branch (HB).

Regardless of whether hysteresis happens or not, both BH and NS LMXBs move through a hard (rms $>$ 20%), intermediate (5% $<$ rms $<$ 20%) and soft (rms $<$ 5%) state. This means that while the luminosity of a source is a determining factor of the transition mode (horizontal transitions above $\sim 0.5\,L_{\rm Edd}$ and hysteresis below that), the variability and spectral state of a source are directly and likely intrinsically related, regardless of other factors.

1.5.7 Proposed QPO models

Despite having been discovered in the 1980s and therefore being known for decades now, QPOs remain poorly understood, and their physical origin is still largely debated, even though it is commonly accepted that they must originate in the innermost regions of the accretion flow. The centroid frequencies of QPOs can be measured with high accuracy, giving us the opportunity to probe the distorted spacetime in the strong gravitational field regime close to compact objects (van der Klis, 2006).

Many different models have been proposed for QPOs, and this section briefly reviews some of them. In many cases the models assume a truncated disc / hot inner flow geometry, where the cool ($T \sim 1$ keV), geometrically thin, optically thick disc is truncated at a radius larger than the ISCO, and the accretion flow inside the thin disc takes the form of a hot, geometrically thick, optically thin inner accretion flow, where LF QPOs arise due to the Lense-Thirring precession (due to the effect of frame-dragging - see Section 1.2.3) of the hot inner flow (Ingram et al. 2009; Ingram and Done 2012a; Lodato and Facchini 2013; Motta et al. 2018). Where this geometry is assumed below, $r_{\rm in}$ and $r_{\rm out}$ denotes the inner and outer radius of the inner flow, respectively. This summary is based on the review in Ingram and Motta (2020).

- **Corrugation modes:** These modes (also called *c modes*) are transverse standing waves in the disc height, with a resonant angular frequency w_c, trapped between the inner disc radius $r_{\rm in}$ and the *inner vertical resonance* radius $r_{\rm ivr}$. They are excited by perturbations in disc quantities such as density (see e.g. Kato and Fukue 1980; Wagoner 1999; Kato 2001; Wagoner et al. 2001). These density modes have resonant frequencies in the observed LF QPO frequencies. Gravity and pressure modes oscillate at higher frequencies and have been associated with HF QPOs (Wagoner et al., 2001).
- **Accretion ejection instability:** This is an instability occurring in the inner part of thin discs threaded by strong vertical (poloidal) magnetic fields, giving rise to spiral waves in density and scale height. (Tagger and Pellat, 1999). A spiral density wave in the disc, driven by magnetic stresses, becomes unstable by exchanging angular momentum with a Rossby vortex. This angular momentum is transferred as Alfvén waves[20] towards the corona of the disc and provides an energetic source for a jet or a wind. This instability forms standing spiral patterns which could provide explanations for LF QPOs.
- **Propagating oscillatory shock:** The propagating oscillatory shock model (Molteni et al., 1996; Chakrabarti et al., 2008) is based on a Keplerian disc

[20] Alfvén waves are low-frequency magnetohydrodynamic waves where ions oscillate to a restoring force provided by an effective tension on the magnetic field lines.

interposed between the upper and lower parts of a sub-Keplerian corona, as well as an inner sub-Keplerian halo. These two components form accretion flows with differential rates, separated by a shock radius at r_{shk} as the density transitions from the outer disc to the inner halo. (Titarchuk and Hua, 1995). According to this model, the oscillation of the shock location around a mean value $r_{\rm shk}$ is proposed to produce LF QPOs in the X-ray flux.

- **Pressure or accretion rate modes:** In certain QPO models, the system geometry is assumed to stay constant while other relevant quantities such as pressure or accretion flow rates vary to produce resonant oscillations (Ingram and Motta, 2020). In one of these models, that of Cabanac et al. (2010), white noise pressure perturbations at the outer radius r_{out}, in an inner flow/truncated disc geometry, cause pressure waves in the corona. The reflection of these waves at the inner flow radius gives rise to resonant modes. These oscillations in the pressure is thought to cause LF QPOs by modulating the X-ray flux through Compton up-scattering. Other suggestions, based on magnetohydrodynamic (MHD) simulations, have also been made: large-scale, low-frequency dynamo cycles found in global MHD simulations were reported by O'Neill et al. (2011), Wang et al. (2012) proposed toroidal Alfvén wave oscillations as the cause of LF QPOs, and Machida and Matsumoto (2008) found that a constant angular momentum torus formed in a subset of their MHD simulations, deforming itself quasi-periodically and in turn modulating mass accretion and outflow rates.
- **The relativistic precession model:** The relativistic precession model (RPM, Stella and Vietri 1998, 1999) associates the Type-C QPO with the Lense-Thirring precession frequency at some characteristic radius, and the lower and upper HF QPOs with periastron precession and the orbital frequency, respectively. Chapters 3 and 4 focus on the RPM, and so this model is discussed in more detail in Section 1.5.8 below.
- **The rigid precession model:** The rigid precession model (Ingram et al., 2009) assumes a truncated disc geometry where the BH or NS spin axis is

misaligned ($\sim 10° - 15°$) with the rotational axis of the binary. This causes the entire inner flow to precess, giving rise to the Type-C QPO. The rigid precession model, like the RPM, is discussed in more detail in Section 1.5.8 below.

1.5.8 The relativistic precession model

The RPM, proposed by Stella and Vietri (1998), is based on the fact that general relativity predicts that the presence of a spinning mass will affect the motion of matter around it (see Section 1.2.3 on the Kerr metric). In these systems nodal, or Lense-Thirring, precession occurs when the spin axis of the compact object is misaligned with the orbital axis, so that there is a precession of the orbit's spin axis around the compact object's spin axis with a frequency $\nu_{\rm nod} = \nu_\phi - \nu_\theta$ (with orbital frequency ν_ϕ and vertical frequency ν_θ). Periastron precession, on the other hand, is the precession of the elliptical orbit's semi-major axis with a frequency $\nu_{\rm per} = \nu_\phi - \nu_{\rm r}$ (with radial epicyclic frequency $\nu_{\rm r}$). The RPM associates nodal (Lense-thirring) precession with the Type-C QPO (or HBO/HBO-like QPO in NS systems), periastron precession with the lower HF QPO (lower kHz QPO in NS systems) and the orbital frequency with the upper HF QPO (upper kHz QPO in NS systems). Observed simultaneously, this set of three QPOs are known as a 'triplet' and can be used to test the RPM. With all three signals emitted from the same characteristic radius r, the inward motion of the accretion inner truncation radius can be used to explain the co-evolution of these QPOs towards higher frequencies (Stella et al., 1999).

The RPM has been used to interpret QPOs in both NS (Stella and Vietri 1999; Ingram and Done 2010; du Buisson et al. 2020), and BH systems (Motta et al., 2014a,b). A good example of this is the papers by (Motta et al. 2014a,b), in which three simultaneous QPOs found in an observation were used to solve the three equations (with three unknowns) of the RPM to obtain the spin a, BH mass M and emission radius r of GRO 1655-40. The mass measurement was found to correspond well with the dynamical mass measurement for the same source as given by Beer

and Podsiadlowski (2002). A case where the RPM was used unsuccessfully is that of Altamirano et al. (2012) - this is discussed in detail in Chapter 4.

Initially it was thought that the equations yielded by the RPM had no analytical solution, and so computationally intensive numerical simulations were used to solve them (Motta et al. 2014a; Bambi et al. 2014; Stefanov 2014). Since then, Ingram and Motta (2014) have found an analytical solution for the case where three simultaneous QPOs are detected, and it is these equations we use in order to determine the mass M and spin a of the compact object, as well as the emission radius r, where the three QPOs are thought to originate from.

For a test mass orbiting a spinning BH (or NS) in a plane that is slightly perturbed from the equatorial, it can be shown that in the Kerr metric (Bardeen et al., 1972; Merloni et al., 1999) the orbital frequency ν_ϕ, periastron precession frequency $\nu_{\rm per}$ and nodal precession frequency $\nu_{\rm nod}$ are given by

$$\nu_\phi = \pm\frac{\beta}{M}\frac{1}{r^{3/2}\pm a} \tag{1.45}$$

$$\nu_{\rm per} = \nu_\phi\left[1-\sqrt{1-\frac{6}{r}\pm\frac{8a}{r^{3/2}}-\frac{3a^2}{r^2}}\right] \tag{1.46}$$

$$\nu_{\rm nod} = \nu_\phi\left[1-\sqrt{1\mp\frac{4a}{r^{3/2}}+\frac{3a^2}{r^2}}\right], \tag{1.47}$$

where r is the emission radius in units of $R_g = GMM_\odot/c^2$, M is the BH (or NS) mass in solar masses, and $\beta = c^3/(2\pi GM_\odot) = 3.237\times10^4$ Hz. The dimensionless spin parameter is denoted by a, where $a = (cJ)/(GM^2)$, with J the angular momentum of the object expressed as $J = I\omega$, I being the moment of inertia and ω being the angular frequency expressed as $\omega = 2\pi\nu$, with ν being the spin frequency of the compact object. The top sign in all equations refers to prograde orbits while the bottom refers to retrograde orbits, and we take $r > r_{\rm ISCO}$.

The RPM takes $\nu_{\rm LF} = |\nu_{\rm nod}|$, $\nu_l = |\nu_{\rm per}|$ and $\nu_u = |\nu_\phi|$, where $\nu_{\rm LF}$, ν_l and ν_u denote the Type-C QPO, lower HF QPO and upper HF QPO (or HBO/HBO-like QPO, lower kHz QPO and upper kHz QPO for NS systems), respectively. The

RPM equations (Equations 1.45 - 1.47) depend on M, a, r and the three frequencies $\nu_{\rm nod}$, $\nu_{\rm per}$ and ν_ϕ. If we have all three QPOs measured simultaneously, it is possible to solve for M, a and r, assuming all frequencies are associated with the same radius. Re-arranging Equations 1.46 and 1.47, one obtains

$$\Gamma \equiv \left(1 - \frac{\nu_{\rm per}}{\nu_\phi}\right)^2 = 1 - \frac{6}{r} \pm \frac{8a}{r^{3/2}} - \frac{3a^2}{r^2} \tag{1.48}$$

$$\Delta \equiv \left(1 - \frac{\nu_{\rm nod}}{\nu_\phi}\right)^2 = 1 \mp \frac{4a}{r^{3/2}} + \frac{3a^2}{r^2}. \tag{1.49}$$

For the constraint $r > r_{\rm ISCO}$, Γ and Δ obey $0 < \Delta < 1$, $0 < \Gamma < 1$ and $\Delta > \Gamma$. To get a in terms of r, Equations 1.48 and 1.49 are added together to obtain

$$a = \pm \frac{r^{3/2}}{4}\left[\Delta + \Gamma - 2 + \frac{6}{r}\right]. \tag{1.50}$$

Adding twice Equations 1.49 to Equation 1.48, substituting Equation 1.50 into the result and re-arranging gives a quadratic in r, which can be solved to obtain

$$r = \frac{2}{3}\frac{6 - \Delta - 5\Gamma + 2\sqrt{2(\Delta - \Gamma)(3 - \Delta - 2\Gamma)}}{(\Delta + \Gamma - 2)^2}. \tag{1.51}$$

From here, the spin can be determined using Equation 1.50, after which M can be found from Equation 1.45. M, r and $|a|$ can initially be determined assuming prograde orbits, and this assumption can be tested afterwards by measuring the highest frequency that the Type-C QPO reaches - if it extends to within the ISCO for $a = -|a|$, the assumption of prograde orbits is correct.

Ingram and Motta (2014) have, furthermore, found simple solutions to the case where two QPOs and an independent mass measurement is present, as the simultaneous occurrence of three QPOs is rare; although not entirely analytic, it is still faster than previous fully numerical methods. Using their work, it is also possible to place limits on the parameters a, M and r for the case where two QPOs were found, and where no independent mass measurement is available.

The rigid precession model

An argument against the test particle RPM is that it is expected for any local disc feature (the emission of which is responsible for the Type-C QPO) to be sheared out by differential rotation. The rigid precession model (Ingram et al. 2009) tackles this problem by making the global, rigid precession of a toroidal structure responsible for the existence of the Type-C QPO, instead of the precession of a single test particle. For this, the truncated disc model geometry is assumed, and Type-C QPOs arise due to the Lense-thirring precession (due to the effect of frame-dragging) of the hot inner flow (Ingram et al. 2009). Instead of having the nodal precession frequency $\nu_{\rm nod}$ as before, the rigid precession frequency $\nu_{\rm p}$ is calculated (see Ingram and Done 2012a; Lodato and Facchini 2013; Motta et al. 2018) as

$$\nu_{\rm p} = \frac{\int_{r_{\rm in}}^{r_{\rm out}} \nu_{\rm nod}(r) L(r) 2\pi r \, {\rm d}r}{\int_{r_{\rm in}}^{r_{\rm out}} L(r) 2\pi r \, {\rm d}r}, \tag{1.52}$$

where $r_{\rm in}$ and $r_{\rm out}$ denotes the inner and outer radii of the globally precessing thick disc and $L(r) = \Sigma(r)\Omega_{\rm K} r^2 \propto \Sigma(r) r^{1/2}$ denotes the specific angular momentum, with $\Omega_{\rm K}$ given by the relativistic correction to the Keplerian angular velocity and $\Sigma(r)$ being the radial surface density (Motta et al. 2018). It is assumed by Motta et al. (2018) that $r_{\rm in}$ of the thick precessing disc always coincides with $r_{\rm ISCO}$ while $r_{\rm out}$ (corresponding to the thin disc inner truncation radius) can be any value larger than $r_{\rm ISCO}$, with $\nu_{\rm p}$ asymptotically tending to $\nu_{\rm nod}$ as $r_{\rm out}$ and r (the emission radius from the test particle case) approaches the ISCO for a fixed BH (or NS) mass and spin (see Fig. 2 in Motta et al. 2018). It is found that this model can produce Type-C QPO frequencies matching those typically observed in BH systems.

Energy spectrum modulations due to orbital frequencies

The precessing inner flow model, where Type-C QPO frequencies are associated with the Lense-Thirring precession of the hot inner flow while the disc remains stationary (Ingram et al., 2009), makes a distinctive prediction regarding the iron emission line in X-ray spectra (generated through the reflection of continuum photons off the accretion disc). As the hot inner flow precesses, it should illuminate different

azimuths of the accretion disc such that an observer at an incline should see a blue-shifted iron line when approaching sides of the disc are illuminated, and a red-shifted iron line when receding sides of the disc are illuminated — the iron line energy should therefore change systematically with QPO phase (Ingram and Done, 2012b). Ingram et al. (2016) used XMM-Newton and NuSTAR observations of H1743-322 to show that the iron line centroid energy indeed varies systematically over the QPO cycle, thereby providing strong evidence for the Lense-Thirring precession origin of the QPO. Ingram et al. (2017) modeled this physically and fitted it to the H1743-322 data, finding that the data is well described by the model and that the reflection fraction varies with QPO phase.

The periastron precession and orbital frequencies ($\nu_{\rm per}$ and ν_{ϕ}) are very fast compared to Lense-Thirring precession, and being sensitive to the spectral changes they might introduce is problematic. Although current instruments have high time resolutions, the issue of collecting enough photons in the short time-scales commensurate with these frequencies remain a problem for time-resolved spectroscopy. Furthermore, folding the data on a period is likewise not feasible, as the frequency of the QPOs associated to these frequencies change too quickly in time, such that a deconvolution like the one of Ingram and van der Klis (2015) would be ineffective. See also Section 1.5.7 for a discussion on several more QPO models.

1.6 Experimental Background

This section describes the instruments and experiments that later chapters in this thesis rely on. Section 1.6.1 introduces the concept of interferometry, and Section 1.6.2 discusses Gaia and its contribution to our stellar knowledge. Section 1.6.3 builds on the interferometry section by introducing gravitational wave interferometry, discussing detector strain and performance, and elaborating on current and future gravitational wave detectors. Finally, Section 1.6.4 discusses the Rossi X-ray Timing Explorer (RXTE).

1.6.1 Interferometry

Interferometry is a set of techniques that combines waves in order to produce interference patterns for the extraction of information. Most interferometers work on the basic premise of splitting coherent light into two beams, after which the beams will travel along separate optical paths to be re-combined afterwards using the principle of superposition to produce interference patterns. A linear variation in the optical path difference produces a sinusoidal variation in the intensity pattern that can be used for making inferences about the paths followed by the beams (Hariharan, 2006). One of the most common configurations for interferometry is the Michelson interferometer (Michelson and Morley, 1887), minimally consisting of a beam splitter and two mirrors. A coherent light (laser) source emits light incident on a beam splitter that transmits part of the beam through to one mirror, and directs the rest in the direction (orthogonal to the other beam) of the other mirror. The beams are then reflected off the mirrors and re-combined to produce an interference pattern incident on the detector.

Astronomical interferometry, widely used in radio astronomy and less often used in optical astronomy, increases the angular resolution of telescopes through aperture synthesis, whereby signal waves from different telescopes are interfered. The effect of this is a combined telescope that has a resolution equivalent to a single antenna with diameter equal to the distance between the two antennae in the array furthest apart. As angular resolution θ is proportional to the relation λ/D, with λ the source radiation wavelength and D the diameter of the telescope (or in the case of an interferometer, the length of the longest baseline), it is easy to see why this would lead to a vast improvement - the largest optical telescopes in the world have diameters $\sim 10\,\mathrm{m}$, while optical interferometric baselines can stretch over hundreds of meters. The high angular resolutions achieved by interferometers are required for precise astrometry: precise measurements of stellar positions and, if multiple observations of stars' positions are made over time, for precise measurements of their proper motions.

Although not an interferometer, the Gaia Space Telescope has succeeded in providing high angular resolutions with which it is possible to make very precise measurements of distances, positions and proper motions of over a billion stars in the Milky Way. Gaia and its contributions to our stellar knowledge are discussed in Section 1.6.2.

1.6.2 The Gaia Space Telescope

Gaia[21] is a European Space Agency (ESA) space observatory that was launched in 2013 and is expected to be operational until roughly 2025. It was designed mainly for astrometry, and is able to provide unprecedented positional and radial velocity measurements with the aim of constructing the largest and most precise three-dimensional space catalogue to date, containing roughly 1.7 billion stars from our Galaxy and throughout the Local Group (amounting to $\sim 1\%$ of the Galactic stellar population), in order to study the formation, evolution, structure and dynamics of the Milky Way. During its first five years of operation, Gaia observed each of its one billion sources roughly 70 times, creating a record of the brightness and position of all sources over time. It continues to do so, and is currently in its extended mission. Gaia is the much-improved successor of Hipparcos[22], the first satellite to chart the position of stars, that released a primary catalogue of 118 000 stars and a secondary catalogue containing over 2 million stars. Gaia collects roughly 30 times more light, and measures positions and motions of objects roughly 200 times more accurately, than Hipparcos.

By the early 1990s, the notion of using interferometry in space for high-precision astrometry has been around for a few years - always as part of pointed missions having only a small number of selected targets. This changed when a proposal for the Global Astrometric Interferometer for Astrophysics (GAIA, Lindegren et al. 1994) was submitted to ESA in 1993, detailing the use of interferometry to increase the resolution and precision of a continuously scanning survey satellite.

[21] Gaia home: `https://sci.esa.int/gaia`
[22] Hipparcos home: `https://www.cosmos.esa.int/web/hipparcos`

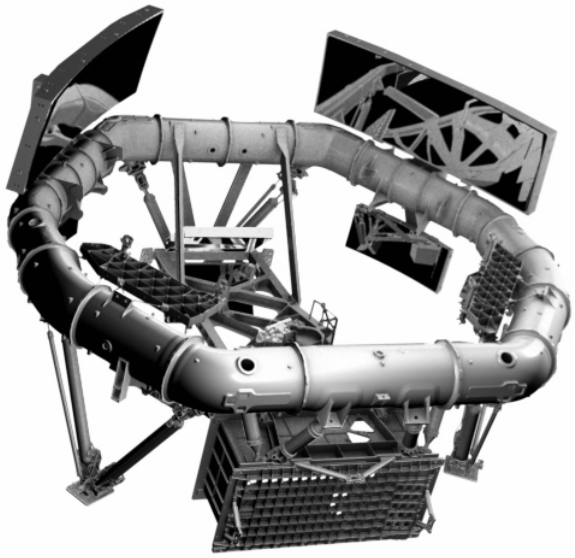

Figure 1.20: A schematic overview of Gaia's payload, without its protective tent. Figure taken from the work by Gaia Collaboration et al. (2016).

The early proposed GAIA comprised of two Fizeau interferometers[23] that were mechanically connected and set to point in different directions with a fixed basic angle between them. Although ESA viewed the proposal favourably, studies by Matra Marconi Space soon showed that using a filled aperture was far superior to the interferometric configuration using two smaller apertures. With a large enough focal length and focal plane, direct imaging on the CCDs were possible, which increased the limiting magnitude to $V \sim 20$ and the number of potential targets to more than a billion. The 'GAIA' acronym was dropped as the telescope was no longer an interferometer, and the name 'Gaia' was instead picked.

Gaia's focal plane consists of the following main parts: the sky mapper, the astrometric field, blue and red photometers, and the radial-velocity spectrometer (RVS) - these can be seen in Figure 1.21. The sky mapper detects objects down to $V \sim 20$ entering the fields of view, and communicates star transits to subsequent CCDs. The astrometric field contains 62 CCDs, and is used for making positional measurements - it provides the star position (two angles), proper motion (two

[23]A telescope in which light enters through two small apertures, and is then combined in the focal plane in order to form stellar images interweaved by interference fringes. The Fizeau makes it possible to observe many stars simultaneously in a large field of view.

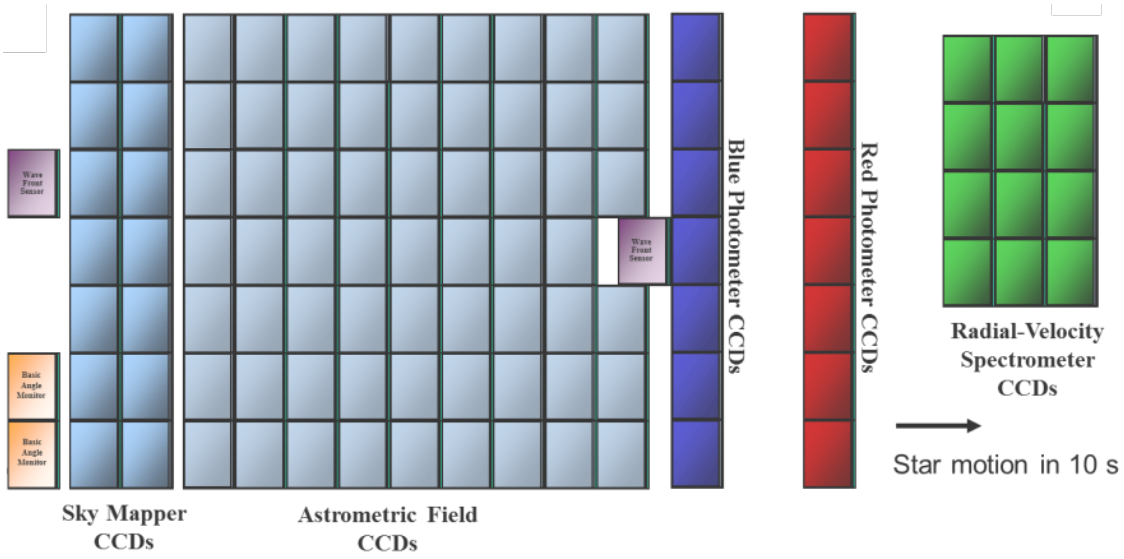

Figure 1.21: Gaia's 1.0×0.4 m focal plane, including its sky mapper, astrometric instrument, photometric instrument, and radial velocity spectrometer (RVS). Credit: ESA.

time derivatives of position), and parallax (distance) of objects. The blue and red photometers provide spectro-photometric measurements of objects for general astrophysics purposes, and to calibrate telescope-induced chromatic image shifts in measurements, and the RVS collects the spectra of objects brighter than $V \sim 17$ for the derivation of radial velocities and stellar atmospheric parameters.

Gaia's design and the fact that it is placed in space enables a combination of sky coverage, sensitivity, accuracy and dynamic range that is practically impossible for any ground-based telescopes to achieve. The Gaia spectroscopic survey is the largest of its kind, and its spectro-photometric measurements provides detailed properties of observed stars, characterising their effective temperature, elemental composition, luminosity and gravity. Gaia's astrometry is unique as its space environment makes it possible to do global, micro-arcsecond astrometry (measuring positions with an accuracy down to ~ 24 micro-arcseconds). There has been three Gaia data releases to date: data release 1 (DR1) covered 14 months of observations and was released in September 2016; DR2 covered 22 months of observations and was released in April 2018; DR3, covering 34 months of observations, have been split into two parts, with the early DR3 (EDR3) having been released on 3 December

2020 (Gaia Collaboration et al., 2020). Together, they have made a significant contribution to our knowledge of the Galaxy; below is a summary of some of Gaia's main contributions to our knowledge of stars. At the time of writing this, EDR3 has just been released, and so the reader should be aware of ongoing contributions that are not necessarily included here - this summary mainly concerns DR1 and DR2.

Helmi et al. (2018) used Gaia data to demonstrate that the Milky Way's inner halo was dominated by debris from the remains of a dwarf galaxy, referred to as Gaia-Enceladus, that merged with our Galaxy roughly 10 billion years ago and that contributed to the formation of the Galactic thick disk. Myeong et al. (2019) found that a second merger event, termed the Sequoia event, happened shortly after the Gaia-Enceladus event. Ruiz-Lara et al. (2020) used Gaia DR2 data to discover that past perturbations to the Galactic disk caused by Sagittarius (a satellite galaxy 10 000 times smaller than the Milky Way that has been orbiting the Galaxy's core for billions of years) coincide with episodes of enhanced star formation that happened 5.7, 1.9 and 1.0 billion years ago, respectively - the former coincides with the period in which the Sun and the Solar System formed. This suggests that Sagittarius played a very important role in our Galaxy's stellar mass build-up and Galaxy structure. A group of stars moving in a snail shell-like pattern in the Milky Way disk, discovered by Antoja et al. (2018) using Gaia DR2 data, for example, is thought to be the result of Sagittarius' latest interaction with our Galaxy.

Malhan et al. (2018) used Gaia DR2 data to uncover a rich network of stellar streams in the Galactic halo, believed to be the remnants of star clusters and small satellite galaxies drawn in to the Milky Way. Using DR2 data, Alves et al. (2020) recently discovered the largest coherent gas structure known in the Galaxy - the 'Radcliffe Wave' - a 9000 light-years long undulating wave part of the Local Arm, and made up of interstellar gas clouds. Previous to this discovery, it was thought that such gas clouds in the Solar neighbourhood formed part of the Gould Belt instead. Massari et al. (2018) presented the precise proper motions of the stars in the Sculptor dwarf galaxy using data from Gaia DR1 and the Hubble Space Telescope. Their measurements showed that Sculptor has a high-inclination

elongated orbit around the Milky Way, and that the orbit takes the dwarf galaxy much farther away than previously thought. Torrealba et al. (2019) discovered Antlia 2, a dwarf galaxy located behind the Galactic disk, in Gaia DR2. At 10 000 times fainter than the Large Magellanic Cloud, it has the faintest surface brightness of any galaxy discovered to date. Price-Whelan et al. (2019) discovered a young open star cluster, named Price-Whelan 1, in the Milky Way halo using Gaia DR2 data. They found that it most likely comes from the Magellanic Clouds, and form part of the Magellanic Stream - the discovery suggests that the stream is roughly half as far from the Milky Way as previously thought.

The HR-diagram obtained by using data from Gaia DR2 is the most detailed to date (see Figure 1.22), and contains roughly 100 times more stars than the HR-diagram compiled by ESA's Hipparcos mission. The improvement from Hipparcos to Gaia is particularly visible when looking at the white dwarf region on the diagram - Hipparcos presented reliable distance measurements of a handful of white dwarfs only; in comparison, Figure 1.22 includes more than 35 000 white dwarfs. This enabled astronomers to study finer features of this population, such as the differentiating signatures between white dwarfs with hydrogen-rich cores, and those that are helium-dominated, presenting themselves as two distinct and roughly parallel populations in the broader white dwarf strip.

A number of 486 641 white dwarf candidates, with 260 000 being high-confidence candidates, have been catalogued by Gentile Fusillo et al. (2019) using Gaia DR2 - a vast improvement as, until recently, only roughly 30 000 white dwarfs have been discovered. This newly discovered vast quantity of white dwarfs opens doors to discoveries of new classes, configurations and effects previously unknown to us. Perpinyà-Vallès et al. (2019) discovered the first triple white dwarf system, surprisingly consisting of same-age stars; the Gaia catalogue contains particularly cool white dwarfs, usually difficult to study due to their dimness - some of these are reported on by Blouin et al. (2018) and Ourique et al. (2019); Tremblay et al. (2019) discovered a pile-up in the cooling sequence of white dwarfs, arising from the release of latent heat and the freeing of gravitational energy due to element sedimentation

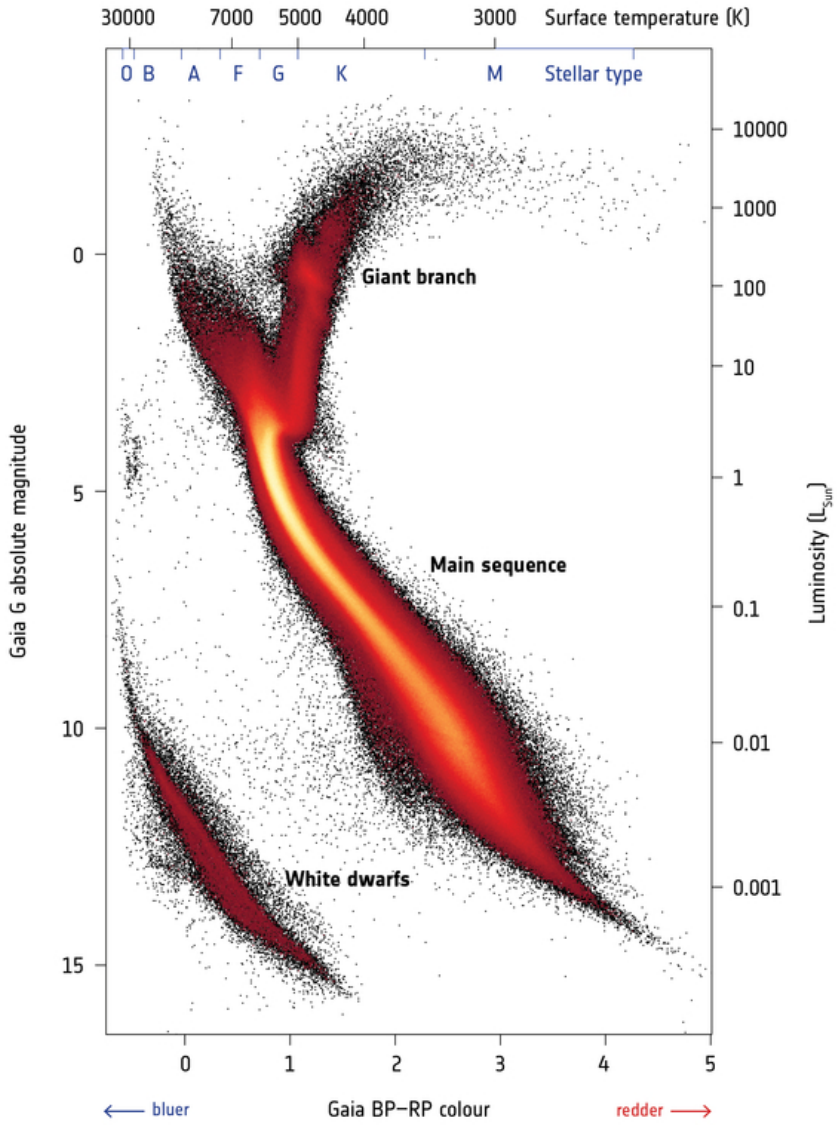

Figure 1.22: Gaia's HR diagram, based on Gaia DR2 data of more than four million stars within roughly 5 000 light-years from the Sun. Lighter colours correspond to increasingly higher numbers of stars. Credit: ESA.

as the cores crystallise - the first direct observational evidence of this phenomenon; Melis et al. (2018) discovered the first metal-polluted single white dwarf; Xu et al. (2018) studied two white dwarfs showing infrared variability, and suggested that the variability could be caused by exoplanets disrupting the white dwarfs' circumstellar dusty disks; Pelisoli et al. (2019) described many new extremely low-mass white dwarfs present in the Gaia catalogue - the study of these can lead to new insights on stellar evolution and the equation of state; Gaia is furthermore enabling the

study of pulsating white dwarfs in greater detail: Stiller et al. (2018) investigated the interaction between a pulsating white dwarf and its companion, a red dwarf, while Kilic et al. (2018) looked for millisecond pulsars with pulsating white dwarf companions; Joyce et al. (2018) used Gaia DR2, Hubble Space Telescope and Far Ultraviolet Spectroscopic Explorer (FUSE) data on a sample of white dwarfs and found that they support the theoretical white dwarf mass-radius relation; due to their specific cooling rates, white dwarfs can be used as age-indicators in our Galaxy - Kilic et al. (2019) used roughly 150 000 white dwarfs in our Galaxy and estimate the Galactic inner halo's age to be approximately 11 billion years; Gaia is also used to study white dwarf progenitors: Cummings et al. (2018) and El-Badry et al. (2018), for example, explored the initial-final mass relationship between progenitor stars and the white dwarfs they evolve into. Shen et al. (2018) further identified three hypervelocity white dwarfs in the Milky Way with speeds exceeding $1000\,\mathrm{km\,s^{-1}}$ in DR2 - possible evidence of the double-degenerate double-detonation SNe Ia scenario where it is thought that the companion white dwarf triggers a double detonation in the primary white dwarf, survives the explosion, and is flung away at velocities equal to the orbital velocity it had before the explosion.

Riess et al. (2018) furthermore used Gaia DR2 data to determine distances to a selection of Milky Way Cepheids more accurately, in turn calibrating distances to SNe Ia and making the most precise SN-based measurement of the Hubble constant yet, and by doing so worsening the discrepancy with Hubble constant measurements based on early-universe observations. Using first Gaia DR1 and then DR2, Marchetti et al. (2017) and Marchetti et al. (2019) found 20 unbound hypervelocity stars - seven of these coming from the Galactic disk and exiting the Milky Way, and the remaining 13 flying towards the Milky Way at high velocities, possibly originating either from as-of-yet unidentified extragalactic sources (providing a unique opportunity to investigate such sources), or alternatively from the Milky Way's halo. Using EDR3 data, Marchetti (2020) narrowed this down to a total of 17 stars most likely to be unbound from our Galaxy - 10 being ejected from the Galactic disk, and seven of extragalactic origin. Belokurov et al. (2020) used Gaia DR2 data to study the

evolution of the binary fraction across the HR-diagram, showing it is higher for massive young stars, drops with stellar mass, and is lowest for white dwarfs. Hwang et al. (2020) used Gaia DR2 data to show that the wide-binary fraction depends strongly on metallicity - as the metallicity increases, the fraction also does, until it peaks and reaches a negative correlation at the high metallicity end. They also find an age-dependence: younger stars have a higher wide-binary fraction. Hartman and Lepine (2020) further used Gaia DR2 to create a catalogue containing 99 203 high-probability wide binary systems; the DR2 catalogue also includes 9 575 classified as Cepheids and 140 784 classified as RR Lyrae stars (Clementini et al., 2019).

Gaia is providing astronomers with new tools and a vast amount of new information with which to study star clusters, probes of the evolution and structure of the Galactic disk, and fundamental to the study of stellar formation and evolution. Castro-Ginard et al. (2018) used a clustering algorithm on a subset of Gaia's DR1 and DR2 to discover and confirm the existence of 21 new nearby open clusters in the Milky Way. This work was followed by that of Cantat-Gaudin et al. (2018), who re-analysed all previously reported clusters using DR2. They confirmed detections of roughly 1200 clusters, and in the process discovered 60 new clusters. Cantat-Gaudin et al. (2019) studied the stellar motions within the nearby stellar group Vela OB2, revealing its overall expansion and the fact that it consists of multiple smaller stellar groupings. They found that Vela OB2's evolution is most likely linked to that of a nearby expanding gas shell, thought to have been caused by a supernova explosion - it is now thought that this event also triggered the formation of Vela OB2's stars.

Soubiran et al. (2018) used DR2 and studied the kinematics of 861 star clusters, finding that open clusters follow the velocity distribution of field stars in the solar neighbourhood. Two studies, by Meingast and Alves (2019) and Röser et al. (2019) respectively, revealed the ongoing evaporation of the Hyades cluster and reported on the discovery of its two tidal tails. Clusters were historically thought of as containing a single population of stars with similar ages, and that therefore a cluster's age could be determined by using its turn-off point on an HR-diagram. Recent years, however, showed evidence that clusters could contain more than

one stellar population, as indicated by many of them having multiple HR-diagram turn-off points. With the onset of Gaia, however, several studies (Marino et al., 2018a,b; Lim et al., 2019; Cordoni et al., 2018) have found that these multiple turn-off points can also be explained by taking into proper account the spin of cluster stars, and its effects on their predicted colours.

1.6.3 Gravitational wave interferometry

Although they are much more complicated and sophisticated, gravitational-wave interferometers essentially rely on the fundamental configuration of the Michelson interferometer. They share an L-shaped structure with mirrors at the end of the detector arms where beams (that were split from a single light source by a beam splitter) are reflected in order to be re-combined and to produce interference patterns. Gravitational wave detectors work on the basic premise that gravitational waves will compress space in one direction while stretching it in a perpendicular direction, and vice versa in a cyclical way, as it propagates through space (see Section 1.2.5). This means the length of one arm of the detector will be stretched/compressed while the other will be compressed/stretched, and this oscillatory behaviour will continue for as long as the wave is passing through the detector. This will keep changing the length of the detector arms relative to one another in what is termed *differential arm motion*, and will produce an interference pattern in the process that can be used to determine the strain of the wave.

The strength of a gravitational wave is referred to as the *gravitational wave strain*, and is a dimensionless number denoted here by h. It is defined as the difference between the fractional changes in proper lengths of the x- and y-axes induced by the wave (see Section 1.2.5 for the orientation of the system), and can be expressed as

$$h = \left(\frac{\delta L_x}{L_x} - \frac{\delta L_y}{L_y} \right). \tag{1.53}$$

As gravity is an extremely weak force, gravitational wave strain is generally incredibly small, and therefore notoriously difficult to detect - as an example, the peak gravitational wave strain during the first detection of gravitational waves was

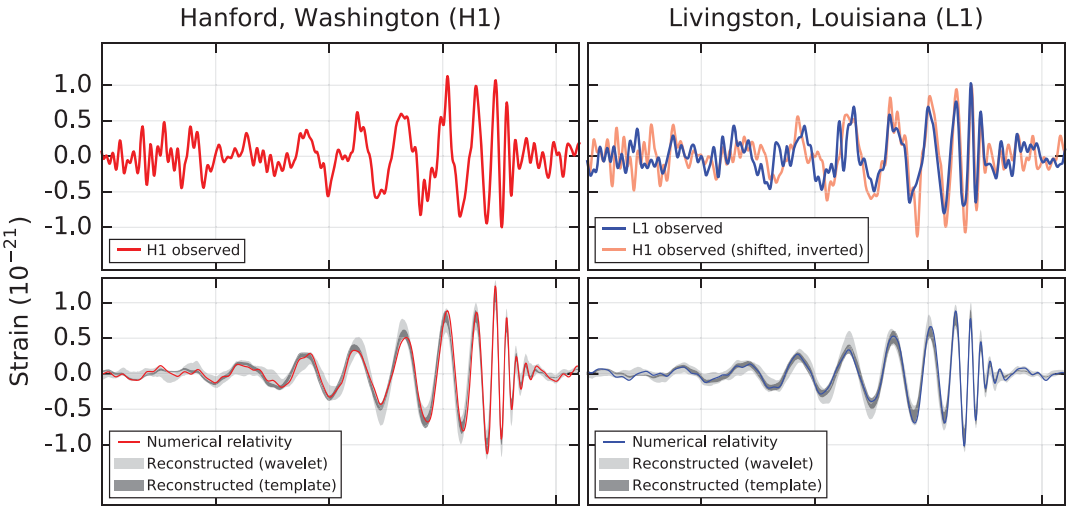

Figure 1.23: The gravitational-wave event GW150914 as observed by aLIGO's two detectors on the 14$^{\text{th}}$ of September 2016 (left column: Hanford detector; right column: Livingston detector). Figure adapted from Abbott et al. (2016b).

of the order of 10^{-21} (Abbott et al., 2016b; Królak and Patil, 2017). It took a large amount of effort over many decades to arrive at an experimental setup that was sensitive enough to directly detect gravitational waves for the first time. On the 14$^{\text{th}}$ of September 2016, however, the two detectors of the Advanced Laser Interferometer Gravitational-Wave Observatory (aLIGO) simultaneously observed a gravitational-wave signal (see Figure 1.23) matching the waveform predicted for the inspiral and merger of a pair of BHs (Abbott et al., 2016b), thereby experimentally verifying Einstein's prediction while at the same time opening up a completely new window through which to observe the Universe.

Interferometric detector strain and performance

The strain $s(t)$ of a gravitational-wave interferometer detector responding to the gravitational waves from a BH binary inspiral can be expressed as

$$s(t) = \sum_{A=+,\times} D^{ij} \epsilon_A^{ij} h_A(t), \tag{1.54}$$

where D^{ij} denotes the detector tensor, ϵ_A^{ij} denotes the polarisation tensor and the gravitational wave component in polarisation A is given by $h_A(t)$ (see Forward

1978; Estabrook 1985; Schutz and Tinto 1987; Maggiore 2008 for a full account of this definition).

The performance of an interferometric gravitational-wave detector depends on two main factors: the frequency range over which the detector can observe gravitational waves effectively, $[f_l, f_h]$, and the detector noise. Strain measured by current detectors is on the order of $10^{-21} - 10^{-22}$, and detector noise is therefore one of the most important aspects determining whether a detection would pass the required level of statistical significance or not.

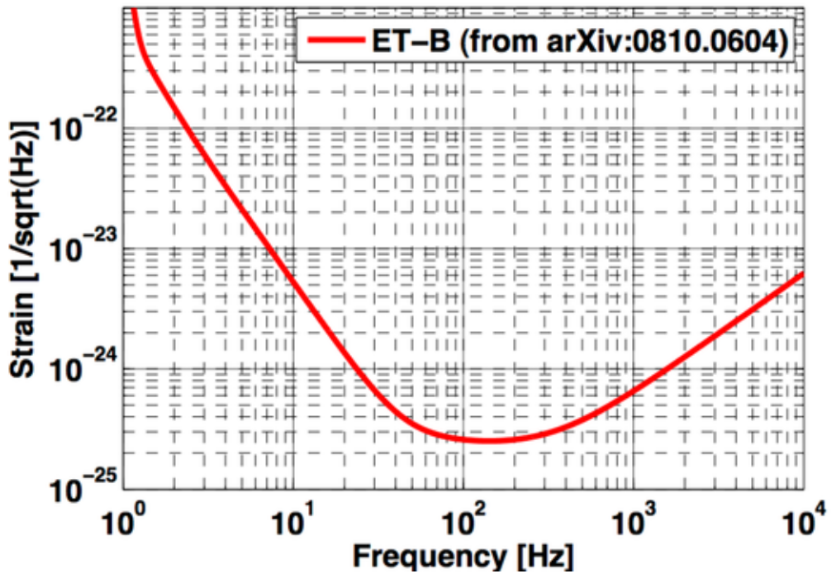

Figure 1.24: An example of the noise power spectral density $\sqrt{|S_n(f)|}$ plotted against frequency f, taken from the Einstein Telescope (ET) project Web Site[a]. The data shows one of the originally proposed target sensitivities for the ET (Hild et al., 2008).

[a]The Einstein Telescope project Web Site: `http://www.et-gw.eu`

Detector noise in gravitational-wave detectors is frequency dependent, and is usually described by plots showing the square root of the noise power spectral density $\sqrt{|S_n(f)|}$ (in units of $1/\sqrt{\text{Hz}}$) against frequency f. The noise power spectral density $S_n(f)$ is here the Fourier transform of the noise strain $S_n(t)$, and a typical example of such a plot can be seen in Figure 1.24.

The frequency range over which a detector is sensitive determines the gravitational sources it can study. As examples, the cosmic microwave background can

be studied at frequencies around 10^{-16} Hz, inspiralling binary supermassive black holes can be studied between $10^{-10} - 10^{-4}$ Hz and upwards of 10^{-2} Hz compact binary systems, pulsars and supernovae can be investigated.

Current and planned gravitational wave detectors

Current gravitational-wave detectors are referred to as second-generation detectors. Two of the most important current observatories (and the ones of importance to Chapter 2 of this Thesis) are aLIGO and Advanced Virgo (AdV).

LIGO[24] (Aasi et al., 2015; Castelvecchi, 2019) first went online in 2002 and consists of two L-shaped interferometric gravitational-wave detectors (each with arms 4 km long) - one is located at the Hanford Observatory in Washington, and the other is at the Livingston Observatory in Louisiana. aLIGO, an upgraded version of the LIGO project, came online in September 2015. It operates over the frequency range 10 Hz to 10 kHz, and is responsible for the first direct detection of gravitational waves made on 14 September 2015 (Abbott et al. 2016b, see also Figure 1.23).

Virgo[25] is a 3 km interferometric gravitational-wave detector located at the European Gravitational Observatory in Santo Stefano a Macerata near the city of Pisa in Italy, and is a collaboration between laboratories from Italy and France, the Netherlands, Poland, Hungary and Spain. Since 2007, Virgo and LIGO have shared and jointly analysed their data, and also jointly published their results. AdV covers the frequency range $10 - 6000$ Hz, came online in September 2017 and has since been observing in conjunction with LIGO.

Other noteworthy detectors include the interferometric 3-km-arm underground Kamioka Gravitational Wave Detector (KAGRA[26]) in Japan and the GEO600[27] in Germany.

Detectors in their early design stage are referred to as third-generation gravitational-wave detectors - they will build on the technology of detectors that came before

[24]LIGO home: `https://www.ligo.caltech.edu`
[25]Virgo home: `http://www.virgo-gw.eu`
[26]KAGRA home: `https://gwcenter.icrr.u-tokyo.ac.jp/en`
[27]GEO600 home: `https://www.geo600.org/1037150/GEO_High_Frequency`

them. The Einstein Telescope[28] (ET, Sathyaprakash et al. 2012) is a proposed detector that will have much-improved noise performance and will be sensitive to the range of gravitational waves between 1 Hz and 10 kHz. It will most likely be underground to limit seismic noise, and will consist of three arms (each 10 km long) in an equilateral triangle. The Laser Interferometer Space Antenna[29] (LISA, Amaro-Seoane et al. 2012) will consist of three spacecraft arranged in an equilateral triangle with sides 2.5 million km long and will be sensitive over the low-frequency range of $10^{-4} - 1$ Hz. Its launch date is currently set in 2034. Finally, the Cosmic Explorer[30] (Abbott et al., 2017a) is a proposed U.S.-based ground-based L-shaped interferometric detector with arms 40 km long.

1.6.4 The Rossi X-ray Timing Explorer

The satellite carrying the Rossi X-ray Timing Explorer (RXTE)[31] (Bradt et al., 1993) was launched into low-Earth circular orbit from the National Aeronautics and Space Administration's (NASA) Kennedy Space Center on 30 December 1995 with the aim of exploring the variability of X-ray sources such as BHs, NSs, X-ray pulsars and X-ray bursts. The idea was to accomplish this by obtaining a time domain picture of X-ray emission with unprecedented time resolution, and combining that with moderate spectral resolution. Originally expected to have a lifetime between two and five years, it surpassed this goal and extraordinarily was only decommissioned on 5 January 2012, yielding 16 years worth of observational data. The RXTE, shown in Figure 1.25, consists of three observational instruments: the All Sky Monitor (ASM), the High Energy X-ray Timing Experiment (HEXTE) and the Proportional Counter Array (PCA).

The ASM (Levine et al., 1996) has three wide-angle shadow cameras fitted with proportional counters[32], and has a total collecting area of 90 cm^2. Operating in

[28]Einstein Telescope home: `http://www.et-gw.eu`
[29]Einstein Telescope home: `http://www.et-gw.eu`
[30]Cosmic Explorer home: `https://cosmicexplorer.org`
[31]RXTE home: `https://heasarc.gsfc.nasa.gov/docs/xte/xtegof.html`
[32]A proportional counter is a gaseous ionization detector that measures particles of ionising radiation. It measures the energy of radiation by producing an output proportional to that of the radiation energy.

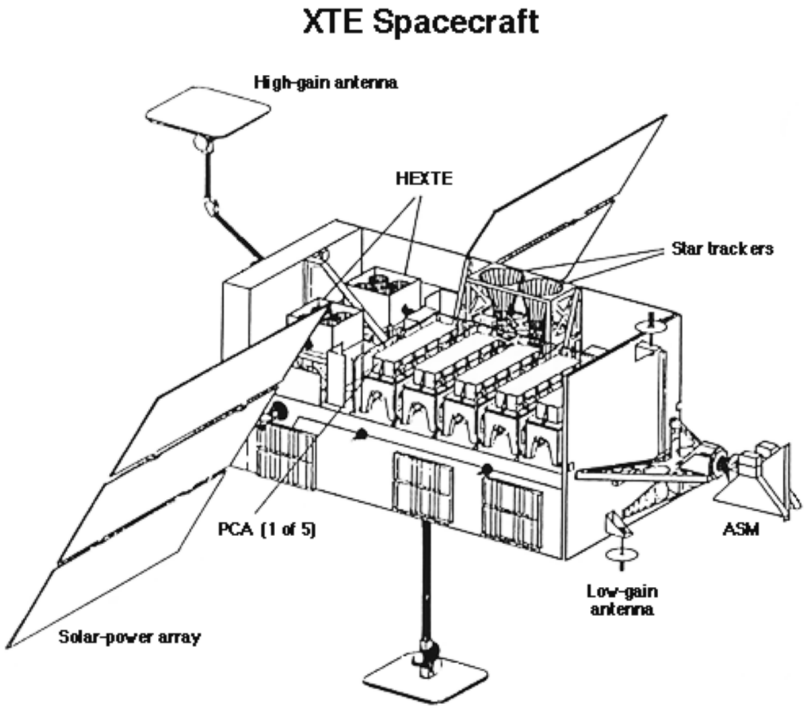

Figure 1.25: The RXTE and its three observational instruments: the ASM, the HEXTE and the PCA. This figure was adapted from Bradt et al. (1993).

the $2 - 10$ keV range with a spatial resolution of $3' \times 15'$ and a time resolution of 0.125 s, it observed 80% of the sky with every 90 minute orbit of the RXTE. The ASM allowed the monitoring of the long-term behaviour of bright X-ray sources, and played a role in identifying outbursts and state transitions of transient sources which would then trigger follow-up observations by other instruments.

The HEXTE (Rothschild et al., 1998) comprises of two clusters, each consisting of four scintillation detectors[33] and a collection area of 800 cm^2. It operated in the $15 - 250$ keV range, had an energy resolution of 15% at 60 keV, a time resolution of 8 μs and a 1° field of view. The clusters could oscillate in order to provide background measurements either 1.5° or 3° away from the source every 16 to 128 seconds to resolve the background estimation issues related to the instrument's large field of view and lack of spatial resolution.

The PCA (Jahoda et al., 2006) is the main instrument aboard the RXTE, and the one of importance for this thesis. It is a pointed instrument that is co-aligned

[33] An instrument measuring ionising incident radiation from the excitation effect the radiation has on a scintillator material - the instrument detects the resulting light pulses.

with HEXTE, consists of five proportional counters with a total collecting area of 6500 cm^2, operated in the $2 - 60$ keV range with a maximum time resolution of 1 μs and a field of view of 1°, and has an energy resolution of 18% at 6 keV.

RXTE data has been involved in many discoveries during and since the time of its operation. It was responsible for the first direct evidence of the frame-dragging effect predicted by the theory of general relativity (Cui et al., 1998), and was used to show that the Galactic ridge X-ray emission (GRXE) intensity follows the Galactic near-infrared surface brightness, therefore tracing the Galactic stellar mass distribution and proving that the diffuse X-ray background in the Galaxy originates from previously undetected white dwarfs and other stars' coronae (Revnivtsev et al., 2007). The RXTE was further used to infer the mass of the smallest known BH at 3.8 $M_\odot$ (Shaposhnikov and Titarchuk, 2008), used to find the first millisecond pulsar in an accreting binary star system (Marshall et al., 1998), and was (and still is) used for many other findings and discoveries.

1.7 Summary and Outline of Thesis

The work in this thesis will focus on compact and double compact binary systems as rich laboratories with which to investigate an array of different natural phenomena - the ones of interest here being the binary stellar evolution involved in producing stellar-mass double BH binaries close enough to merge in a Hubble time, as well as the probing of strong-field general relativity and the study of accretion using NS LMXBs. The general layout of the thesis and the grouping of these topics into its various chapters are discussed below.

Chapter 2 has as its aim the estimation of binary black hole (BBH) merger and pair-instability supernova (PISN) rates based on the supposition that close BBH systems can form through a process of chemically homogeneous evolution (CHE), whereby the rapid rotation of massive stars in very close binaries induces enough mixing to keep stars chemically homogeneous, enabling them to avoid the traditional expansion that is characteristic of the post-main sequence phase. When the stars in these systems eventually collapse into BHs close enough to merge in a Hubble time,

they would be similar to the binaries whose mergers were recently detected for the first time by aLIGO and VIRGO, thereby providing the theoretical framework for the existence of these systems. I conduct a binary population synthesis simulation incorporating detailed cosmological calculations of the metal-dependent SFR of the Universe in order to investigate the population properties, cosmological rate estimates and aLIGO detection rates of binary black hole mergers formed through the process of CHE. I further examine the effect that momentum kicks during BH collapse would have on these properties, estimate the cosmological- and magnitude limited PISN rates and gauge the effects that high-redshift deviations in SFR would have on eventual merger rates. If rates predicted here correspond well with the findings of aLIGO in the future, CHE could be a worthy contender for explaining close binary evolution for massive rapidly rotating stars.

Chapter 3 investigates the NS LMXB system 4U1608-52, a transient atoll source that has been thoroughly observed by the RXTE. I analyse its fast-time variability by finding and inspecting its quasi-periodic oscillations (QPOs), commonly found in the X-ray power density spectra (PDS) of accreting compact binaries, in order to probe the strong-field gravity effects by estimating the spin and mass of the NS based on the relativistic precession model (RPM). 4U1608-52 is an ideal source for such investigations as its PDS shows evidence of a rich phenomenology including various different types of QPOs, as well as Type-I X-ray bursts. Estimations of the mass and spin of the NS can furthermore be found in the literature, giving us the opportunity to compare them with the results of our calculations involving the RPM. The implications of our findings are discussed in the context of equation of state predictions, physically allowed spin ranges, emission proximity to the innermost stable circular orbit and possible model inaccuracies.

Chapter 4 consists of a re-analysis of the RXTE observations of IGR J17480-2446, an 11 Hz accreting pulsar located in the globular cluster Terzan 5, during its 2010 outburst. General relativistic predictions state that, in the vicinity of a spinning compact object, frame-dragging induces the precession of matter orbiting the object. This effect can be observed as QPOs with a characteristic frequency in

the X-ray light curves of accreting compact objects - such QPOs have historically been classified as horizontal branch oscillations (HBOs) in NS systems, and for a NS spinning at 11 Hz these oscillations are expected at frequencies below 1 Hz. Previous studies of IGR J17480-2446, however, have classified QPOs found in the frequency range $35 - 50$ Hz as HBOs, thereby bringing the frame-dragging nature of such QPOs (and the RPM, which relies on this assumption) into question. In this chapter, I employ different methods of analysis to study the fast-time variability properties of the source over a large frequency range: I search for QPOs with centroid frequencies ranging from the mHz to the kHz, and discuss the implications of the findings on the nature of all groups of QPOs detected.

Finally, Chapter 5 summarises the main results and discussions of the previous chapters, and concludes the thesis.

No sympathy for the Devil, keep that in mind. Buy the ticket, take the ride.

Hunter S. Thompson, Fear and Loathing in Las Vegas

2

Cosmic Rates of Black Hole Mergers and Pair-Instability Supernovae from Chemically Homogeneous Binary Evolution

2.1 Abstract

During the first three observing runs of the Advanced gravitational-wave detector network, the LIGO/Virgo collaboration detected several black hole binary (BHBH) mergers. As the population of detected BHBH mergers grows, it will become possible to constrain different channels for their formation. Here we consider the chemically homogeneous evolution (CHE) channel in close binaries, by performing population synthesis simulations that combine realistic binary models with detailed cosmological calculations of the chemical and star-formation history of the Universe. This allows us to constrain population properties, as well as cosmological and aLIGO/aVirgo detection rates of BHBH mergers formed through this pathway. We

The work here has been published in the Monthly Notices of the Royal Astronomical Society as du Buisson et al. (2020); doi: 10.1093/mnras/staa3225, and has been adapted for use here as a chapter.

predict a BHBH merger rate at redshift zero of $5.8\,\mathrm{Gpc}^{-3}\mathrm{yr}^{-1}$ through the CHE channel, to be compared with aLIGO/aVirgo's measured rate of $53.2^{+55.8}_{-28.2}\,\mathrm{Gpc}^{-3}\mathrm{yr}^{-1}$, and find that eventual merger systems have BH masses in the range $17-43\,\mathrm{M}_\odot$ below the pair-instability supernova (PISN) gap, and $>124\,\mathrm{M}_\odot$ above the PISN gap. We investigate effects of momentum kicks during black hole formation, and calculate cosmological and magnitude limited PISN rates. We also study the effects of high-redshift deviations in the star formation rate. We find that momentum kicks tend to increase delay times of BHBH systems, and our magnitude limited PISN rate estimates indicate that current deep surveys should be able to detect such events. Lastly, we find that our cosmological merger rate estimates change by at most $\sim 8\%$ for mild deviations of the star formation rate in the early Universe, and by up to $\sim 40\%$ for extreme deviations.

2.2 Introduction

From its first, second and third observing runs (referred to as the O1, O2 and O3 runs, respectively), the LIGO/Virgo collaboration has reported several detections of gravitational-wave signals from merging binary black holes (BHBHs, Abbott et al. 2019; Abbott et al. 2019b), and several more candidate detections[1]. Further BHBH merger candidates have been identified by other groups (Venumadhav et al., 2019; Nitz et al., 2019). These BHBH merger detections match the inspiral and merger of BHs covering a range of masses, the smallest progenitor masses belonging to GW170608 at $11.0^{+5.5}_{-1.7}\mathrm{M}_\odot$ and $7.6^{+1.4}_{-2.2}\mathrm{M}_\odot$ (Abbott et al., 2017c), and the largest progenitor masses belonging to GW170729 at $50.2^{+16.2}_{-10.2}\mathrm{M}_\odot$ and $34.0^{+9.1}_{-10.1}\mathrm{M}_\odot$ (Abbott et al., 2019b). These detections have provided us with the first direct evidence that binary stellar-mass black hole mergers at the present epoch exist. The estimated local merger rate, provided by the aLIGO and Virgo Collaborations after the second observation run, lies in the range $53.2^{+55.8}_{-28.2}\,\mathrm{Gpc}^{-3}\mathrm{yr}^{-1}$, pointing towards the possibility of many BHBH merger detections per year as the detectors reach their full sensitivity (Abbott et al., 2019b,a).

[1]Gravitational Wave Candidate Event Database: `https://gracedb.ligo.org`

It was already known that binary systems consisting of stellar remnants that merge in a Hubble time existed — consider e.g. the double neutron star (NS) systems such as the Hulse-Taylor binary (Hulse and Taylor, 1975; Weisberg et al., 2010) and the double pulsar system PSR J0737-3039 (Burgay et al., 2003). BHBHs however, have up to very recently eluded us due to their lack of electromagnetic radiation. Therefore, although one can empirically estimate the merger rate of double NS systems based on direct observations of binary NS populations (Phinney, 1991; Narayan et al., 1991; Kim et al., 2003; O'Shaughnessy and Kim, 2010), this is not the case with BHBHs due to the lack of observational evidence. Estimates of BHBH merger rates have therefore historically been very uncertain (Abadie et al., 2010) and reliant on predictions from population synthesis simulations assuming specific stellar and binary evolutionary models.

As black holes constitute the most massive of the stellar remnants, the gravitational-wave radiation from their mergers will be stronger than that emanating from binary NS or binary white dwarf mergers. Indeed, several groups had predicted that BHBH mergers could be the dominant source of detections for LIGO (Lipunov et al., 1997; Voss and Tauris, 2003; Belczynski et al., 2010; Dominik et al., 2015; Abadie et al., 2010). With the confirmed gravitational-wave detections of BHBH mergers, we now have the first empirical "observations" of such events. As more and more detections are made and the population of known BHBH mergers grows, it will become possible to constrain the various proposed formation channels for BHBH mergers (Bulik and Belczyński, 2003; Mandel and O'Shaughnessy, 2010; Stevenson et al., 2015; Mandel et al., 2015; Farr et al., 2017; Zevin et al., 2017).

There are different suggestions of possible evolutionary pathways to explain the eventual formation of a BHBH system able to merge at the present epoch. Some examples include dynamical formation (see Section 1.4.2), classical common-envelope evolution (see Section 1.4.3), and chemically homogeneous evolution (CHE, see Section 1.4.5). CHE evolution is possible in very close binaries (de Mink et al., 2009; de Mink and Mandel, 2016a; Marchant et al., 2016) that have both stars nearly in contact at the start of the hydrogen burning phase. The stars are then tidally locked

to the orbit which enforces rapid rotation, induces rotational mixing and keeps the stars chemically homogeneous during most of the core hydrogen burning phase, dramatically changing their further evolution (Maeder, 1987; Langer, 1992; Heger and Langer, 2000; Yoon et al., 2006). This is discussed in more detail in Section 1.4.5.

In this chapter, we use the results from detailed simulations of the CHE scenario as developed by Marchant et al. (2016) and combine these with the cosmological simulations of the chemical and star formation history of the Universe by Taylor and Kobayashi (2015b) to conduct a binary population synthesis study and to investigate the population properties, cosmological rates and aLIGO detection rates of BHBHs. We also determine the cosmological pair-instability supernova (PISN) rate in this scenario.

PISNe are rare events that occur when pair production in the core of a very massive star softens the equation of state (EoS) causing it to become unstable before oxygen is ignited in its core. This leads to a partial collapse followed by a runaway thermonuclear explosion that blows the star apart, leaving no remnant (Fowler and Hoyle, 1964; Rakavy and Shaviv, 1967). This is expected to happen to low-metallicity stars with a final helium core mass $M_{\rm He,f}$ in the range of roughly $60 \lesssim M_{\rm He,f}/M_{\odot} \lesssim 130$ (Heger and Woosley 2002; Woosley 2017; Marchant et al. 2018). We refer to this as the PISN gap[2] - see Section 1.3.3 for the relevant background on PISNe and the PISN gap. These events are also of interest as they can be used to probe stellar evolution in low-metallicity regimes.

We find cosmological BHBH merger rates through the CHE channel that may represent a non-negligible fraction of the total merger rate (Abbott et al., 2019b) and show that we might soon be detecting massive mergers from above the PISN gap. In addition, the presence of systems with very small delay times may make it possible to use future detections of high-redshift mergers to provide insight to the evolution of massive stars in the early Universe.

[2]A BHBH merger with one or both components in the PISN mass gap, GW190521 (Abbott et al., 2020d), was observed while this thesis was under review; as discussed by Abbott et al. (2020c), it may have originated from other evolutionary channels - see Section 1.3.3 for more detail.

The chapter is structured as follows: Section 2.3.1 gives an overview of the hydrodynamical simulations and resulting star formation history of Taylor and Kobayashi (2015b) that is used in our simulations, Section 2.3.2 describes the work of Marchant et al. (2016) and the binary calculations used in this study, and Section 2.3.3 summarizes our simulations, the overall setup and the assumptions made. Section 2.4 presents our main results: final population properties and rates, the effects of possible momentum kicks during black-hole formation, the outcomes of deviations in the high-redshift star formation rate[3] (SFR) and the calculation of PISN rates and their detectability. Lastly, Section 2.5 gives concluding remarks and discusses future work.

2.3 Methods

2.3.1 Star formation history and metallicity distribution

As was shown by Marchant et al. (2016), the properties of the BHBH mergers formed through the CHE channel (see Section 1.4.5), e.g. the final black-hole masses and the delay times, are a strong function of the metallicity[4] of the progenitors. Therefore, to estimate the merger rates at the current epoch (or any other epoch), one needs not only the star formation history of the Universe as a function of redshift but also its dependence on metallicity (see also Chruslinska et al. 2019, Chruslinska and Nelemans 2019, Belczynski et al. 2017 and Neijssel et al. 2019 on the uncertainties in the metallicity-specific SFR). We obtain these distributions from the cosmological simulation by Taylor and Kobayashi (2015b) – a self-consistent, hydrodynamical simulation in a $(25h^{-1}\mathrm{Mpc})^3$ volume that includes star formation, feedback from supernovae, active galactic nuclei (Taylor and Kobayashi, 2014), and the effects of chemical enrichment. Here h is the dimensionless Hubble constant, taken to be 0.7. The resolution of simulated galaxies is $1.4 \times 10^7 h^{-1}\mathrm{M}_\odot$, meaning that the smallest reliable galaxies would lie around $\sim 10^9\mathrm{M}_\odot$ and that galaxies below this resolution are not constrained from observations. However, the contributions

[3]The star formation rate gives the total mass of stars formed over time.
[4]Metallicity is defined as the mass fraction of elements heavier than helium.

of such low-mass galaxies to stellar mass and metallicities are small, and thus we include all particles of the simulation volume in the analysis of this paper. Note that, however, given the extremely low metallicity of dwarf galaxies, they can be important environments for the formation of massive black hole progenitors (see e.g. Toffano et al. 2019). If the metallicities of such dwarf galaxies in the simulations are overestimated by >> 0.5 dex (due to non-universal nucleosynthesis yields or the initial mass function), then it could affect the rates determined in this paper.

This simulation uses the most recent chemical enrichment sources: the nucleosynthesis yields are taken from Kobayashi et al. 2006 (see also Nomoto et al. 2013), which are consistent with the elemental abundances observed in the Milky Way. The modeling of Type Ia supernova progenitors here is based on the single degenerate scenario and includes metallicity effects, which affect the timescale for iron enrichment. The simulation assumes a Kroupa initial mass function (IMF) for all galaxies (Kroupa, 2001). This simulation can reproduce various observations of galaxies: the so-called M-σ relation[5], the black hole mass to bulge mass relation, the galaxy size to mass relation and, most importantly for our study, the stellar and gas-phase mass-metallicity relations (Taylor and Kobayashi, 2015b) as the black-hole merger production will depend crucially on these relations. In the simulation, active galactic nuclei (AGN) cause large-scale metal-enriched outflows (Taylor and Kobayashi, 2015a), the mass-metallicity relation evolves as a function of time (Taylor and Kobayashi, 2016), and the metallicity radial gradients loosely correlate with the galaxy mass (Taylor and Kobayashi, 2017).

The simulation tracks the formation redshift and metallicity at the formation time for all stars that have formed up to redshift zero, with cosmological parameters $\Omega_M = 0.28$ and $\Omega_\Lambda = 0.72$. We can therefore track the SFR as a function of both redshift and metallicity. In order to obtain a figure of merit that will allow us to draw from the SFR distribution as a joint function of redshift and metallicity, we produce a two-dimensional matrix displayed in Figure 2.1, showing the differential SFR per unit metallicity. Also shown in the figure are the percentiles for the SFR,

[5]The correlation between the stellar velocity dispersion σ in the bulge of a galaxy and the mass M of the supermassive BH at its centre.

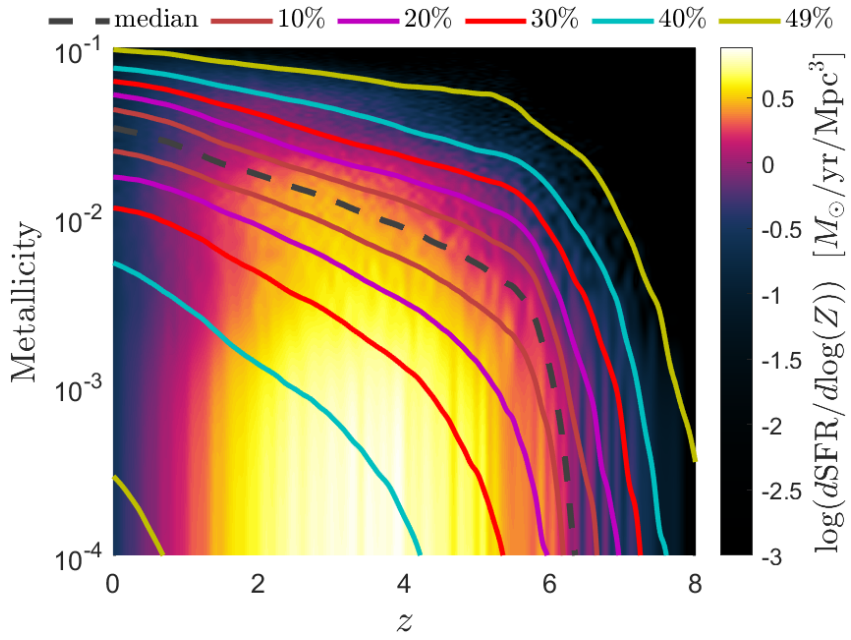

Figure 2.1: The density distribution of the star formation rate (SFR) as a function of metallicity (Z) and redshift (z), obtained from the hydrodynamical simulations of Taylor and Kobayashi (2015b), described in Section 2.3.1. The curves show quantiles of the cumulative metallicity distribution of star formation at a given redshift. One can clearly see that the median metallicity increases towards low redshifts and that the SFR becomes insignificant at high redshifts of the order of $z \sim 8$. This distribution provides the statistical formation redshift and metallicity input to our CHE modelling.

given a certain redshift and metallicity. By integrating this joint function over all metallicities the usual Madau plot is obtained (Madau and Dickinson 2014): Figure 2.2 shows the Madau plot for different metallicity ranges, as well as the overall SFR in red, with $Z_\odot$ the Solar metallicity taken as 0.017 (Grevesse et al., 1996). The expectation that the metallicites are modelled correctly and self consistently allow us to use the resulting SFR distribution to model low-metallicity binaries at all redshifts — these are the systems acting as possible BHBH progenitors in our Monte Carlo simulations. By integrating the SFR over the observable Universe, we can calculate the total mass converted into stars as $2.4 \times 10^{20} M_\odot$.

2.3.2 Results from detailed CHE evolution models

The binary calculations used in this study are based on the CHE scenario (see Section 1.4.5) as described by Marchant et al. (2016), where they studied close binaries consisting of stars with initial masses larger than $\sim 20\,\mathrm{M}_\odot$ (see Section 1.4.5

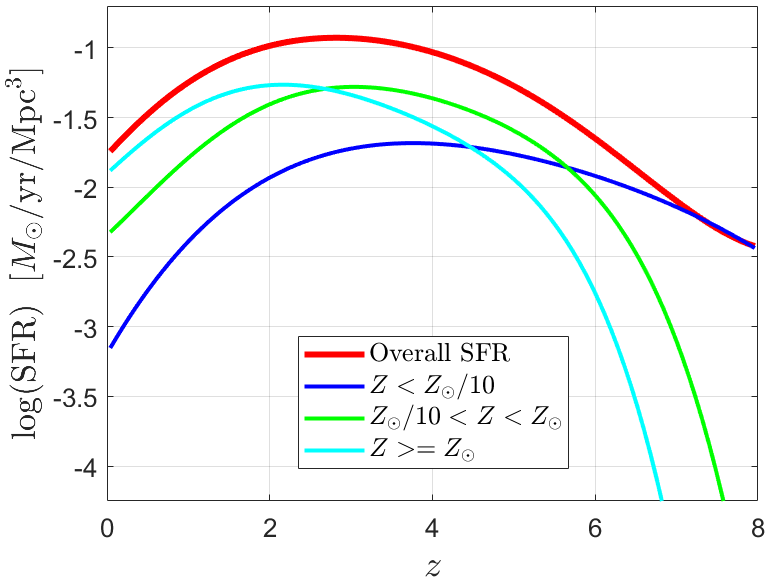

Figure 2.2: The Madau plot shown for different ranges of metallicity for the hydrodynamical simulations of Taylor and Kobayashi (2015b), discussed in Section 2.3.1. **Red:** The Madau plot for all ranges of metallicity; **Dark blue:** For metallicities $Z < Z_\odot/10$; **Green:** $Z_\odot/10 < Z < Z_\odot$; **Light blue:** $Z > Z_\odot$. For this work, solar metallicity $Z_\odot$ is taken to be 0.017 as in Grevesse et al. (1996). For the metallicity range considered in our Monte-Carlo simulation ($-5.0 < \log(Z) < -2.375$, as discussed in Section 2.3.3), the dark blue and green curves are the only relevant curves.

and also Maeder (1987), Langer (1992), and Heger and Langer (2000) on why massive stars allow for efficient rotational mixing). Here, the calculations were extended until core carbon depletion, and covers a much larger range of initial conditions. Using the MESA v11701 stellar evolution code (Paxton et al., 2011, 2013, 2015, 2018, 2019), we extended these calculations to obtain a fine grid of models as a function of metallicity, initial primary mass and initial orbital period for a fixed initial mass ratio $q_\mathrm{i} = M_{2,\mathrm{i}}/M_{1,\mathrm{i}} = 1$. The metallicity range was taken as $-5.0 \leq \log(Z) \leq -2.375$, where $\log(Z) = -2.375 \approx \log(Z_\odot/3)$). The initial primary mass range was taken as $25 \leq M_{1,\mathrm{i}}/M_\odot \leq 500$ (see Marchant et al. (2016), Section 1.4.5, and above on the physical origin of the lower mass limit for chemically homogeneous evolution), and the initial orbital period range was taken as $0.4 \leq P_\mathrm{i}/\mathrm{d} \leq 4.0$ (see Appendix A for details). In total, we calculated roughly 150,000 new binary evolution sequences

(as compared to about 2,000 used in Marchant et al. 2016)[6].

To account for the occurrence of PISNe, we use the results from the hydrodynamical simulations of Marchant et al. (2019) who find that stars that deplete core carbon with helium core masses between $60.8 < M_{\rm He,f}/M_\odot < 124$ are completely disrupted and leave no remnant. Stars just below the PISNe threshold are also expected to become unstable due to pair-creation in their cores, but the resulting thermonuclear explosion only removes a fraction of the total mass. The star can then undergo multiple pulsations and associated mass loss events before finally collapsing to a BH, a process which is called a pulsational-PISN (PPISN, Fraley 1968; Woosley 2017). To account for mass loss before BH formation from PPISNe we also consider the results of Marchant et al. (2019) who find this outcome to happen for stars with helium core masses between $35.1 < M_{\rm He,f}/M_\odot < 60.8$ at core carbon depletion (see also Farmer et al. 2019). For stars falling in this mass range we interpolate the final BH masses predicted by Marchant et al. (2019). The impact on the orbit of mass ejected through a PPISN is modeled as a single Blaauw kick (Blaauw, 1961), which modifies the semi-major axis of the binary and its eccentricity.

Afterwards, we assume that the system circularizes while conserving orbital angular momentum, resulting in an orbital separation $a = a_0(1 - e_0^2)$ where a_0 and e_0 are the semi-major axis and eccentricity resulting from the Blaauw kick. This is motivated by the results of Marchant et al. (2019), who find that PPISNe occurring in binary systems compact enough to produce a merging BHBH would lead to Roche-lobe overflow before BH formation. Stars that deplete carbon with $M_{\rm He,f} < 35.1 M_\odot$ or $M_{\rm He,f} > 124 M_\odot$ are assumed to directly collapse into a BH with no mass loss.

An example of one of our model grids for $\log(Z) = -3$ is shown in Figure 2.3, with each rectangle corresponding to one detailed binary evolution model and showing the final fate of each system (the final fate being a function of the final calculated binary parameters). Possible fates include systems that fail to evolve

[6]The results of our MESA simulations, including tables summarizing the outcomes and the necessary input files to reproduce them, are available at `https://doi.org/10.5281/zenodo.3348337`. The source code used for our Monte Carlo calculations, as well as the results of our Monte Carlo simulations, are provided here as well.

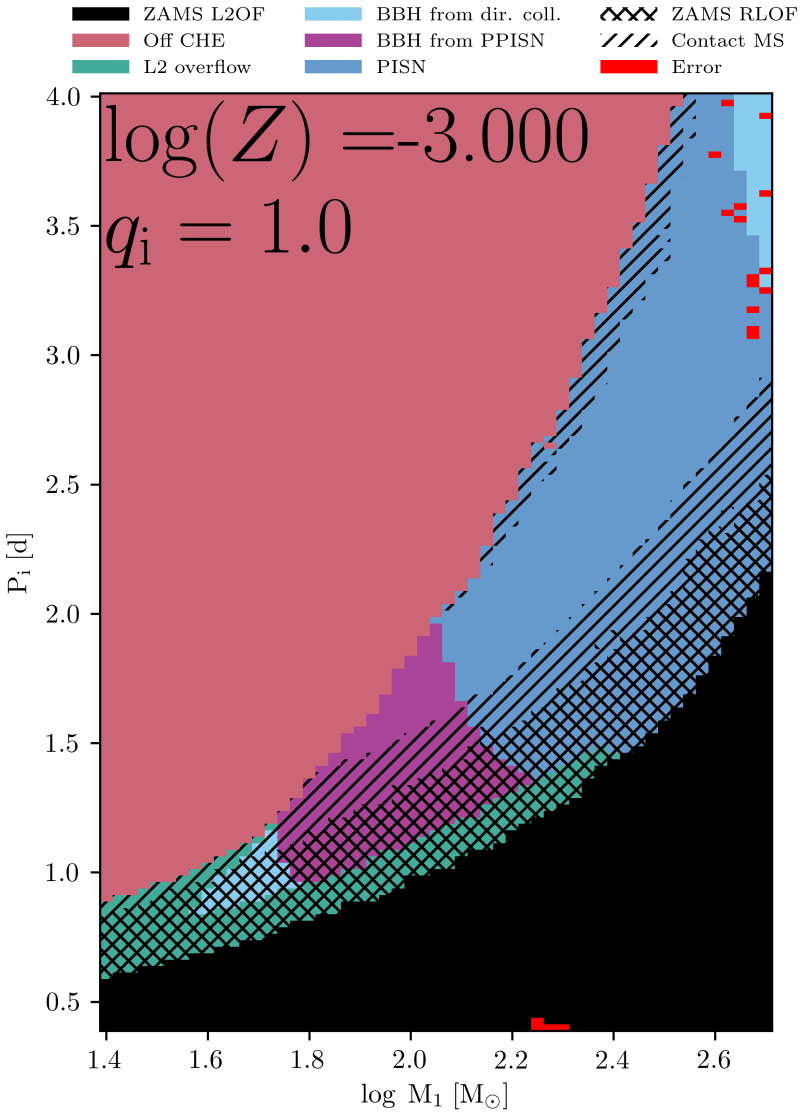

Figure 2.3: An example of a grid of binary systems showing their initial period P_i (in days) and initial primary mass $M_{1,i}$ for $\log(Z) = -3$ and $q_i = 1$, with their final outcomes colour-coded according to the legend at the top. Black regions have initial periods small enough to have L2 overflow at the ZAMS, while green areas are systems reaching L2 overflow during the main sequence – for both of these scenarios, systems rapidly merge. Pink areas depict systems where rotational mixing is not efficient enough and where at least one component no longer evolves chemically homogeneously; these systems are thus not considered progenitors of BHBH systems in this CHE study. Blue regions successfully form double He star binaries that will either collapse to form BHBH systems (light blue) or whose members will explode in pair-instability supernovae (dark blue) at a later stage. Purple denotes areas forming BHBH systems via the PPISN path. Single hatch-marks show systems experiencing contact during the main sequence, while double hatch-marks are models in contact at the ZAMS already. Red regions show models for which the simulations did not converge. For more information and examples of grids, see Appendix A. (ZAMS: Zero Age Main Sequence).

chemically homogeneously, systems that have L2 overflow at the ZAMS or on the main sequence and therefore rapidly merge long before collapsing into black holes, and systems that successfully form double He stars (see Fig. 2.3 for more information). We are interested in the latter group, as they will either collapse to form BHBHs or become pair-unstable. It can be seen that, for double massive He stars to be the final outcome, initial primary masses above $\sim 40\,\mathrm{M}_\odot$ are required, and that the range of initial periods of progenitor systems for these binaries widens with an increase in primary mass. It is worth noting that, for most binaries below the PISN regime, overcontact systems dominate the progenitor space, and that contact-free evolution is only really found in systems having initial primary masses above $100\,\mathrm{M}_\odot$. See Appendix A for further examples of the grids used.

2.3.3 Monte Carlo simulations

We systematically explore CHE evolution by carrying out Monte Carlo simulations that draw massive binary systems from a co-moving box of fixed co-moving volume[7] V_{MC} stretching from the birth of the Universe to $z = 0$. We then transform the rates calculated from this to rates observable from Earth by integrating over our light cone. This section first describes the general outline of the simulation and the way in which binaries are sampled, whereafter a discussion of the rates and their normalisation follows.

Sampling

The Monte Carlo method is used to draw the birth redshift (z_0), metallicity (Z_0), initial orbital period (P_{i}) and initial primary mass ($M_{1,\mathrm{i}}$) of each binary system over parameter ranges corresponding to that of our binary evolution model grids (see Section 2.3.2).

In order to sample binaries from the required ranges of metallicity ($-5.0 \leq \log(Z) \leq -2.375$) and redshift ($0 < z < 8$), we produce a sampler that samples birth redshifts z_0 and metallicities Z_0 via rejection sampling, as described in Appendix B.

[7]Co-moving volume is defined as the volume measure for which number densities of objects locked into Hubble flow remain constant with redshift.

Initial primary masses were obtained by sampling a Salpeter initial mass function[8] (IMF) over the range $25 \leq M_{1,\mathrm{i}}/M_{\odot} \leq 500$ (Salpeter, 1955), and the mass ratio $q_{\mathrm{i}} = M_{2,\mathrm{i}}/M_{1,\mathrm{i}}$ is assumed to be 1. The initial orbital period P_{i} is drawn from a flat distribution in $\log(P_{\mathrm{i}})$ over the range $0.4 \leq P_{\mathrm{i}}/\mathrm{d} \leq 4.0$ (see also Marchant et al. 2016). We sample a billion binaries formed within these reduced parameter ranges in a co-moving volume[9] of $1.90 \times 10^5\,\mathrm{Mpc}^3$.

Fate and final parameter values

Once the initial parameters for a given binary are determined, we perform a series of steps to predict first the fate and thereafter the final parameter values of the system. For this, we use our grid of detailed binary evolution models. This grid has three dimensions: one for metallicity, one for the initial primary mass and one for the initial orbital period for the binary, for the ranges listed in Section 2.3.2 (and corresponding to the ranges over which our initial parameters are sampled - see Section 2.3.3). Each point in the grid has a corresponding final fate assigned to it (as the evolution for each point was followed, where possible, up to core carbon depletion, whereafter the fate of the binary was taken to be determined - see Section 2.3.2).

Possible fates include systems that fail to evolve chemically homogeneously, systems that have L2 overflow at the ZAMS or on the main sequence and therefore rapidly merge long before collapsing into black holes, and lastly those systems that successfully form double He stars — these include systems that collapse directly into BH binaries, systems that undergo pulsational mass loss before collapsing into BH binaries, and systems that end as PISNe (see Figure 2.3 for a slice of the grid at $\log(Z) = -3.0$ and a description of the various model outcomes).

We use a weighted nearest-neighbour method to determine the fate (or 'class') of each new Monte Carlo binary using our grid. For each of the 8 grid points surrounding a binary, its weight w is calculated as $w = e^{-d^2}$, where d is the 3-dimensional grid distance between the binary and the grid point under consideration

[8] An initial mass function is a function, usually in the form of a probability distribution, describing the masses of a forming population of stars.

[9] See Eq. B.10 and Appendix B.0.2 for the calculation of the co-moving volume V_{MC}.

(the 3 dimensions of the grid have units of $\log(\mathrm{M}/M_\odot)$, $\log(Z)$ and days for this calculation). The weights from grid points of the same class are added, and the binary is assigned the class corresponding to the greatest cumulative weight. We note here that, due to practical reasons, not all data points in the grids gave converged results, mainly because the highest metallicities and highest masses lead to simulation complexities resulting in unreasonably long run times (see the red areas in Figure 2.3). These points were treated as their own class by the nearest-neighbours method.

Once a binary system is classified as eventually either directly collapsing into a BH binary ('direct collapser'), undergoing pulsational mass loss before collapsing ('PPISN system') or resulting in a PISN ('PISN system'), our next step is to determine the final mass ($M_{\mathrm{He,f}}$) of its components and the final orbital period (P_{f}) at core carbon depletion. Both the primary and secondary component in the binary are taken to have the same final mass ($M_{1,\mathrm{He,f}} = M_{2,\mathrm{He,f}} = M_{\mathrm{He,f}}$). Our grid provides these values for each grid point corresponding to one of these three classes. Additionally, for grid points classified as PPISN systems, the grid supplies the final mass and period parameter values for both the case in which we ignore PPISN mass loss, as well as the case where we include it — this gives us the option of either including or excluding the effects of pulsational mass loss in our binary population synthesis. Final mass and period values for our binaries are obtained by applying a B-spline kernel[10] to the surrounding grid points of similar classes. As we assume that systems essentially remain the same after core carbon depletion, these are the masses and periods direct collapsers and PPISN systems will have after collapsing to form BHBH binaries, and it is also the masses and periods of PISN systems at the point where they become pair-unstable and explode.

BHBH and PISN calculations

For direct collapsers and PPISN systems, we next calculate the delay time t_{d} of the system in order to determine whether it will merge at the present epoch and as such contribute to the present merger rates. Delay time is here defined as the

[10]The B-spline kernel is of 3$^{\mathrm{rd}}$ order in $M_{1,\mathrm{i}}$ and P_{i} and 2$^{\mathrm{nd}}$ order in metallicity.

time passing between the system's collapse into a BHBH system and its eventual merger. For our standard model, we assume that regular core-collapse supernovae allow He stars to collapse into black holes without any mass loss or kicks (Fryer, 1999), but incorporate mass loss (though not kicks) for PPISNe, as described below. The delay time is then calculated using Peters (1964):

$$t_{\rm d} = \frac{5a^4c^5}{256\mu M_{\rm b}^2 G^3}. \tag{2.1}$$

Here $M_{\rm b}$ is the sum of the two black hole masses, given by $M_{\rm b} = 2M_{\rm He,f}$, μ is the reduced mass of the system, which here is just $\mu = M_{\rm He,f}/2$, G is the gravitational constant, a is the orbital separation and c is the speed of light. Once the delay time is determined, the merging redshift z_m of the binary can be calculated.

If, on the other hand, a binary is classified as a PISN system, we estimate each component's Ni mass $M_{\rm Ni}$ by making use of a power law fit in log to the results of Heger and Woosley (2002), whose He mass range spans $65 - 130\,M_\odot$:

$$\log(M_{\rm Ni}/M_\odot) = r(M_{\rm He,f}/M_\odot)^s + t. \tag{2.2}$$

Here $r = -5.02 \times 10^4$, $s = -2.179$ and $t = 2.887$. From this, we next calculate the peak bolometric magnitude due to Ni decay $M_{\rm bol,Ni}^{\rm peak}$ with the use of an Arnett-like relation (Arnett, 1982)

$$M_{\rm bol,Ni}^{\rm peak} = -19.2 - 2.5\log\left(\frac{M_{\rm Ni}}{0.6M_\odot}\right), \tag{2.3}$$

from which the bolometric peak luminosity $L_{\rm bol,Ni}^{\rm peak}$ can be obtained from

$$\log\left(\frac{L_{\rm bol,Ni}^{\rm peak}}{L_\odot}\right) = \frac{M_{\rm bol,\odot} - M_{\rm bol,Ni}^{\rm peak}}{2.5}, \tag{2.4}$$

where $M_{\rm bol,\odot}$ is the solar bolometric magnitude (taken as 4.75 - see Casagrande et al. 2006) and $L_\odot$ the solar luminosity. Low-mass PISNe produce very little Ni ($M_{\rm Ni} \sim 2 \times 10^{-4} M_\odot$ for the lowest-mass PISNe), such that the luminosity of the shock heating starts to dominate; the peak luminosity of the PISN is then determined by the explosion energy of the PISN instead of its Ni mass. From Herzig et al.

(1990) it can be seen that the peak luminosity of a $61M_{\odot}$ He core SN is dominated by the explosion energy, and from Kasen et al. (2011) it is evident that for a $70M_{\odot}$ SN, the peak luminosity is still only barely powered by Ni. For our calculations we make the assumption that the turning point occurs at roughly $70.5M_{\odot}$ (where the explosion magnitude and the magnitude resulting from Ni decay are roughly equivalent), and with the help of Equations 2.2 and 2.3 we then determine the explosion peak bolometric magnitude $M^{\rm peak}_{\rm bol,exp}$ to be -15.2 and convert that to the equivalent luminosity $L^{\rm peak}_{\rm bol,exp}$ using the form of Equation 2.4. We further assume that this explosion luminosity is constant for all PISNe, regardless of He mass. As this explosion magnitude is faint and only dominates the peak luminosity for the faintest PISNe, the effect of this assumption will be negligible for brighter PISNe and any magnitude limited results should be relatively insensitive to this. The total peak luminosity $L^{\rm peak}_{\rm bol,tot}$ of a PISN system is then just $L^{\rm peak}_{\rm bol,Ni} + L^{\rm peak}_{\rm bol,exp}$.

Obtaining the maximum absolute bolometric magnitude $M^{\rm peak}_{\rm bol}$ from $L^{\rm peak}_{\rm bol,tot}$ from Equation 2.4, using the luminosity distance $d_{\rm L}$ of the PISN system and ignoring any obscuration effects, it is then possible to calculate its maximum apparent bolometric magnitude $m^{\rm peak}_{\rm bol}$ as

$$m^{\rm peak}_{\rm bol} = M^{\rm peak}_{\rm bol} + 5\log\left(\frac{d_{\rm L}}{10{\rm pc}}\right), \tag{2.5}$$

which can then be used to determine whether a specific system will be detectable with a magnitude limited survey or not. These statistics can then be obtained to estimate the observable PISN rate.

Figure 2.4 shows the relation between the final He mass $M_{\rm He,f}$ of a star and the absolute peak bolometric magnitude $M^{\rm peak}_{\rm bol}$ associated with its PISN, as determined by Equations 2.2 and 2.3. We note that we do not apply K corrections that would tend to reduce the apparent magnitude at large redshifts. This therefore leads to an overestimate of the observable PISN rate at large redshifts.

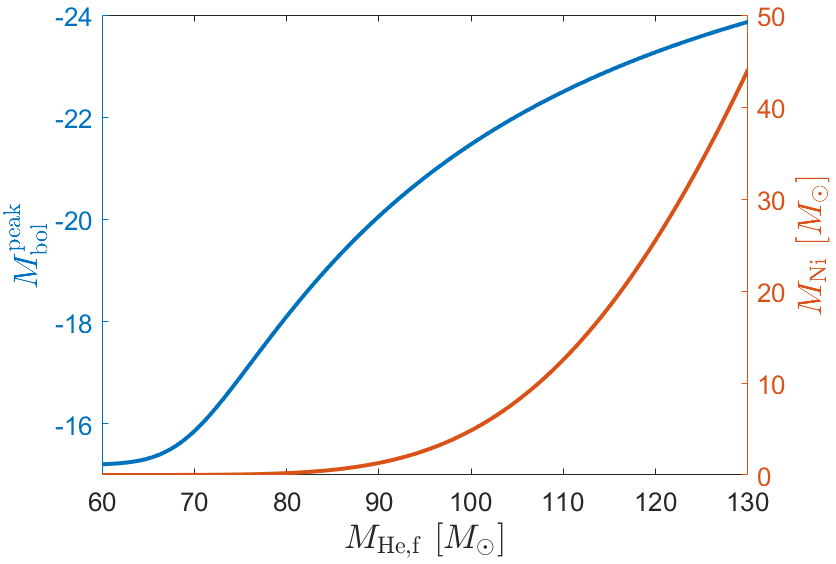

Figure 2.4: The relation between the final He mass $M_{\rm He,f}$ of a star and the absolute peak bolometric magnitude $M_{\rm bol}^{\rm peak}$ associated with its PISN, as determined by Equations 2.2 and 2.3, and corrected as described below Equation 2.4. The relation between $M_{\rm He,f}$ and the Ni mass $M_{\rm Ni}$ of a star is also shown. We further note that the calculations done for this figure assume no extinction.

Rates and Monte Carlo normalisation

We calculate BHBH merger rates as detected by the O1, O3 and full design aLIGO sensitivities as well as by the Einstein Telescope's (ET) predicted sensitivity, and also determine the cosmological BHBH merger rate. We further determine the intrinsic PISN rate along with the PISN detection rates for various magnitude limited surveys. The mathematical background for our rate calculations and for the normalisation of our set of Monte Carlo draws can be found in Appendix B. Figure B.2 shows the various strain sensitivities of aLIGO and ET.

2.4 Results

The results of our Monte Carlo simulations are detailed in this section. More precisely, Section 2.4.1 discusses the final BHBH population properties while Section 2.4.2 presents the overall BHBH merger rates and aLIGO detectability. Section 2.4.3 explores the effects of momentum kicks on the BHBH population,

Section 2.4.4 discusses derived PISN population properties and Section 2.4.5 provides scenarios in which the high-redshift SFR deviates from our standard cosmological simulations and discusses the effects of that on the previously derived BHBH population properties. It should be noted that, although we have a default scenario, we altogether investigate four different configurations. The default case includes pulsational mass loss effects, and is denoted by *PPISN*. The three other cases are as follows: that of including both pulsational mass loss and momentum kicks (*PPISN + Kicks*), that of excluding pulsational mass loss (*NON-PPISN*) and that of excluding pulsational mass loss while including momentum kicks (*NON-PPISN + Kicks*). Whenever not specified, the default configuration is assumed. In this section, we consider both co-moving volumetric merger rates (denoted by $d^2N/dV_c/dt$) as a function of merger redshift (see Equations B.11 and B.12), as well as these volumetric rates integrated over our light cone to obtain rates observable from Earth, denoted by R (see Equations B.13/B.14). Where the need arises to specifically distinguish between detected and cosmological rates, different subscripts will be used. As examples, $d^2N_m/dV_c/dt$ would be the cosmological volumetric merger rate, and R_{det} would be the detected observable merger rate. We only consider BHBH mergers and PISNe that evolved through the CHE channel; this should be kept in mind for the BHBH merger and PISN rates presented here. Finally, we conducted tests to ensure the correct functioning of our simulation and code. This can be seen in Appendices B.1.1 and B.1.2.

2.4.1 Final population properties

Figure 2.5 shows the distribution of the total final binary mass and final orbital period $P_{\rm f}$ of all the systems in our simulations that resulted in close He star pairs at the point of helium exhaustion. The range of final periods for systems at high metallicity is larger than that for low-metallicity systems due to stellar wind mass loss affecting systems of different masses differently at different metallicities. For systems at high metallicities with high initial masses, stellar winds will result in more mass loss and cause a more dramatic widening of the system, producing

systems with longer orbital periods and lower final masses, while systems with lower initial masses at the same metallicity will be less affected. This explains the occurrence of systems with lower final masses and a larger final period range for high metallicities. On the other hand, for low metallicities, systems of high initial mass are much less affected by stellar wind mass loss (and lower masses are of course even less affected); systems can therefore retain more mass and avoid a significant widening of their orbits, which explains the larger range of final masses and smaller range of final periods for these metallicities. The upwards trend of final parameter values moving from higher final masses and lower final periods to lower final masses with longer final periods is caused by the inclusion of pulsational mass loss, whereby the mass loss causes a widening of the orbital period.

Figure 2.5 also indicates the merger times of the systems, assuming that all systems will collapse into black holes without any kicks or associated mass loss. All binaries falling above the 13.8 Gyr line will not be able to merge in a Hubble time. At $\log(Z) = -2.4$ there is a small parameter range where systems will merge in a Hubble time, while for most other systems at $Z > Z_{\odot}/10$, all but the lowest masses will not merge. When moving to lower metallicities, an increasing number of systems are able to produce short-period systems, and below $\log(Z) \sim -3.5$ most systems are able to merge in a Hubble time. This shows that the population of BHBH mergers should be dominated by low-metallicity populations. Note that the empty area between the two vertical red lines are due to systems resulting in PISNe ($60.8 \lesssim M_{\mathrm{He,f}}/M_{\odot} \lesssim 124$) and systems that undergo PPISN mass loss, resulting in an effective "PISN + PPISN gap" of $43.9 \lesssim M_{\mathrm{He,f}}/M_{\odot} \lesssim 124$.

The initial periods and primary masses of systems eventually forming BHBH systems merging within the lifetime of the Universe are shown in Figure 2.6, coloured according to their metallicity. It is clear that there are two progenitor populations – one on either side of a gap caused by systems that eventually result in PISNe or undergo PPISN mass loss. For systems with high metallicities, the initial periods and primary masses fall in a narrow range, whereas lower metallicities give rise to a wider range of possible parameter values. This is due to the effects of stellar wind

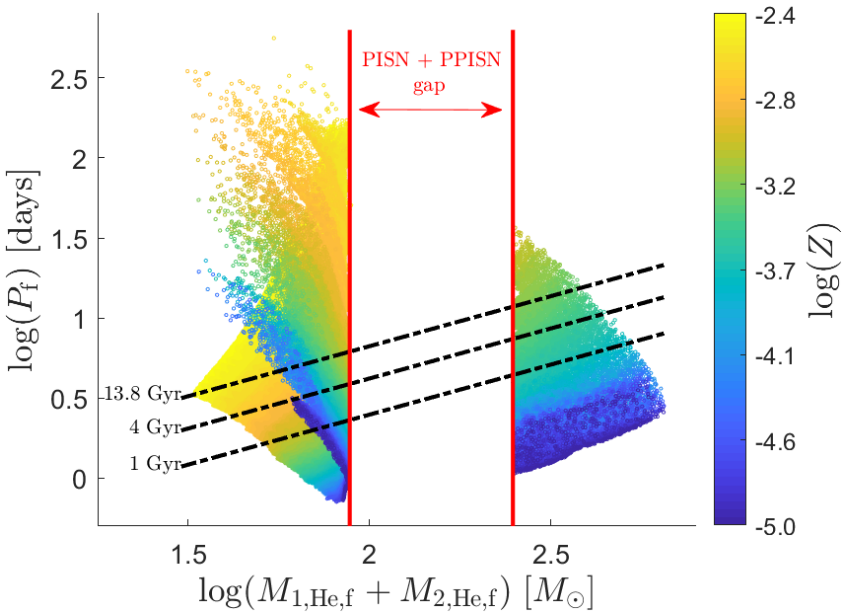

Figure 2.5: The distribution of final periods and final combined masses of systems that reached core carbon depletion for the default (*PPISN*) case. Note that the final He-core masses correspond to the final BH masses. The three black curves represent the delay time of mergers, with systems below the bottom curve merging in less than 1 Gyr, systems below the middle curve merging in less than 4 Gyr and systems below the topmost curve merging in less than 13.8 Gyr. The colouring of different points shows the metallicity (in $\log(Z)$) of the systems. Systems between the vertical red lines experience either PISNe or PPISN mass loss, and this area is referred to as the "PISN + PPISN gap", where no BHBHs form. Note that there is a significant number of very high-mass systems with very low metallicity merging in a Hubble time.

mass loss, where the effects at high metallicities are more severe and orbits can be widened more significantly, giving rise to only a small range of initial periods leading to BHBH systems with periods small enough for timely mergers. As the effects of winds increase with stellar mass, the successful higher-metallicity systems are constrained to smaller masses, in contrast to the systems at lower metallicities.

The cosmological and aLIGO full design sensitivity chirp mass distributions of BHBH mergers merging in the lifetime of the Universe is shown in Figure 2.7 for both the *PPISN* and *NON-PPISN* case (see Appendix B.2 for the detector strain sensitivity curves and the calculation of the detection probability of mergers). The clear gap in the middle is due to PISNe for the *NON-PPISN* case, and due to both PISNe and PPISN mass loss for the *PPISN* case. For the *PPISN* cases, the peaks in the distributions are due to PPISN pile-up, as discussed in Stevenson et al. (2019).

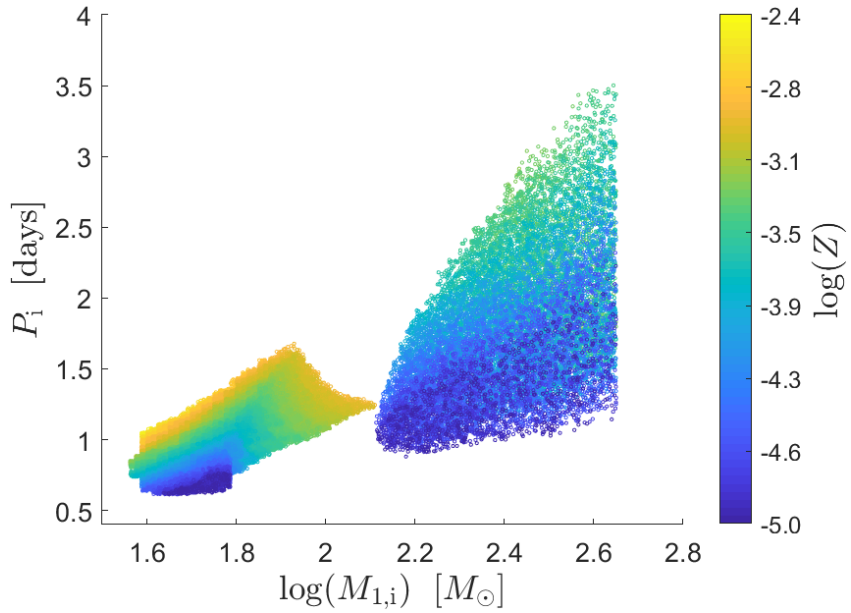

Figure 2.6: The distribution of initial masses and initial periods for systems that will produce BHBH systems merging within the lifetime of the Universe, where the colour indicates the metallicity. The trend towards longer periods at higher masses can also be seen from the grids in Appendix A.

The mergers above the PISN gap are mostly comprised of very low-metallicity systems (as can be seen in Figure 2.5), while those below the PISN gap also have contributions from higher metallicity systems. As the amplitude of gravitational waves resulting from the merger of two black holes is strongly dependent on the chirp mass, the smaller number of high chirp masses shown in the figure might still be a significant contributor to the BHBH detection rate, suggesting that very massive BHBH mergers may be detected from systems above the PISN gap. For our default *PPISN* case, we find that eventual merger systems have BH masses in the range $17-43$ M$_\odot$ below the PISN gap and $124-338$ M$_\odot$ above the PISN gap (a range that includes intermediate-mass black holes). It should be noted that the upper mass of 338 M$_\odot$ is a function of the highest stellar masses (at ~ 500 M$_\odot$) we consider.

Next, Figure 2.8 shows the delay time distribution of BHBH systems merging in the lifetime of the Universe, showing a large range of delay times. Whereas de Mink and Mandel (2016a) predict only delay times larger than 3.5 Gyr and Marchant et al. (2016) predict delay times no smaller than ~ 0.4 Gyr, our smallest delay time is ~ 0.02 Gyr. As Figure 2.5 shows, delay times systematically decrease

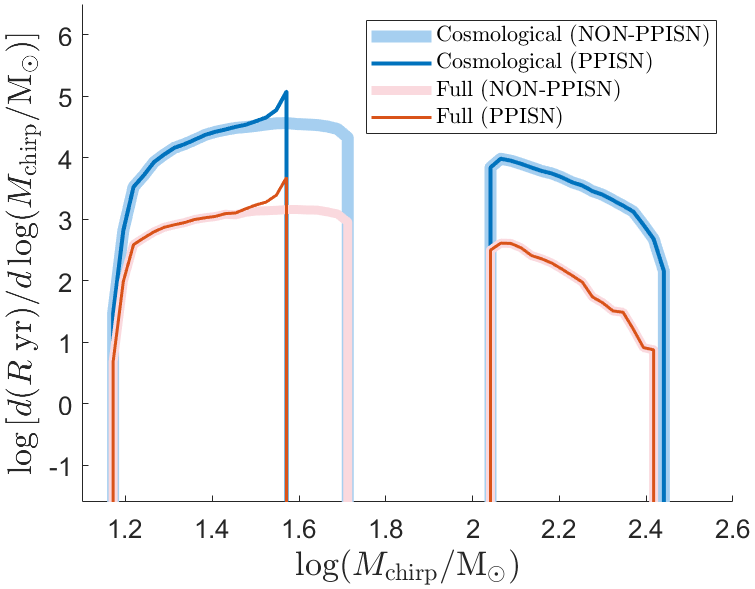

Figure 2.7: The cosmological and aLIGO full design sensitivity chirp mass distribution of BHBH systems merging in the lifetime of the Universe for the *PPISN* and *NON-PPISN* cases. R denotes the BHBH merger rate observable from Earth (see Eq. B.13 and B.14). The total number of BHBH mergers in each of these four histograms correspond to their associated entries in Table 2.1. The clear gap in the middle is caused by PISNe (for the *NON-PPISN* case) and by PISNe and PPISN mass loss (for the *PPISN* case).

with decreasing metallicity: at lower metallicities, the binary components are more compact and stellar winds affect them less, resulting in tighter BHBH systems with generally shorter delay times. de Mink and Mandel (2016a) do not find this effect in their BHBH systems as they consider only one metallicity for all their binary models ($\log(Z) = -2.4$), near the threshold for chemically homogeneous evolution (Yoon et al., 2006), a metallicity that is close to the highest considered in this study ($\log(Z) = -2.375$). Marchant et al. (2016), on the other hand, considered four different metallicities for their original detailed models, the smallest of which was $\log(Z) = -3.47$, and therefore found delay times much shorter than 3.5 Gyr. As here we consider a continuous range of metallicities from $\log(Z) = -2.375$ all the way down to $\log(Z) = -5.0$, we are able to find even smaller delay times, pointing to the possibility of high-redshift merger detections with future detectors that are able to probe higher redshifts. The distribution of time delays will be highly dependent on the physical assumptions made. In the case of a flat initial $\log(P_{\rm i})$

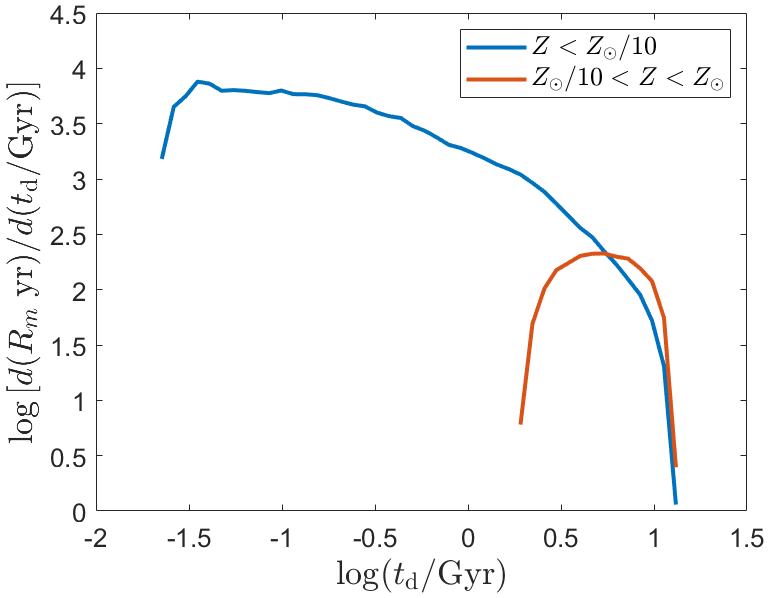

Figure 2.8: The delay time (t_d) distribution of BHBH systems merging at the present epoch, with R_m denoting the cosmological merger rate observable from Earth (see Eq. B.13 and B.14). Integrated over the delay time, the unit is therefore yr^{-1}. Mergers were divided into two metallicity ranges: $Z < Z_\odot/10$ and $Z_\odot/10 < Z < Z_\odot$ (also see Figure 2.2). These distributions have been normalised to the cosmological BHBH merger rate to give the total integrated BHBH merger rate shown in Table 2.1.

distribution and only gravitational radiation, we would expect a $1/t_\mathrm{d}$ distribution in time delay. However, here our time delay distribution depends both on gravitational radiation as well as the binary populations and their metallicity effects, the period distribution and stellar astrophysics.

2.4.2 Black hole merger rates

Using Appendix B.1 and B.2, we find the cosmological, O1, O3 and full design aLIGO sensitivity merger rates for all four of the configurations we investigate. These are summarised in Table 2.1. As an interesting aside, in order to investigate potential future gravitational-wave detector capabilities, we decided to also inspect the predicted sensitivity of the Einstein Telescope[11] (ET, Sathyaprakash et al. 2012), set to start operating in the next decade (see also the Cosmic Explorer[12], Abbott et al. 2017a). Figure B.2 shows the most recent predicted sensitivity of

[11]Einstein Telescope home: `http://www.et-gw.eu/`
[12]Cosmic Explorer home: `https://cosmicexplorer.org/`

the ET, along with those of aLIGO, and Appendix B.2 details the calculation of the detection probability of mergers. The ET is expected to find 83.8% of BHBH mergers whose signal reaches Earth at the present epoch, as is shown in Table 2.1. At full aLIGO design sensitivity, Marchant et al. (2016) estimated the merger rate below the PISN gap to fall in the range $19 - 550\,\mathrm{yr}^{-1}$, and that above the PISN gap to fall between $2.1 - 370\,\mathrm{yr}^{-1}$. Their results therefore compare well to ours, as expected, and point towards potentially many detections per year of BHBH mergers produced by the CHE scenario.

In Figure 2.9 we show how the detection probability p_k of BHBH mergers varies with the chirp mass M_{chirp} and merger redshift z_m at aLIGO's full design sensitivity. Note how quickly the detection probability drops to essentially zero as the redshift increases. Figure 2.7 shows the chirp mass distribution of mergers detectable by an aLIGO run at full design sensitivity. It predicts that massive mergers above the PISN gap should be detected. Furthermore, Figure 2.10a shows how the detection probability varies as a function of merger redshift for systems both above and below the PISN gap, while Figure 2.10b and 2.10c show the detection probability as a function of merger redshift for the O1, O3 and full aLIGO sensitivities for one system below ($M_{\mathrm{chirp}} = 35\mathrm{M}_{\odot}$) and one system above ($M_{\mathrm{chirp}} = 180\mathrm{M}_{\odot}$) the PISN gap, respectively. These three figures in combination with Figure 2.9 give an idea of the detection probability values of systems with different chirp masses.

Figure 2.11a shows the cosmological, ET sensitivity and O1-, O3-, and full sensitivity aLIGO co-moving volumetric BHBH merger rates (denoted by $d^2N/dV_c/dt$) as a function of merger redshift (see Eq. B.11 and B.12), while Figure 2.11b shows these rates integrated over our light cone, denoted by R (see Equation B.13/B.14). Figure 2.11a shows that the aLIGO volumetric merger rates decline rapidly with redshift (as suggested by Figures 2.9 and 2.10) and further that the cosmological co-moving volumetric merger rate peaks around $z \sim 2.5$. We find a local co-moving merger rate of $5.8\,\mathrm{Gpc}^{-3}\mathrm{yr}^{-1}$, to be compared with the aLIGO/Virgo Collaboration's estimated local co-moving volumetric merger rate of $53.2^{+55.8}_{-28.2}\,\mathrm{Gpc}^{-3}\mathrm{yr}^{-1}$ after completion of the O2 run (Abbott et al., 2019b,a). It is

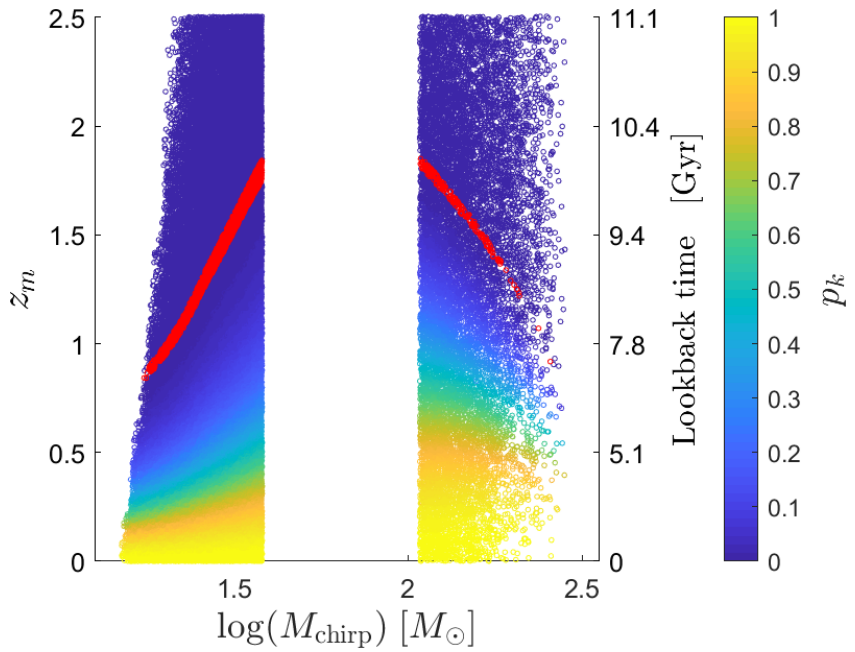

Figure 2.9: The aLIGO detection probability p_k at full design sensitivity of BHBH binaries merging in the lifetime of the Universe, given their merger redshift z_m and chirp mass $M_{\rm chirp}$. The corresponding lookback time is given as a secondary y-axis. Note the quick drop in detection probability as the redshift increases. Red points indicate those mergers for which $p_k = 0$; mergers above the red line therefore has no probability of detection.

also worthwhile investigating whether this BHBH merger rate follows the redshift evolution of the SFR at $z = 0$. From Madau and Dickinson (2014) we have that the co-moving volumetric rate of star formation follows the relation SFR $\propto (1+z)^{2.7}$ near $z = 0$. Similarly assuming a power law form for the cosmological BHBH volumetric merger rate near $z = 0$, we find $d^2N_m/dV_c/dt = 5.8\,(1+z)^{1.17}$. This is illustrated in Figure 2.11a, thus showing that the BHBH volumetric merger rate evolution differs slightly from that of the SFR. Figure 2.11b shows that the cosmological merger rate observable from Earth peaks around $z \sim 2$ and in Figures 2.11c and 2.11d, the cumulative distribution of the total number of detections per year (detected by the O1 and full design sensitivities, respectively) is shown as a function of both merger and formation redshift of the binary systems, comparing well to that found by de Mink and Mandel (2016a).

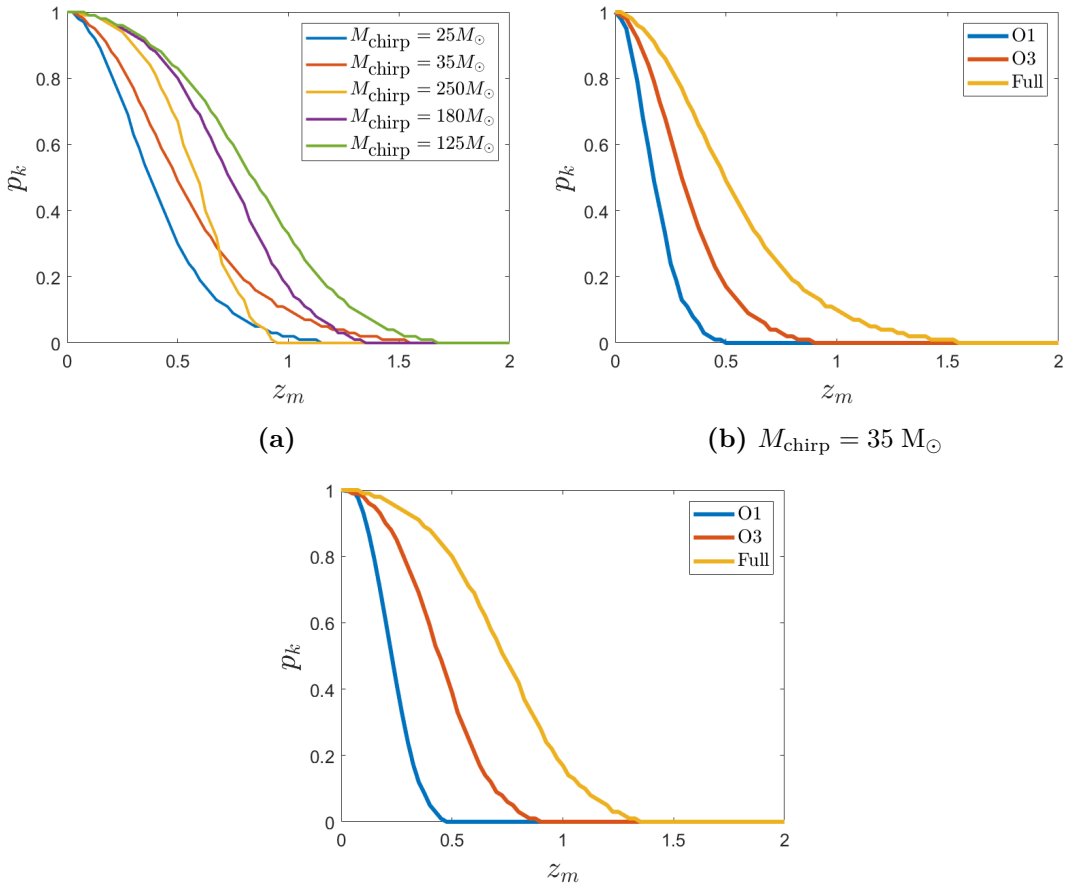

(a)

(b) $M_{\rm chirp} = 35\ {\rm M}_\odot$

(c) $M_{\rm chirp} = 180\ {\rm M}_\odot$

Figure 2.10: **(a)** The aLIGO detection probability p_k at full design sensitivity as a function of merger redshift z_m for two mergers below the PISN gap ($M_{\rm chirp} = 25$ and $35\ {\rm M}_\odot$) and three systems above the PISN gap ($M_{\rm chirp} = 125, 180$ and $250\ {\rm M}_\odot$). As Figure 2.9 also indicates, we expect no detections above a merger redshift of $z_m = 2$. The most massive systems above the PISN gap, although easier to detect at lower merger redshifts, are less detectable (in comparison with systems below the PISN gap) at higher redshifts. This is due to the frequency sensitivity of aLIGO (see Figure B.2). **(b)** The detection probability at full design, O1 and O3 aLIGO sensitivities as a function of merger redshift for a system below the PISN gap with chirp mass $M_{\rm chirp} = 35\ {\rm M}_\odot$. **(c)** Similar to **(b)**, but now for a system above the PISN gap with a chirp mass of $M_{\rm chirp} = 180\ {\rm M}_\odot$.

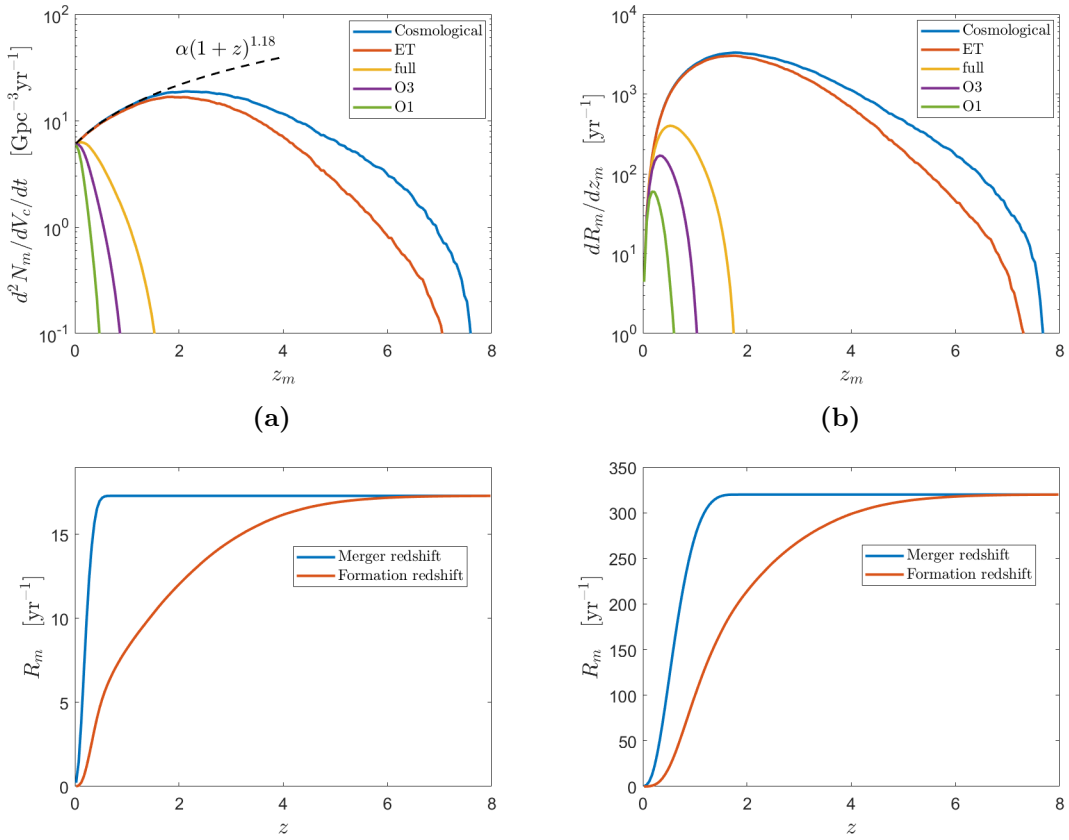

Figure 2.11: **(a)** The cosmological, ET sensitivity and O1-, O3-, and full sensitivity aLIGO co-moving volumetric BHBH merger rates as a function of merger redshift z_m. Both the cosmological and detected volumetric rates are here denoted by $d^2N/dV_c/dt$ for simplicity. Also shown is a power law fit to the cosmological BHBH volumetric merger rate close to $z = 0$, for purposes of comparison with the redshift evolution of the SFR close to $z = 0$ (Madau and Dickinson, 2014). **(b)** The cosmological and detected merger rates observable from Earth (both groups denoted by R for simplicity, see also Eq. B.13 and B.14) binned in terms of merging redshift z_m. **(c)** The cumulative distribution of the total number of O1-detectable mergers observable from Earth per year as a function of both merging and formation redshift. **(d)** Similar to (c), but for the full aLIGO sensitivity.

2.4.3 Momentum kicks

Up to this point we assumed that massive stars (those not in the PISN regime) either directly collapsed into black holes without any associated loss in mass or energy (direct collapsers) or that they lost mass via multiple pulsations before arriving at their final He-core mass, and collapsed into black holes after this point, again with no losses associated to the actual BH collapse (PPISNe). We could therefore take the final He masses and orbital periods of these binary stars (as

shown in Figure 2.5) to represent the masses and periods of the BHBH systems after collapse. In reality, however, the post-collapse parameter values of the resulting BHBH systems also depend on the BH formation process itself. Taking those effects into account will alter the post-collapse parameters, thereby introducing differences in previously calculated merger delay times that might affect eventual BHBH merger population properties.

BH formation may include a momentum kick similar to those experienced by NSs at birth (Janka, 2012). This is particularly true if the progenitor collapses to a black hole via a two-step process that includes both an explosion and a subsequent collapse by fallback (Brandt et al., 1995; Chan et al., 2018). In the case of NS formation, the magnitude of the imparted kicks are fairly well constrained from observations of young radio pulsars (Hobbs et al., 2005; Igoshev and Verbunt, 2018). This is not the case for BH formation, however: measured masses of observed stellar black holes are relatively small, ranging from $\sim 4 - 50 M_{\odot}$ (McClintock et al., 2014; Orosz et al., 2007; Prestwich et al., 2007; Abbott et al., 2019b), with inferred BH kicks ranging anywhere from virtually nothing (Nelemans et al., 1999) to kicks of several 100 km/s (Janka 2013; Mandel 2016; Repetto et al. 2017). For the more massive stellar black holes, like those of particular interest to us, the situation could be quite different since the progenitor stars are more likely to collapse directly into black holes (see Fryer 1999) without an accompanying SN explosion, leading to very low kick velocities. Other uncertainties include the amount of mass lost during the collapse, which has a further effect on the post-collapse eccentricity and orbital period of the BHBH system.

To illustratively consider the possible impact of these effects, we administer a kick to all binary systems (not in the PISN regime) upon BH formation using the equations set forth in Brandt and Podsiadlowski (1994): we assume a uniform distribution in fractional mass loss between 0.0 and 0.2, an imparted kick velocity selected from a uniform distribution in the range $0.0 < |v_{\rm kick}| < 300$ km/s, and a random kick velocity direction. For simplicity, we include only one kick per system (cf. Marchant et al. (2016)), but results can easily be generalised. The new

post-collapse orbital period, mass and eccentricity of the BHBH systems can then be used to calculate the time delay $t_{\rm d}$ as shown in Peters (1964):

$$t_{\rm d} = \frac{12}{19}\frac{c_0^4}{\beta}\int_0^{e_0}\frac{e^{29/19}[1+(121/304)e^2]^{1181/2299}}{(1-e^2)^{3/2}}de. \tag{2.6}$$

In Equation 2.6, e is the eccentricity of the system, with e_0 being the eccentricity immediately after the collapse; β is defined as

$$\beta = \frac{64}{5}\frac{G^3 M_{\rm b1,f} M_{\rm b2,f}(M_{\rm b1,f}+M_{\rm b2,f})}{c^5}, \tag{2.7}$$

with G being the gravitational constant, $M_{\rm b1,f}$ and $M_{\rm b2,f}$ the two post-collapse BH masses of the system and c the speed of light. Furthermore, c_0 can be calculated using

$$a_0 = \frac{c_0 e_0^{12/19}}{(1-e_0^2)}\left[1+\frac{121}{304}e_0^2\right]^{870/2299}, \tag{2.8}$$

where e_0 and a_0 are the eccentricity and semi-major axis, respectively, of the orbit after collapse.

It is found that only a very small percentage of BHBH systems formerly produced in our co-moving box by our default Monte Carlo simulation, 6.3%, are completely disrupted by an applied kick, implying that momentum kicks generally have very little effect on the survival rate of these systems. This is expected, as the kicks considered are typically small compared to the orbital velocity of the progenitors. We are, of course, very interested in the effect on eventual BHBH merger populations, as momentum kicks can either lengthen or shorten the post-collapse orbit and so influence the delay time of merger systems. Our results show that, in our co-moving simulation box, 97% of surviving systems merge on a longer timescale than before, with the rest merging on a shorter timescale. Furthermore, of the systems that originally merged in the lifetime of the Universe, 26% continue to merge irrespectively, 73% now merge outside of that timescale, and only 1% are disrupted completely. In totality, whereas for the original case 45% of all BHBH systems in our simulations would merge in the lifetime of the Universe, only roughly 12% now continue to do so.

Figure 2.12 shows the probability distribution of the ratio of BHBH delay times where a kick is applied to that where it is not applied (including all mergers and non-mergers alike) in our simulations. Systems falling below a ratio of 1 will merge at higher redshifts than before, making them more difficult to detect by aLIGO, while other systems will merge at lower redshifts than before. In the latter case, some mergers will shift to redshifts more detectable by aLIGO, while others will shift far enough to not have merged yet (see Figure 2.9). In our case, the general trend is for kicks to lengthen the delay time of systems, and so there is an overall downwards shift in the population's merger redshifts. It is interesting to note that for roughly half of our systems, the delay time is increased by a factor of more than $\sim 20 - 30$. The general trend of increased delay times leads to an influx of mergers into the redshift ranges detectable by aLIGO and ET. It simultaneously leads to systems that were once in detectable redshift ranges not merging in the lifetime of the Universe anymore. These two effects combined results in the less pronounced decrease in detected mergers when compared to the larger decrease in the cosmological merger rate. Details of this are presented in Table 2.1.

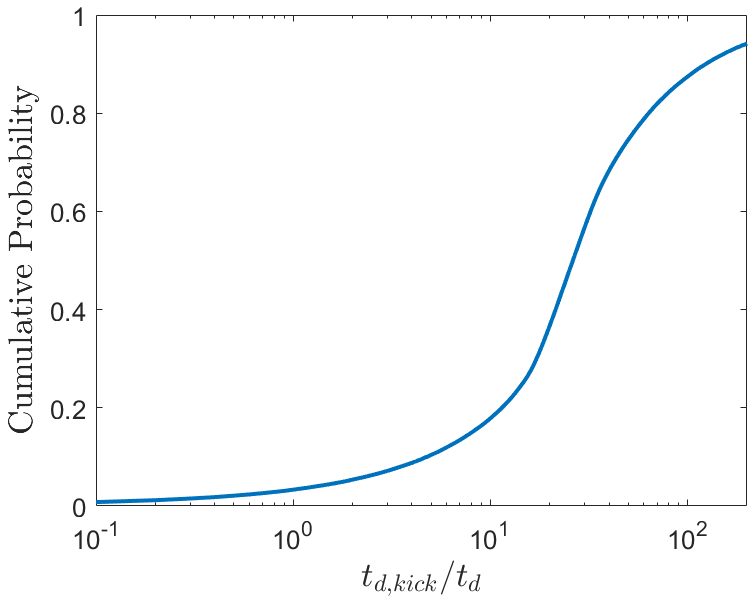

Figure 2.12: The cumulative distribution function of the time delay ratio of BHBH systems in our *PPISN + Kicks* case (mergers and non-mergers alike), where the ratio is taken to be the delay time of a system with an applied kick ($t_{d,kick}$) to the delay time when no kick is applied. Systems with ratios smaller than 1 correspond to binaries whose merging redshift would be higher after a kick is applied (their delay times have been shortened). All other systems will have merger redshifts shifting to lower values, in many cases enough to avoid merging before the current epoch.

Table 2.1: The cosmological BHBH merger rates (in units of yr^{-1}) and the BHBH merger detection rates for aLIGO at O1, O3 and full design sensitivity and for the planned Einstein telescope (ET) for both the *PPISN* and *NON-PPISN* cases, both with and without the inclusion of momentum kicks. Total merger rates are further broken down into mergers above and below the PISN gap.

		Cosmological	**aLIGO O1**	**aLIGO O3**	**Full aLIGO**	**ET**
PPISN	Total	8510	16.8	80.6	310	7130
	Above PISN gap	1830	3.59	16.4	65.0	1220
	Below PISN gap	6680	13.2	64.2	245	5910
PPISN + Kicks	Total	1480	9.52	41.1	138	1340
	Above PISN gap	645	4.12	17.8	62.5	565
	Below PISN gap	839	5.40	23.3	75.0	770
NON-PPISN	Total	10100	20.0	98.3	382	8580
	Above PISN gap	1830	3.59	16.4	65.0	1220
	Below PISN gap	8290	16.4	81.9	317	7360
NON-PPISN + Kicks	Total	2070	12.8	57.0	193	1880
	Above PISN gap	645	4.12	17.8	62.5	565
	Below PISN gap	1420	8.68	39.2	131	1310

2.4.4 Pair-instability supernovae

As mentioned in Section 2.2, PISNe are rare events that have not been identified observationally in an unambiguous way, although there are various candidate events discussed in the literature (Woosley et al., 2007; Gal-Yam et al., 2009; Terreran et al., 2017; Gomez et al., 2019). These events could help us to better understand the evolution of massive stars in low-metallicity regimes. Using the methods and calculations outlined in Sections 2.3.3 and Appendix B.1, we calculate the intrinsic PISN rate along with various PISN detection rates in magnitude limited surveys in order to estimate whether these events are likely to be detected by available instruments. We explore peak bolometric magnitude ($m_{\rm bol}^{\rm lim}$) limits of $17, 19, 21, 23$ and 25, corresponding to a wide range of completed surveys (those with limiting magnitudes of up to roughly 21, e.g. the Sloan Digital Sky Survey (SDSS)[13] and the Palomar Transient Factory (PTF)[14]), ongoing deeper surveys (that can observe to magnitudes of up to roughly 23, e.g. the Dark Energy Survey (DES)[15], the Panoramic Survey Telescope And Rapid Response System (Pan-STARRS)[16] as well as deeper surveys like the Subaru Hyper Suprime-Cam (HSC)[17]), and future surveys (that will observe up to magnitudes of roughly 25, e.g. the Large Synoptic Survey Telescope (LSST)[18] and the Zwicky Transient Facility (ZTF)[19]). These results are given in Table 2.2, where both the PISN and CCSN rates are given for the intrinsic and magnitude limited cases.

The numbers in Table 2.2 show that the intrinsically fainter PISNe ($M_{\rm bol}^{\rm peak} > -19$) will remain for the most part unobserved. The detection rate of PISNe is dominated by the intrinsically bright events ($M_{\rm bol}^{\rm peak} \leq -19$), which would be observed as superluminous Type I SNe (SLSN-I; their most precise rate to date is that measured by Frohmaier et al. (2021), who found the SLSN-I to CCSN ratio in the local

[13]SDSS home: `http://www.sdss.org`
[14]PTF home: `http://www.ptf.caltech.edu`
[15]DES home: `http://www.darkenergysurvey.org`
[16]Pan-STARRS home: `http://pswww.ifa.hawaii.edu/pswww`
[17]HSC home: `http://hsc.mtk.nao.ac.jp/ssp/`
[18]LSST home: `http://www.lsst.org`
[19]ZTF home: `https://www.ztf.caltech.edu`

Table 2.2: PISN and CCSNe rates (for the intrinsic/cosmological and magnitude limited cases) in units of yr^{-1} for the default configuration: bright PISNe have an absolute peak bolometric magnitude $M_{\mathrm{bol}}^{\mathrm{peak}} \leq -19$, while faint PISNe have $M_{\mathrm{bol}}^{\mathrm{peak}} > -19$. The last column shows the total number of PISNe expected per 1000 CCSNe for each of the magnitude limited cases, as well as for the cosmological case. The values in this table are given for the whole sky.

	Bright PISNe	**Faint PISNe**	**CCSNe**	**CC ratio**
Cosmological	8070	12000	7.51×10^8	0.027
$\boldsymbol{m_{\mathrm{bol}}^{\mathrm{lim}} = 25}$	2970	44.4	2.46×10^6	1.23
$\boldsymbol{m_{\mathrm{bol}}^{\mathrm{lim}} = 23}$	643	4.15	2.28×10^5	2.84
$\boldsymbol{m_{\mathrm{bol}}^{\mathrm{lim}} = 21}$	79.5	0.335	17500	4.56
$\boldsymbol{m_{\mathrm{bol}}^{\mathrm{lim}} = 19}$	7.79	0.0243	1240	6.32
$\boldsymbol{m_{\mathrm{bol}}^{\mathrm{lim}} = 17}$	0.659	0.00164	82.5	8.01

Universe to be $\sim 1/3500^{+2800}_{-720}$). As bright PISNe originate from the most massive stars, they will be tracing the IMF at the highest stellar masses. A detection of such supernovae at a rate comparable to those given in Table 2.2 would strongly support our predicted BH merger rate for BH masses above the PISN gap. Nicholl et al. (2013) find that the lack of unambiguous nearby PISN events suggests a local rate of occurrence of less than 6×10^{-6} times that of the CCSN rate. This is a factor of ~ 2 (or more) smaller than the ratio we find. We highlight that, using the HSC, Moriya et al. (2021) conducted a long-term deep transient survey in order to constrain the rates of SNe lasting for more than a year (PISNe are predicted to have a duration of more than a year in the observer frame). No such SNe were found, and they constrained the PISN rate up to $z \simeq 3$ to be less than $0.01 - 0.1\%$ of the CCSN rate (a factor of at most $10 - 100$ larger than the ratio we find).

PISNe are not expected to produce a large amount of dust themselves (Cherchneff and Dwek, 2009), but because their progenitors are very massive stars, they are expected to be found in actively star-forming galaxies. Some star-forming galaxies (such as luminous- and ultraluminous infrared galaxies) are known to have large extinctions, and SNe from such dusty galaxies can only be properly observed in the near-infrared, a possible reason for why optical transient surveys are missing them

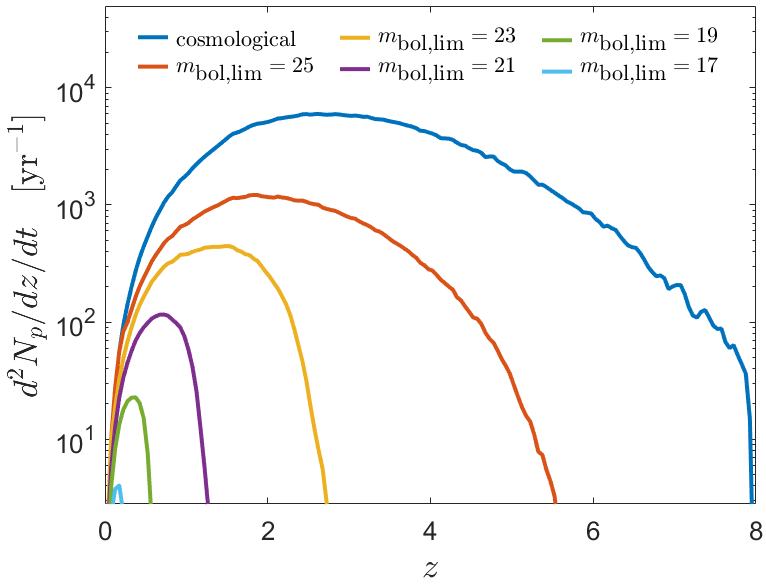

Figure 2.13: PISN rates (for the intrinsic/cosmological and magnitude limited cases) as a function of redshift z, as discussed in Section 2.4.4. There is a clear intrinsic peak at $z \sim 3$, and it can be seen that a significant number of PISNe occur at higher redshifts.

(Kankare et al., 2021). Since extinction is not included in our binary population synthesis simulations, it is therefore possible that the above discrepancy with the results of Nicholl et al. (2013) is partly due to extinction caused by PISN host galaxies. Apart from observational uncertainties like the extinction, a large theoretical uncertainty regarding the stellar evolution of massive stars is the mass-loss rate (Sander and Vink, 2020). The real mass-loss rate of massive stars may be higher (or lower) than what is assumed here – if that is the case, fewer (or more) stars would explode as PISNe, resulting in another possible cause of the above observed discrepancies. We therefore conclude that our PISN rate predictions lie in a reasonable region of rate estimates, given the uncertainties which exist both observationally and theoretically. The uncertainties with regard to the mass-loss rate of massive stars are furthermore also a possible cause of discrepancies in our predicted BHBH merger rate above the PISN gap vs. the observed aLIGO/AdV rate, and this is further discussed in Section 2.5.

For CCSNe, we assume a peak bolometric magnitude $M^{\rm peak}_{\rm bol,Ni}$ of -17.0 and then follow the same procedure as for PISNe. Figure 2.13 further shows the

PISN rates (both for the intrinsic and magnitude limited cases) as a function of redshift, showing a clear intrinsic peak at $z \sim 3$ and a significant number of PISNe occurring at high redshifts. We note that our channel may not be the only one producing PISNe - they could also form from very massive single stars at low metallicity (Langer et al., 2007; Yusof et al., 2013) or via the merger of massive evolved stars (Vigna-Gómez et al., 2019).

2.4.5 High-redshift deviations in SFR

Finally, we investigate the effects of deviations in the SFR at high redshift on the final BHBH merger populations. Although lower-redshift SFR uncertainties and the uncertainty in the metallicity-specific star formation history could also have a significant impact on merger rates (Neijssel et al., 2019), we choose to explore here the effects of deviations in the high-redshift SFR only. The SFR at high redshifts is presently poorly constrained by observations, and so it makes sense to explore possible deviations in order to quantify the possible effects on the merger rates we expect to eventually observe. For this purpose, the SFR is modulated at high redshifts through the use of a sigmoid function

$$f(z) = \frac{A}{1 + e^{-az+b}} + 1; \tag{2.9}$$

any resulting changes to the metallicity distribution are assumed to be negligible. In all cases, the SFR is modulated only from its peak at $z \sim 2.5$ onwards, and four scenarios are explored: Case 1 gradually increases the original SFR up to a factor of 3 at $z = 8$; Case 2 gradually decreases the original SFR down to a factor of 1/3 at $z = 8$; Case 3 assumes a roughly constant SFR from the peak onwards; Case 4 assumes that the SFR quickly drops to zero after its peak. Figure 2.14 shows each of these four cases. The global CCSN rate is adjusted for each case.

Results are shown in Figure 2.15 and Table 2.3. The overall higher SFR of Cases 1 and 3 have higher (cosmological) total BHBH merger rates as their outcomes, while the opposite is true of Cases 2 and 4. As expected, Cases 3 and 4 result in the most extreme deviations from the original BHBH merger rate. For aLIGO's full

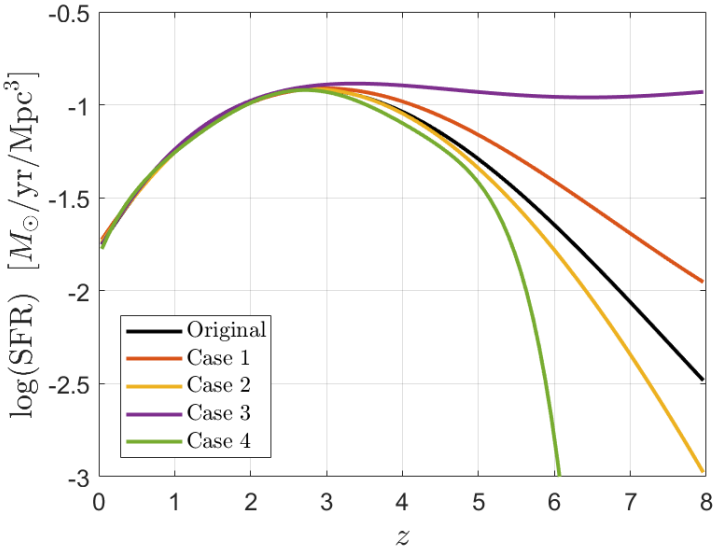

Figure 2.14: The various adopted deviations in high-redshift SFR. To obtain these four cases, the original SFR (represented here by the black curve) was modulated by the sigmoid function given in Equation 2.9 by adjusting the value of A, a and b. **Case 1:** $A = 2.3306$, $a = 1.25$, $b = 8.2$; the original SFR is increased by up to a factor of 3 at $z = 8$. **Case 2:** $A = -0.7769$, $a = 1.25$, $b = 8.2$; the original SFR is decreased by up to a factor of 1/3 at $z = 8$. **Case 3:** $A = 84.7591$, $a = 1.25$, $b = 10.5$; the SFR remains roughly constant from its peak onwards. **Case 4:** $A = -5.2990$, $a = 1.25$, $b = 9.0$; the SFR quickly drops to zero after its peak.

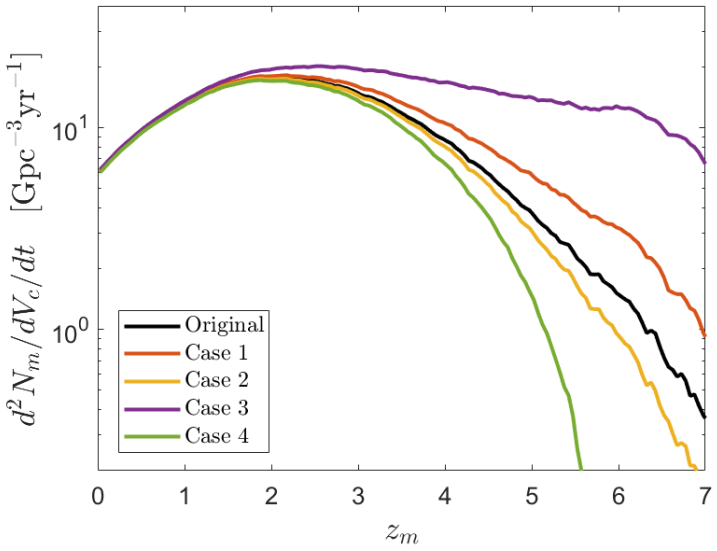

Figure 2.15: The co-moving cosmological BHBH merger rate for the default SFR case (labeled "Original" in the figure) as well as for each of the four cases of high-redshift deviations in SFR, as a function of merger redshift z_m. To see the four cases, see Figure 2.14.

Table 2.3: The cosmological, full aLIGO and ET design sensitivity BHBH merger rate results (in units of yr^{-1}) for SFR deviations at high redshifts (see Figure 2.14 for the four different SFR cases). Total merger rates are further broken down into mergers above and below the PISN gap. The simulation results for the original SFR are also given for easy comparison (see Table 2.1).

		Cosmological	**Full aLIGO**	**ET**
	Total	8510	310	7130
Original	Above PISN gap	1830	65.0	1220
	Below PISN gap	6680	245	5910
	Total	9190	311	7540
Case 1	Above PISN gap	2020	64.5	1250
	Below PISN gap	7170	246	6290
	Total	8270	310	6980
Case 2	Above PISN gap	1760	65.0	1210
	Below PISN gap	6510	245	5770
	Total	11900	314	9110
Case 3	Above PISN gap	2840	63.3	1360
	Below PISN gap	9070	251	7750
	Total	7780	309	6670
Case 4	Above PISN gap	1640	65.4	1190
	Below PISN gap	6140	244	5480

sensitivity, the rate deviations from the original case are very small; this is due to the fact that SFR deviations at high redshifts influence the formation of binary stars only at high redshifts, which then have to merge between a redshift of 0 and ~ 1.5 to have a chance of being detected by aLIGO (see Figure 2.10a). Looking at Figure 2.15 it can be seen that cosmological deviations in merger rate is essentially non-existent below $z_m = 1.5$, explaining the lack of deviation detectable by aLIGO. For all cases but Case 3, the cosmological BHBH merger rate deviation is less than or around $\sim 8\%$; for Case 3 however, deviation is more prominent with a $\sim 40\%$ change.

2.5 Concluding remarks

We have performed detailed Monte Carlo simulations in order to investigate the population properties, rate estimates and aLIGO detection rates of BHBH mergers evolving through the CHE channel in the version proposed by Marchant et al. (2016). The results from their detailed simulations, which we vastly extended for this study, as well as the SFR/metallicity distributions from the cosmological simulations of Taylor and Kobayashi (2015b), were used for this purpose.

The cosmological and ET sensitivity BHBH merger rates as well as the O1, O3, and full design sensitivity aLIGO detection rates obtained are summarized in Table 2.1. At full aLIGO sensitivity, Marchant et al. (2016)'s predicted BHBH merger rate ranges of $2.1 - 370\,\mathrm{yr}^{-1}$ above and $19 - 550\,\mathrm{yr}^{-1}$ below the PISN gap compares well to our estimates of $65.0\,\mathrm{yr}^{-1}$ above and $245\,\mathrm{yr}^{-1}$ below the PISN gap in the case where we include the effects of pulsational-PISNe (PPISNe) and $65.0\,\mathrm{yr}^{-1}$ above and $317\,\mathrm{yr}^{-1}$ below the PISN gap in the case where we omit the effects of PPISNe, as is expected. Our results are more precise as we investigated a continuous range of metallicities and used the joint SFR and metallicity distributions from the detailed, realistic cosmological simulations of Taylor and Kobayashi (2015b). From Figure 2.11a we predict a local co-moving merger rate of $5.8\,\mathrm{Gpc}^{-3}\mathrm{yr}^{-1}$, comparing well to estimates and predictions by Abbott et al. (2019b) and Abbott et al. (2016a).

For a more intuitive idea of how our CHE rate estimates compare to the detections made by aLIGO/AdV to date, we consider the fraction of aLIGO/AdV BHBH detections with component mass ratios q in the range assumed for the CHE channel: $0.8 \leq q \leq 1.0$ (see Marchant et al. 2016 and Appendix B.0.1). Figure 2.16 shows the mass ratios of the BHBH detections made during the O1 and O3a runs (see Table 3 in Abbott et al. 2018b and Table 6 in Abbott et al. 2020b), with the region $0.8 \leq q \leq 1.0$ shaded in blue.

In order to determine the number of aLIGO/AdV detections falling in the theoretical CHE q-range indicated in Figure 2.16, we use the complimentary error

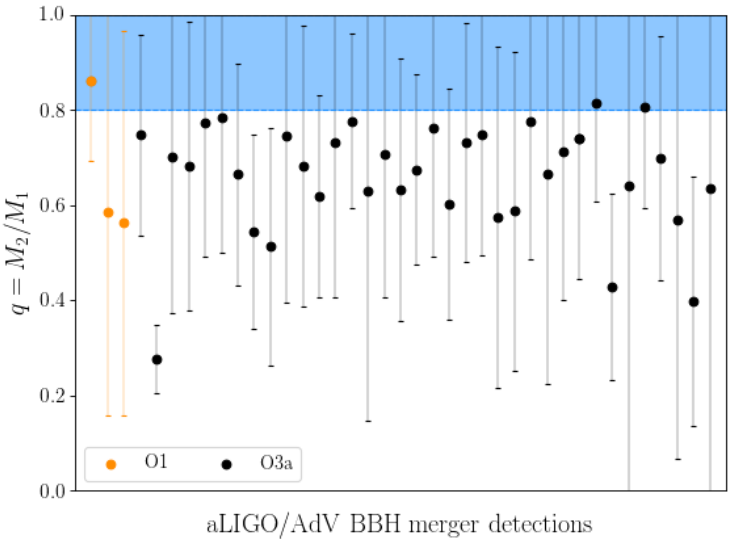

Figure 2.16: The mass ratio $q = M_2/M_1$ of the BBH merger gravitational wave detections made by aLIGO/AdV during the O1 (three observations in orange) and O3a (36 observations in black) runs (see Abbott et al. 2019a and Abbott et al. 2020b for tables of the detections); observations are arranged in order of detection from left to right on the x-axis. We omit the O2 detections as our analysis does not include the O2 run. The lower edge of the shaded region is located at $q = 0.8$, above which BBH mergers resulting from the CHE channel should lie.

function[20] to weight detections according to the fractions of their error bars falling in the shaded area. This procedure gives the probability that a given detection by aLIGO/AdV falls in the predicted q-range assumed by the approximations made in our simulations. It assumes that the error distribution of each aLIGO/AdV detection is Gaussian, and that the value of q calculated for each detection from the information given by aLIGO/AdV is the median of the probability density function of the mass ratio. These results would change if the posteriors of the probabilities have shapes other than a Gaussian, however this procedure would give a good indication of how compatible the aLIGO/AdV detections are with our assumed q-range of $0.8 \leq q \leq 1.0$. The result of these calculations can be seen in the second column of Table 2.4.

[20]The error function is defined as $\mathrm{erf}(z) = (2/\sqrt{\pi}) \int_0^z e^{-x^2} dx$. For a normally distributed random variable Y (with mean 0 and variance 1/2), $\mathrm{erf}(z)$ is the probability of Y falling in the range $[-z, z]$, where z is non-negative. The complimentary error function is defined as $\mathrm{erfc}(z) = 1 - \mathrm{erf}(z)$.

Table 2.4: A comparison of our predicted BHBH merger rates with the aLIGO/AdV detection rates of BHBH mergers having component mass ratios in a range compatible with the CHE channel. The effective time duration (in days) for aLIGO/AdV's O1 and O3a runs is indicated in the first column (see text for more detail). The second column reports the number of aLIGO/AdV detections in O1 and O3a with mass ratios falling in the range $0.8 \leq q \leq 1.0$ (i.e. falling into the shaded area in Figure 2.16). The third column transforms this into a yearly aLIGO/AdV CHE rate based on the respective durations of the runs in which the detections were made, and the last column shows our predicted BHBH merger rates below the PISN gap (taking into account all four of the cases we analysed; see Table 2.1).

	Duration	**aLIGO CHE det.**	**aLIGO CHE rate**	**Our rates**
O1	$\sim 48\,\mathrm{d}$	1.14	~ 8.7	$5.40 - 16.4$
O3a	$\sim 177\,\mathrm{d}$	10.3	~ 21	$23.3 - 81.9$

Next, we transform these numbers into yearly rates using the effective time durations of the O1 and O3a runs, respectively. Although O1 ran from 12 Sep. 2015 to 19 Jan. 2016, and O3a ran from 1 Apr. to 1 Oct. 2019, the effective time used for data analysis of these observing runs are less due to aLIGO/AdV's different analysis pipelines, certain data segments being unusable, and times during which detectors are non-operational due to repairs and other factors. From Abbott et al. 2019a and Abbott et al. 2020b, the effective times for the O1 and O3a runs (using the aLIGO/AdV GstLAL analysis pipeline) were ~ 48 days and ~ 177 days, respectively. These time durations are indicated in the first column of Table 2.4, and the yearly aLIGO/AdV rate of BHBH mergers having $0.8 \leq q \leq 1.0$ can be seen in the third column for O1 and O3a.

Based on Table 2.4, our O1 rates compare well to what aLIGO/AdV have detected thus far, and the range of our O3 rates fall just above that detected by aLIGO/AdV. It should, however, be noted that these are rough estimates, and that a full comparison with the aLIGO/AdV results is not within the scope of this chapter simply because it would depend on details of the aLIGO/AdV data analysis that we cannot fully estimate here. Uncertainties would include any slight changes in actual sensitivity curves compared to what was used for our analysis, effective time spent on detection during the nominal operational time of the runs, and the actual amount of usable data aLIGO/AdV acquired and used.

It should also be mentioned that our analysis made the simplifying assumption that grids at $q = 1$ are representative of the range $0.8 \leq q \leq 1.0$ assumed by Marchant et al. (2016) for the CHE pathway[21]. It has to be noted that most of the aLIGO/AdV detections fall just outside this band, around ~ 0.7. Although this apparent trend needs a higher number of detections to be confirmed, it is a possible indication of the need to improve our simulations and assumptions and to include different initial mass ratios (instead of using $q = 1$ for all our binaries), or to modify other modeling parameters to see whether the final distribution of mass ratios could accommodate a slightly smaller average mass ratio (see the below discussion on the discrepancy between predicted and observed massive BHBH mergers for further comments on this). A follow-up of this work in future analyses should therefore allow for the more realistic case of binaries having different q-values from a distribution in the q-range — this would influence the eventual predicted BHBH merger rate, and would allow for a more robust comparison with the observed detections of aLIGO/AdV falling in this q-range. These improvements on the modeling are, however, beyond the scope of this thesis.

It is further interesting to note that our results point to the possible detection of massive BHBH mergers from above the PISN gap (see Figure 2.7), even though none has been observed by aLIGO/AdV as of yet (Abbott et al., 2018b, 2020b). For the default PPISN case in our analysis, we predict a BHBH merger rate of $3.59\,\mathrm{yr}^{-1}$ for O1, and $16.4\,\mathrm{yr}^{-1}$ for O3, above the PISN gap (see Table 2.1). Seeing as O1 effectively ran for ~ 48 days, and O3a for ~ 177 days (see above), these rates translate to predictions of ~ 0.47 detections for O1 and 7.95 detections for O3a. In contrast to these predictions, no mergers above the PISN gap were observed in any of the aLIGO/AdV runs.

To determine whether the difference between predicted and observed detections of mergers above the PISN gap is significant, we assume a Poisson distribution and equate the mean (and therefore also the variance), to the predicted number of detections. For O1, this means that the standard deviation is given by $\sqrt{0.47}$.

[21] As a reminder, we assume $q = 1$ for all our binaries, and normalise our rates using the range $0.8 \leq q \leq 1.0$ (see Appendix B.0.1).

Calculating whether the observed detections fall further than three standard deviations (i.e. a $3\,\sigma$ significance) from the predicted value, the difference is divided by the standard deviation, i.e. $0.47/\sqrt{0.47}$, to find $0.69\,\sigma$. Repeating this calculation for O3a, we find a significance of $2.8\,\sigma$. As the significance of the difference between predicted and observed BHBH mergers above the PISN gap is below $3\,\sigma$ for both O1 and O3a, it is not yet indicative that our model and simulations are not working, but we note and recognise the tension between the predicted and the observed predictions. Furthermore, the stellar evolution models can most likely be slightly modified to account for a certain mismatch between modeling and data.

A likely candidate for the current mismatch is the large uncertainties present in mass-loss rate prescriptions for massive stars (Sander and Vink, 2020). Many of these prescriptions have been included in the modeling of such stars, for example in the MESA stellar evolution code (Paxton et al., 2011, 2013, 2015, 2018, 2019). The mass-loss rate prescription used by Marchant et al. (2016) is that of a tenth of Hamann et al. (1995) (see Sander and Vink 2020 for a comparison of this to other mass-loss rate prescriptions), and so the same assumption is present in the work here — it is, however, important to note that it is not known which mass-loss rate prescription follows reality most closely. Another concern is the uncertainties involved in the metallicity dependence of mass-loss — Marchant et al. (2016) assumed a metallicity scaling of $(Z/Z_{\odot})^{0.85}$, but again, this might be different from reality. All of these uncertainties combined could account for the discrepancies we see in terms of predicted vs. observed rates, both in the case of PISNe (where extinction plays an additional role — see Section 2.4.4) and in the case of BHBH mergers, especially pertaining to massive ones, for example those above the PISN gap. Uncertainties in mass-loss rate can further cause tension for predictions such as the one made by Marchant et al. (2016) that CHE results in BHBH systems with $0.8 \leq q \leq 1.0$ — in fact, it is clear from Figure 2.16 that most of aLIGO/AdV's observed BHBH mergers seem to have a q around ~ 0.7, therefore falling slightly below the range of Marchant et al. (2016). If uncertainties are large enough, assumptions like Marchant et al. (2016)'s q-range of $0.8 \leq q \leq 1.0$, and our simplification of $q = 1$ for BHBH

mergers forming through the CHE pathway might not hold. In order to test these uncertainties, the different mass-loss prescriptions need to be modeled for further comparison, a task that falls outside the scope of this thesis.

At our estimated full sensitivity merger rate of $310\,\mathrm{yr}^{-1}$ for the default case where we include the effects of PPISNe (with a significant number of those coming from above the PISN gap - see Table 2.3), mergers resulting from the CHE scenario could very well turn out to be a significant source of aLIGO detections. As mentioned, we also estimated the detection rates for the projected ET sensitivity and found that the ET would be able to detect 83.8% of BHBH mergers at the present epoch, an astounding improvement on aLIGO.

Our simulation results further give an insight as to the population properties of BHBH systems eventually merging at the present epoch. Figure 2.5 shows that the range of final orbital periods for systems at high metallicity is larger than for those at low metallicities, a direct consequence of the strong metallicity dependence of stellar wind mass loss. It further shows that systems with delay times short enough to merge within the lifetime of the Universe have predominantly low metallicities (less than $\sim Z_{\odot}/10$). At very low metallicities, systems can have very short delay times (see Figure 2.8), pointing to the possibility of future high-redshift detections and an opportunity to probe the evolution of massive stars in the early Universe.

Furthermore, natural by-products and variants of our Monte Carlo code enabled us to calculate the effects of momentum kicks during black-hole formation on the population properties of BHBH progenitors, cosmological and magnitude limited PISN rates, and the effects of deviations in the SFR at high redshifts. It is found that the overall effect of momentum kicks is such that it tends to increase the delay time of a BHBH system, as is shown in Figure 2.12. This causes a general downwards shift in the population's merger redshifts (moving some of the systems into the redshift ranges detectable by aLIGO and ET) meaning that the observed percentage decrease in aLIGO and ET merger detections is less pronounced than the accompanying decrease in cosmological mergers. We furthermore calculated various magnitude limited PISN detection rates, which show that with current

ongoing deeper surveys and future surveys like the LSST, these rare events should be detectable. Lastly, in studying high-redshift deviations in the SFR and the effects it has on BHBH merger rates, it is found that in cases of mild SFR deviations the effects on the overall cosmological BHBH merger rate is not significant (merger rate estimates change only at the $\sim 8\%$ level), but that it is pronounced in cases of extreme deviation (with changes of up to $\sim 40\%$).

"You may not instantly see why I bring the subject up, but that is because my mind works so phenomenally fast, and I am at a rough estimate thirty billion times more intelligent than you. Let me give you an example. Think of a number, any number."
"Er, five," said the mattress.
"Wrong," said Marvin. "You see?"

Douglas Adams, The Hitchhiker's Guide to the Galaxy

3

Mass and spin measurements for the neutron star 4U1608-52 through the relativistic precession model

3.1 Abstract

Neutron stars present environments for studying matter under the most extreme conditions of pressure and density; as their equation of state is not yet known, accurate measurements of their mass and spin will eventually allow for the discrimination between various models. We present a systematic analysis of the complete set of observations of the neutron star low-mass X-ray binary 4U1608-52 obtained by the *Rossi X-ray Timing Explorer's Proportional Counter Array*. We study the spectral and fast-time variability properties of the source in order to determine the mass and spin of the neutron star via the relativistic precession model. We find 24 observations containing usable sets of the necessary three quasi-periodic oscillations (triplets, see Section 1.5.8) with which to accomplish this task,

The work here has been published in the Monthly Notices of the Royal Astronomical Society as du Buisson et al. (2019); doi: 10.1093/mnras/stz1160, and has been adapted for use here as a chapter.

along with a further seven observations containing two of the three quasi-periodic oscillations each. We calculate the spin and mass of the source for each of the triplets, and find that our results consistently cluster around physically realistic values in the spin range $0.19 < a < 0.35$ and mass range $2.15 < M/\mathrm{M}_{\odot} < 2.6$. We discuss the implications of our findings in the context of equation of state predictions, physically allowed spin ranges, emission proximity to the innermost stable circular orbit and possible model inaccuracies.

3.2 Introduction

4U1608-52 is a fairly bright transient NS Atoll source that has been sparsely monitored over a 16-year period with RXTE. It shows a very rich fast time-variability phenomenology: it contains twin kHz QPOs, LF QPOs, likely Hecto-Hz QPOs, Type-I X-ray bursts and burst oscillations. Thanks to these burst oscillations, the spin of 4U1608-52 has been measured to be 619 Hz, making it one of the most rapidly rotating accreting NSs (Galloway et al., 2008).

In this study we characterise 4U1608-52 in terms of its fast time-variability and spectral behaviour using all available RXTE/PCA data on the source. We find altogether 31 QPO triplets with which to test the relativistic precession model (RPM, see Section 1.5.8) - this is the first time that more than one triplet from the same BH or NS binary system is used for such a quantitative test, and it therefore enables us to more accurately test the reliability of the model in determining the mass and spin of NSs in LMXBs.

NSs are natural laboratories for studying some of the most extreme conditions of pressure and density found in the Universe, and their equation of state (EoS) is as of yet still unknown (Demorest et al., 2010). The mass and spin are essential parameters for determining and constraining the Eos of NSs, and the RPM supplies us with a way in which to obtain independent measurements of both these quantities, thereby playing a potentially important role in uncovering the extreme physics governing NS interiors.

This chapter is structured as follows. Section 3.3 details our timing and spectral analysis, selection of observations, the power spectral fitting and the classification of our observed QPO sets. Section 3.4 states our results, Section 3.5 discusses them and Section 3.6 discusses the testability and falsifiability of our work. Section 3.7 summarises and concludes the study. The relevant background on the RPM can be found in Section 1.5.8.

3.3 Observations and Data Analysis

We analysed all publicly available archival RXTE PCA data on the NS LMXB 4U1608-52, observed over a time period from March 1996 to December 2011. We removed time segments containing Type-I X-ray bursts from observations and excluded all observations with source count rates below 10 cts/s/PCU[1] to ensure an adequately high signal-to-noise ratio (SNR). Along with the cutting of certain long observations into shorter independent segments (see Section 3.3.3), this left us with a total of 1030 usable observations.

3.3.1 Timing analysis

For each observation we considered Event, Binned, Single Bit and Good Xenon PCA data modes (Jahoda et al., 1996; Bradt et al., 1993) and calculated the PDS using custom software under IDL[2] in the energy band $2-115$ keV (absolute PCA channels 0 to 249). We used a time resolution of 1/8192 s ($\sim 122\,\mu s$) where possible, and divided each observation into intervals of 16 seconds. Averaging the Leahy-normalised PDS (without subtracting the Poissonian noise, which we fit together with the source PDS) for each observation, these choices resulted in PDS with a Nyquist frequency of 4096 Hz and a frequency resolution of 0.0625 Hz. We then convert the PDS to rms-normalised PDS following Belloni and Hasinger (1990), and measure the fractional root mean square (rms) of the data in the $0.1-64$ Hz range (van der Klis, 1989a).

[1]PCU: proportional counter unit
[2]GHATS: `http://www.brera.inaf.it/utenti/belloni/GHATS_Package/Home.html`

3.3.2 Colour analysis

The count rates necessary for the computation of the HID were obtained using the Standard 2 energy spectra extracted from PCU unit 2 that covers the $2-60$ keV energy band across 129 channels. For each observation, the source count rate was determined using the $2-16$ keV energy band with the hardness measure defined as the ratio of counts in two energy bands A and B as $H_{\rm HID} = A/B$, where A stretches between $6-10$ keV and B stretches between $4-6$ keV. The Standard 2 channels corresponding to these energy ranges shift slightly depending on the corresponding RXTE gain epoch[3] and were adjusted for accordingly.

3.3.3 Selection of observations and power spectral fitting

In order to find the QPOs present in the dataset, we preselected the PDS of observations that, by visual inspection, contained these features. Due to the movement of QPOs in frequency as time progresses, it often happens that the resulting averaged PDS of a long observation contains significantly broadened features, where a 'long observation' is here defined as being of the order of roughly 12000 s or more in length. In such cases the observation was cut into shorter consecutive independent segments, and an averaged PDS for each of these resulting shorter observations was then calculated and used for the fitting and classification of QPOs.

The narrow and broad features of each power spectrum were fit with Lorentzians and a power-law component by means of the XSPEC[4] package (Arnaud, 1996); Lorentzians have their peak at the centroid frequency υ_c of a feature. We excluded all non-significant features from the analysis: for very low frequencies where red noise or flat-top noise were present, this meant excluding features below a significance[5] of 2σ; at all other frequencies features had to be significant at or above 3σ. For a feature

[3]RXTE gain epochs: `https://heasarc.gsfc.nasa.gov/docs/xte/e-c_table.html`

[4]XSPEC is a spectral fitting routine that can be used to fit PDS provided a 1-to-1 energy-frequency conversion matrix is applied. XSPEC can be found here: `https://heasarc.gsfc.nasa.gov/xanadu/xspec/`

[5]Significance is calculated as the integral of the power of the Lorentzian used for the fitting of the feature divided by the negative 1σ error on this integral.

to be classified as a QPO its significance had to be at or above 3σ and its quality factor Q (a measure of the coherence of the Lorentzian) had to be $Q \geq 2$, where $Q = v_c/FWHM$ and FWHM is the full width at half maximum of the Lorentzian.

The main focus of this work is the testing of the RPM using the nodal, periastron precession and orbital frequencies of the system. It is therefore specifically important for us to identify PDS of observations which simultaneously show the occurrence of the associated three features: an HBO-like QPO, a lower kHz QPO and an upper kHz QPO. Following Motta et al. (2017) and Casella et al. (2005), we classified HBO-like QPOs as those found between a few mHz and ~ 60 Hz having a fractional rms between a few percent and $\sim 20\%$, and falling on the rms-frequency track associated with HBO and HBO-like QPOs, as shown by Motta et al. (2017) (see Figure 3.4 and Section 3.4.1). kHz QPOs were found between ~ 400 Hz and ~ 1500 Hz with fractional rms mostly lower than $\sim 20\%$.

3.3.4 Classification of triplets

We remind the reader that the simultaneous occurrence of an HBO-like QPO, a lower kHz QPO and an upper kHz QPO in the PDS of an observation is referred to as a *triplet*. We distinguish between three groups of triplets for this work: *confirmed*, *tentative* and *incomplete* triplets.

We define confirmed triplets as those containing QPOs that all have a significance of 3σ or above, and where none of the fitting parameters had to be constrained or fixed - as such, these triplets have the highest probability of being real. Tentative triplets are those where one or more of the QPOs needed fitting parameters to be constrained in order for the QPO's significance to be adequately high - the QPOs in these triplets have a small chance of being the result of statistical fluctuations. We take this into account in our analysis. We note that, for kHz QPOs, this was only done when a possible QPO could be distinguished clearly through visual inspection. Incomplete triplets only have 2 out of the 3 necessary QPOs present. Using Ingram and Motta (2014), these can still be used to place limits on the mass, spin and emission radius of the system, and so they are included in our analysis.

We found a total of 9 confirmed triplets, 15 tentative triplets and 7 incomplete triplets. The confirmed and tentative triplets found can be seen in Table C.1, while the incomplete triplets are found in Table C.2. Observation 90408-01-01-03 contains two LF QPOs (one at 23^{+1}_{-1} Hz and the other at 37^{+2}_{-2} Hz) that are both good candidates for an HBO, and so we include both these possible triplets for completeness. The presence of two possible HBOs might be the result of the movement in frequency of one QPO over time (see Section 1.5) - presenting at two different positions in the averaged PDS. An alternative explanation would be that one of the LF QPOs is an HBO-like QPO, while the other is an as-of-yet unidentified QPO altogether. Seeing as the nature of these two QPOs is not the focus of the work here, they are both included as possible HBO-like QPOs forming parts of triplets with which to test the RPM. In cases in our analysis where only one of the possible triplets of observation 90408-01-01-03 could be used, the triplet containing the LF QPO with the highest significance was used.

For the incomplete triplets, we only have cases where either the lower or upper kHz QPO is missing in observations. In all cases where the HBO-like QPO was missing, we included a Lorentzian with a starter width and frequency equal to the respective average characteristics calculated from the confirmed triplets. The width was then kept constrained, while the centre frequency was free to vary so as to see whether the significance of the feature would reach a sufficiently high value. In all these cases significant QPOs were found, and these former incomplete triplets are therefore rather grouped with the tentative triplets.

3.4 Results

We produced the light curves, the HIDs and the frequency-rms diagrams for the LF QPOs and kHz QPOs in order to analyse 4U1608-52, whereafter we used the RPM to calculate the spin a, mass M and emission radius r using the various groups of triplets found in our data.

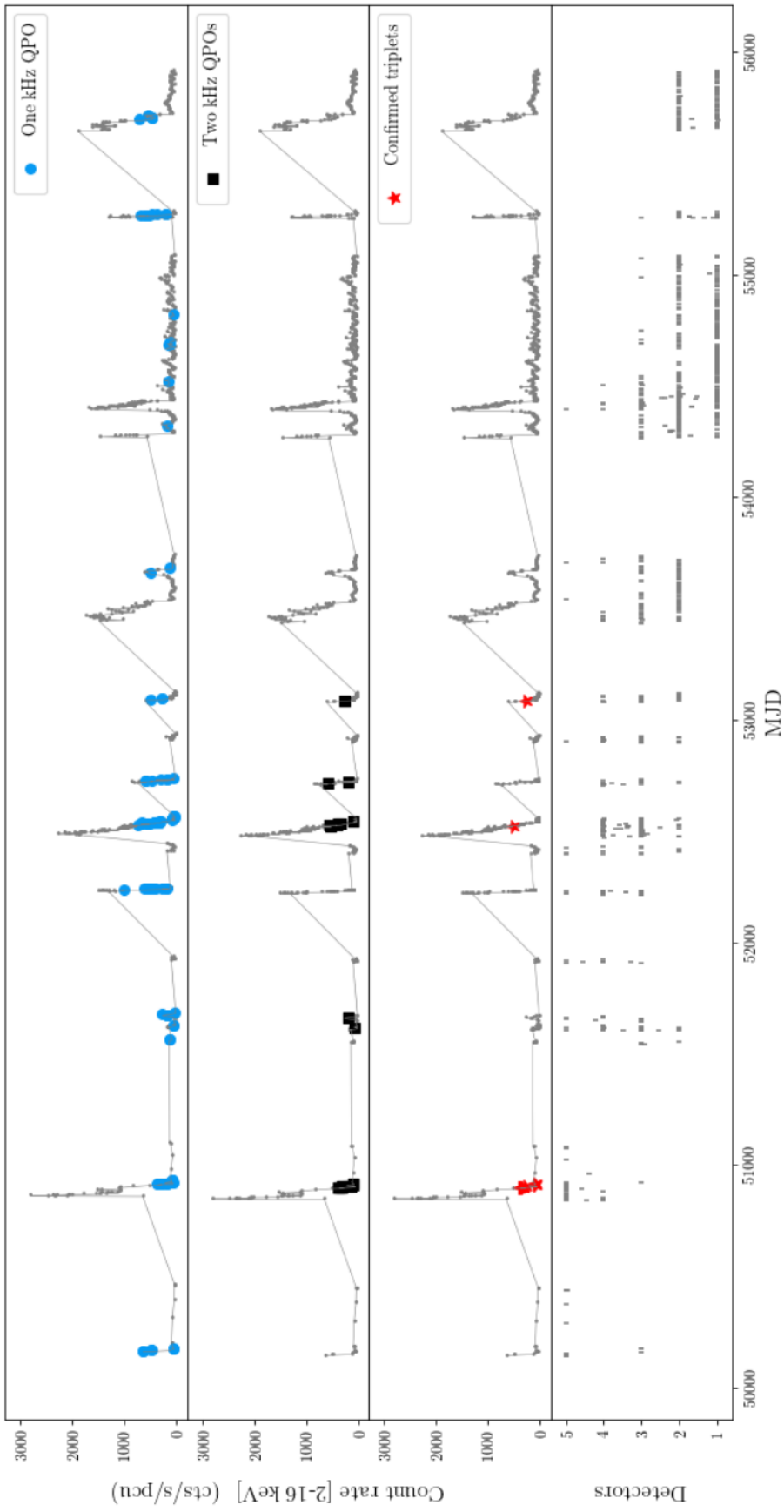

Figure 3.1: Top three panels: The light curve of 4U1608-52, showing the source count rate of observations taken from March 1996 to December 2011, with each data point representing an observation, is displayed in each of the top three panels. The light blue circles in the top panel are observations containing one or more kHz QPOs, black squares in the second panel are observations containing two or more kHz QPOs (they comprise of both the confirmed and tentative triplets) and red stars in the third panel represent observations containing confirmed triplets. Red starred observations are a subset of the observations denoted by black squares, which in turn is a subset of the blue circular observations. **Bottom panel:** The number of PCU detectors working in each observation. When the number of PCUs is not an integer, it means that one or more PCUs turned on/off during the observation.

3.4.1 Colour analysis and general behaviour

The top three panels in Figure 3.1 shows the light curve (the source count rate and date of each observation) of 4U1608-52, covering roughly 15 years, from March 1996 to December 2011. Coloured data points give an indication of where kHz QPOs and confirmed triplets were found - light blue observations contain one or more kHz QPOs, black observations contain two kHz QPOs and red observations contain confirmed triplets. The black data points comprise of the tentative and confirmed triplets put together, so in all cases where a black dot is not overlapped by a red one, the observation contains a tentative triplet. The bottom panel in Figure 3.1 shows the number of PCU detectors used for each observation. It is noted that as time progresses there is a tendency for fewer detectors to be used.

The HID for our data is shown in Figure 3.2, showing the source count rate and hardness ratio of each observation in our analysis. Consecutive observations are connected via thin lines, and the coloured data points have the same meaning as they did in Figure 3.1. The diagram shows a span of more than two orders of magnitude in source count rate, along with hysteresis patterns showing distinct excursions to very high luminosity, softer states, corresponding to the high luminosity phases present in the light curve in Figure 3.1. The source is shown to be harder during the rise of outbursts, and follows diagonal transitions (as noted by Muñoz-Darias et al. 2014) to the brighter soft state. For 4U1608-52, the harder state corresponds to a fractional rms larger than ~ 20 % while the soft state corresponds to a fractional rms smaller than ~ 5 %, consistent with other atoll sources (see Muñoz-Darias et al. 2014). Eventually, the luminosity (roughly tracked by the source count rate) decreases, preceding a reverse diagonal transition back to the harder state. Bright atolls often have bright excursions where they enter a soft, low-variability state in which the correlation between variability and hardness breaks down (Muñoz-Darias et al. 2014) and hysteresis stops. The HID of 4U1608-52 shows such bright excursions - they have a corresponding roughly constant fractional rms of $\sim 2 - 3$ % (not immediately visible in the plots presented here).

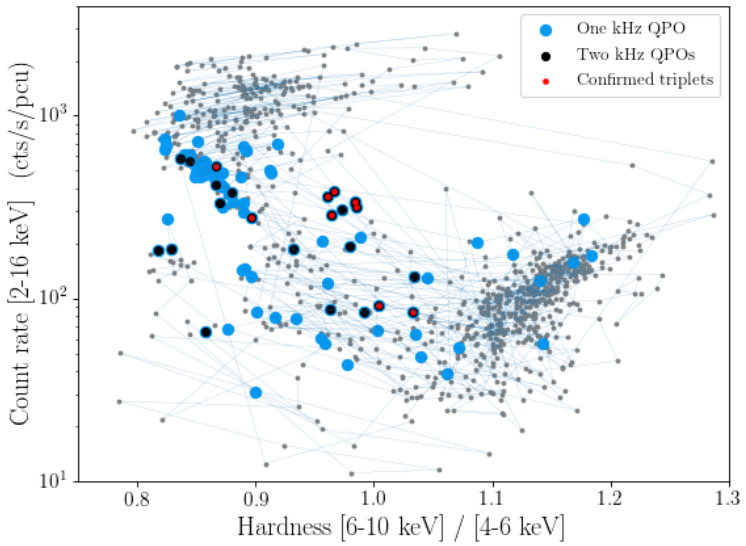

Figure 3.2: The HID of 4U1608-52, with the source count rate on the y-axis and with each data point representing an observation. Similar to Figure 3.1, light blue observations contain one or more kHz QPOs, black observations contain two or more kHz QPOs (and comprise of both the confirmed and tentative triplets), while red observations only comprise of confirmed triplets. Consecutive observations are connected.

In order to classify between lower and upper kHz QPOs in cases where only one of them is present in an observation, we plotted their centre frequencies ν_c against a hardness measure, following Belloni et al. (2007), who used similar plots and found that upper and lower kHz QPOs generally follow two distinct tracks. QPOs along the top track of their plot were found to be upper kHz QPOs, while those along the bottom track were lower kHz QPOs. We use the same method to classify our kHz QPOs. Hardness $H_{\rm split}$ is here defined as $H_{\rm split} = C/D$, where C is the number of counts in the energy band stretching from $9.7 - 16.0$ keV and D is the number of counts in the band $6.4 - 9.7$ keV in an observation - these ranges were taken from Pawar et al. (2013), as they proved to separate the different groups of QPOs best for our purposes. Our results are shown in Figure 3.3. Stars denote upper kHz QPOs and crosses mark lower kHz QPOs. Open circles are those that do not clearly fall on either of the branches, and classification is therefore withheld. The kHz QPOs encircled and numbered in red correspond to those that are part of the incomplete triplets - in this way, Figure 3.3 is used to classify the missing kHz QPOs

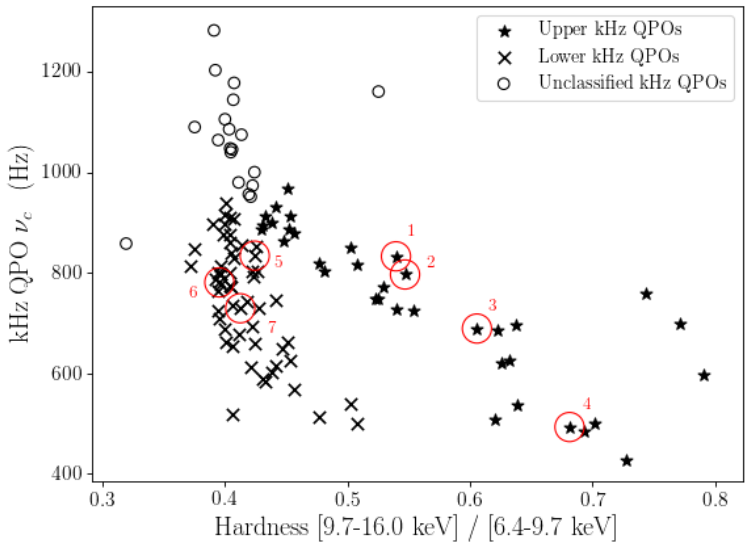

Figure 3.3: The frequency and hardness of the kHz QPOs found in our dataset. Hardness $H_{\rm split}$ is taken as the ratio of counts in two energy bands C and D as $H_{\rm split} = C/D$, where C is the band stretching between $9.7 - 16.0$ keV and D stretches between $6.4 - 9.7$ keV for each observation. Stars denote upper kHz QPOs, crosses denote lower kHz QPOs and open circles denote either of the two in cases where it is hard to distinguish between them based solely on the figure. Red encircled points denote those kHz QPOs that form part of our set of incomplete triplets - the numbering aids the identification of the corresponding observations in Tables C.2 and 3.2.

in these triplets. The numbers are used to identify the corresponding observations (see Table C.2). We note two exceptions to this classification - numbers 4 and 7 in Figure 3.3 - where we believe that usage of the figure leads to a misclassification of kHz QPOs. The reasons for this are discussed in Section 3.4.2.

We next plot the rms-frequency diagrams for the LF QPOs and the kHz QPOs found in our data, as is shown in Figure 3.4 and 3.5, respectively. When fitting these, fixed widths for QPOs were allowed if that resulted in them having a sufficiently high significance to be classified as QPOs. Red and blue data points show those QPOs that form part of either our confirmed or tentative triplets, respectively.

The frequency-rms diagram depicting the LF QPOs in our dataset (see Figure 3.4) shows similar features to Figure 2 from the work of Motta et al. (2017), with LF QPOs spanning similar frequency and rms ranges. From their LF QPO classification we can identify the QPOs forming part of the curve stretching from the upper left to

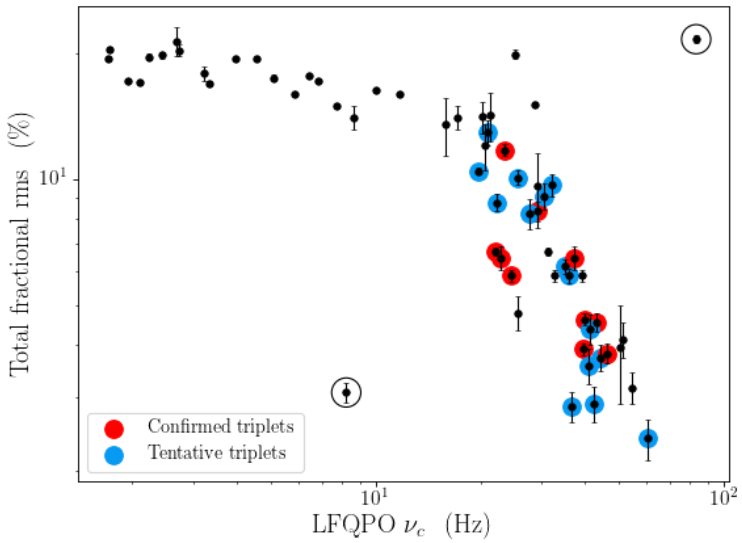

Figure 3.4: The total fractional rms and frequency of all significant LF QPOs found in the dataset, with each data point representing one observation per LF QPO. The track stretching from the upper left to bottom right constitute HBO-like QPOs, the bottom outlier (encircled) is most probably an FBO-like QPO and the top outlier (also encircled) is a hecto hertz QPO. The red data points are those HBO-like QPOs that form part of our confirmed triplets, while the blue data points form part of the tentative triplets.

the lower right as HBO-like QPOs. The top outlier (encircled) possibly represents a hectohertz QPO (Altamirano et al., 2008a). Following Motta et al. (2017)'s scheme, the bottom outlier (also encircled) is most probably an FBO-like QPO. Furthermore, it can be seen from Figure 3.4 that QPO frequency increases as rms decreases along outbursts (also noted by Muñoz-Darias et al. 2014 and many others), corresponding to predictions by the Lense-Thirring effect whereby the HBO (or HBO-like) QPO's frequency depends on the outer radius of the precessing optically thin, geometrically thick inner accretion flow - the smaller the radius, the higher the frequency.

Figure 3.5, showing the frequency-rms diagram of the kHz QPOs found in our dataset, shows features similar to those in Figure 5 of Motta et al. (2017) - two tracks, predominantly falling in the rms range $2 - 20$ %. Using Figure 3.3, we find that the top kHz QPO track mostly corresponds to upper kHz QPOs, while the bottom track corresponds mostly to lower kHz QPOs. Note that the error bars on the observations along the lower part of the lower branch appear large mostly

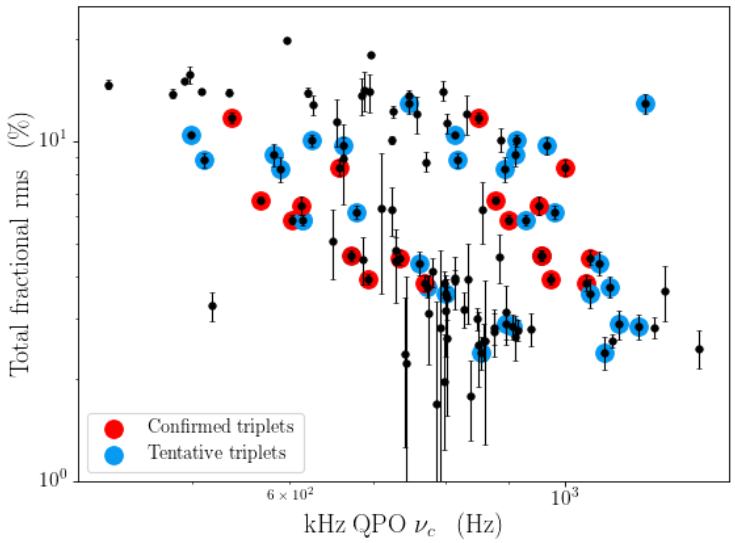

Figure 3.5: The total fractional rms and frequency of all significant kHz QPOs found in the dataset, with each data point representing one observation per kHz QPO. The red data points are those QPOs that form part of the confirmed triplets, while the blue data points form part of the tentative triplets.

due to the logarithmic scaling of the axis.

3.4.2 Relativistic precession model

We used the RPM (see Section 1.5.8) to calculate the spin a, mass M and emission radius r of 4U1608-52 using each of our confirmed, tentative and incomplete triplets. Due to the non-linearity of the equations in a, M and r, error estimates are obtained using a Monte Carlo simulation and following the procedure provided in Ingram and Motta (2014). The results are shown in Table 3.1 and 3.2, and in Figure 3.6, 3.7 and 3.8.

Figure 3.6 shows the mass M and spin a calculated from each of our confirmed (red squares) and tentative (blue circles) triplets. The two outlier triplets (in black: 50052-01-04-00 to the bottom and 70059-03-02-01 to the top) are part of the tentative triplets - we mark them as having the lowest probability of being real, as both contain upper kHz QPOs with Q-factors significantly higher than the other triplets here used (see Table 3.1). We exclude these two outliers in further figures in order to avoid the risk of biassing our results. The dashed black lines

Table 3.1: The spin, mass and emission radius of the confirmed and tentative triplets as determined with the RPM. The frequencies of the LF QPOs are also included so that information shown in Figure 3.7 can be seen clearly.

Confirmed Triplets				
Obs ID	**a**	**M/M$_\odot$**	**r**	**LF QPO (Hz)**
30062-02-01-00	0.293 ± 0.006	2.54 ± 0.05	5.54 ± 0.04	40^{+1}_{-1}
30062-02-01-01-1	0.211 ± 0.004	2.42 ± 0.04	5.99 ± 0.03	$24.5^{+0.5}_{-0.6}$
30062-02-01-01-3	0.202 ± 0.003	2.39 ± 0.02	6.14 ± 0.02	$22.2^{+0.4}_{-0.4}$
30062-02-01-02-1	0.30 ± 0.01	2.44 ± 0.06	5.37 ± 0.06	46^{+2}_{-3}
30062-01-01-00-1	0.291 ± 0.009	2.32 ± 0.04	5.54 ± 0.04	43^{+2}_{-2}
30062-01-02-01	0.222 ± 0.007	2.47 ± 0.07	6.13 ± 0.09	$23.5^{+0.5}_{-0.6}$
30062-01-02-05-1	0.227 ± 0.006	2.18 ± 0.06	5.99 ± 0.05	$29.2^{+0.9}_{-0.9}$
70059-01-20-00	0.285 ± 0.009	2.50 ± 0.04	5.53 ± 0.04	40^{+1}_{-1}
90408-01-01-03	0.194 ± 0.008	2.19 ± 0.09	6.18 ± 0.08	23^{+1}_{-1}
	0.30 ± 0.01	2.4 ± 0.1	5.80 ± 0.09	37^{+2}_{-2}
Tentative triplets				
30062-02-01-01-4	0.29 ± 0.01	2.48 ± 0.04	5.75 ± 0.05	36^{+2}_{-2}
30062-01-01-00-2	0.29 ± 0.01	2.2 ± 0.1	5.53 ± 0.09	44^{+2}_{-2}
30062-01-01-02	0.261 ± 0.009	2.38 ± 0.08	5.70 ± 0.06	35^{+2}_{-2}
30062-01-01-03	0.20 ± 0.01	2.46 ± 0.07	6.3 ± 0.1	20^{+1}_{-1}
30062-01-02-05-2	0.213 ± 0.008	2.43 ± 0.08	5.9 ± 0.1	$25.6^{+0.7}_{-0.7}$
50052-01-20-00	0.24 ± 0.02	2.5 ± 0.1	5.93 ± 0.09	28^{+2}_{-2}
50052-01-20-01	0.26 ± 0.02	2.40 ± 0.08	5.96 ± 0.08	30^{+2}_{-2}
50052-01-04-00	0.149 ± 0.008	1.73 ± 0.04	6.34 ± 0.08	21^{+1}_{-1}
70058-01-37-00	0.35 ± 0.04	2.6 ± 0.1	5.0 ± 0.2	60^{+8}_{-9}
70059-03-01-01	0.26 ± 0.02	2.4 ± 0.1	5.4 ± 0.1	41^{+4}_{-4}
70059-03-02-00	0.25 ± 0.06	2.3 ± 0.1	5.4 ± 0.2	42^{+6}_{-16}
70059-03-02-01	0.40 ± 0.05	3.1 ± 0.2	5.6 ± 0.2	41^{+4}_{-8}
70059-01-26-00	0.246 ± 0.009	2.37 ± 0.05	5.78 ± 0.05	32^{+1}_{-1}
80406-01-02-02	0.22 ± 0.02	2.15 ± 0.04	5.51 ± 0.07	37^{+4}_{-3}
80406-01-03-03	0.221 ± 0.008	2.53 ± 0.04	6.18 ± 0.05	22^{+1}_{-1}

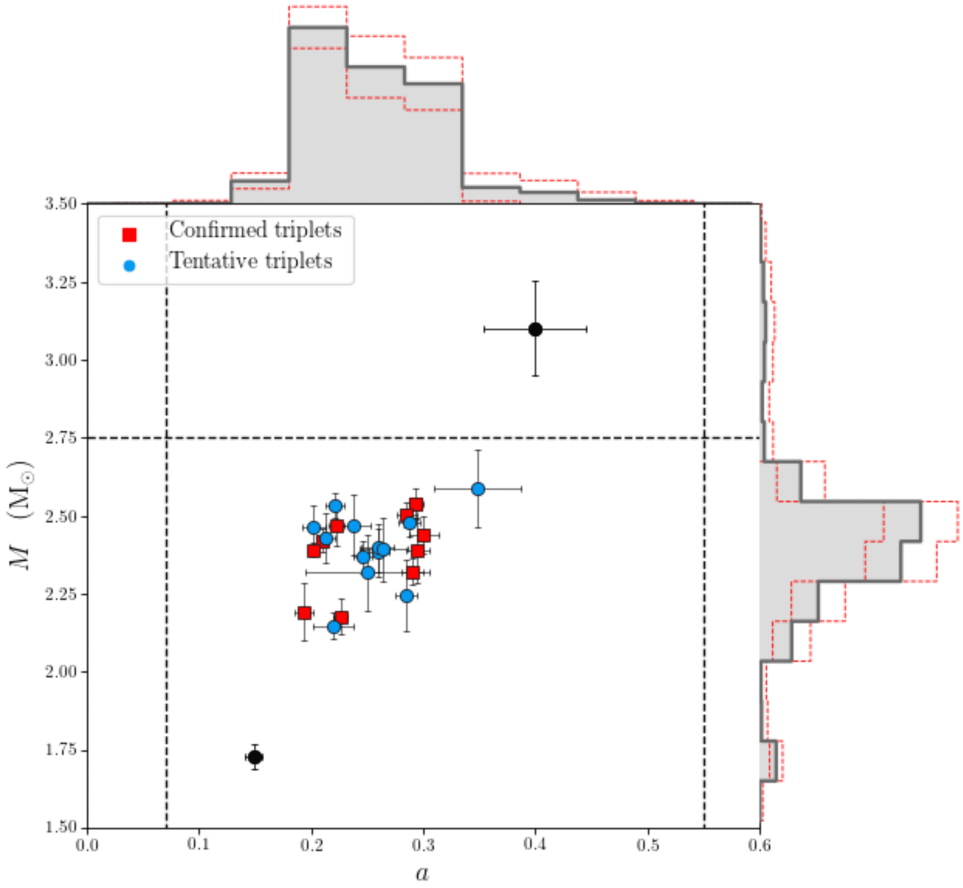

Figure 3.6: The mass and spin estimates of both the confirmed (red squares) and tentative (blue circles) triplets, as predicted by the RPM. The black data points denote tentative triplets containing QPOs with Q-factors 4-5 times larger than that of other triplets - these can therefore very possibly not be real. The marginal distributions of the spin and mass can be seen at the top and to the right of the figure, respectively, with the 1σ error on these quantities also given. The broken black lines indicate theoretical physical limits for the spin and the mass, taking into account current models of the equation of state and approximating the NS as both a hollow and a solid sphere.

indicate theoretical upper and lower physical limits for the mass and spin of our system by making use of the equation of state (EoS) and approximating the NS as both a hollow and solid sphere, respectively.

To calculate the physical limits of the dimensionless spin parameter, we took the spin frequency of the NS to be $\nu = 619$ Hz (Galloway et al. 2008) and the mass as $2.38\,M_\odot$, the average of the masses predicted by using the confirmed triplets in the RPM (we used the first of the instances of 90408-01-01-03 listed in Table 3.1, as its LF QPO is slightly more significant than the alternative). Assuming that

the radius R of a NS falls between 7 km and 15 km (Demorest et al., 2010) and approximating the NS as a hollow and solid sphere (in order to calculate its moment of inertia), respectively, we calculated the maximum spin, for a hollow sphere with $R = 15$ km, as $a_{\max} = 0.55$ using the definition of the dimensionless spin parameter given in Section 1.5.8 as $a = (cJ)/(GM^2)$, with J the angular momentum of the object. The minimum spin, for a solid sphere with $R = 7$ km, was found to be $a_{\min} = 0.07$. These limits are indicated in Figure 3.6.

Upper and lower limits for the allowable mass of a NS were obtained by making use of the predictions of the EoS (Demorest et al. 2010) - the upper limit being $\sim 2.75\,\mathrm{M}_\odot$ and the lower limit being $\sim 0.35\,\mathrm{M}_\odot$ (the upper limit is indicated in Figure 3.6). These limits represent the most extreme allowed physical limits, and give an idea of where acceptable mass and spin values should lie. It can be seen that, in all but one case, the RPM results in mass and spin values that fall within these limits. Furthermore, except from the two outlier cases (in black), all the values cluster roughly between spin values of $0.19 < a < 0.35$ and mass values of $2.15 < M/\mathrm{M}_\odot < 2.6$.

In order to calculate estimates of the radius R of the neutron star, we assume a solid sphere for its moment of inertia equation, and then use each of the confirmed triplets' spin-mass parameter value pairs in turn (see Table 3.1) in the expression for dimensionless spin to find that its radius falls in the range $11.0 < R < 14.6$ km.

The marginal distributions of the spin and mass are supplied in the form of histograms at the top and to the right of Figure 3.6. We calculated these distributions by using a Monte Carlo approach. For each triplet, values for the frequencies of the LF QPO, lower kHz QPO and upper kHz QPO were drawn from Gaussian distributions having the respective fitted frequency values (see Table C.1) as their means, and the average error on each of these quantities as their standard deviations. The numerous combinations of these three frequency values were then used to calculate corresponding values for a, M and r with the RPM equations. This was done for each of our confirmed and tentative triplets, after which all results for a and M were binned separately in order to obtain the marginal distributions.

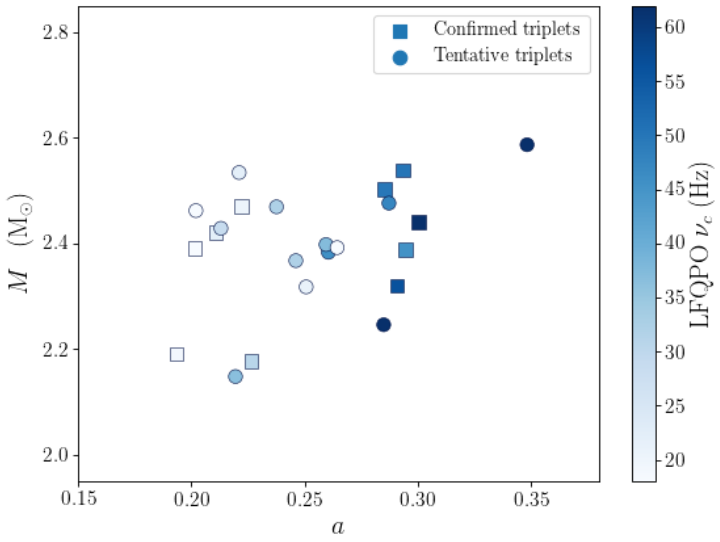

Figure 3.7: The mass and spin estimates of the confirmed and tentative triplets as predicted by the RPM, coloured according to the LF QPO frequency.

The standard deviation in each bin was used as the 1σ error, indicated in red dashed lines on the histograms in the figure.

Next, we plotted the calculated values of a and M of the confirmed and tentative triplets, colour coded according to their LF QPO frequencies, in Figure 3.7. Lighter colours indicate lower LF QPO frequencies while darker colours indicate higher frequencies, and squares and circles denote confirmed and tentative triplets, respectively. It can be seen that lighter colours tend towards the bottom left of the figure, and that moving upwards and right brings about darker colours.

Finally, Figure 3.8 shows, in different shades of grey, the spin and mass of the confirmed and tentative triplets along with the theoretical physical limits these parameters are allowed to have, as was also shown in Figure 3.7. Added to this, however, are the limits on a and M imposed by each of our incomplete triplets (see Table 3.2), with starred triplets being those lacking lower kHz QPOs and crossed triplets those that lack upper kHz QPOs. When the kHz QPOs of triplets 4 and 7 are classified using Figure 3.3, we find triplet 4's limits to be $M \leq 4.66\mathrm{M}_{\odot}$ and $a \geq 0.45$, while triplet 7 results in limits of $M \leq 1.16$ and $a \leq 0.18$. These limits

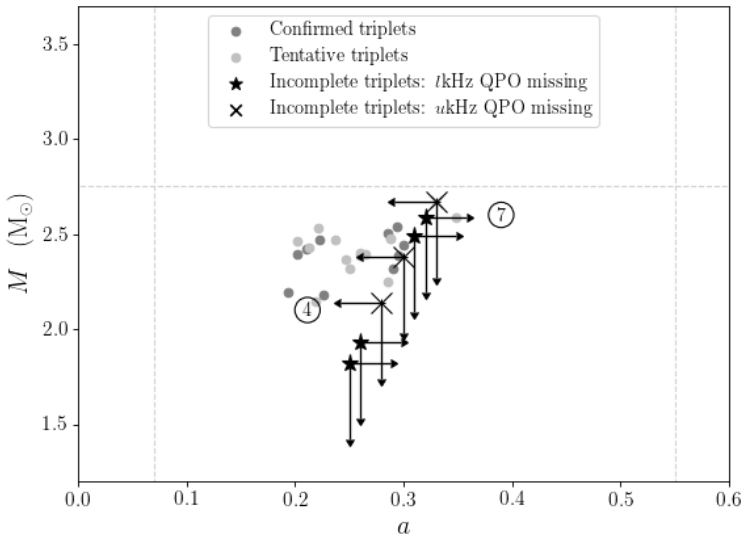

Figure 3.8: The mass and spin estimates of the confirmed and tentative triplets along with the mass and spin constraints given by incomplete triplets either lacking an upper kHz QPO (ukHz QPO) or a lower kHz QPO (lkHz QPO).

make triplets 4 and 7 extreme outliers, an indication that classifying kHz QPOs using Figure 3.3 might result in the misclassification of some of the isolated peaks.

The low value of triplet 4's detected kHz QPO of 493 Hz places further doubt on its classification as an upper kHz QPO by Figure 3.3. However, classifying triplet 4 and 7's kHz QPOs as a lower kHz QPO and upper kHz QPO (see Table C.2), respectively, results in limits on their a and M values clustering with the rest of the triplets, as shown in Figure 3.8 and Table 3.2.

We note that kHz QPOs have been classified also based on their phase lags (see e.g. Nowak et al. 1999 on the calculation of lags), which in some sources show a dependence on the type of kHz QPO detected (i.e. upper or lower) - see e.g. de Avellar et al. (2013, 2016), Barret (2013) and Peille et al. (2015) for their work on NS QPO lags, and Méndez et al. (2013) for their work on BH QPO lags in this regard. However, since the classification based on the phase lags suffers from uncertainties, a careful and detailed study of the lags associated to the QPOs in 4U1608-52 would be required to obtain reliable and solid results. Such a study is however beyond the scope of this chapter, and is left to a future work.

Table 3.2: Limits placed on the spin, mass and emission radius by making use of the incomplete triplets, as calculated with the RPM. Numbers assigned to observations in the second column correspond to the numbers similarly assigned in Table C.2 and Figure 3.3.

Incomplete Triplets					
Obs ID	#	**a**	$\mathbf{M/M_\odot}$	**r**	**LF QPO (Hz)**
70069-01-03-01	1	≥ 0.26	≤ 1.93	≥ 7.34	$20.7^{+0.8}_{-0.7}$
70069-01-03-06	2	≥ 0.25	≤ 1.82	≥ 7.86	$17.2^{+0.4}_{-0.3}$
50052-01-24-00	3	≥ 0.31	≤ 2.49	≥ 7.02	$21.4^{+0.4}_{-0.4}$
60052-03-01-00	4	≤ 0.28	≤ 2.14	≥ 5.71	$28.7^{+0.8}_{-1.2}$
95334-01-03-11	5	≤ 0.30	≤ 2.38	≥ 5.29	50^{+3}_{-2}
70059-03-02-03	6	≤ 0.33	≤ 2.67	≥ 5.16	51^{+4}_{-3}
95334-01-03-05	7	≥ 0.32	≤ 2.59	≥ 7.2	$25.6^{+0.7}_{-0.6}$

3.5 Discussion

We have examined all publicly available RXTE/PCA data from the NS LMXB 4U1608-52, taken between March 1996 and December 2011. Our main aim was to find observations containing QPOs - particularly those containing QPO triplets - to be used in the testing of the RPM. In total we found 9 confirmed triplets, 15 tentative triplets and 7 incomplete triplets (see Table C.1 and C.2), the latter being cases where only two out of the three QPOs in a triplet were present in an observation.

High luminosity phases along 4U1608-52's light curve (top three panels, Figure 3.1) can be seen clearly, and it is noted that observations are more frequent on the downward slopes than on the rise. This is due to a combined effect: the rise time of the high luminosity phase being shorter than the fall, as well as activity only being spotted when the outbursts make the sources adequately bright - it was therefore monitored predominantly from such points onwards. It is further noted that as time progresses, the number of detectors typically used per observation (bottom panel, Figure 3.1) steadily decreases. We ascribe the lack in detections of any triplets after an MJD of roughly 53200 to the steady decrease in measured total source count rate per observation due to the decrease in the number of PCUs used.

The results we obtained by applying the RPM to our confirmed, tentative and incomplete triplets are summarised in Table 3.1 and 3.2 and Figure 3.6, 3.7 and 3.8. We note that our estimates are not completely consistent, as can be seen in Figure 3.6, and we identify several reasons at the base of these inconsistencies in Section 3.5.1. It is, however, very reassuring that the vast majority of estimates fall within physically allowable limits (indicated in broken lines in Figure 3.6), even considering that these limits are very conservative ones (the NS being approximated as both a hollow and solid sphere, respectively). Additionally, apart from the two outliers (in black, discussed in Section 3.4.2), most estimates cluster together. Our mass estimates fall towards the higher end of the currently predicted allowable NS mass ranges, and are compatible with many of the EoS models. However, if our measurements are correct, our results would be ruling out some of the more exotic models investigated in Demorest et al. (2010). We further note that in the case of our mass measurements being correct (i.e. falling in the range $2.15 < M/\mathrm{M}_{\odot} < 2.6$), the NS in 4U1608-52 would be one of the heaviest known to date. The known NS with the highest mass is PSR J2215+5135 (Linares et al., 2018) at $2.27^{+0.17}_{-0.15}\,\mathrm{M}_{\odot}$, closely followed by PSR J0348-0432 with a mass of $2.01 \pm 0.04\,\mathrm{M}_{\odot}$ (Antoniadis et al., 2013).

Based on the current knowledge of compact objects, heavy NSs can only be produced by stiff EoSs, and it is therefore believed that the softest EoSs are likely unrealistic (Horvath and de Souza, 2017). However, the fact that stiffer EoSs are needed to explain such heavy NSs poses a problem for certain models of the internal composition, like the hyperon model (Horvath and de Souza, 2017). Hyperons, existing as part of the natural baryonic sector, have been included in some dense matter studies of NSs for the last 40 years. Their inclusion softens stiff EoSs considerably, precluding precisely the higher masses of NSs - this is called the "hyperon puzzle" (Horvath and de Souza, 2017; Özel and Freire, 2016). Including hyperons, EoSs barely accommodate NSs reaching $2\mathrm{M}_{\odot}$. For a NS as large as that in 4U1608-52, therefore, other alternatives would have to be considered. One solution would be the possible suppression of hyperons, which however should be ascribed to some as-of-yet unknown mechanism; an alternative explanation would

be that there is enough repulsion from them to explain these effects (Özel and Freire, 2016; Horvath and de Souza, 2017).

Using spectral-timing data from the Neutron star Interior Composition Explorer[6] (NICER), two research groups have, respectively and independently of one another, constrained the mass and radius of the isolated millisecond pulsar (MSP) J0030+0451 more precisely than has ever been done for a neutron star before. Riley et al. (2019) found a mass of $1.34^{+0.15}_{-0.16}\,\mathrm{M}_\odot$ and a radius of $12.71^{+1.14}_{-1.19}\,\mathrm{km}$, while Miller et al. (2019) found a mass of $1.44^{+0.15}_{-0.14}\,\mathrm{M}_\odot$ and a radius of $13.02^{+1.24}_{-1.06}\,\mathrm{km}$. The two groups estimated these parameters via pulse-profile modeling, and performed relativistic ray-tracing of the emission from the hot regions on the pulsar's surface. Riley et al. (2019) assumed two distinct hot regions (based on two clear pulsed components in the pulse-profile data), while Miller et al. (2019) explored the modelling of both two and three hot regions, respectively. A number of forms for each hot region were then explored, and the accompanying mass and radius inferred. Riley et al. (2019)'s results strongly favour a pulse-profile model where both hot regions are located in the same rotational hemisphere, while Miller et al. (2019)'s best-fit model includes three oval hot regions in the same rotational hemisphere. Future primary target MSP sources for NICER's M-R constraints include the massive PSRs J0740+6620 and J1614-2230 (Bogdanov et al., 2019) with masses of $2.14^{+0.10}_{-0.09}\,\mathrm{M}_\odot$ (Cromartie et al., 2020) and $1.97 \pm 0.04\,\mathrm{M}_\odot$ (Demorest et al., 2010), respectively.

In 2017, aLIGO/AdV detected a binary neutron star merger, GW170817, with component masses between $1.36-1.60\,\mathrm{M}_\odot$ and $1.17-1.36\,\mathrm{M}_\odot$, respectively, assuming low spins consistent with binary neutron stars merging in a Hubble time (Abbott et al., 2017b). For a high-spin prior, the component masses range between $1.36-2.26\,\mathrm{M}_\odot$ and $0.86-1.36\,\mathrm{M}_\odot$, respectively. The component radii have been constrained to $11.9^{+1.4}_{-1.4}\,\mathrm{km}$ for both the larger and smaller neutron star components (Abbott et al., 2018a). In January 2020 a second signal, GW190425, consistent with the merger of a binary neutron star system was detected by aLIGO/AdV, with component masses ranging between $1.12-2.52\,\mathrm{M}_\odot$ and radii $R < 15\,\mathrm{km}$ (Abbott et al., 2020a).

[6]NICER home: `https://heasarc.gsfc.nasa.gov/docs/nicer/`

The constraints on the mass and radius of neutron stars recently obtained by NICER and aLIGO, and NICER's future planned investigations, seems to suggest that any valid EoS should allow for neutron stars with masses at least slightly above $\sim 2\,M_\odot$, and possibly more (e.g. the upper limit of $2.26\,M_\odot$ and $2.52\,M_\odot$ for the heavier components of GW170817 and GW190425, respectively). These mass ranges overlap with our estimates of the neutron star in 4U1608-52's mass. Our radius estimates ranges between 11.0 km and 14.6 km, a wide range, and so overlaps with radius estimates above.

X-ray and gravitational wave results has proven effective at constraining parameters of neutron stars, and has been used for fitting data to different models parameterising the EoS of neutron stars. The combination of X-ray and gravitational wave datasets is degenerate and tends to tighten mutual constraints (Al-Mamun et al., 2021). In most EoS parameterisations currently under consideration, NS radii have a small dependence on the NS mass, implying that estimates on the radii of NSs tend to be compatible between datasets (Miller et al., 2019). This in turn leads to a large range of viable high density EoSs, which can be further constrained by the deformability measured from gravitational wave data (Al-Mamun et al., 2021). The results from Abbott et al. (2018a) on the deformability of NSs does allow for higher-mass neutron star EoSs, and in these cases further constraints are imposed on the masses of the neutron stars merging in GW170817.

Stella et al. (1999) already noticed that the RPM tends to yield relatively high masses. As an explanation they proposed that the HBO associated to the kHz QPOs in triplets is the second harmonic of the real Lense-Thirring frequency, therefore the Lense-Thirring frequency would correspond to half of the centroid frequency measured in the PDS (see also Motta et al. 2017). Taking this into account and assuming that the HBO frequency we measured corresponds to the second harmonic of a non-detected fundamental frequency, we find that the spin and mass values for 4U1608-52 would fall in the ranges $0.10 < a < 0.19$ and $1.97 < M/M_\odot < 2.33$. This is shown in Figure D.1. It is noted that even with this lowered mass range, the mass is still large enough to cause problems for stiff EoS models in light of

the "hyperon puzzle". If the mass were to lie towards the lower end of this range, some of these more exotic models of the EoS would still (even though only barely) apply (Demorest et al., 2010; Horvath and de Souza, 2017). We furthermore also calculated the spin and mass values for 4U1608-52 assuming that the upper kHz QPO is associated with the vertical epicyclic frequency ν_θ, instead of with the orbital frequency ν_ϕ (as is standard for the RPM). The results are shown in Figure E.1 in Appendix E, where it can be seen that mass values now fall in the range $2.04 < M/\mathrm{M}_\odot < 2.41$ and spin values fall in the range $0.19 < a < 0.34$. Both these ranges are slightly lower than for the case with standard assumptions (see Figure 3.6), and error bars are larger due to the added uncertainties introduced in associating the upper kHz QPO with the vertical frequency. As above, the slightly lower mass does not significantly change the implications for possible EoS models.

Figure 3.7 shows estimates corresponding to lower LF QPO frequencies tending to lower spin and mass values, while those associated with higher frequencies tend towards higher spins and masses. Seeing as all QPO frequencies reach their highest allowed values at the innermost stable circular orbit[7] (ISCO), we know that those estimates with higher frequencies were found closer to the ISCO than those with lower frequencies. The RPM is an increasingly better approximation of the rigid precession model (Ingram et al. 2009) the closer to the ISCO the LF QPO originates from. As the rigid precession model appears to be a more realistic description of what is believed to be the true behaviour of matter close to a compact object, estimates of a and M obtained from QPOs at higher frequencies are more likely to be a better representation of the real system parameters (see Section 3.5.1 for a further elaboration). Seeing as the estimate relating to the highest-frequency LF QPO results in the largest spin and mass values, all other lower-frequency estimates constitute lower limits to these values. Based on this reasoning, if one further assumes that this same LF QPO is emitted at the ISCO, the ISCO radius can be calculated and used as an upper limit to the radius of the NS. Using the

[7]The innermost stable circular orbit, in general relativity, describes the smallest stable orbit a test particle can occupy around a massive object.

relation between the ukHz QPO's centroid frequency and the radius of the ISCO (r_{ms}) given in van der Klis (2006), we find $r_{ms} = 18.6$ km.

In Figure 3.8, it is once again reassuring to see that the estimates (and their imposed limits) given by the incomplete triplets seem to cluster with those predicted by the confirmed and tentative triplets.

3.5.1 Caveats

We outline three caveats to this study and to the results obtained that should be kept in mind when interpreting findings involving the RPM.

Firstly, assuming the correctness of the RPM, the most obvious source of biases in our spin and mass measurements resides in the QPO classification - given the intrinsic difficulty in classifying NS QPOs (NS PDSs are more complex than those of BHs, and QPOs are less clearly discernible), it is possible that some of our triplets involve QPOs that are not HBO-like QPOs. This implies that they could return untrustworthy results. Furthermore, as mentioned in Section 3.5, it is possible that incorrectly classified kHz QPOs in incomplete triplets could lead to further erroneous results.

Secondly, the RPM constitutes a simplified model of what is a certainly more complex behaviour of an ensemble of particles, like the accretion flow is. A more accurate description of the origins of QPOs around compact objects is perhaps given by the rigid precession model (Ingram et al., 2009), which is still a work in progress and is itself currently limited to LF QPOs. The RPM, however, is a good approximation of the rigid precession model (see Section 3.2) when used with QPOs produced close to the ISCO (see Motta et al. 2018). Therefore, assuming that our triplets all consist of correctly classified QPOs, it might be possible that our results are flawed by the use of QPOs produced far from the ISCO. Indeed, we show that proximity to the ISCO has a visible effect on our estimates (see Figure 3.7).

Finally, it is of course possible that neither the RPM nor the rigid precession model constitute good descriptions of the real properties of the accretion flow (see Section 3.6). Further investigations will clarify this point, however we are

inclined to believe that this will not be the case, given that these models successfully describe observational facts in a quantitative way and in a number of different contexts (Stella and Vietri, 1999; Ingram and Done, 2010; Ingram and Motta, 2014; Motta et al., 2014a,b).

3.6 Testability and Falsifiability

The main method of testing the RPM based on the analysis presented here, is to determine whether the model predicts physically realistic estimates for the mass and spin of the NS LMXB 4U1608-52. For our work here, this translates to ascertaining whether QPO triplets, as prescribed by the RPM (see Section 1.5.8), results in NS mass and spin estimates in the range $\sim 0.35 < M/\mathrm{M}_\odot < 2.75$ and $0.07 < a < 0.55$ — see Section 3.4 for the calculation and reasoning behind these limits, and specifically Figure 3.6 for a visualisation of the physically realistic regions of parameter space. In order to falsify the RPM in the context of our analysis it is therefore necessary to find triplets consisting of correctly classified QPOs that result in mass-spin estimates falling outside the possible region of parameter space allowed by standard theories of GR. If mass-spin estimates are found outside this region, it would bring into question either the RPM or GR itself, and given current tests of GR, the issue would most likely lie with the RPM.

To avoid the possibility that a single triplet falling in an unphysical region of parameter space is in fact due to, for example, different physical processes (e.g. a doublet of correct QPOs, and a third QPO due to a noise process), and therefore lead to misinterpretation, one would need several predictions from triplets falling in physically unrealistic parameter ranges in order to obtain a statistically robust prediction. In other words, to falsify the RPM in this regard, the model needs to predict mass-spin estimates in a physically unrealistic region of parameter space through the use of many different triplets from different sources.

Our analysis of 4U1608-52 uncovered one triplet falling in an unphysical parameter space at the $1\,\sigma$ error level: using the tentative triplet in observation 70059-03-02-01 (see Table C.1), the RPM predicts a NS mass of $3.1 \pm 0.2\,\mathrm{M}_\odot$ and a

spin of 0.40 ± 0.05 (see Table 3.1). While the spin estimate falls within a physically realistic range, the mass estimate falls above such a range at the $1\,\sigma$ level. Although close, this estimate still falls within the physically acceptable parameter range shown in Figure 3.6 at the $3\,\sigma$ level, and so is not cause for concern just yet. Furthermore, we chose to ignore this data point in our analysis as, apart from being a tentative triplet (and therefore more uncertain than our confirmed triplets), it also contained kHz QPOs with Q-factors significantly higher than other triplets we used. We therefore marked it as having a low probability of being real (see Section 3.4.2).

By refining our analysis, it would be possible to determine with more certainty whether this triplet constitutes a 'confirmed' triplet or not. However, even in such a case, and even if it falls outside physically acceptable parameter space at the $3\,\sigma$ level, one triplet alone would constitute poor proof of a falsification of the RPM. To rule out a scenario where such a triplet is in fact due to more than one physical process (as mentioned above), one would need the model to predict mass-spin estimates in a physically unrealistic region of parameter space using many triplets from different sources. This can be done by, in the future, carrying out the analysis done here on more NS LMXB sources, and ascertaining whether their RPM triplets predict physically realistic estimates of NS mass and spin.

Another test with which to falsify the RPM is to see whether its mass-spin predictions are consistent with one another. When inspecting Figure 3.6, for example, it is clear that our use of the RPM on the triplets of 4U1608-52 results in inconsistent estimates in the NS mass-spin parameter space, even though said estimates mostly cluster together (Section 3.5 details why the outlier data points were ignored).

Here it is necessary, however, to note the uncertainties we introduce to our analysis, and the uncertainties inherent to the model. The RPM assumes all three QPOs in a triplet to be emitted simultaneously at the same radius r. In our analysis, we therefore made the assumption that QPOs seen in the same averaged PDS occurs simultaneously and at the same radius. This, however, introduces uncertainties: our averaged PDS contain information from observations of up to 12000 s in length, meaning the QPOs that are seen in a PDS might not have happened at the same

time, or at the same radius. Furthermore, even in the case where all QPOs seen in a PDS happen simultaneously at the same radius, QPOs are known to move in frequency over time, and the PDS therefore shows only the average QPO centre frequency. Finally, as mentioned in Section 3.5.1, possible classification errors and the use of QPOs produced too far from the ISCO will lead to further uncertainties.

If the above uncertainties introduced by the analysis could be lessened to an agreeable extent, one is still left with the fact that the RPM is a very oversimplified model of what is a much more complex system (see the second caveat mentioned in Section 3.5.1). In this case, inconsistencies in estimates would be an indication that the model and its assumptions are too simplified to predict precise mass-spin estimates, and needs to be further refined and adjusted (see for example the discussion regarding the rigid precession model in the caveats in Section 3.5.1).

Given the limitations inherent to our analysis outlined above and in Section 3.5.1, we conclude that it is not fully within the scope of the work in this Chapter to use these inconsistencies as a test with which to possibly falsify the RPM. However, obtaining inconsistent results in follow-up analyses, where attempts are made to lessen and remove some of the analysis uncertainties (as outlined), would be an indication that the model is too simplified (or potentially wrong) and needs adjustments.

Further analysis is therefore necessary to determine whether these inconsistencies hold — in the meantime, the fact that our results cluster together (see the discussion in Section 3.5) is a positive indication that there is truth to the model, and the inconsistencies point towards the possibility that a more refined version of the model is needed.

3.7 Summary and Conclusions

We have analysed all the available RXTE/PCA data on the NS LMXB 4U1608-52 and produced the light curve, the HID and the frequency-rms diagrams for the LF QPOs and kHz QPOs found in the data. The HID shows the hysteresis patterns that we typically expect for atoll sources, along with bright soft-state

excursions that reach "bright atoll" luminosities. The frequency-rms diagrams show the characteristic tracks associated with HBO-like QPOs and upper and lower kHz QPOs in the literature. We found in total 9 confirmed QPO triplets, 15 tentative triplets and seven incomplete triplets with which to test the RPM.

By solving the RPM using the triplets we found, we obtained a set of spin-mass estimates, which mostly cluster in ranges of $0.19 < a < 0.35$ and $2.15 < M/\mathrm{M}_{\odot} < 2.6$, well within the physically allowed spin and mass limits determined based on the NS EoSs. While our spin and mass estimates are not fully consistent, we identified and discussed reasons for the presence of both scatter in our estimates and the presence of outliers. In particular, we showed that these values tend to increase with proximity to the ISCO as the RPM becomes an increasingly good approximation of the real behaviour of matter in proximity to the NS for decreasing radii. If our estimates are correct, 4U1608-52 would be one of the heaviest NSs known to date. Our results would rule out some of the more exotic models of the EoS.

We plan to extend this study to include a larger set of sources in order to better test the RPM on NS systems.

When shall we three meet again, in thunder, lightning, or in rain?
When the hurlyburly's done, when the battle's lost and won.

Shakespeare, Macbeth

4

Very low-frequency oscillations from the 11 Hz pulsar in Terzan 5: frame-dragging back on the table.

4.1 Abstract

This chapter consists of a re-analysis of 47 Rossi X-ray Timing Explorer observations of the 11 Hz accreting pulsar IGR J17480-2446 in Terzan 5 during its 2010 outburst. The fast time-variability properties of the source were studied to search for quasi-periodic oscillations (QPOs) in a large frequency range. General Relativity predicts that frame-dragging occurs in the vicinity of a spinning compact object and induces the precession of matter orbiting said object. The relativistic precession model predicts that this frame-dragging can be observed as QPOs with a characteristic frequency in the light curves of accreting compact objects. Such QPOs have historically been classified as horizontal branch oscillations (HBOs) in neutron star systems, and for a neutron star spinning at 11 Hz these oscillations are expected at

The work here has been published in the Monthly Notices of the Royal Astronomical Society as du Buisson et al. (2021); doi: 10.1093/mnras/stab422, and has been adapted for use here as a chapter.

frequencies below 1 Hz. However, previous studies of IGR J17480-2446 have classified QPOs at $35-50$ Hz as HBOs, thus casting doubts on the frame-dragging nature of such QPOs. Here the detection of 7 very low-frequency QPOs is reported. These very low-frequency QPOs were previously undetected, have centroid frequencies below 0.3 Hz, and can be ascribed to frame-dragging. The possible nature of the QPOs detected at $35-50$ Hz in this alternative scenario is also discussed.

4.2 Introduction

The relativistic precession model (RPM, see Section 1.5.8), originally proposed by Stella and Vietri (1998), considers the motion of matter orbits slightly tilted with respect to the spin of a compact object, and associates such motions to specific types of QPOs visible in the PDS (see Section 1.5.8). In particular, the nodal precession ascribed to the motion of matter related to the frame-dragging occurring around spinning compact objects - known as the Lense-Thirring effect (LT, Bardeen and Petterson 1975, see also Section 1.2.3) - is associated to the HBO and HBO-like QPOs observed in NS LMXBs. The precession of the elliptical orbit's semi-major axis - the periastron precession - and the orbital frequency are instead associated to the lower and upper kHz QPOs, respectively.

The RPM has been used to interpret QPOs in both NS (Stella and Vietri, 1999; Ingram and Done, 2010; du Buisson et al., 2020) and BH systems (Motta et al., 2014a,b). A remarkable exception is however represented by a NS LMXB located in the stellar system Terzan 5, the 11 Hz accreting pulsar[1] IGR J17480-2446, which seems to show QPOs that cannot be explained in terms of LT precession (Altamirano et al. 2012, ALT2012 from here onwards). ALT2012 analysed the fast-time variability of the source using data from the Rossi X-ray Timing Explorer (RXTE), and found LF QPOs in the range $\sim 35-50$ Hz in 6 observations, and kHz QPOs in the range $\sim 800-920$ Hz, which in some cases appeared simultaneously with the LF QPOs. These authors classified the LF QPOs as HBOs, and showed that

[1] A pulsar is a rapidly rotating neutron star whose high magnetic fields result in the emission of beams of electromagnetic radiation from its magnetic poles.

given the slow spin rate of the NS in the system, they could not be interpreted as the effect of LT precession, which should instead result in QPOs at frequencies strictly below 0.82 Hz, which were however not detected. These findings thus cast doubt on the LT interpretation of HBOs in NS LMXBs and, by extension, on the RPM.

In this chapter the results of a new analysis of the RXTE observations of IGR J17480-2446 during its 2010 outburst is presented. We systematically searched for QPOs at very low frequencies in the data from the RXTE/PCA (see Section 1.6.4) in order to reassess the presence or absence of HBOs. We also searched for QPOs at up to a few thousand hertz in order to reproduce the findings by ALT2012 and allow a direct comparison to be made.

The chapter is structured as follows: Section 4.3 provides background information on IGR J17480-2446, Section 4.4 details our sample selection and data analysis, and Section 4.5 describes our results. In Section 4.6, an independent test of the significance of the claimed VLF QPO detections were carried out by conducting a search for the same QPOs in a different source – 4U1608-52. In Section 4.7 we discuss our results, and Section 4.8 summarises and concludes the chapter. The necessary background on the RPM can be found in Section 1.5.8.

4.3 Background on IGR J17480-2446

The transient NS LMXB IGR J17480-2446 was first detected by the International Gamma-Ray Astrophysics Laboratory (INTEGRAL) on the 10^{th} of October 2010 (Bordas et al., 2010) in the complex dense stellar system Terzan 5 located roughly 5.9 ± 0.5 kpc away in the Galactic bulge (Lanzoni et al., 2010). Terzan 5 was thought to be an ordinary globular cluster (although very millisecond-pulsar dense) until the discovery that it comprised of two distinct stellar populations differing in metallicity (Ferraro et al., 2009; Origlia et al., 2011; Massari et al., 2012), with another minor third metallicity population having since been discovered (Origlia et al., 2013; Massari et al., 2014), stretching the internal metallicity range of the stellar system to over more than 1 dex. Ferraro et al. (2016) determined the age of the two main stellar populations as 12 Gyr (for the dominant sub-solar metallicity

population) and 4.5 Gyr (for the component at super-solar metallicity), giving Terzan 5 a similar age distribution and chemical abundance pattern as the Galactic bulge, and opening the possibility of it being a fossil relic of one of the structures that contributed to the bulge's formation (see also Ferraro et al. 2020). It contains roughly 25% of the entire pulsar population so far identified in globular clusters, and three known NS LMXBs (Cadelano et al., 2018; Bahramian et al., 2014).

The first detection of IGR J17480-2446 was initially attributed to the known LMXB transient EXO 1745-248, until follow-up Swift observations refined the position of the source, severing its connection to EXO 1745-248. A Chandra observation then further confirmed this (Pooley et al., 2010). Subsequent RXTE observations of the source showed coherent pulsations at 11 Hz and the presence of thermonuclear Type-I X-ray bursts, burst oscillations locked with the pulsations, and lunar occultations (Altamirano et al., 2010b; Strohmayer and Markwardt, 2010; Strohmayer et al., 2010; Chenevez et al., 2010; Chakraborty and Bhattacharyya, 2011; Linares et al., 2011; Motta et al., 2011). The first Type-I X-ray burst from this source was observed by the RXTE on the 13^{th} of October during its 2010 outburst (Strohmayer and Markwardt, 2010). Interestingly, recurrent bursts followed for the next few days (Altamirano et al., 2010a; Papitto et al., 2011) - as source intensity increased, burst frequency increased while burst fluency decreased, until the bursts disappeared only to reappear again in decreasing frequency and increasing burst fluency as the source intensity decreased (Chakraborty and Bhattacharyya, 2010; Motta et al., 2011); mHz QPOs associated to these bursts have also been found (Altamirano et al., 2010a; Linares et al., 2010). The timing analysis of the pulse period revealed an orbital period of roughly 21 hours (Strohmayer et al., 2010), and the companion star mass was constrained to $0.41 - 1.5$ $M_{\odot}$ (Papitto et al., 2011). The magnetic field of IGR J17480-2446 has been constrained to $\sim 10^8 - 10^{10}$ G (Miller et al., 2011; Cavecchi et al., 2011; Papitto et al., 2011).

With a period of ~ 90 ms, IGR J17480-2446 was the first detected accreting millisecond X-ray pulsar with a period in the $10 - 100$ ms range (typical millisecond X-ray pulsars have spin frequencies of the order of several hundreds Hz). As

IGR J17480-2446 exhibits properties in between those of the other known slow accreting millisecond pulsars and those of faster millisecond pulsars (e.g. the fact that its spin frequency and magnetic field strength lies in between the ranges populated by the two groups, and the fact that it is a slow millisecond X-ray pulsar showing thermonuclear bursts - usually a property of faster millisecond pulsars), Patruno et al. (2012) concluded that IGR J17480-2446 is most likely a mildly recycled pulsar that has started a spin-up phase exceptionally recently. The source is one of the only two that has been seen to move from the atoll to the Z-phase (Altamirano et al., 2010a), the other being XTE J1701-462 (Homan et al., 2010).

4.4 Observations and Data Analysis

We analysed all publicly available archival RXTE observations of the 11 Hz accreting pulsar IGR J17480-2446 during its 2010 outburst, consisting of 47 observations. All observations had source count rates above 10 cts/s/PCU[2], ensuring adequately high signal to noise ratios (SNR) for the subsequent analysis.

For each observation we considered Binned, Event, Single Bit and Good Xenon PCA data modes (Jahoda et al., 1996; Bradt et al., 1993) and calculated the PDS using a custom software under IDL[3]. We used a maximum time resolution of 1/8192 s ($\sim 122\,\mu s$), and divided each observation into segments of both 16 s and 512 s, respectively, for average PDS production (see *Case 1* and *Case 2* below). We excluded from the analyses in *Case 1* and *Case 2* short observations which contained fewer than 5 such segments (as they would provide poor SNR), and we averaged the Leahy-normalised PDS created from each segment to produce one averaged PDS per observation with a Nyquist frequency of 4096 Hz, or two or more average PDS in the case of observations longer than 12000 s. We did not subtract the contribution of the Poisson noise *a priori*, but fitted it when modeling the PDS. We note that observation 95437-01-01-00 contains a lunar eclipse which was cut from the observation before any further analysis (Motta et al. 2011, Riggio et al. 2012). In

[2]PCU: Proportional Counter Unit
[3]GHATS: `http://www.brera.inaf.it/utenti/belloni/GHATS_Package/Home.html`

cases of sudden drops in an observation's count rate (usually towards the beginning or end of an observation) that can be ascribed to the re-pointing of the satellite, the beginning/end of an observation is clipped away to prevent the inclusion of low-quality data. It should be noted that all data gaps are removed prior to any FFT being carried out. Our method of PDS production differed depending on the type of QPO we were attempting to detect, as described in *Case 1* and *Case 2* below.

We also computed the HID for the 47 observations of IGR J17480-2446 we consider here (see Figure 4.6). The count rates necessary for the computation of the HID were obtained using energy spectra extracted from STANDARD 2 data, and only using PCU unit 2 as it was operational during the entire RXTE mission, and never showed particular problems. For each observation, the source intensity was measured in the $2-16$ keV energy band, while the hardness was calculated as the ratio of counts in two energy bands as $H_{\rm HID} = A/B$, where A stretches between $6-10$ keV and B stretches between $4-6$ keV (STANDARD 2 channels 6-9 and 11-19, respectively).

4.4.1 Case 1: Searching for very low-frequency QPOs

Following the prescriptions of the RPM, ALT2012 calculated that the HBO QPO of IGR J17480-2446 should fall strictly below 0.82 Hz. In order to detect such very low-frequency (VLF) QPOs, it is necessary to calculate PDS with a frequency resolution of 0.08 Hz or better. We therefore divided our observations into segments of 512 s, from which we calculated PDS with a frequency resolution of 1/512 Hz ~ 0.002 Hz, sufficient for the task at hand.

The observations of IGR J17480-2446 contain, however, a large number of Type-I X-ray bursts (see Motta et al. 2011). These bursts have a soft, thermal spectrum, but their short recurrence times (down to about 200s) introduces quasi-periodic variability in the light curve that can take the form of a QPO in the PDS (in this case generated from the NS surface) that is not easily distinguishable from other (accretion-driven) types of QPOs, thereby obstructing the process of finding VLF QPOs. The short Type-I X-ray burst recurrence time implies that - in most cases -

cutting the bursts out of our observations leaves too little data for an appropriate analysis. In other words, apart from for a few cases, it was impossible to recover data stretches long enough to reach the frequency resolution needed for our analysis.

We therefore instead performed an energy selection on our data, considering only photons in higher energy bands. In order to select bands that sufficiently removed Type-I X-ray bursts, we applied the following cuts to the entire dataset and inspected the resulting light curves:

- $0 - 120$ keV (absolute PCA channels $0 - 249$)
- $8 - 120$ keV (absolute PCA channels $20 - 249$)
- $10 - 120$ keV (absolute PCA channels $25 - 249$)
- $12 - 120$ keV (absolute PCA channels $30 - 249$)
- $15 - 120$ keV (absolute PCA channels $35 - 249$)
- $17 - 120$ keV (absolute PCA channels $40 - 249$).

An example of the effect of the above energy cuts on an observation's light curve can be seen in Figure 4.1. From this assessment, it was found that cuts associated to the $15 - 120$ keV and $17 - 120$ keV bands adequately removed the Type-I X-ray bursts. We finally decided to use the $15 - 120$ keV band (absolute PCA channels 35 to 249) to derive our PDS, as this still allowed for a high enough S/N in the PDS for the subsequent analysis. We also note that the accretion-driven aperiodic and quasi-periodic variability tend to have a hard spectrum (e.g., Sobolewska and Życki 2006), which implies that our strategy effectively reduces the number of soft, non-variable photons, thus emphasising the remaining variability - QPO significance is therefore largely unaffected by the soft energy cuts and the resulting overall decrease in S/N. Following the described strategy, we effectively minimise the contribution of Type-I X-ray bursts in our PDS while retaining possible HBO QPOs.

The recurrence time of the Type-I X-ray bursts in our observations vary between 200 s to well over 500 s, depending on the observation. Their presence could therefore generate peaks in PDS at frequencies smaller than 0.005 Hz. Even though we minimise the contribution of Type-I X-ray bursts by selecting higher energy bands for our analysis, we therefore also conservatively exclude all significant QPO-like

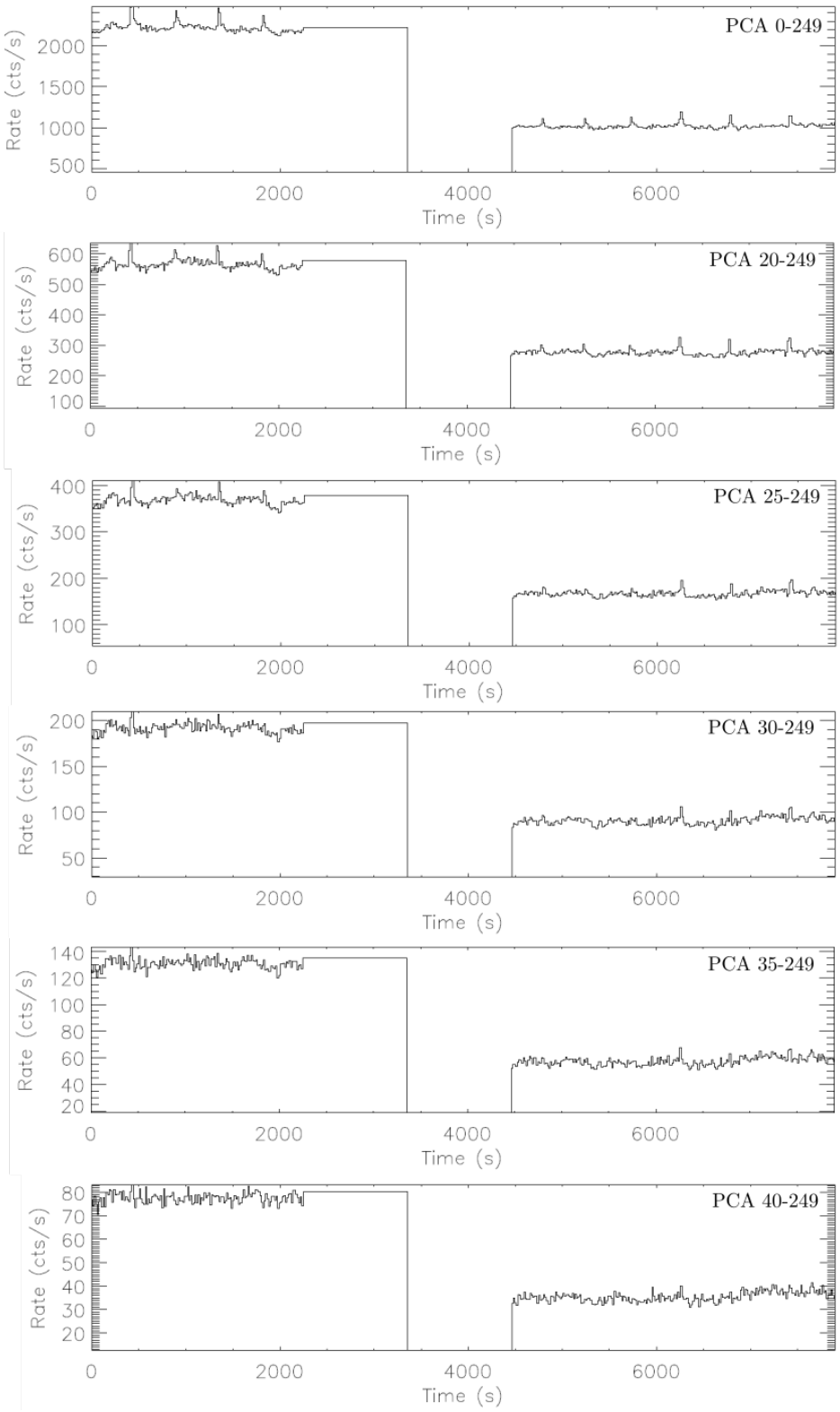

Figure 4.1: The effect of our energy cuts on the light curve of Obs ID 95437-01-10-02. From top to bottom, the cuts are as follows: $0-120$ keV, $8-120$ keV, $10-120$ keV, $12-120$ keV, $15-120$ keV, and $17-120$ keV. Absolute PCA channels used are indicated in the figure.

features falling below 0.009 Hz from our analysis (which could still be due to residual X-ray burst contributions) in order to avoid any possible contamination of our results.

4.4.2 Case 2: Searching for LF QPOs and kHz QPOs

ALT2012 found LF QPOs in the $\sim 35 - 50$ Hz range, and kHz QPOs between ~ 800 Hz and 920 Hz. In order to find these features in the observations considered here, we divided each of our observations into intervals of 16 seconds for the calculation of PDS, resulting in a frequency resolution of 0.0625 Hz. This is preferable to the 512s intervals used for *Case 1*, as the large number of PDS produced in this way is averaged, significantly increasing the SNR. However, it can happen that the averaged PDS from long observations contain broadened features due to the movement of QPOs in frequency as time progresses. For the cases where an observation was longer than 12000s, we split the observation into shorter segments of approximately 3500s in length, and calculated an averaged PDS for each of them, which we fitted individually.

We then investigated three different methods of PDS production to determine which one resulted in the optimal detection of LF QPOs and kHz QPOs. First, we simply derived the PDS using the energy band $\sim 2 - 120$ keV (absolute PCA channels 0 to 249). Next we used the same energy band, but also cut the Type-I X-ray bursts out of observations. The short time intervals used to calculate PDS allowed us to generate a good SNR for the average PDS using the time intervals between consecutive Type-I X-ray bursts. Finally, we produced PDS in the energy band $\sim 15 - 120$ keV (absolute PCA channels 35 to 249) without any burst cuts. The first method presented us with the best results, and it was therefore employed to search for LF QPOs and kHz QPOs.

4.4.3 Power spectral fitting

To find the QPOs present in our dataset, we preselected the PDS of observations that visually contained these features for each of the cases above. The features of each power spectrum were fit with a combination of Lorentzians and a power-law

component (to account for the Poisson noise) by means of the XSPEC package (Arnaud, 1996) by using a one-to-one energy-frequency conversion for our PDS and a unity response matrix. We excluded all non-significant features from the analysis: for very low frequencies (where flat-top noise or red noise were present), this meant excluding features below a significance[4] of 2σ (in order to account for the lower relative frequency resolution); at all other frequencies features had to have a statistical significance of 3σ or higher. QPOs were identified by requiring that a given feature is detected with a significance of 3σ or above, and has a quality factor $Q \geq 2$ (taking uncertainties into account). Here $Q = v_c/\Delta\nu$, where v_c is the center frequency and $\Delta\nu$ the FWHM[5] of the Lorentzian.

Due to the X-ray pulsar nature of the NS in IGR J17480-2446, a very narrow peak corresponding to the 11 Hz pulsation is visible in our PDS (its coherence quantified by a very high Q factor). We do not cut this peak from the PDS - instead, we fit it along with the rest of the features.

4.5 Results

We report in Table 4.1 the VLF QPOs found by carrying out the analysis described in Case 1 and fitting the resulting PDS, as well as the LF and kHz QPOs found through the analysis described in Case 2. We found seven VLF QPOs having center frequencies in the range $\sim 0.01 - 0.03$ Hz, three LF QPOs in the range $\sim 44 - 50$ Hz and three kHz QPOs in the range $\sim 840 - 870$ Hz. The PDS of the seven observations in which VLF QPOs were found are shown in Figure 4.2, and more information on the fitting of the PDS of these seven observations can be found in Appendix F. The frequency ranges of our LF and kHz QPOs fall within those reported by ALT2012. We note, however, that the analysis performed by these authors differed slightly form ours, and a list of the six observations they considered is not available in their work. It is therefore not trivial to determine if and when our detections correspond exactly to those reported in ALT2012.

[4]Significance is calculated as the integral of the power of the Lorentzian used for the fitting of the feature divided by the negative 1σ error on this integral.

[5]FWHM: full width at half maximum

Table 4.1: A list of observations and their QPOs detected. VLF QPOs were found following *Case 1* analysis (see Section 4.4.1), and the PDS of all seven observations found to contain them can be seen in Figure 4.2. VLF QPO observations with a star next to their Obs IDs indicate observations for which significant second harmonics of the VLF QPOs were also found. These are not listed in the table as they do not form part of our analysis, but more detail regarding fit parameters for observations containing VLF QPOs can be found in Appendix F. LF and kHz QPOs were found through *Case 2* analysis (see Section 4.4.2). In the cases where observations were cut into two or more independent segments, an extra digit attached at the end of their observation IDs indicate which segment was used. See the text for more details. All errors reported in this table are $1\,\sigma$ errors.

Obs ID	Frequency (Hz)	Q factor	Significance
VLF QPOs			
95437-01-02-01	$0.0101^{+0.0011}_{-0.0008}$	1.9 ± 0.7	$4.3\,\sigma$
95437-01-10-05	$0.010^{+0.002}_{-0.001}$	1.6 ± 0.8	$6.2\,\sigma$
95437-01-11-03	0.016 ± 0.002	2 ± 1	$3.2\,\sigma$
95437-01-11-06*	0.020 ± 0.001	4 ± 1	$3.9\,\sigma$
95437-01-12-04*	0.0175 ± 0.0006	5 ± 2	$4.2\,\sigma$
95437-01-13-04	0.029 ± 0.002	3 ± 1	$3.8\,\sigma$
95437-01-14-00	0.014 ± 0.002	2 ± 1	$3.2\,\sigma$
LF QPOs			
95437-01-07-00	47.5 ± 0.5	3.2 ± 0.4	$11.9\,\sigma$
95437-01-08-00-1	$49.2^{+0.8}_{-0.9}$	5 ± 2	$4.8\,\sigma$
95437-01-09-00	44.7 ± 0.6	5 ± 1	$6.9\,\sigma$
kHz QPOs			
95437-01-07-00	840^{+13}_{-11}	12 ± 5	$3.3\,\sigma$
95437-01-09-00	854 ± 4	22 ± 8	$4.9\,\sigma$
95437-01-10-01	870^{+6}_{-7}	21 ± 10	$3.7\,\sigma$

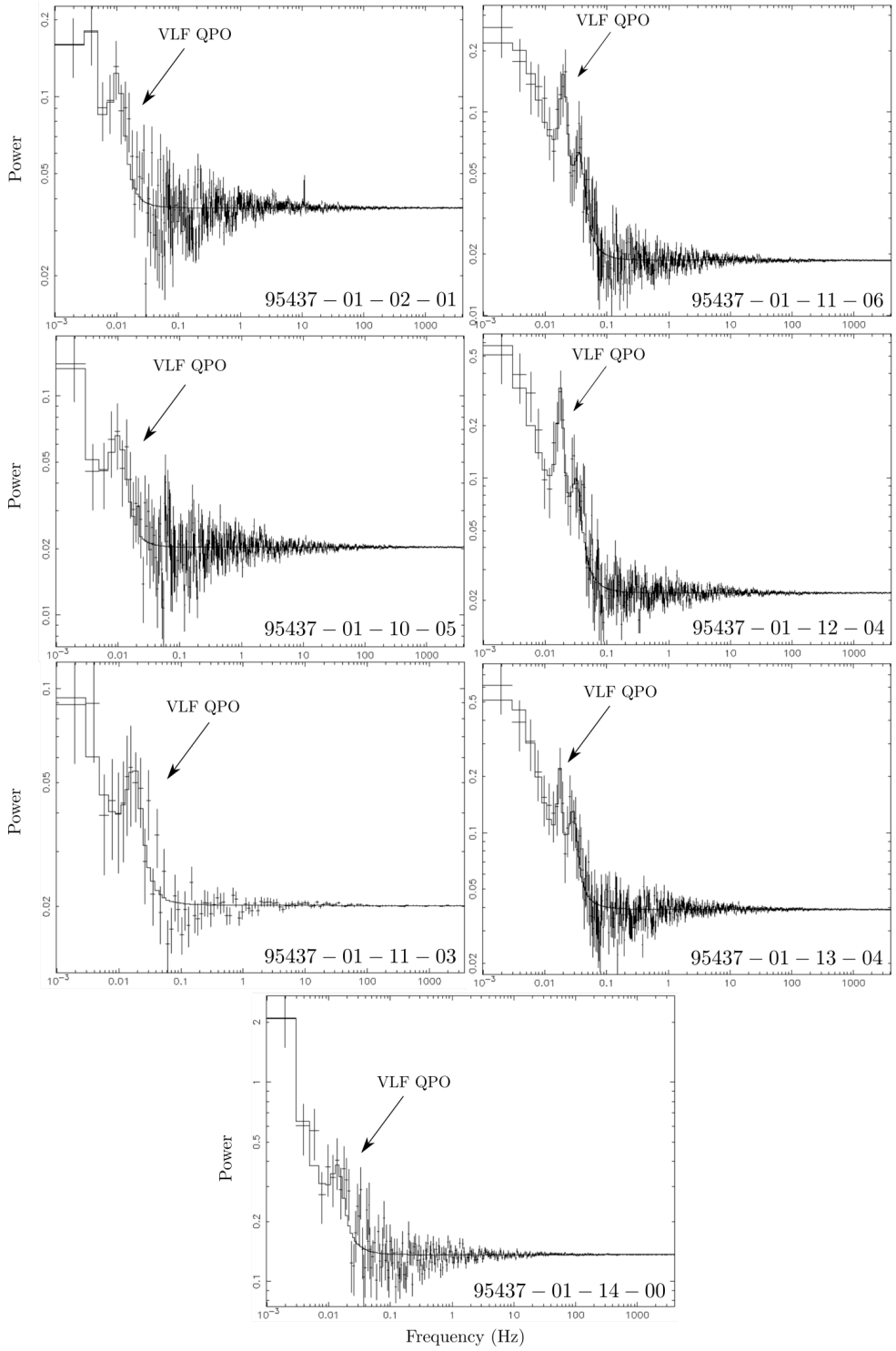

Figure 4.2: The PDS of the seven observations in which VLF QPOs were found (see Table 4.1), with Obs IDs indicated at the bottom right of each spectrum. The second, smaller peak in the PDS of both Obs IDs 95437-01-11-06 and 95437-01-12-04 is most likely the second harmonic of the first peak - the first peak is therefore regarded as the VLF QPO in both observations, and documented as such in Table 4.1. The second peak in Obs ID 95437-01-13-04 has a significance less than 3σ, and so is not regarded as a QPO (see Section 4.4.3). Its VLF QPO is the first peak, and is documented as such.

To show the effect of the energy cut used in Case 1 (see Section 4.4.1), the PDS of four of the observations in which we find VLF QPOs are shown before and after the cut was made. This can be seen in Figure 4.3, where the fitted PDS on the right (after application of the energy cut) are the same ones shown in Figure 4.2. We further note that for the observations in which VLF QPOs were found, the recurrence times for Type-I X-ray bursts were all > 670 s - this would translate to a peak (if any) in the PDS at < 0.0015 Hz. Our conservative exclusion of all significant QPO-like features below 0.009 Hz from our analysis (see Section 4.4.1) is therefore sufficient in that no mHz QPO (or its second harmonic) caused by Type-I X-ray bursts in our analysis can fall in the frequency range used for finding VLF QPOs in the observations where they were found.

In order to compare the quasi-periodic features we detected with the predictions of the RPM, we used the RPM equations given in Motta et al. 2014a (see also Section 1.5.8) to plot the theoretical estimates of $\nu_{\rm nod}$, $\nu_{\rm per}$ and ν_{ϕ} as a function of the emission radius r. We used the measured spin frequency $\nu = 11$ Hz of the source, and calculated the minimum and maximum dimensionless spins (a_{min} and a_{max}) using the definition $a = (cJ)/(GM^2)$ (see Section 1.5.8) and assuming a minimum and maximum moment of inertia for the NS (I_{min} and I_{max}), respectively. To do so, we followed Mukherjee et al. 2018 (their figure is shown here in Figure 4.4), which shows the moment of inertia as a function of different NS masses inferred for a number of realistic candidate NS equations of state (EoSs). We found $I_{min} = 0.75 \times 10^{45}$ g cm^2 for a NS mass of $M_{min} = 1.0$ M$_{\odot}$, and $I_{max} = 5 \times 10^{45}$ g cm^2 for a mass of $M_{max} = 2.7$ M$_{\odot}$. We then calculated the minimum and maximum dimensionless spin parameters a_{min} and a_{max}, to find $0.0054 \leq a \leq 0.0059$. Next, we used Equations 9, 6 and 1 in Ingram and Motta (2014) to determine the minimum and maximum theoretical estimates of $\nu_{\rm nod}$, $\nu_{\rm per}$ and ν_{ϕ} as a function of the emission radius r, assuming first a_{min} and M_{min}, and then a_{max} and M_{max}. Our result is displayed in Figure 4.5, where we also marked the frequency ranges where we detected QPOs in our data.

The HID for our data is shown in Figure 4.6, showing the source count rate and hardness of each observation in our analysis. Consecutive observations are connected

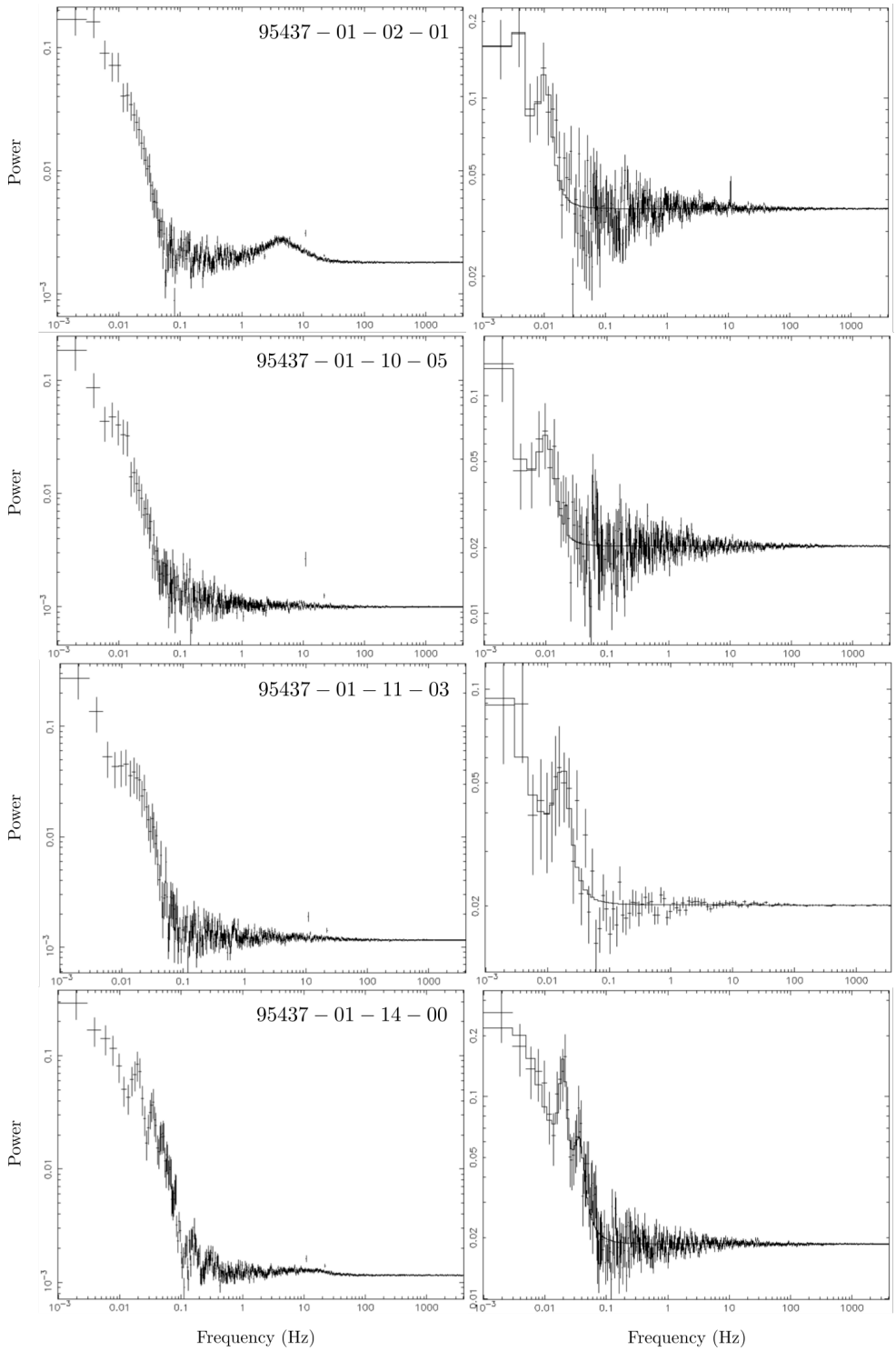

Figure 4.3: The PDS of four observations in which VLF QPOs were found (see Table 4.1), both before (left panel) and after (right panel) the energy cut for the Case 1 analysis were made (see Section 4.4.1). Obs IDs are given on the left panel for each pair of PDS.

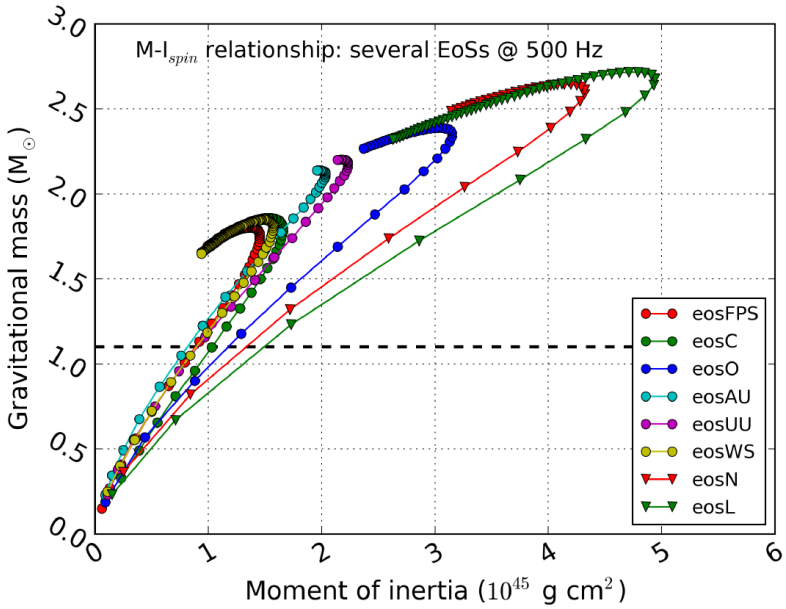

Figure 4.4: The mass M vs. the moment of inertia along the spin-axis I_{spin} for different realistic NS EoSs. Plausible values for the mass of a NS lies between $\sim 1.0\,M_\odot$ and the maximum mass allowed by the particular EoS under investigation. This figure has been taken from Mukherjee et al. (2018).

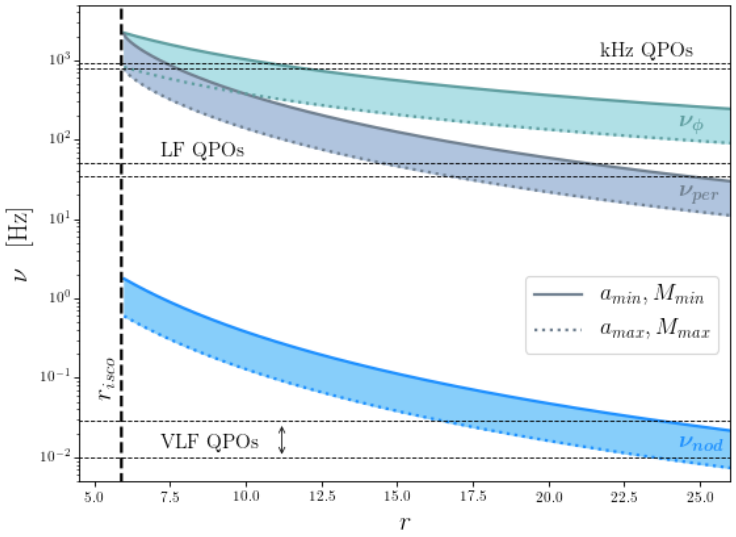

Figure 4.5: The minimum and maximum theoretical values of $\nu_{\rm nod}$, $\nu_{\rm per}$ and ν_ϕ as a function of the emission radius r for IGR J17480-2446, inferred using the RPM. Coloured lines indicate the maximum and minimum predicted values, respectively. Straight horizontal dashed lines mark the frequency ranges in which QPOs were found.

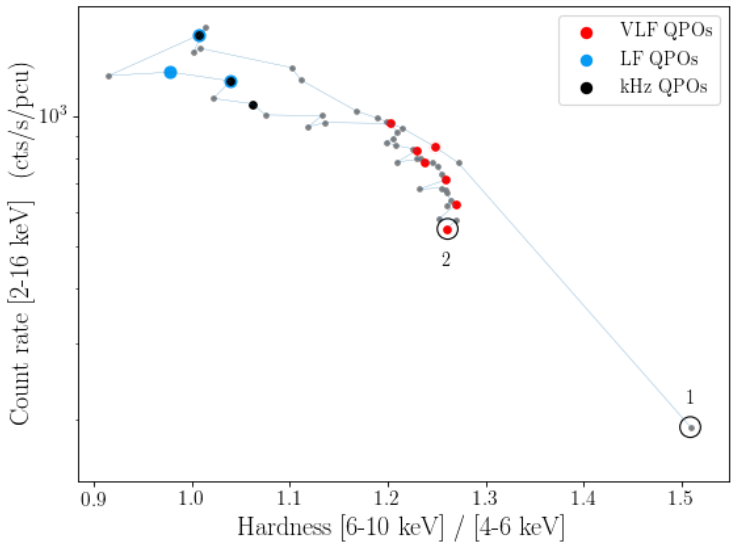

Figure 4.6: The HID of IGR J17480-2446, where the source count rate is plotted against the spectral hardness. Each data point represents an observation, and consecutive observations are connected. The first and last observation considered are marked on the plot and denoted by the numbers 1 and 2, respectively. Red observations contain VLF QPOs, light blue observations contain LF QPOs and black observations contain kHz QPOs (see also Table 4.1). A colour version of this figure is available online.

via thin lines, with the earliest and latest observations circled and numbered as 1 and 2, respectively. Red data points indicate observations containing VLF QPOs, light blue observations contain LF QPOs and black observations contain kHz QPOs (note that in two cases LF QPOs and kHz QPOs are detected simultaneously). VLF QPOs are detected both at the beginning and at the end of the outburst, in a hard state, while LF QPOs and kHz QPOs are found in a relatively soft state, close to the peak of the outburst which, according to Motta et al. (2011), reached and possibly crossed the Eddington limit.

4.6 Searching for VLF QPOs in 4U1608-52

In order to carry out an independent test on the significance of the claimed detections of VLF QPOs in the 11 Hz pulsar IGR J17480-2446, we next conducted a search for such low-frequency QPOs in the data of a source with a higher spin: we

looked for QPOs falling in the $10 - 100$ mHz range in the data of 4U1608-52, used also for analysis in Chapter 3.

4.6.1 Observations and Data Analysis

We analysed the publicly available archival RXTE PCA data on the NS LMXB 4U1608-52, excluding all observations with source count rates below 10 cts/s/PCU in order to ensure adequately high signal-to-noise ratios. As before, we considered Binned, Event, Single Bit and Good Xenon PCA data modes (Jahoda et al., 1996; Bradt et al., 1993), and calculated the PDS using GHATS[6], a custom software under IDL. We used a maximum time resolution of 1/8192 s ($\sim 122\,\mu s$), and divided each observation into segments of 512 s for PDS production – this large time segment results in a PDS frequency resolution of 1/512 Hz ~ 0.002 Hz, a sufficiently high resolution for finding QPOs in the $10 - 100$ mHz range.

We averaged the Leahy-normalised PDS created from each time segment in order to produce one averaged PDS per observation with a Nyquist frequency of 4096 Hz, or two or more averaged PDS in the case of observations longer than roughly 12000 s. In the case of long observations split into shorter independent observations, an extra digit appended to the end of an observation's Obs ID indicates which section of the original observation was used for its creation (similar to the notation used throughout Chapters 3 and the rest of 4). Observations containing fewer than five 512 s segments were excluded from the analysis, as they provide poor signal-to-noise ratios. Poisson noise were not subtracted, but instead fitted when modelling the PDS. In cases of sudden drops in an observation's count rate (usually towards the beginning or end of an observation) due to instrumental issues, the beginning/end of an observation is clipped away to prevent the inclusion of low-quality data. It should be noted that all data gaps are removed prior to any FFT being carried out. Excluding observations that are too short along with those having source count rates below 10 cts/s/PCU, leaves us with 181 observations.

[6]GHATS: `http://www.brera.inaf.it/utenti/belloni/GHATS_Package/Home.html`

Of these 181 observations, 25 contained Type-I X-ray bursts. Instead of cutting them from the observations, as was previously done for the analysis presented in Chapter 3, we opt here instead to remove them in a similar way as was done for IGR J17480-2446 – by applying energy cuts to our data. This ensures that the search for VLF QPOs are carried out in similar ways for both sources, for better comparison of results. Depending on whether an observation contained Type-I X-ray bursts or not, the analysis was carried out as follows:

Group A: Observations containing Type-I X-ray bursts

To remain consistent with the analysis of IGR J17480-2446, we performed an energy selection on the 25 observations containing Type-I X-ray bursts, considering only photons in higher energy bands. In order to select bands that sufficiently removed these bursts, we applied a range of energy cuts and inspected the resulting light curves to ensure sufficient removal. In addition to the energy cuts inspected for IGR J17480-2446 (outlined in Section 4.4.1), we included some additional energy selections, as Type-I X-ray bursts proved more difficult to remove in the case of 4U1608-52. Observations containing bursts fell into the $3^{\rm rd}$, $4^{\rm th}$, or $5^{\rm th}$ RXTE gain epochs[7], and the PCA channel ranges were adjusted for accordingly (see brackets next to each energy band):

- $0-120$ keV (all epochs: PCA $0-256$)
- $8-120$ keV (ep.3: PCA $22-256$; ep.4: PCA $19-256$; ep.5: PCA $20-256$)
- $10-120$ keV (ep.3: PCA $28-256$; ep.4: PCA $24-256$; ep.5: PCA $25-256$)
- $12-120$ keV (ep.3: PCA $33-256$; ep.4: PCA $29-256$; ep.5: PCA $30-256$)
- $15-120$ keV (ep.3: PCA $42-256$; ep.4: PCA $36-256$; ep.5: PCA $35-256$)
- $17-120$ keV (ep.3: PCA $47-256$; ep.4: PCA $40-256$; ep.5: PCA $40-256$)
- $19-120$ keV (ep.3: PCA $52-256$; ep.4: PCA $45-256$; ep.5: PCA $46-256$)
- $21-120$ keV (ep.3: PCA $58-256$; ep.4: PCA $50-256$; ep.5: PCA $51-256$)

[7]RXTE gain epochs: `https://heasarc.gsfc.nasa.gov/docs/xte/e-c_table.html`

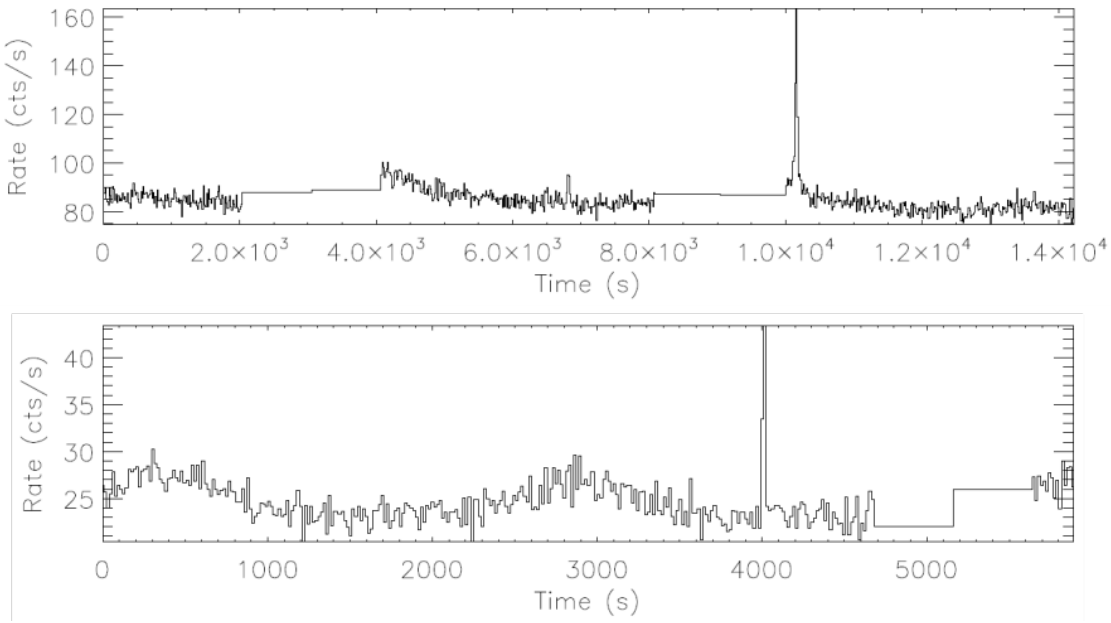

Figure 4.7: Examples of light curves from the 4U1608-52 dataset still containing Type-I X-ray bursts at the $21-120$ keV energy band. **Top:** Observation 60052-03-02-04. **Bottom:** Observation 93408-01-28-06. The sinusoidal modulation is due to the background emission along the satellite's orbit around Earth - it is visible in observations with lower source count rates.

The $15-120$ keV energy band previously used succeeded in removing Type-I X-ray bursts in only three of the 4U1608-52 observations. Further cuts were therefore necessary to obtain a larger number of observations without bursts: at $21-120$ keV, 13 out of the 25 observations were free of bursts, while the rest still contained them (see Figure 4.7 for examples of light curves at $21-120$ keV still containing bursts). Although energy cuts above $21-120$ keV succeeded in removing Type-I X-ray bursts from a progressively larger number of observations, $21-120$ keV were chosen as an acceptable balance between the number of observations cleared of Type-I X-ray bursts and the remaining overall count rate. PDS of the 12 cleared observations were subsequently produced for the analysis, while the remaining 13 were excluded.

Group B: Observations without Type-I X-ray bursts

For the analysis of the remaining 156 observations in our 4U1608-52 dataset, we decided to use the same energy band of $21-120$ keV as determined above. This serves two purposes. First, it ensures consistency with the analysis carried out for

Group A. Second, the observations of 4U1608-52 are known to show evidence of the oscillatory behaviour attributed to marginally stable nuclear burning of He on the NS surface, known to cause mHz QPOs at soft energies below ~ 5 keV (Revnivtsev et al., 2001; Heger et al., 2007; Mancuso et al., 2021). In fact, Mancuso et al. (2021) found such mHz QPOs (which they detected using the $\sim 2-5$ keV interval, where oscillations are found to be the strongest - see Altamirano et al. 2008b) in 49 of the RXTE observations of 4U1608-52, with center frequencies ranging between $\sim 4.2-13.4$ mHz, detected while the source was either in the soft or intermediate state. Excluding soft energies in our analysis by using the $21-120$ keV band, we are therefore prohibiting mHz QPOs caused by marginally stable burning from being present in our PDS and being confused with the VLF QPOs we are looking for, which have harder spectra (see Section 4.4.1).

Power spectral fitting

Power spectral fitting of the PDS produced from Groups A and B was carried out in accordance with what is described in Section 4.4.3 for the fitting of IGR J17480-2446's PDS. As before, a QPO classification required a detection significance of $3\,\sigma$ or above, and a quality factor $Q \geq 2$ (see Section 4.4.3).

4.6.2 Results and discussion

We did not find any peaks satisfying our criteria for QPOs in the $10-100$ mHz range in the PDS of any of the observations in Group A or B.

Significance of IGR J17480-2446 VLF QPO detections: Group A

Group A consists of observations comparable in characteristics to the observations of IGR J17480-2446, in that the observations of both these groups contained Type-I X-ray bursts that had to be removed before producing PDS in order to ensure that any VLF QPOs detected were not in fact due to their presence.

In IGR J17480-2446's *Case 1* analysis (see Section 4.4.1), 43 burst-containing observations were analysed[8] to detect seven VLF QPOs in the $10-100$ mHz range,

[8]Four observations were too short and had to be excluded from the original 47 observations.

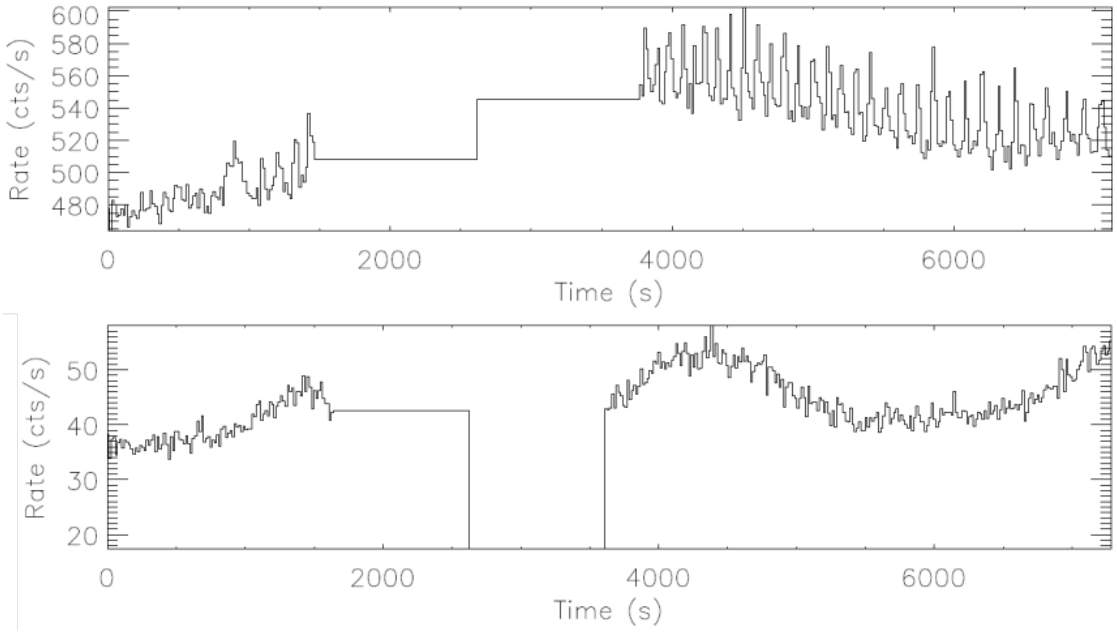

Figure 4.8: An example of marginally stable burning in 4U1608-52. **Top:** The light curve of observation 95334-01-03-06, taken over the entire available energy range. As confirmed by Mancuso et al. (2021), the second orbit shows evidence of marginally stable burning, resulting in them detecting a mHz QPO with a downward frequency drift from ~ 12 mHz to ~ 8 mHz. **Bottom:** The same observation's light curve, this time using the $21-120$ keV energy band. As marginally stable burning is present at soft energies ($\sim 2-5$ keV for this observation, see Mancuso et al. 2021), the higher energy selection of $21-120$ keV removes its presence so that no resulting mHz QPOs due to the phenomenon will be detected in PDS. As in Figure 4.7, the sinusoidal modulation is due to the background emission along the satellite's orbit around Earth, which is visible in observations with lower source count rates.

translating to roughly one VLF QPO detected for every six observations. If we assume that all NS LMXB observations containing Type-I X-ray bursts will present with fundamentally the same characteristics, then their observations should contain VLF QPOs in similar proportions (however see the caveats section below). For 4U1608-52's 12 observations from Group A, this predicts the detection of two VLF QPOs. Instead, we find none.

To determine whether the difference between predicted and observed detections in 4U1608-52 is adequately significant, we assume a Poisson distribution and take the predicted number of detections (i.e. two) as the mean (and therefore also as the variance) – the standard deviation is therefore given by $\sqrt{2}$. Calculating whether the observed detections fall further than three standard deviations (i.e. a

$3\,\sigma$ significance) from the predicted value, we find that the difference divided by the standard deviation, i.e. $2/\sqrt{2}$, is $1.41\,\sigma$. The difference between the predicted and observed VLF QPOs in the burst-containing observations of 4U1608-52 is therefore not indicative of a meaningful difference between it and IGR J17480-2446.

Significance of IGR J17480-2446 VLF QPO detections: Group A + B

Alternatively assuming that all NS LMXBs are fundamentally the same (regardless of whether bursts are present or not), we can include all 168 observations used in the analysis of 4U1608-52 (156 observations from Group B and 12 from Group A) in the assessment of significance. The predicted number of VLF QPO detections for 4U1608-52 then becomes 28, while the observed detections are still zero. Repeating the above calculations to determine whether the observed detections in 4U1608-52 fall further than three standard deviations from the predicted detections, we find $28/\sqrt{28} = 5.3\,\sigma$, indicative of a statistically significant difference between it and IGR J17480-2446.

Caveats

The analysis presented here is limited in many ways, all having possible implications for the resulting calculated significances:

1. Implicit in the above analysis are the assumption that the overall quality characteristics (e.g. the signal-to-noise ratio) of the observations are similar, regardless of whether they are from 4U1608-52 or IGR J17480-2446. This includes, for example, our assumption that observations are of comparable length, or that the differences in their lengths or the intrinsic luminosities of the different sources do not lead to any significant differences in the signal-to-noise ratios of the PDS estimates. This also includes our assumption that the different energy bands chosen for 4U1608-52 and IGR J17480-2446 ($15 - 120$ keV and $21 - 120$ keV, respectively), do not introduce any significant quality differences between the observations of the respective sources.

2. As IGR J17480-2446 and 4U1608-52 are variable sources, another important assumption we make is that the duty cycle of both sources are the same, where the 'duty cycle' here refers to the fraction of a source's observations taken during a time of its outburst cycle when VLF QPOs would be present. In other words, we assume that the physical conditions which create these VLF QPOs happen with the same probability in both sources. Clearly this need not be the case, in which case our lack of VLF QPOs in 4U1608-52 simply means that the frequency with which these events happen, if they do indeed happen, is much less frequent than in IGR J17480-2446.
3. An important limitation to this independent test is that it was only carried out on one source - 4U1608-52. Using more sources and more observations that span a wider range of physical properties and signal-to-noise ratios would make our findings more robust, and could potentially remove the two caveats above.

Discussion

What do our results mean? For the calculation involving only Group A, the analysis suffers from having a very low number of observations to use (i.e. 12), and the results likewise suffers in robustness. We therefore here consider the results of the calculation involving both Groups A and B, where the significance was found to be $5.3\,\sigma$ - an indication that the difference between predicted and observed VLF QPOs is significant. This, however, can mean one (or more) of three things:

1. That 4U1608-52's VLF QPO duty cycle is significantly lower than that of IGR J17480-2446, such that far fewer VLF QPOs should actually be predicted when that is taken into account.
2. That the VLF QPOs in 4U1608-52 have lower signal-to-noise ratios (due to, for example, any of the reasons mentioned in the Caveats section). This would make them harder to detect, and would explain their absence in the observations of 4U1608-52.
3. That 4U1608-52 and IGR J17480-2446 are intrinsically different in a way that allows one to have VLF QPOs, but not the other.

The conclusion, therefore, is that although there is a significant difference between the number of VLF QPO detections in IGR J17480-2446 and 4U1608-52, i.e. at the $5.3\,\sigma$ level, this could mean a number of different things, including an intrinsic difference between the sources, a difference in the duty cycle of such VLF QPOs, or a difference in data quality. For a more robust independent test, the assumptions and limitations outlined should be better constrained, and a larger number of sources and observations should be included in the analysis. As this falls outside the scope of the work for this thesis, this is left for future studies.

4.7 Discussion

Based on the assumption that all types of QPOs, both in NS and in BH systems, should show at least a mild dependence on the spin of the compact object, we hypothesised that given the very low spin of IGR J17480-2446 (11 Hz, i.e. over an order of magnitude smaller than the average spin of accreting NSs, see van Doesburgh and van der Klis 2017), HBOs should be detected at very low frequencies in this system (i.e. significantly below 1 Hz), a hypothesis made by ALT2012 themselves. We therefore repeated the analysis of the RXTE observations of IGR J17480-2446, following a method specifically aimed at evidencing PDS features with very low centroid frequencies. We also searched for QPOs up to a few thousand hertz in order to reproduce the results of ALT2012 and to allow for a direct comparison to be made. We found seven VLF QPOs with center frequencies in the range $\sim 0.01-0.03$ Hz (see Table 4.1), consistent with the values predicted by ALT2012 for HBOs in a slow-spinning NS. We also found 3 LF QPOs and 3 kHz QPOs (see Table 4.1), with centroid frequencies consistent with those reported by the same authors.

We estimated the theoretical values of $\nu_{\rm nod}$, $\nu_{\rm per}$ and ν_{ϕ} as a function of emission radius r, obtained assuming a NS with mass M between 1 and 2.7 $M_{\odot}$, and adopting a dimensionless spin parameter $0.0054 \leq a \leq 0.0059$. By comparing our estimates with the QPOs we detected we observe the following:

1. The VLF QPOs we detected are consistent with being HBOs - QPOs generated through LT precession of the accretion flow - at a radius larger than approximately 15 R_g ($\approx$ 35 km) from the NS center. This is supported by the fact that these features all appear in a relatively hard state, as is clear from the HID, where the inner disc radius is believed to be truncated far from the NS surface (see e.g. Done et al. 2007).
2. The kHz QPOs that we detected are consistent with being either the upper or lower kHz QPOs, thus associated to the orbital or periastron precession frequency of matter at a radius lower than approximately 12 R_g ($\approx$ 25 km) from the NS center. The lack of a simultaneous detection of two kHz QPOs prevents any further classification.
3. As already noted by ALT2012, the LF QPOs detected are not consistent with the nodal precession frequency around a NS spinning at 11 Hz, but they are in principle consistent with the periastron precession frequency of matter orbiting at a distance of $15 - 25\,R_g$ from the NS. However, we note that two of our LF QPOs are detected together with a kHz QPO at $\sim$ 840 Hz (see Table 4.1, observation 95437-01-07-00 and 95437-01-09-00).

Concerning point (iii) we also tested for the non-simultaneity of the two QPOs in observations 95437-01-07-00 and 95437-01-09-00 by splitting each into several smaller segments, but both features seem to be present during a large fraction of these two observations. Assuming the correctness of the RPM, the simultaneity of the kHz QPOs and LF QPOs point to two main scenarios: either that the QPO associated to the periastron precession frequency (that at $\sim$ 47.5 Hz) is generated at a radius larger than that at which the orbital frequency QPO (that at $\sim$ 840 Hz) arises from, thus effectively invalidating a key assumption of the RPM; or that the LF QPOs we detected are not associated to any of the three motions relevant for the RPM, having already stated in (iii) that they cannot be explained by LT precession.

The first scenario pushes us toward the same conclusion drawn by ALT2012, i.e. that the RPM cannot explain the frequency properties of at least some of the QPOs, at least not in its simplest form. The second scenario, instead, further

stresses the question of the real nature of the LF QPOs observed between 35 and 50 Hz in IGR J17480-2446. ALT2012 classified the QPOs at $35 - 50$ Hz based on their frequency (comparable with the values typically seen in other NS systems), and based on the position these features occupied in the so-called Wijnands & van der Klis correlation (Wijnands and van der Klis 1999), formed by the frequency of a broad PDS component (called L_b) and the frequency of the HBO. The small number of QPOs detected by both ALT2012 and by ourselves, however, does not really allow for the evidencing of a correlation, and the fact that most of the components identifiable in a NS PDS correlate with one another (see Psaltis et al. 1999) suggests that ALT2012's classification of the LF QPOs at $35 - 50$ Hz might not be correct. Unfortunately, given the very low frequency of the VLF QPOs that we report in this work, it is not possible to determine whether these do fit into the Wijnands & van der Klis correlation (the L_b component's centroid frequency would be visible below 10 mHz, which is lower than our frequency resolution, assuming HBO frequencies lower than 0.1 Hz). Only a new outburst form this source and new data will therefore allow us to reach more conclusive results.

Is there an alternative explanation for these LF QPOs? PDS from NS systems are notoriously more structured and feature-rich than those from BH systems, and among the still-largely unknown features typical of NS systems are hectohertz QPOs (see e.g. Altamirano et al. 2008a). These QPOs have been detected in a number of Atoll sources (4U0614+09, 4U1608-52, 4U1728-34 and 4U1636-53) around ~ 100 Hz. Interestingly, all these sources contain NSs spinning at fairly high frequencies (415, 620, 363 and 581 Hz, respectively). While there is no known correlation between the NS spin and the frequency of hectohertz QPOs, it seems plausible that in a slowly spinning NS such as the one in IGR J17480-2446 hectohertz QPOs can appear at frequencies lower than ~ 100 Hz. We therefore speculate that the LF QPOs detected in IGR J17480-2446 might be relatively low-frequency hectohertz QPOs.

4.8 Summary and conclusions

We have examined all 47 RXTE PCA observations of the 11 Hz accreting pulsar IGR J17480-2446 located in the stellar system Terzan 5 during its 2010 outburst. We searched for QPO features located between 0.01 Hz and $\sim$ 4000 Hz.

We found seven VLF QPOs with center frequencies in the range $\sim 0.01 - 0.03$ Hz, three LF QPOs in the range $\sim 44 - 50$ Hz, and three kHz QPOs in the range $\sim 840 - 870$ Hz. We compared the theoretical values of the nodal frequency $\nu_{\rm nod}$, periastron precession frequency $\nu_{\rm per}$ and orbital frequency ν_{ϕ} as a function of the emission radius as predicted by the RPM to our findings. We find that the centroid frequencies of our detected VLF QPOs are consistent with the predicted nodal frequencies if generated at radii larger than 15 R_g. We also find that our LF QPOs detected at $40 - 50$ Hz could be consistent with the periastron precession frequency of material orbiting at approximately 15 R_g from the NS center. The presence of kHz QPOs simultaneous to these LF QPOs, however, either disproves the above hypothesis or invalidates one of the main assumptions of the RPM, namely that QPOs relevant for the RPM are produced at the same radius if they are observed simultaneously.

We have shown that VLF QPOs at frequencies consistent with those expected for LT driven modulations are present in the data, even though more data are required to confirm the classification of such features. We carried out an independent test of the significance of this finding in Section 4.6 and, while found to be significant, the assumptions and limitations in the analysis (outlined in Section 4.6) need to be addressed for a more robust verdict. While not conclusive, our results cast doubt on the nature of the $35 - 50$ Hz QPOs detected in IGR J17480-2446. These LF QPOs could either be associated with the periastron precession frequency (though in this case a key assumption of the RPM needs to be relaxed significantly), or with a type of QPO known as hectohertz QPOs, observed here at smaller frequencies possibly due to the low NS spin. It is also, of course, entirely possible that these LF QPOs are simply a new type of QPO, possibly peculiar to this unique system, or

perhaps typical of slowly spinning accreting NS LMXBs, of which IGR J17480-2446 is currently the only example.

"Wine is just purified sunshine."

Kumeren Govender

5 Conclusions and Future Work

5.1 Conclusions

In this Thesis we have studied compact and double compact binaries, namely black hole binary systems and neutron star low-mass X-ray binaries (LMXBs), in order to investigate binary stellar evolution pathways and accretion processes.

We firstly investigated the chemically homogeneous evolution of close binary systems consisting of rapidly rotating, massive stars at low metallicities and its role in producing massive black hole binary systems close enough to merge in a Hubble time. Understanding the different possible forms and variants of stellar evolution in binary systems yields insight as to the vast array of characteristics observed when studying stars, both single and in binary- or multi-star systems. It further informs us as to observed stellar fates and activity rates observed in the Universe.

We further explore accretion processes in neutron star LMXBs by investigating the relativistic precession model, based on the association of quasi-periodic oscillations (QPOs) to the different motions of matter orbiting a compact object in a strong gravitational field. Probing accretion processes in neutron star LMXBs offers unique tests of general relativity in the strong field, and also helps us to understand similar phenomena in other systems. Being able to determine parameters such as the mass and spin of compact objects using a model - such as the relativistic

precession model - offers the crucial opportunity to constrain the equation of state in conditions of extreme density and pressure, such as that found in neutron stars.

In Chapter 2, we investigated the role of the chemically homogeneous evolution channel in producing massive stellar binary black hole systems close enough to merge in the current epoch. The investigation was carried out by performing population synthesis simulations that combined realistic binary models based on the chemically homogeneous evolution pathway with, for the first time, detailed cosmological calculations of the chemical and star-formation history of the Universe (Taylor and Kobayashi, 2015b). Based on our joint star formation rate and metallicity distribution with a continuous range of metallicities, we constrained population properties and determined cosmological and aLIGO/AdV detection rates of binary black hole mergers formed through this evolutionary pathway more precisely than before. We predict a local co-moving merger rate that compares well to estimates and predictions by Abbott et al. (2019b) and Abbott et al. (2016a), and find that at our estimated full sensitivity aLIGO/AdV merger rates, the chemically homogeneous evolution pathway could be a significant source of aLIGO events (with a significant fraction of detections falling above the pair-instability supernova gap). For an intuitive idea of how our CHE rate estimates compare to the detections made by aLIGO/AdV to date, we considered the fraction of aLIGO/AdV BHBH detections with component mass ratios q in the range assumed for the CHE channel, $0.8 \leq q \leq 1.0$. Taking into account that this is a rough comparison only, we find that our O1 rates compare well to what aLIGO/AdV have detected, and that the range of our O3 rates fall just above that detected by aLIGO/AdV. Furthermore, although we predict BHBH mergers from above the PISN gap, aLIGO/AdV have detected none thus far. We find that this difference is not yet significant, and note that a likely candidate for the current mismatch is the large uncertainties present in mass-loss rate prescriptions for massive stars (Sander and Vink, 2020). We furthermore found that momentum kicks during black-hole formation generally lead to an increase in merger delay times, and that only extreme cases of high-redshift star formation rate deviations lead to pronounced changes in detection rates. Lastly, we find that

our pair-instability supernovae rate predictions lie in a reasonable region of rate estimates, given the uncertainties which exist both observationally and theoretically.

In Chapter 3 we analysed the complete set of observations of the neutron star LMXB 4U1608-52 obtained by the RXTE. This study presents the first source (including both black hole and neutron star LMXBs) for which more than one usable set of the necessary three QPOs (a triplet) has been found in its X-ray observations, and for which multiple tests of the relativistic precession model could be carried out. We found 24 observations containing triplets with which to test the relativistic precession model, along with a further seven observations each containing two of the three QPOs. We calculated the spin and mass of the source for each of the triplets, and found that they cluster around physically realistic values. We showed that spin and mass estimates tend to increase with proximity to the innermost stable circular orbit, as the relativistic precession model becomes an increasingly good approximation of the real behaviour of matter in proximity to the neutron star for decreasing radii. Furthermore, if our estimates are correct, 4U1608-52 would be one of the heaviest neutron stars known to date. This implies that our results would rule out some of the more exotic models of the equation of state.

In Chapter 4, we investigated the 11 Hz accreting pulsar IGR J17480-2446 in the stellar system Terzan 5. General relativity predicts that frame-dragging will occur in the vicinity of a spinning compact object, an effect that can be observed as a low-frequency QPO in neutron star system power density spectra according to the relativistic precession model and other QPO models. For a neutron star spinning as slowly as IGR J17480-2446, these oscillations are expected at frequencies below 1 Hz. However, previous studies of IGR J17480-2446 (Altamirano et al., 2008a) have classified QPOs at $35 - 50$ Hz as the frame-dragging QPO, thus casting doubt on their nature, and on the validity of the relativistic precession model. We searched a large frequency range for QPOs in the RXTE observations of IGR J17480-2446, and found seven very low-frequency QPOs below 0.3 Hz that were previously undetected, and that can be ascribed to frame-dragging. We further conclude that the QPOs found between $35-50$ Hz must either be a kHz QPO, shifted downwards in frequency

due to the low spin of IGR J17480-2446, or a different type of QPO altogether. Finally, we conducted an independent test by repeating the analysis for 4U1608-52 in order to see if any VLF QPOs could be found in its observations, and found none.

5.2 Future Work

Binary population synthesis simulations like that carried out in Chapter 2 are fundamental to the understanding of the evolutionary channels leading up to the formation of close binary black hole systems, such as those currently detected by aLIGO/AdV. As more and more mergers will be detected with the planned increases in sensitivity of the detectors, the population of detected mergers will grow, further enabling statistical analyses and comparisons with simulations in order to constrain possible channels of evolution more accurately. A direct follow-up of the work contained in Chapter 2 is that of exploring the effect of spin on the final black hole population property distribution in order to compare it with aLIGO/AdV findings. Another follow-up should allow for the more realistic case of binaries having different q-values from a distribution in the q-range, instead of all being assigned $q = 1$ as was done for the work in Chapter 2 — this would influence eventual predicted BHBH merger rates, and would allow for more robust comparisons with aLIGO/AdV's detections. Further, from the results of Chapter 2 it is clear that there is potential tension between the predicted and observed BHBH merger rate above the PISN gap. A potential reason for these discrepancies is the large uncertainties involved in mass-loss rate prescriptions of massive stars. A rewarding avenue for future work would therefore be to investigate how these different prescriptions influence not only the BHBH merger rates, but also the predicted mass ratio q of BHBH systems having evolved through the CHE pathway. Finally, an analysis on how the results of any future aLIGO/AdV runs and their sensitivities compare to our findings here would further be extremely important and interesting in helping to constrain evolutionary pathways.

Testing the relativistic precession model on neutron star LMXBs such as 4U1608-52 in Chapter 3 is fundamental to the investigation of QPO models. In

order to offer a more robust test of the relativistic precession model, a future follow-up to this work would need the analysis to be carried out on a larger sample of neutron star LMXBs to ascertain whether their RPM triplets predict physically realistic estimates of neutron star mass and spin. Additionally, in order to use the consistency (or inconsistency) of mass and spin estimates as a more reliable test of the relativistic precession model, future analyses should lessen or remove some of the analysis uncertainties outlined in Section 3.6. In Chapter 4, we carried out an independent test of the significance of the detection of VLF QPOs in IGR J17480-2446 and, while found to be significant, the assumptions and limitations of the test should be better constrained — this can be done in a follow-up by including a larger number of sources and observations in the test analysis. The better understanding of QPO models like the relativistic precession model leads to a better understanding of the physical processes behind QPOs, and of accretion in general. Not only can the better understanding of accretion on small scales (e.g. for neutron star LMXBs) help us to understand these phenomena on larger scales (e.g. for active galactic nuclei in the centre of galaxies), but methods like the relativistic precession model can help us to determine the spin and mass of compact binary components, in turn helping us to constrain valid models of the equation of state for matter under conditions of extreme pressure and density (such as those found in neutron stars). In order to properly constrain such models, a larger sample of neutron star LMXBs have to be tested using the analysis and techniques presented in this thesis. With X-ray instruments featuring high sensitivity and high time resolution (such as the Neutron Star Interior Composition Explorer), this is now an even more worthwhile avenue to explore.

Appendices

A

Grids of detailed binary stellar evolution models

Marchant et al. (2016) explored the evolution of massive close binaries by computing large grids of detailed binary evolution models using the MESA code (Paxton et al., 2015, 2013, 2011), which they extended to allow for contact binaries having mass ratios close to one. Here we use similar, but more detailed grids for 22 different metallicities ranging from $\log(Z) = -5.0$ to $\log(Z) = -2.375$ in steps of $\log(Z) = 0.125$, computed for mass ratios $q_\mathrm{i} = M_2/M_1 = 1$. These grids cover initial binary periods in the range $0.4 \leq P_\mathrm{i}/\mathrm{d} \leq 4.0$ in intervals of 0.025 days, and initial primary masses in the range $1.4 \leq \log(M_1/M_\odot) \leq 2.7$ with intervals of 0.025 dex. As an example, six of these grids showing the final binary outcomes are shown in Fig. A.1. These grids (and the rest of the data they were created from) were used to determine the final outcomes and final parameters of binary systems in our Monte Carlo simulations after their initial parameter values have been determined.

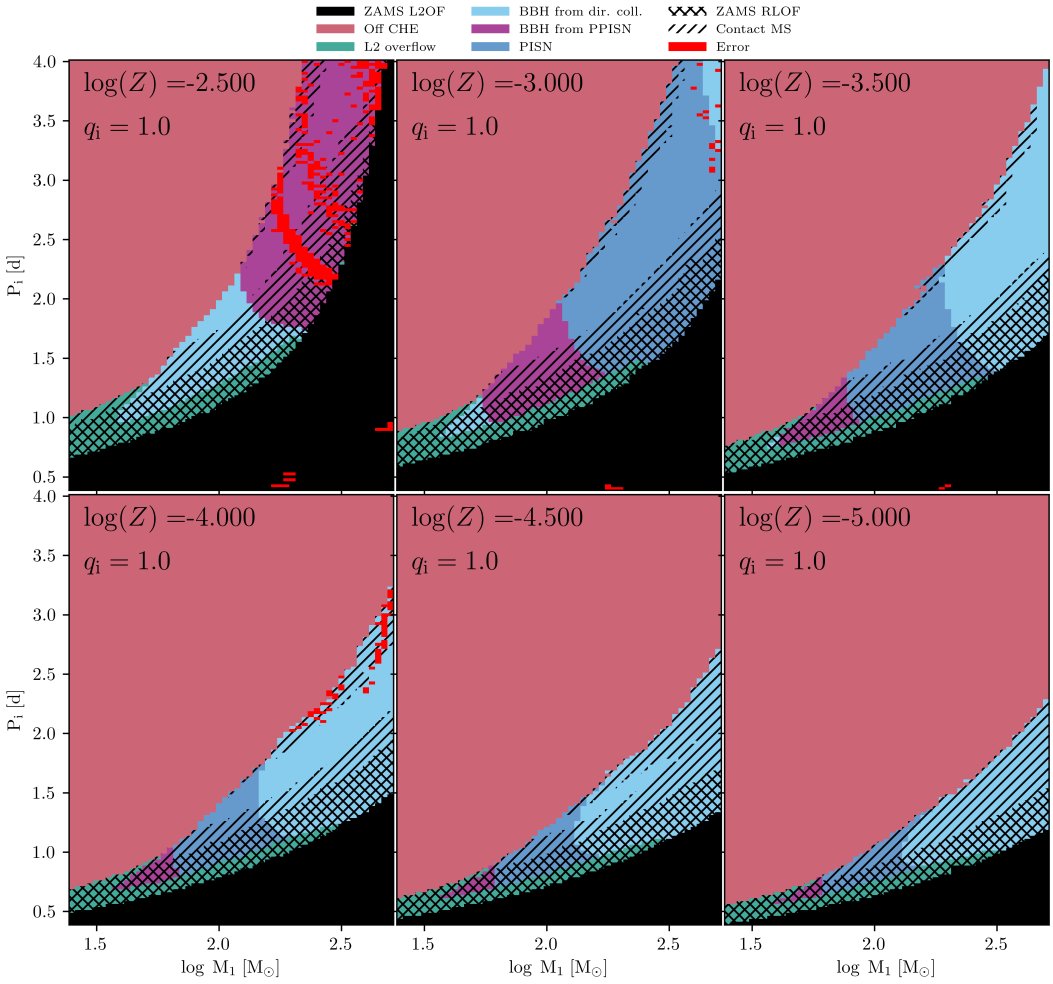

Figure A.1: A selection of six grids of binary systems showing their initial period and initial primary mass for $q_i = 1$, with final outcomes coded according to the legend at the top. Black regions show where the initial orbital period of a system was small enough to have L2 overflow at the ZAMS, while green areas are systems reaching L2 overflow during the main sequence – systems in both these scenarios will merge during their early evolution. Pink areas depict systems that reached a point where the central and surface He abundance of one of the stars differ by more than 0.2 – the star is therefore not evolving chemically homogeneously anymore. Blue regions successfully form double He binaries that will either collapse to form BHBH systems (light blue) or go pair-unstable (dark blue). Purple denotes areas forming BHBH systems via the PPISN path. Single hatch-marks show systems experiencing overcontact during the main sequence, while double hatch-marks are models in overcontact at the ZAMS already. Red regions show models for which the simulations didn't converge.

B

Binary simulation details

In order to perform a simulation using the cosmic star formation history of Taylor and Kobayashi (2015b), we use a Monte Carlo method to sample birth redshifts and metallicities of binary systems representative of the evolution of a co-moving box. In this case, the probability of a system being formed with a redshift between z and $z + dz$, and a metallicity between $\log Z$ and $\log Z + d\log Z$ is proportional to

$$F(z, Z)\ dz\ d\log(Z) = \frac{d^2\mathrm{SFR}}{d\log(Z)\ dV_c}\frac{dt}{dz}\ dz\ d\log(Z), \tag{B.1}$$

where t represents the co-moving time coordinate and $d^2\mathrm{SFR}/d\log(Z)dV_c$ is the star formation rate per unit dex in metallicity and unit co-moving volume. To obtain a set of Monte Carlo draws satisfying this distribution function, we sample (z_0, Z_0) from a flat distribution in redshift and metallicity and then reject samples with a probability equal to the ratio

$$p_{\mathrm{reject}}(z_0, Z_0) = F(z_0, Z_0)/\mathrm{Max}(F(z, Z)). \tag{B.2}$$

Here Max denotes the maximum of the function F in the ranges chosen for the Monte Carlo. This rejection sampling algorithm produces binaries with the desired distribution in redshift and metallicity. As the distributions for the masses, orbital

periods and mass ratios of binary systems are assumed to be independent of metallicity and redshift, these are sampled separately.

B.0.1 Monte Carlo Efficiency

The Monte Carlo is made more efficient by sampling the binary parameters only over the ranges covered by the grids, and correcting for the uncovered parameter space. Our grids cover the following ranges:

- $25 \leq M_{1,\mathrm{i}}/\mathrm{M}_{\odot} \leq 500$
- $0.4 \leq P_{\mathrm{i}}/\mathrm{d} \leq 4.0$
- $q = M_2/M_1 = 1.0$
- $-5.0 \leq \log(Z) \leq -2.375$

Integrating these distributions, we can calculate the fraction of stars in our co-moving box coming from the ranges covered by the grids. The mass, period, ratio and metallicity fractions are denoted by C_M, C_P, C_q and C_Z, respectively. For C_M, assuming a Salpeter initial mass function and taking the lower mass limit for CCSNe as $8\mathrm{M}_{\odot}$, we find

$$C_M = \frac{\int_{25}^{500} M^{-2.35} dM}{\int_{8}^{\infty} M^{-2.35} dM} = 0.211, \tag{B.3}$$

and for C_P, taking into account that the period P is drawn from a flat distribution in $\log(P)$[1], we find

$$C_P = \frac{\int_{\log(0.4)}^{\log(4.0)} d\log(P)}{\int_{\log(0.4)}^{\log(365.25)} d\log(P)} = 0.3378. \tag{B.4}$$

We assume that grids at $q = 1$ are representative of the range $0.8 \leq q \leq 1.0$, and so we have that $C_q = 0.2$. For C_Z, we have the effective calculation

[1]Note that we here assume a maximum binary period of 365.25 days. If the reader prefers a different maximum period, $C_{P,new}$ can easily be recalculated and merger rates adjusted accordingly. E.g., assuming a maximum period of 4000 days according to Sana et al. (2012), one finds $C_{P,new} = 0.25$. Merger rates can then be adjusted as $R_{new} = R_{old}(C_{P,new}/C_{P,old})$.

Table B.1: The metallicity fraction C_Z for the default SFR case (labeled "Original") as well as for each of the four cases of high-redshift deviations in SFR (displayed in Figure 2.14).

	Metallicity fraction C_Z
Original	0.165
Case 1	0.169
Case 2	0.163
Case 3	0.183
Case 4	0.160

$$C_Z = \frac{\int_0^{\infty}\int_{-5}^{-2.375} \frac{d^2\mathrm{SFR}}{d\log(Z)\ dV_c} d\log(Z)\ dz}{\int_0^{\infty}\int_{-\infty}^{0} \frac{d^2\mathrm{SFR}}{d\log(Z)\ dV_c} d\log(Z)\ dz}. \tag{B.5}$$

This integral is performed via Monte Carlo integration, and the results for C_Z for our original SFR, as well as for the four modified SFR cases we consider, can be seen in Table B.1.

B.0.2 Normalization

Although our Monte Carlo method provides a set of models that satisfy the assumed distribution functions, in order to compute expected rates of events it is necessary to normalize results. To do this, given a total number of simulated binaries N_{MC}, we compute a corresponding co-moving volume V_{MC} for which the sampled set is representative of all binaries formed in it throughout the history of the universe. We first define the star formation rate per unit co-moving volume as SFR_V:

$$\mathrm{SFR}_V(z) \equiv \frac{d\mathrm{SFR}}{dV_c} = \int_{-\infty}^{\infty} \frac{d^2\mathrm{SFR}}{d\log(Z)\ dV_c} d\log(Z). \tag{B.6}$$

Following Marchant et al. (2017), we assume the conversion constant between the mass created per unit time in stars to the co-moving supernova rate per unit co-moving volume $R_{\mathrm{SN},V}(z)$ to be

$$\frac{R_{\mathrm{SN},V}(z)}{\mathrm{SFR}_V(z)} = 0.01\mathrm{M}_\odot^{-1}, \tag{B.7}$$

and that the conversion constant between $R_{\mathrm{SN},V}$ and the co-moving formation rate of massive binaries per unit co-moving volume $R_{\mathrm{MB},V}$ is

$$R_{\mathrm{MB},V}(z) = \frac{f_b}{1+f_b} R_{\mathrm{SN},V}(z). \tag{B.8}$$

Here, f_b is the binary fraction, defined as the ratio between the number of binaries formed to the number of binaries and single stars formed. We assume that two out of three massive stars will form in a binary, such that $f_b = 0.5$ (Marchant et al. 2017). In this framework we can compute the number of massive binaries that are expected to form per unit co-moving volume during the lifetime of the Universe:

$$N_{\mathrm{MB},V} = \frac{f_b}{1+f_b}\left(\frac{R_{\mathrm{SN},V}}{\mathrm{SFR}_V}\right)\int_0^\infty\int_{-\infty}^\infty \frac{d^2\mathrm{SFR}}{d\log(Z)\,dV_c}\frac{dt}{dz} d\log(Z)\; dz. \tag{B.9}$$

Given $N_{\mathrm{MB},V}$, we can directly evaluate the value of the co-moving volume V_{MC} representative of a number N_{MC} of Monte Carlo draws of massive binaries,

$$V_{\mathrm{MC}} = \frac{N_{\mathrm{MC}}}{C_M C_P C_q C_Z N_{\mathrm{MB},V}}, \tag{B.10}$$

where we have included the factors used to make the Monte Carlo sampling more efficient. Since our Monte Carlo simulation draws only massive stars, and since CCSNe have a lower mass limit of $8\mathrm{M}_\odot$, the lower mass end of the Salpeter IMF we draw from can be ignored. Considering only higher-mass stars, our Salpeter IMF is essentially equivalent to using a Kroupa IMF (similar to that used by Taylor and Kobayashi 2015b), except for a slight variation on the slope at high mass (with an exponent of 2.35 for Salpeter and 2.3 for Kroupa). Since our rates are normalised based on the number of SNe per solar mass formed, we can compare how the value of the $0.01\mathrm{M}_\odot^{-1}$ we adopted in Equation B.7 compares to a value instead derived from a Kroupa IMF. Independent of whether we consider a Kroupa IMF capped at $50\mathrm{M}_\odot$ or extrapolated to $500\mathrm{M}_\odot$, we find that the number of stars

with mass $M > 8\mathrm{M}_{\odot}$ per solar mass of star formation is 0.010. This is in excellent agreement with our adopted value.

B.1 Rate calculations

One can assume that for the given number of Monte Carlo draws N_{MC}, all the massive binaries ever formed in a simulation box of co-moving volume V_{MC} have been simulated. Adding the delay times to those systems that collapse to form merging BHBHs gives the distribution of such systems in the co-moving box. Binning this distribution in redshift intervals Δz (centred on redshifts z_i) and counting the number of BHBH mergers $N_{m,i}$ in each bin, the co-moving volumetric merger rate is

$$\frac{dN_m}{dtdV_c}(z_i) \simeq \frac{N_{m,i}}{\Delta z \times V_{\mathrm{MC}}} \frac{dz}{dt}. \tag{B.11}$$

We are also interested in the detection rates resulting from the O1, O3 and full design aLIGO strain sensitivities, as well as the Einstein Telescope's (ET) predicted strain sensitivity. Each of these have a corresponding noise power spectrum S_{n}, which can be seen in Figure B.2. Given the merging redshift and masses for a BHBH merger, we can estimate its detection probability p_k for each different noise power spectrum - see Appendix B.2 for a description of how this is calculated. The co-moving rate of mergers per unit co-moving volume V_{MC} detectable locally at $z = 0$ is then obtained by adding the detection probabilities of all mergers in a redshift bin (denoted by $N_{det,i}$) to obtain

$$\frac{dN_{det}}{dtdV_c}(z_i) \simeq \frac{N_{det,i}}{\Delta z \times V_{\mathrm{MC}}} \frac{dz}{dt}, \tag{B.12}$$

similar to what was done before. In the case of all detection probabilities equalling $p_k = 1.0$, Equation B.11 and B.12 are equivalent. The co-moving volumetric merger rate $dN_m/dtdV_c$ can next be transformed into a cosmological rate observable from Earth as

$$R_m = \int_0^{\infty} \frac{1}{1+z} \frac{dN_m}{dtdV_c} \frac{dV_c}{dz} dz, \tag{B.13}$$

which in practice can be computed as

$$R_m \simeq \sum_i \frac{1}{1+z_i} \frac{dN_m}{dt dV_c} \frac{dV_c}{dz} \Delta z. \tag{B.14}$$

To calculate PISNe rates, the procedure is equivalent, except that the redshift of the event is the same as its formation redshift, and each of our binary models produce two PISNe.

B.1.1 Necessary and sufficient conditions for testing of code

In order to test whether our code functions correctly, it is first necessary to outline the necessary and sufficient conditions for which, if satisfied, it can safely be assumed that our code is working. The necessary conditions are as follows:

1. If we assume a given rate with a fixed delay time for the merging of all binaries, then it is necessary that this rate is invariant under a time shift, if plotted against cosmic time and for a given cosmological volume. In other words, the shape of the rate as a function of cosmic time should be constant.
2. If we assume a given rate and a fixed delay time for the merging of all binaries, this rate should maintain the same value in our output as a function of cosmic time under a time translation for a box of fixed cosmic volume. This is true given that we are physically simulating a box in the Universe, and that the number of binaries in this box is conserved (and therefore the number of black hole mergers is conserved, if each binary is made to result in a black hole merger).

The above two conditions are also sufficient, as our problem is linear – our rates are calculated given the sum of simulated mergers resulting from binaries with different formation redshifts. If the above two conditions are satisfied specifically for all formation redshifts and all delay times, then they are sufficient and should work for all distributions. In order to test our code, we therefore need to perform a test that satisfies the above two conditions for a range of fixed delay times. This is done in Section B.1.2.

B.1.2 Testing of Rate Calculations

In order to verify that our code for computing rates works as expected, we perform a synthetic test in order to see whether the necessary and sufficient conditions for correctness, outlined in Section B.1.1, is satisfied. Given the boundaries of our grid of binary models, and the assumption that our $q = 1$ models are representative of systems with $0.8 \leq q \leq 1$, the co-moving rate of formation of binaries covered by our grids is

$$R_{\mathrm{grid},V}(z) = 0.01 M_{\odot}^{-1} \times C_M C_P C_q \frac{f_b}{1+f_b} \int_{-5}^{-2.375} \frac{d^2\mathrm{SFR}}{d\log(Z)\, dV_c} d\log(Z). \quad \text{(B.15)}$$

If we were to ignore our binary evolution calculations and instead assume all binaries in the range of our grids form a merging BHBH with zero time delay between the time when the stars are formed and the moment the BHs merge, then the co-moving volumetric merger rate would satisfy

$$\frac{dN_m}{dt dV_c}(z) = R_{\mathrm{grid},V}(z). \quad \text{(B.16)}$$

Moreover, if one assumes all merging BHBHs have a fixed delay time between formation and merger, then the co-moving volumetric rate of mergers would match $R_{\mathrm{grid},V}(z)$ shifted in lookback time by the amount chosen for the delay time. This allows us to test our calculations, since we can directly use the star formation data to compute $R_{\mathrm{grid},V}(z)$ and compare to the resulting co-moving volumetric rate from our Monte Carlo calculations. The result of this exercise is displayed in Fig. B.1, where we show the outcome of assuming fixed delay times of 1 Gyr and 9 Gyrs.
Shifting

As the shape of the output remains constant as a function of cosmic time, condition 1 in Section B.1.1 is satisfied. Furthermore, this test was performed for a range of fixed delay times (as is required by the conditions in Section B.1.1), and seeing as it maintains the same peak value (thereby satisfying condition 2 for the range of delay times considered), we can safely conclude that our code is functioning correctly.

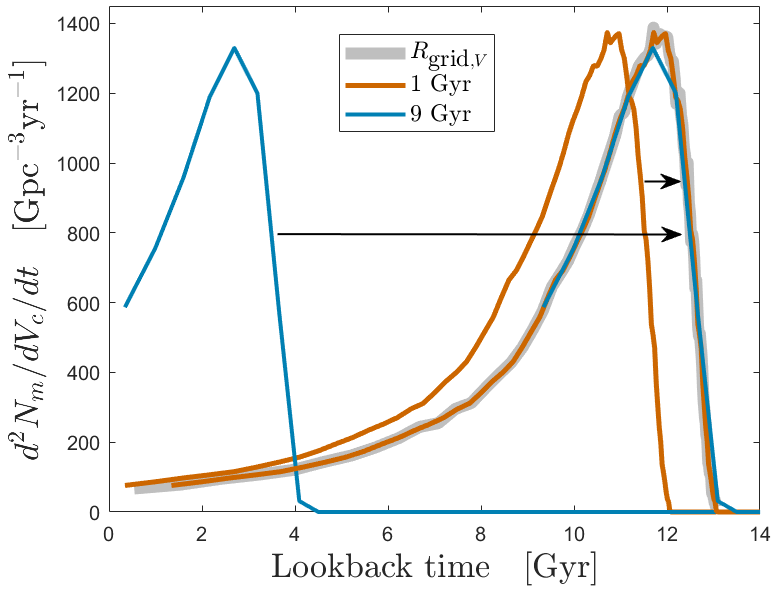

Figure B.1: Synthetic test performed to check our method of computing merger rates. See the text of Section B.1.2 for details. The 1 Gyr and 9 Gyr test curves are also shown shifted (as indicated by the arrows) to asses how well their shapes match that of $R_{\mathrm{grid},V}$.

In these calculations we also assumed that the mass of the BHs formed matched the initial mass of their progenitor stars, and verified that the mass distribution of merging BHBHs matched the Salpeter distribution used for the stellar masses.

B.2 Detection Probability

In order to calculate the merger rate detectable by aLIGO, the probability of detection of each one of our simulated BHBH systems that merge in the lifetime of the Universe needs to be determined. To do this, an isotropic Universe is assumed and hence each binary can be located anywhere in the sky with equal probability. Given that the sensitivity of aLIGO is dependent on the location of the binary in the sky, the signal from each simulated binary will have a different signal to noise ratio (SNR) depending on its location in the sky. The probability of detection p_k for a BHBH merger is hence defined as the fractional area in the sky where its SNR achieved a sufficiently high value to yield a reliable detection, and can be written as

$$p_k = 1 - \mathcal{C}\left[\min\left(\frac{8}{n_{\mathrm{SNR}}}, 1\right)\right]. \tag{B.17}$$

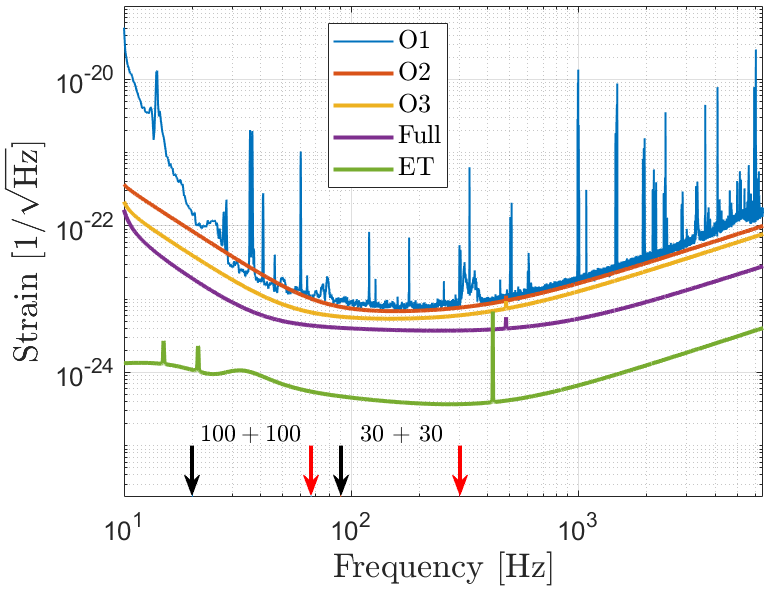

Figure B.2: The strain sensitivities of the O1, O2, O3 and full design sensitivity aLIGO runs (Abbott et al., 2016c). Conservative predicted estimates are shown for the O2, O3 and full sensitivity runs, whereas the actual data for the O1 run are shown. The O1, O3 and full sensitivities are used when calculating the various aLIGO detection rates - the O2 sensitivity is excluded from this analysis as it is similar to that of O1. To illustrate the capabilities of future gravitational-wave detectors, we also include the Einstein Telescope's (ET) predicted sensitivity (see Section 2.4.2). The arrows at the bottom of the figure show the merger (in black) and ringdown frequency (in red, assuming a remnant spin of 0.7) of $30 + 30$ $\mathrm{M}_{\odot}$ and $100 + 100$ $\mathrm{M}_{\odot}$ BHBH mergers at $z = 0$, respectively. The typical gravitational-wave frequency at the inspiral-merger transition is $\sim$ 4kHz ($\mathrm{M}_{\odot}/M$), where M is the total BHBH mass; the quasi-normal ringdown peaks at a frequency of $\sim 10 - 20$ kHz ($\mathrm{M}_{\odot}/M$), depending on the final remnant spin (Ajith et al., 2011).

Here, we have adopted a SNR detection threshold of 8, and $\mathcal{C}$ is the inverse of the cumulative distribution function of projection coefficients (and is an integral over inclination, orientation and sky location) and can be used as a representation of detector sensitivity (see de Mink and Mandel 2016b). The maximum SNR n_{SNR} for a specific BHBH merger is calculated in Fourier space and is determined by the merger's chirp mass M_{chirp} and redshift (which determines the strength at which the signal will arrive at Earth), as well as the noise properties of the aLIGO detector. This can be expressed as

$$n^2_{\mathrm{SNR}}(z_m, M_{\mathrm{chirp}}) = 4 \int_0^{\infty} \frac{|h(f, z_m, M_{\mathrm{chirp}})|^2}{S_{\mathrm{n}}(f)} df, \tag{B.18}$$

where h is the waveform of the face-on, overhead gravitational-wave signal of a BHBH merger placed at redshift z_m with chirp mass $M_{\rm chirp}$, and $S_{\rm n}$ is the noise power spectrum of the detector. The description and assumptions in this section are based on the work of de Mink and Mandel (2016b).

C

Confirmed, tentative and incomplete triplets

Table C.1: **Confirmed Triplets**: All observations in which all three constituent QPOs of the RPM (HBO, lower kHz QPO and upper kHz QPO] could be found. This is our most certain and prime source of triplets for 4U1608-52; none of the component parameters used in the spectral fitting of these observations were fixed or constrained in order to improve the significance or the Q factor of a potential QPO. **Tentative Triplets**: Observations which, with the help of some parameters being constrained during spectral fitting, also contained all three QPOs. A starred value for a Q factor means that the width of the QPO with said Q factor was fixed in order for it to either have a qualifying Q factor or a qualifying significance, or both.

Confirmed triplets											
Obs ID	**MJD**	***l*kHz QPO (Hz)**	**Q factor**	**Sign.**	***u*kHz QPO (Hz)**	**Q factor**	**Sign.**	**LF QPO (Hz)**	**Amplitude**	**Q factor**	**Sign.**
30062-02-01-00	50896.91833	671^{+2}_{-2}	28 ± 3	11.5	956^{+10}_{-10}	8 ± 1	8.8	40^{+1}_{-1}	$1.1 \times 10^{-3}{}^{+1 \times 10^{-4}}_{-1 \times 10^{-4}}$	2.6 ± 0.5	9.9
30062-02-01-01-1	50897.58019	$601.7^{+0.6}_{-0.6}$	49 ± 5	20.5	899^{+7}_{-7}	7 ± 2	7.5	$24.5^{+0.5}_{-0.6}$	$3 \times 10^{-4}{}^{+1 \times 10^{-4}}_{-1 \times 10^{-4}}$	9 ± 5	3.3
30062-02-01-01-3	50897.58019	$567.9^{+0.8}_{-0.9}$	27 ± 4	13.1	879^{+4}_{-4}	8 ± 1	11.6	$22.2^{+0.4}_{-0.4}$	$3 \times 10^{-4}{}^{+2 \times 10^{-4}}_{-1 \times 10^{-4}}$	8 ± 4	3.1
30062-02-01-02-1	50898.58019	$770.4^{+0.8}_{-0.8}$	37 ± 3	17.8	1040^{+13}_{-12}	9 ± 3	4.7	46^{+2}_{-3}	$1.1 \times 10^{-3}{}^{+3 \times 10^{-4}}_{-2 \times 10^{-4}}$	2 ± 1	4.9
30062-01-01-00-1	50899.51955	$735.8^{+0.4}_{-0.4}$	50 ± 3	35.9	1046^{+9}_{-10}	10 ± 4	4.7	43^{+2}_{-2}	$5 \times 10^{-4}{}^{+2 \times 10^{-4}}_{-2 \times 10^{-4}}$	4 ± 2	3.0
30062-01-02-01	50906.64556	538^{+13}_{-20}	5 ± 3	3.1	850^{+7}_{-7}	10 ± 3	5.4	$23.5^{+0.5}_{-0.6}$	$2.0 \times 10^{-3}{}^{+6 \times 10^{-4}}_{-5 \times 10^{-4}}$	4 ± 2	4.1
30062-01-02-05-1	50914.17628	658^{+2}_{-2}	25 ± 4	10.2	1000^{+13}_{-14}	10 ± 5	3.7	$29.2^{+0.9}_{-0.9}$	$4.1 \times 10^{-3}{}^{+5 \times 10^{-4}}_{-5 \times 10^{-4}}$	2.1 ± 0.4	8.5
70059-01-20-00	52524.10185	694^{+2}_{-3}	17 ± 2	9.9	974^{+7}_{-7}	10 ± 2	7.8	40^{+1}_{-1}	$8 \times 10^{-4}{}^{+2 \times 10^{-4}}_{-1 \times 10^{-4}}$	2.0 ± 0.5	6.1
90408-01-01-03	53088.39759	613^{+1}_{-1}	45 ± 8	9.8	951^{+22}_{-21}	7 ± 2	3.9	23^{+1}_{-1}	$7 \times 10^{-4}{}^{+4 \times 10^{-4}}_{-2 \times 10^{-4}}$	6 ± 4	4.3
	53088.39759	613^{+1}_{-1}	45 ± 8	9.8	951^{+22}_{-21}	7 ± 2	3.9	37^{+2}_{-2}	$1.7 \times 10^{-3}{}^{+6 \times 10^{-4}}_{-5 \times 10^{-4}}$	4 ± 2	3.5
Tentative triplets											
30062-02-01-01-4	50897.58019	614^{+1}_{-1}	25 ± 2	18.2	930^{+7}_{-7}	10 ± 2	7.0	36^{+2}_{-2}	$2.2 \times 10^{-3}{}^{+2 \times 10^{-4}}_{-2 \times 10^{-4}}$	2.1*	11.0
30062-01-01-00-2	50899.51955	$773.9^{+0.6}_{-0.6}$	54 ± 3	29.0	1086^{+32}_{-29}	5.0*	4.6	44^{+2}_{-2}	$7 \times 10^{-4}{}^{+2 \times 10^{-4}}_{-2 \times 10^{-4}}$	4 ± 1	4.4
30062-01-01-02	50901.34889	$678.8^{+0.3}_{-0.4}$	48 ± 5	24.2	980^{+17}_{-17}	8 ± 2	4.7	35^{+2}_{-2}	$2.2 \times 10^{-3}{}^{+2 \times 10^{-4}}_{-2 \times 10^{-4}}$	2.1*	9.7
30062-01-01-03	50902.52537	499^{+18}_{-15}	6 ± 3	3.0	815^{+6}_{-6}	6.3 ± 0.8	11.4	20^{+1}_{-1}	$1.8 \times 10^{-3}{}^{+3 \times 10^{-4}}_{-3 \times 10^{-4}}$	2.1*	6.3
30062-01-02-05-2	50914.17628	625^{+26}_{-26}	5.2*	3.3	913^{+9}_{-10}	10 ± 3	4.9	$25.6^{+0.7}_{-0.7}$	$4.6 \times 10^{-3}{}^{+4 \times 10^{-4}}_{-4 \times 10^{-4}}$	2.0*	12.7
50052-01-20-00	51660.04616	590^{+3}_{-4}	33 ± 16	4.0	893^{+18}_{-18}	9 ± 5	3.1	28^{+2}_{-2}	$3.9 \times 10^{-3}{}^{+7 \times 10^{-4}}_{-7 \times 10^{-4}}$	2.0*	5.3
50052-01-20-01	51660.29390	583^{+6}_{-4}	21 ± 11	3.6	912^{+13}_{-15}	13.6*	3.9	31^{+2}_{-2}	$4.7 \times 10^{-3}{}^{+8 \times 10^{-4}}_{-8 \times 10^{-4}}$	2.0*	5.8
50052-01-04-00	51614.05684	747^{+19}_{-19}	4.8*	5.9	1161^{+9}_{-6}	42.6*	3.4	21^{+1}_{-1}	$4.8 \times 10^{-3}{}^{+8 \times 10^{-4}}_{-8 \times 10^{-4}}$	2.6*	6.2
70058-01-37-00	52525.14340	$855.8^{+0.6}_{-0.4}$	156 ± 52	22.9	1075^{+17}_{-20}	13.3*	3.4	60^{+8}_{-9}	$5 \times 10^{-4}{}^{+1 \times 10^{-4}}_{-1 \times 10^{-4}}$	2.0*	3.6
70059-03-01-01	52528.96521	$800.0^{+0.2}_{-0.2}$	114 ± 42	18.0	1048^{+24}_{-24}	9.5*	3.1	41^{+4}_{-4}	$9 \times 10^{-4}{}^{+2 \times 10^{-4}}_{-2 \times 10^{-4}}$	2.0*	4.4
70059-03-02-00	52531.20519	896^{+1}_{-1}	123 ± 73	13.2	1106^{+11}_{-11}	21.1*	3.7	42^{+6}_{-16}	$4 \times 10^{-4}{}^{+1 \times 10^{-4}}_{-1 \times 10^{-4}}$	2.1*	2.7
70059-03-02-01	52531.48810	1064^{+19}_{-14}	21 ± 10	3.0	$762.7^{+0.4}_{-0.5}$	48 ± 7	18.6	41^{+4}_{-8}	$1.3 \times 10^{-3}{}^{+3 \times 10^{-4}}_{-3 \times 10^{-4}}$	2.0*	4.8
70059-01-26-00	52546.86793	663^{+3}_{-4}	29 ± 17	3.4	966^{+11}_{-11}	17.9*	3.4	32^{+1}_{-1}	$4.9 \times 10^{-3}{}^{+6 \times 10^{-4}}_{-6 \times 10^{-4}}$	2.1*	8.2
80406-01-02-02	52715.71240	908^{+4}_{-5}	50 ± 16	6.0	1145^{+9}_{-9}	17 ± 6	4.6	37^{+4}_{-3}	$5 \times 10^{-4}{}^{+1 \times 10^{-4}}_{-1 \times 10^{-4}}$	2.0*	4.5
80406-01-03-03	52722.11726	512^{+3}_{-4}	29 ± 15	3.4	819^{+6}_{-6}	13 ± 4	5.3	22^{+1}_{-1}	$4 \times 10^{-3}{}^{+4 \times 10^{-4}}_{-4 \times 10^{-4}}$	1.9*	9.5

Table C.2: Incomplete Triplets: Observations in which only two of the three QPOs forming a complete triplet were present, and either the lower kHz QPO (lkHz QPO) or the upper kHz QPO (ukHz QPO) is missing. A starred value for a Q factor means that the width of the QPO in question was fixed in order for it to have a sufficiently high Q factor or significance, or both. Assigned numbers for observations in the second column correspond to the numbers in Figure 3.3.

Incomplete Triplets												
Obs ID	**#**	**MJD**	**lkHz QPO (Hz)**	**Q factor**	**Sign.**	**ukHz QPO (Hz)**	**Q factor**	**Sign.**	**LF QPO (Hz)**	**Amplitude**	**Q factor**	**Sign.**
70069-01-03-01	1	52548.68155	–	–	–	833^{+11}_{-12}	17.5*	3.4	$20.7^{+0.8}_{-0.7}$	$2.9 \times 10^{-3}{}^{+9 \times 10^{-4}}_{-9 \times 10^{-4}}$	6.6*	3.3
70069-01-03-06	2	52554.87674	–	–	–	796^{+11}_{-12}	14.3*	3.6	$17.2^{+0.4}_{-0.3}$	$2.4 \times 10^{-3}{}^{+7 \times 10^{-4}}_{-7 \times 10^{-4}}$	9 ± 3	3.7
50052-01-24-00	3	51672.68155	–	–	–	689^{+12}_{-13}	11.1*	3.5	$21.4^{+0.4}_{-0.4}$	$2.1 \times 10^{-3}{}^{+8 \times 10^{-4}}_{-7 \times 10^{-4}}$	12 ± 7	3.0
60052-03-01-00	4	52233.87058	493^{+13}_{-13}	2.3 ± 0.3	9.4	–	–	–	$28.7^{+0.8}_{-1.2}$	$1.2 \times 10^{-3}{}^{+6 \times 10^{-4}}_{-4 \times 10^{-4}}$	5 ± 3	3.1
95334-01-03-11	5	55270.37815	834^{+3}_{-3}	37 ± 16	4.8	–	–	–	50^{+3}_{-2}	$1.7 \times 10^{-3}{}^{+5 \times 10^{-4}}_{-5 \times 10^{-4}}$	5.7*	3.2
70059-03-02-03	6	52531.55685	$780.8^{+0.4}_{-0.4}$	88 ± 28	15.1	–	–	–	51^{+4}_{-3}	$1.3 \times 10^{-3}{}^{+4 \times 10^{-4}}_{-4 \times 10^{-4}}$	2 ± 1	3.7
95334-01-03-05	7	55272.59963	–	–	–	$729.2^{+0.4}_{-0.5}$	51 ± 11	13.4	$25.6^{+0.7}_{-0.6}$	$7 \times 10^{-4}{}^{+2 \times 10^{-4}}_{-2 \times 10^{-4}}$	6.5*	4.0

D

HBO QPOs as second harmonics

Stella et al. (1999) noticed that the RPM yields high masses; as an explanation, they proposed that the HBO associated to a triplet could in fact be the second harmonic of the real Lense-Thirring frequency. Taking this into account and assuming that each of the HBOs we measured was the second harmonic of a non-detected fundamental frequency, we find the spin and mass ranges for 4U1608-52 to be $0.10 < a < 0.19$ and $1.97 < M/\mathrm{M}_\odot < 2.33$, as can be seen in Figure D.1.

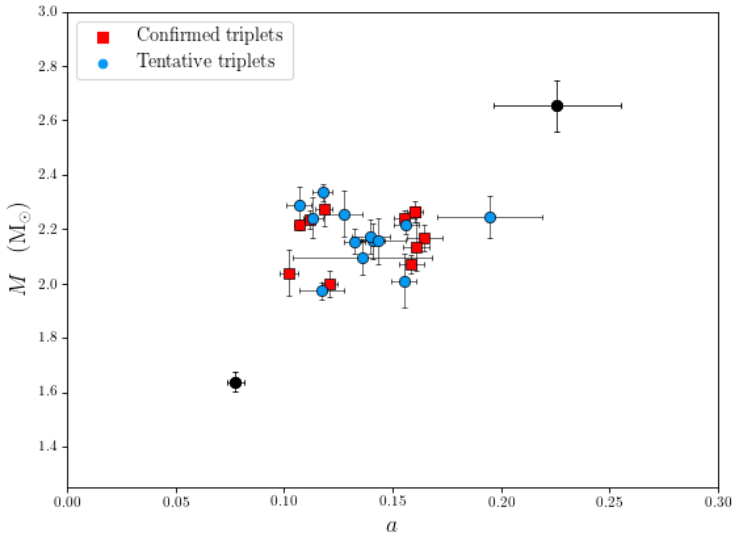

Figure D.1: The mass and spin estimates of the confirmed (red squares) and tentative (blue circles) triplets as predicted by the RPM, assuming that the measured HBO frequencies are in fact the second harmonics of non-detected fundamental frequencies. The black data points are the two tentative triplet outliers discussed in Section 3.4.2.

E

ukHz QPOs as the vertical frequency

Assuming that the upper kHz QPO is associated with the vertical epicyclic frequency ν_θ, instead of with the orbital frequency ν_ϕ (as is standard for the RPM), we calculate the spin and mass ranges for 4U1608-52 to be $0.19 < a < 0.34$ and $2.04 < M/\mathrm{M}_\odot < 2.41$, as can be seen in Figure E.1.

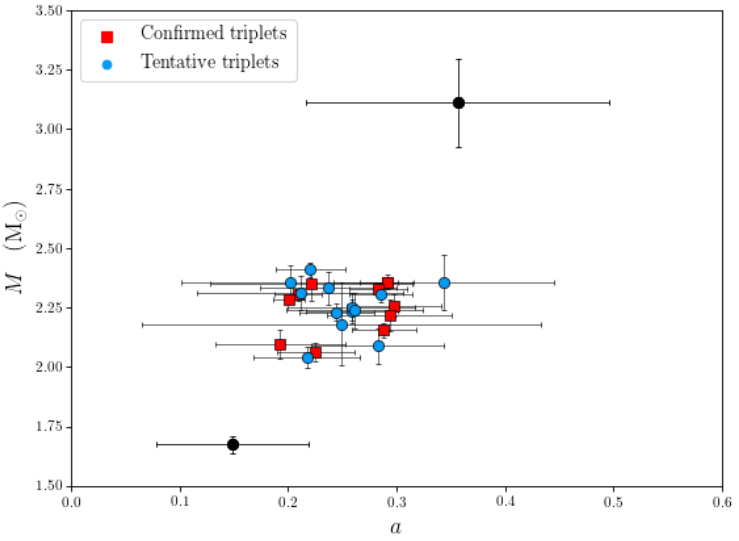

Figure E.1: The mass and spin estimates of the confirmed (red squares) and tentative (blue circles) triplets as predicted by the RPM, assuming that the measured upper kHz QPO frequencies are in fact the vertical epicyclic frequency ν_θ. The black data points are the two tentative triplet outliers discussed in Section 3.4.2.

F

VLF QPO observations: Fitting details

Table F.1: Details of the fit parameters of the PDS containing VLF QPOs, found following the *Case 1* analysis (see Section 4.4.1). Observation IDs are given in the first column, whereafter the next four columns report the center frequency, full width at half maximum (FWHM), integral power of the Lorentzian, and significance of the Lorentzians used for fitting VLF QPOs. Significance is calculated as the integral of the power of the Lorentzian divided by the negative $1\,\sigma$ error on this integral. All errors reported in this table are $1\,\sigma$ errors. The center frequency and FWHM of other Lorentzians used for fitting the remainder of the PDS are reported in the following two columns. In the case that more than one extra Lorentzian were required, the parameters are given on a new line. Obs ID 95437-01-11-06 and 95437-01-12-04 both contain QPOs separate from the VLF QPOs with significances of $4.2\,\sigma$ and $4.1\,\sigma$, respectively. These are underlined and on the second line of each of these observations in the table, and could be second harmonics of the VLF QPOs. Obs ID 95437-01-13-04 includes a peak with a significance of $2.4\,\sigma$ (on the second line of the observation), making it a relevant residual at lower frequencies, but excluding it from being a QPO by our specification requirements (see Section 4.4.3). We note that this peak could possibly be the VLF QPO of this observation, but at this point its significance excludes it from being a contender. The fitting of each observation's PDS further includes a power-law component to account for the Poisson noise, in the form $f(x) = Kx^{-\alpha}$; α is set to 0.0 for each observation, while K is fit - the value of K for each observation can be seen in the last column, along with the reduced χ^2 for each observation's fit. Due to the X-ray pulsar nature of the NS in IGR J17480-2446, a very narrow peak corresponding to the 11 Hz pulsation is visible in some PDS. We fit this peak with a Lorentzian, whereafter we fix its parameters. Obs IDs of observation PDS including the 11 Hz peak is marked with a †. Any other parameters that were fixed during PDS fitting is marked with an asterisk.

	VLF QPO Lorentzian parameters				**Other Lorentzians**			
Obs ID	**Freq. (Hz)**	**FWHM (Hz)**	**Integral power**	**Sign.**	**Freq. (Hz)**	**FWHM (Hz)**	**Reduced χ^2**	K
95437-01-02-01†	$0.0101^{+0.0011}_{-0.0008}$	0.005 ± 0.002	$7 \times 10^{-4} \pm 2 \times 10^{-4}$	$4.3\,\sigma$	0.003*	0.002*	1.1	$0.036820 \pm 7 \times 10^{-6}$
95437-01-10-05	$0.010^{+0.002}_{-0.001}$	0.006 ± 0.003	$4.0 \times 10^{-4}{}^{+1.2 \times 10^{-4}}_{-6 \times 10^{-5}}$	$6.2\,\sigma$	0.0*	7×10^{-8}*	0.97	$0.020404 \pm 5 \times 10^{-6}$
95437-01-11-03	0.016 ± 0.002	$0.006^{+0.003}_{-0.002}$	$4 \times 10^{-4} \pm 1 \times 10^{-4}$	$3.2\,\sigma$	0.0*	$5e-3$*	1.0	$0.020124 \pm 5 \times 10^{-6}$
95437-01-11-06	0.020 ± 0.001	0.005 ± 0.002	$9 \times 10^{-4} \pm 2 \times 10^{-4}$	$3.9\,\sigma$	0.002*	0.010*	1.0	$0.018638 \pm 4 \times 10^{-6}$
					$\underline{0.036^{+0.003}_{-0.002}}$	$\underline{0.015^{+0.007}_{-0.006}}$		
95437-01-12-04	$0.0175 \pm 6 \times 10^{-4}$	$0.004^{+0.002}_{-0.001}$	$1.6 \times 10^{-3} \pm 4 \times 10^{-4}$	$4.2\,\sigma$	0.0*	0.006*	0.94	$0.022009 \pm 5 \times 10^{-6}$
					$\underline{0.032^{+0.003}_{-0.002}}$	$\underline{0.012 \pm 0.003}$		
95437-01-13-04	0.029 ± 0.002	$0.009^{+0.004}_{-0.003}$	$1.2 \times 10^{-3} \pm 3 \times 10^{-4}$	$3.8\,\sigma$	$2.4 \times 10^{-3} \pm 6 \times 10^{-4}$*	$7.3 \times 10^{-3} \pm 8 \times 10^{-4}$*	0.91	$0.038919 \pm 9 \times 10^{-6}$
					$0.0175 \pm 8 \times 10^{-4}$	$0.003^{+0.003}_{-0.002}$		
95437-01-14-00	0.014 ± 0.002	0.007 ± 0.003	$2.2 \times 10^{-3} \pm 7 \times 10^{-4}$	$3.2\,\sigma$	0.0*	0.001*	0.97	$0.13629 \pm 3 \times 10^{-5}$

Bibliography

Aasi, J., LIGO Scientific Collaboration, Abbott, B. P., Abbott, R., Abbott, T., Abernathy, M. R., Ackley, K., Adams, C., Adams, T., Addesso, P., Adhikari, R. X., Adya, V., Affeldt, C., Aggarwal, N., Aguiar, O. D., Ain, A., Ajith, P., Alemic, A., Allen, B., Amariutei, D., Anderson, S. B., Anderson, W. G., Arai, K., Araya, M. C., Arceneaux, C., Areeda, J. S., Ashton, G., Ast, S., Aston, S. M., Aufmuth, P., Aulbert, C., Aylott, B. E., Babak, S., Baker, P. T., Zhu, X. J., Zucker, M. E., Zuraw, S., and Zweizig, J. (2015). Advanced LIGO. *Classical and Quantum Gravity*, 32(7):074001.

Abadie, J., Abbott, B. P., Abbott, R., Abernathy, M., Accadia, T., Acernese, F., Adams, C., Adhikari, R., Ajith, P., Allen, B., and et al. (2010). TOPICAL REVIEW: Predictions for the rates of compact binary coalescences observable by ground-based gravitational-wave detectors. *Classical and Quantum Gravity*, 27(17):173001.

Abbott, B. P., Abbott, R., Abbott, T. D., Abernathy, M. R., Acernese, F., Ackley, K., Adams, C., Adams, T., Addesso, P., Adhikari, R. X., and et al. (2016a). Astrophysical Implications of the Binary Black-hole Merger GW150914. *ApJL*, 818:L22.

Abbott, B. P., Abbott, R., Abbott, T. D., Abernathy, M. R., Acernese, F., Ackley, K., Adams, C., Adams, T., Addesso, P., Adhikari, R. X., and et al. (2016b). Observation of Gravitational Waves from a Binary Black Hole Merger. *Physical Review Letters*, 116(6):061102.

Abbott, B. P., Abbott, R., Abbott, T. D., Abernathy, M. R., Acernese, F., Ackley, K., Adams, C., Adams, T., Addesso, P., Adhikari, R. X., and et al. (2016c). Prospects for Observing and Localizing Gravitational-Wave Transients with Advanced LIGO and Advanced Virgo. *Living Reviews in Relativity*, 19:1.

Abbott, B. P., Abbott, R., Abbott, T. D., Abernathy, M. R., Ackley, K., Adams, C., Addesso, P., Adhikari, R. X., Adya, V. B., Affeldt, C., Aggarwal, N., Aguiar, O. D., Ain, A., Ajith, P., Allen, B., Altin, P. A., Anderson, S. B., Anderson, W. G., Arai, K., Araya, M. C., Arceneaux, C. C., Areeda, J. S., Arun, K. G., Ashton, G., Ast, M., Aston, S. M., Aufmuth, P., Stephens, B. C., Stone, R., Weinstein, A. J., Weiss, R., Wen, L., Weßels, P., Westphal, T., Wette, K., Zuraw, S. E., Zweizig, J., (LIGO Scientific Collaboration, and Harms, J. (2017a). Exploring the sensitivity of next generation gravitational wave detectors. *Classical and Quantum Gravity*, 34(4):044001.

Abbott, B. P., Abbott, R., Abbott, T. D., Abraham, S., Acernese, F., Ackley, K., Adams, C., Adhikari, R. X., Adya, V. B., Affeldt, C., Agathos, M., Agatsuma, K., Aggarwal, N., Aguiar, O. D., Aiello, L., Ain, A., Ajith, P., Allen, G., Allocca, A., Aloy, M. A., Altin, P. A., Amato, A., Ananyeva, A., Anderson, S. B., Anderson, W. G., Angelova, S. V., Zelenova, T., Zendri, J.-P., Zevin, M., Zhang, J., Zhang, L., Zhang, T., Zhao, C., Zhou, M., Zhou, Z., Zhu, X. J., Zimmerman, A. B., Zlochower, Y., Zucker, M. E., and Zweizig, J. (2019b). Gwtc-1: A gravitational-wave transient catalog of compact binary

mergers observed by ligo and virgo during the first and second observing runs. *Phys. Rev. X*, 9:031040.

Abbott, B. P., Abbott, R., Abbott, T. D., Abraham, S., Acernese, F., Ackley, K., Adams, C., Adhikari, R. X., Adya, V. B., Affeldt, C., Agathos, M., Agatsuma, K., Aggarwal, N., Aguiar, O. D., Aiello, L., Ain, A., Ajith, P., Allen, G., Allocca, A., Aloy, M. A., Altin, P. A., Amato, A., and Anand, S. (2020a). GW190425: Observation of a Compact Binary Coalescence with Total Mass $\sim$ 3.4 M. *ApJ*, 892(1):L3.

Abbott, B. P., Abbott, R., Abbott, T. D., Abraham, S., Acernese, F., Ackley, K., Adams, C., Adhikari, R. X., Adya, V. B., Affeldt, C., Agathos, M., Agatsuma, K., Aggarwal, N., Aguiar, O. D., Aiello, L., Ain, A., Ajith, P., Allen, G., Allocca, A., Zhou, Z., Zhu, X. J., Zimmerman, A. B., Zlochower, Y., Zucker, M. E., and and, J. Z. (2019a). Binary black hole population properties inferred from the first and second observing runs of advanced LIGO and advanced virgo. *The Astrophysical Journal*, 882(2):L24.

Abbott, B. P., Abbott, R., Abbott, T. D., Acernese, F., Ackley, K., Adams, C., Adams, T., Addesso, P., Adhikari, R. X., Adya, V. B., Affeldt, C., Afrough, M., and Agarwal, B. (2017b). GW170817: Observation of Gravitational Waves from a Binary Neutron Star Inspiral. *Phys. Rev. Lett.*, 119(16):161101.

Abbott, B. P., Abbott, R., Abbott, T. D., Acernese, F., Ackley, K., Adams, C., Adams, T., Addesso, P., Adhikari, R. X., Adya, V. B., Affeldt, C., and Agarwal, B. (2018a). GW170817: Measurements of Neutron Star Radii and Equation of State. *Phys. Rev. Lett.*, 121(16):161101.

Abbott, B. P., Abbott, R., Abbott, T. D., Acernese, F., Ackley, K., Adams, C., Adams, T., Addesso, P., Adhikari, R. X., Adya, V. B., and et al. (2017c). GW170608: Observation of a 19 Solar-mass Binary Black Hole Coalescence. *ApJ*, 851:L35.

Abbott, B. P., The LIGO Scientific Collaboration, the Virgo Collaboration, Abbott, R., Abbott, T. D., Abraham, S., Acernese, F., and Ackley, K. (2018b). GWTC-1: A Gravitational-Wave Transient Catalog of Compact Binary Mergers Observed by LIGO and Virgo during the First and Second Observing Runs. *arXiv e-prints*, page arXiv:1811.12907.

Abbott, R., Abbott, T. D., Abraham, S., Acernese, F., Ackley, K., Adams, A., Adams, C., Adhikari, R. X., Adya, V. B., Affeldt, C., Agathos, M., Agatsuma, K., Aggarwal, N., Aguiar, O. D., Aiello, L., Ain, A., Ajith, P., and Akcay, S. (2020b). GWTC-2: Compact Binary Coalescences Observed by LIGO and Virgo During the First Half of the Third Observing Run. *arXiv e-prints*, page arXiv:2010.14527.

Abbott, R., Abbott, T. D., Abraham, S., Acernese, F., Ackley, K., et al. (2020c). Properties and astrophysical implications of the 150 Msun binary black hole merger GW190521. *arXiv e-prints*, page arXiv:2009.01190.

Abbott, R., Abbott, T. D., Abraham, S., Acernese, F., et al. (2020d). GW190521: A Binary Black Hole Merger with a Total Mass of 150 $M_{\odot}$. *arXiv e-prints*, page arXiv:2009.01075.

Abbott, R., The LIGO Scientific Collaboration, the Virgo Collaboration, Abbott, T. D., Abraham, S., Acernese, F., Ackley, K., Adams, C., Adhikari, R. X., Adya, V. B., Affeldt, C., Agathos, M., Agatsuma, K., Aggarwal, N., Aguiar, O. D., Aich, A., Aiello, L., Ain,

A., Ajith, P., Allen, G., Allocca, A., Altin, P. A., Amato, A., Anand, S., Ananyeva, A., Anderson, S. B., Anderson, W. G., Zhou, Z., Zhu, X. J., Zimmerman, A. B., Zucker, M. E., and Zweizig, J. (2019). Open data from the first and second observing runs of Advanced LIGO and Advanced Virgo. *arXiv e-prints*, page arXiv:1912.11716.

Abramovici, A., Althouse, W. E., Drever, R. W. P., Gursel, Y., Kawamura, S., Raab, F. J., Shoemaker, D., Sievers, L., Spero, R. E., Thorne, K. S., Vogt, R. E., Weiss, R., Whitcomb, S. E., and Zucker, M. E. (1992). LIGO: The Laser Interferometer Gravitational-Wave Observatory. *Science*, 256(5055):325–333.

Ajith, P., Hannam, M., Husa, S., Chen, Y., Brügmann, B., Dorband, N., Müller, D., Ohme, F., Pollney, D., Reisswig, C., Santamaría, L., and Seiler, J. (2011). Inspiral-Merger-Ringdown Waveforms for Black-Hole Binaries with Nonprecessing Spins. *Physical Review Letters*, 106(24):241101.

Al-Mamun, M., Steiner, A. W., Nättilä, J., Lange, J., O'Shaughnessy, R., Tews, I., Gandolfi, S., Heinke, C., and Han, S. (2021). Combining Electromagnetic and Gravitational-Wave Constraints on Neutron-Star Masses and Radii. *Phys. Rev. Lett.*, 126(6):061101.

Altamirano, D., Homan, J., Linares, M., Patruno, A., Yang, Y., Watts, A., Kalamkar, M., Casella, P., Armas-Padilla, M., Cavecchi, Y., Degenaar, N., Russell, D., Kaur, R., van der Klis, M., Rea, N., and Wijnands, R. (2010a). The transient neutron star LMXB in the globular cluster Terzan 5 has turned into a Z-source. *The Astronomer's Telegram*, 2952:1.

Altamirano, D., Ingram, A., van der Klis, M., Wijnands, R., Linares, M., and Homan, J. (2012). Low-frequency Quasi-periodic Oscillation from the 11 Hz Accreting Pulsar in Terzan 5: Not Frame Dragging. *ApJL*, 759:L20.

Altamirano, D., van der Klis, M., Méndez, M., Jonker, P. G., Klein-Wolt, M., and Lewin, W. H. G. (2008a). X-Ray Time Variability Across the Atoll Source States of 4U 1636-53. *ApJ*, 685:436–450.

Altamirano, D., van der Klis, M., Wijnands, R., and Cumming, A. (2008b). Millihertz Oscillation Frequency Drift Predicts the Occurrence of Type I X-Ray Bursts. *ApJ*, 673(1):L35.

Altamirano, D., Watts, A., Kalamkar, M., Homan, J., Yang, Y., Casella, P., Linares, M., Patruno, A., Armas-Padilla, M., Cavecchi, Y., Degenaar, N., Kaur, R., van der Klis, M., Rea, N., and Wijnands, R. (2010b). Discovery of 11 Hz burst oscillations from the 11 Hz Eclipsing Pulsar in Terzan 5. *The Astronomer's Telegram*, 2932:1.

Alves, J., Zucker, C., Goodman, A. A., Speagle, J. S., Meingast, S., Robitaille, T., Finkbeiner, D. P., Schlafly, E. F., and Green, G. M. (2020). A Galactic-scale gas wave in the solar neighbourhood. *Nature*, 578(7794):237–239.

Amaro-Seoane, P., Aoudia, S., Babak, S., Binétruy, P., Berti, E., Bohé, A., Caprini, C., Colpi, M., Cornish, N. J., Danzmann, K., Dufaux, J.-F., Gair, J., Jennrich, O., Jetzer, P., Klein, A., Lang, R. N., Lobo, A., Littenberg, T., McWilliams, S. T., Nelemans, G., Petiteau, A., Porter, E. K., Schutz, B. F., Sesana, A., Stebbins, R., Sumner, T., Vallisneri, M., Vitale, S., Volonteri, M., and Ward, H. (2012). Low-frequency gravitational-wave science with eLISA/NGO. *Classical and Quantum Gravity*, 29(12):124016.

Antelis, J. M. and Moreno, C. (2017). Erratum: Erratum to: Obtaining gravitational waves from inspiral binary systems using LIGO data. *European Physical Journal Plus*, 132(2):103.

Antoja, T., Helmi, A., Romero-Gómez, M., Katz, D., Babusiaux, C., Drimmel, R., Evans, D. W., Figueras, F., Poggio, E., Reylé, C., Robin, A. C., Seabroke, G., and Soubiran, C. (2018). A dynamically young and perturbed Milky Way disk. *Nature*, 561(7723):360–362.

Antoniadis, J., Freire, P. C. C., Wex, N., Tauris, T. M., Lynch, R. S., van Kerkwijk, M. H., Kramer, M., Bassa, C., Dhillon, V. S., Driebe, T., Hessels, J. W. T., Kaspi, V. M., Kondratiev, V. I., and Langer, N. (2013). A Massive Pulsar in a Compact Relativistic Binary. *Science*, 340:448.

Antonini, F. and Rasio, F. A. (2016). Merging Black Hole Binaries in Galactic Nuclei: Implications for Advanced-LIGO Detections. *ApJ*, 831(2):187.

Antonini, F., Toonen, S., and Hamers, A. S. (2017). Binary Black Hole Mergers from Field Triples: Properties, Rates, and the Impact of Stellar Evolution. *ApJ*, 841(2):77.

Arnaud, K. A. (1996). XSPEC: The First Ten Years. In G. H. Jacoby & J. Barnes, editor, *Astronomical Data Analysis Software and Systems V*, volume 101 of *Astronomical Society of the Pacific Conference Series*, pages 17–+.

Arnett, W. D. (1982). Type I supernovae. I - Analytic solutions for the early part of the light curve. *ApJ*, 253:785–797.

Bahramian, A., Heinke, C. O., Sivakoff, G. R., Altamirano, D., Wijnands, R., Homan, J., Linares, M., Pooley, D., Degenaar, N., and Gladstone, J. C. (2014). Discovery of the Third Transient X-Ray Binary in the Galactic Globular Cluster Terzan 5. *ApJ*, 780(2):127.

Bambi, C., Malafarina, D., and Tsukamoto, N. (2014). Note on the effect of a massive accretion disk in the measurements of black hole spins. *Physical Review D*, 89(12):127302.

Banerjee, S., Baumgardt, H., and Kroupa, P. (2010). Stellar-mass black holes in star clusters: implications for gravitational wave radiation. *MNRAS*, 402(1):371–380.

Bardeen, J. M. and Petterson, J. A. (1975). The Lense-Thirring Effect and Accretion Disks around Kerr Black Holes. *ApJ*, 195:L65.

Bardeen, J. M., Press, W. H., and Teukolsky, S. A. (1972). Rotating Black Holes: Locally Nonrotating Frames, Energy Extraction, and Scalar Synchrotron Radiation. *ApJ*, 178:347–370.

Barret, D. (2013). Soft Lags in Neutron Star kHz Quasi-periodic Oscillations: Evidence for Reverberation? *ApJ*, 770:9.

Beer, M. E. and Podsiadlowski, P. (2002). The quiescent light curve and the evolutionary state of GRO J1655-40. *MNRAS*, 331:351–360.

Belczynski, K., Dominik, M., Bulik, T., O'Shaughnessy, R., Fryer, C., and Holz, D. E. (2010). The Effect of Metallicity on the Detection Prospects for Gravitational Waves. *ApJL*, 715:L138–L141.

Belczynski, K., Heger, A., Gladysz, W., Ruiter, A. J., Woosley, S., Wiktorowicz, G., Chen,

H. Y., Bulik, T., O'Shaughnessy, R., Holz, D. E., Fryer, C. L., and Berti, E. (2016). The effect of pair-instability mass loss on black-hole mergers. *A&A*, 594:A97.

Belczynski, K., Klencki, J., Fields, C. E., Olejak, A., Berti, E., Meynet, G., Fryer, C. L., Holz, D. E., O'Shaughnessy, R., Brown, D. A., Bulik, T., Leung, S. C., Nomoto, K., Madau, P., Hirschi, R., Jones, S., Mondal, S., Chruslinska, M., Drozda, P., Gerosa, D., Doctor, Z., Giersz, M., Ekstrom, S., Georgy, C., Askar, A., Wysocki, D., Natan, T., Farr, W. M., Wiktorowicz, G., Miller, M. C., Farr, B., and Lasota, J. P. (2017). The evolutionary roads leading to low effective spins, high black hole masses, and O1/O2 rates of LIGO/Virgo binary black holes. *arXiv e-prints*, page arXiv:1706.07053.

Belczynski, K., Klencki, J., Fields, C. E., Olejak, A., Berti, E., Meynet, G., Fryer, C. L., Holz, D. E., O'Shaughnessy, R., Brown, D. A., Bulik, T., Leung, S. C., Nomoto, K., Madau, P., Hirschi, R., Kaiser, E., Jones, S., Mondal, S., Chruslinska, M., Drozda, P., Gerosa, D., Doctor, Z., Giersz, M., Ekstrom, S., Georgy, C., Askar, A., Baibhav, V., Wysocki, D., Natan, T., Farr, W. M., Wiktorowicz, G., Coleman Miller, M., Farr, B., and Lasota, J. P. (2020). Evolutionary roads leading to low effective spins, high black hole masses, and O1/O2 rates for LIGO/Virgo binary black holes. *A&A*, 636:A104.

Belloni, T. and Hasinger, G. (1990). An atlas of aperiodic variability in HMXB. *A&A*, 230:103–119.

Belloni, T., Homan, J., Casella, P., van der Klis, M., Nespoli, E., Lewin, W. H. G., Miller, J. M., and Méndez, M. (2005). The evolution of the timing properties of the black-hole transient GX 339-4 during its 2002/2003 outburst. *A&A*, 440(1):207–222.

Belloni, T., Homan, J., Motta, S., Ratti, E., and Méndez, M. (2007). Rossi XTE monitoring of 4U1636-53 - I. Long-term evolution and kHz quasi-periodic oscillations. *MNRAS*, 379:247–252.

Belloni, T. M., Sanna, A., and Méndez, M. (2012). High-frequency quasi-periodic oscillations in black hole binaries. *MNRAS*, 426:1701–1709.

Belokurov, V., Penoyre, Z., Oh, S., Iorio, G., Hodgkin, S., Evans, N. W., Everall, A., Koposov, S. E., Tout, C. A., Izzard, R., Clarke, C. J., and Brown, A. G. A. (2020). Unresolved stellar companions with Gaia DR2 astrometry. *MNRAS*, 496(2):1922–1940.

Bethe, H. A. (1939a). Energy production in stars. *Phys. Rev.*, 55:103–103.

Bethe, H. A. (1939b). Energy production in stars. *Phys. Rev.*, 55:434–456.

Bhattacharyya, S. (2002). Temperature Profiles and Spectra of Accretion Disks around Rapidly Rotating Neutron Stars. *arXiv e-prints*, pages astro–ph/0205133.

Blaauw, A. (1961). On the origin of the O- and B-type stars with high velocities (the "run-away" stars), and some related problems. *Bull. Astron. Inst. Netherlands*, 15:265.

Blouin, S., Dufour, P., and Allard, N. F. (2018). A New Generation of Cool White Dwarf Atmosphere Models. I. Theoretical Framework and Applications to DZ Stars. *ApJ*, 863(2):184.

Bogdanov, S., Guillot, S., Ray, P. S., Wolff, M. T., Chakrabarty, D., Ho, W. C. G., Kerr, M., Lamb, F. K., Lommen, A., Ludlam, R. M., Milburn, R., Montano, S., Miller, M. C., Bauböck, M., Özel, F., Psaltis, D., Remillard, R. A., Riley, T. E., Steiner, J. F., Strohmayer, T. E., Watts, A. L., Wood, K. S., Zeldes, J., Enoto, T., Okajima,

T., Kellogg, J. W., Baker, C., Markwardt, C. B., Arzoumanian, Z., and Gendreau, K. C. (2019). Constraining the Neutron Star Mass-Radius Relation and Dense Matter Equation of State with NICER. I. The Millisecond Pulsar X-Ray Data Set. *ApJ*, 887(1):L25.

Bond, J. R., Arnett, W. D., and Carr, B. J. (1984). The evolution and fate of Very Massive Objects. *ApJ*, 280:825–847.

Bordas, P., Kuulkers, E., Alfonso-Garzón, J., Beckmann, V., Bird, T., Chenevez, S. B. J., Courvoisier, T., Del Santo, M., Domingo, A., Ebisawa, K., Ferrigno, C., Jonker, P., Kretschmar, P., Markwardt, C., Oosterbroek, T., Paizis, A., Pottschmidt, K., Sánchez-Fernández, C., and Wijnand s, R. (2010). A hard X-ray transient in the direction of Terzan 5 detected by INTEGRAL. *The Astronomer's Telegram*, 2919:1.

Boss, A. P. (1992). *Formation of Binary Stars*, page 355. Kluwer Academic.

Bradt, H. V., Rothschild, R. E., and Swank, J. H. (1993). X-ray timing explorer mission. *A&AS*, 97:355–360.

Brandt, W. N. and Podsiadlowski, P. (1994). The Effects of High-Velocity Supernova Kicks on the Orbital Properties and Sky Distributions of Neutron Star Binaries. *ArXiv Astrophysics e-prints*.

Brandt, W. N., Podsiadlowski, P., and Sigurdsson, S. (1995). On the high space velocity of X-ray Nova SCO 1994: implications for the formation of its black hole. *MNRAS*, 277:L35–L40.

Brott, I., de Mink, S. E., Cantiello, M., Langer, N., de Koter, A., Evans, C. J., Hunter, I., Trundle, C., and Vink, J. S. (2011a). Rotating massive main-sequence stars. I. Grids of evolutionary models and isochrones. *A&A*, 530:A115.

Brott, I., Evans, C. J., Hunter, I., de Koter, A., Langer, N., Dufton, P. L., Cantiello, M., Trundle, C., Lennon, D. J., de Mink, S. E., Yoon, S.-C., and Anders, P. (2011b). Rotating massive main-sequence stars. II. Simulating a population of LMC early B-type stars as a test of rotational mixing. *A&A*, 530:A116.

Bulik, T. and Belczyński, K. (2003). Constraints on the Binary Evolution from Chirp Mass Measurements. *ApJL*, 589:L37–L40.

Burgay, M., D'Amico, N., Possenti, A., Manchester, R. N., Lyne, A. G., Joshi, B. C., McLaughlin, M. A., Kramer, M., Sarkissian, J. M., Camilo, F., Kalogera, V., Kim, C., and Lorimer, D. R. (2003). An increased estimate of the merger rate of double neutron stars from observations of a highly relativistic system. *Nat*, 426:531–533.

Cabanac, C., Henri, G., Petrucci, P.-O., Malzac, J., Ferreira, J., and Belloni, T. M. (2010). Variability of X-ray binaries from an oscillating hot corona. *MNRAS*, 404:738–748.

Cadelano, M., Ransom, S. M., Freire, P. C. C., Ferraro, F. R., Hessels, J. W. T., Lanzoni, B., Pallanca, C., and Stairs, I. H. (2018). Discovery of Three New Millisecond Pulsars in Terzan 5. *ApJ*, 855(2):125.

Cantat-Gaudin, T., Jordi, C., Vallenari, A., Bragaglia, A., Balaguer-Núñez, L., Soubiran, C., Bossini, D., Moitinho, A., Castro-Ginard, A., Krone-Martins, A., Casamiquela, L., Sordo, R., and Carrera, R. (2018). A Gaia DR2 view of the open cluster population in the Milky Way. *A&A*, 618:A93.

Cantat-Gaudin, T., Mapelli, M., Balaguer-Núñez, L., Jordi, C., Sacco, G., and Vallenari, A. (2019). A ring in a shell: the large-scale 6D structure of the Vela OB2 complex. *A&A*, 621:A115.

Carr, B., Kühnel, F., and Sandstad, M. (2016). Primordial black holes as dark matter. *Phys. Rev. D*, 94(8):083504.

Carr, B. J. and Hawking, S. W. (1974). Black holes in the early Universe. *MNRAS*, 168:399–416.

Casagrande, L., Portinari, L., and Flynn, C. (2006). Accurate fundamental parameters for lower main-sequence stars. *MNRAS*, 373(1):13–44.

Casella, P., Belloni, T., and Stella, L. (2005). The ABC of Low-Frequency Quasi-periodic Oscillations in Black Hole Candidates: Analogies with Z Sources. *ApJ*, 629:403–407.

Castelvecchi, D. (2019). Gravitational-wave observatory LIGO set to double its detecting power. *Nature*, 566:305.

Castro-Ginard, A., Jordi, C., Luri, X., Julbe, F., Morvan, M., Balaguer-Núñez, L., and Cantat-Gaudin, T. (2018). A new method for unveiling open clusters in Gaia. New nearby open clusters confirmed by DR2. *A&A*, 618:A59.

Cavecchi, Y., Patruno, A., Haskell, B., Watts, A. L., Levin, Y., Linares, M., Altamirano, D., Wijnands, R., and van der Klis, M. (2011). Implications of Burst Oscillations from the Slowly Rotating Accreting Pulsar IGR J17480-2446 in the Globular Cluster Terzan 5. *ApJ*, 740(1):L8.

Chakrabarti, S. K., Debnath, D., Nandi, A., and Pal, P. S. (2008). Evolution of the quasi-periodic oscillation frequency in GRO J1655-40 - Implications for accretion disk dynamics. *A&A*, 489(3):L41–L44.

Chakraborty, M. and Bhattacharyya, S. (2010). Terzan 5 transient IGR J17480-2446: return of thermonuclear bursts or were they always there? *The Astronomer's Telegram*, 3044:1.

Chakraborty, M. and Bhattacharyya, S. (2011). X-ray Bursts from the Terzan 5 Transient IGR J17480-2446: Nuclear Rather than Gravitational. *ApJ*, 730(2):L23.

Chan, C., Müller, B., Heger, A., Pakmor, R., and Springel, V. (2018). Black Hole Formation and Fallback during the Supernova Explosion of a 40 M Star. *ApJ*, 852(1):L19.

Chenevez, J., Kuulkers, E., Alfonso-Garzón, J., Beckmann, V., Bird, T., Bordas, P., Brandt, S., Courvoisier, T., Del Santo, M., Domingo, A., Ebisawa, K., Ferrigno, C., Jonker, P., Kretschmar, P., Markwardt, C., Oosterbroek, T., Paizis, A., Pottschmidt, K., Sánchez-Fern&Ández, C., and Wijnands, R. (2010). Further INTEGRAL observations of the transient X-ray burster EXO 1745-248. *The Astronomer's Telegram*, 2924:1.

Cherchneff, I. and Dwek, E. (2009). The Chemistry of Population III Supernova Ejecta. I. Formation of Molecules in the Early Universe. *ApJ*, 703(1):642–661.

Choksi, N., Volonteri, M., Colpi, M., Gnedin, O. Y., and Li, H. (2019). The Star Clusters That Make Black Hole Binaries across Cosmic Time. *ApJ*, 873(1):100.

Christensen-Dalsgaard, J. (2008). *Lecture Notes on Stellar Structure and Evolution*. Institut for Fysik og Astronomi, Aarhus Universitet, Aarhus, Denmark.

Chruslinska, M. and Nelemans, G. (2019). Metallicity of stars formed throughout the cosmic history based on the observational properties of star-forming galaxies. *MNRAS*, 488(4):5300–5326.

Chruslinska, M., Nelemans, G., and Belczynski, K. (2019). The influence of the distribution of cosmic star formation at different metallicities on the properties of merging double compact objects. *MNRAS*, 482(4):5012–5017.

Church, M. J., Halai, G. S., and Bałucińska-Church, M. (2006). An explanation of the Z-track sources. *A&A*, 460:233–244.

Clementini, G., Ripepi, V., Molinaro, R., Garofalo, A., Muraveva, T., Rimoldini, L., Guy, L. P., Jevardat de Fombelle, G., Nienartowicz, K., Marchal, O., Audard, M., Holl, B., Leccia, S., Marconi, M., Musella, I., Mowlavi, N., Lecoeur-Taibi, I., Eyer, L., De Ridder, J., Regibo, S., Sarro, L. M., Szabados, L., Evans, D. W., and Riello, M. (2019). Gaia Data Release 2. Specific characterisation and validation of all-sky Cepheids and RR Lyrae stars. *A&A*, 622:A60.

Cordoni, G., Milone, A. P., Marino, A. F., Di Criscienzo, M., D'Antona, F., Dotter, A., Lagioia, E. P., and Tailo, M. (2018). Extended Main-sequence Turnoff as a Common Feature of Milky Way Open Clusters. *ApJ*, 869(2):139.

Cromartie, H. T., Fonseca, E., Ransom, S. M., Demorest, P. B., Arzoumanian, Z., Blumer, H., Brook, P. R., DeCesar, M. E., Dolch, T., Ellis, J. A., Ferdman, R. D., Ferrara, E. C., Garver-Daniels, N., Gentile, P. A., Jones, M. L., Lam, M. T., Lorimer, D. R., Lynch, R. S., McLaughlin, M. A., Ng, C., Nice, D. J., Pennucci, T. T., Spiewak, R., Stairs, I. H., Stovall, K., Swiggum, J. K., and Zhu, W. W. (2020). Relativistic Shapiro delay measurements of an extremely massive millisecond pulsar. *Nature Astronomy*, 4:72–76.

Crowther, P. A. (2006). Wolf-Rayet Populations at High Metallicity. *arXiv e-prints*, pages astro–ph/0608076.

Crowther, P. A. (2007). Physical Properties of Wolf-Rayet Stars. *ARA&A*, 45(1):177–219.

Cui, W., Zhang, S. N., and Chen, W. (1998). Evidence for Frame Dragging around Spinning Black Holes in X-Ray Binaries. *ApJ*, 492:L53–L57.

Cummings, J. D., Kalirai, J. S., Tremblay, P. E., Ramirez-Ruiz, E., and Choi, J. (2018). The White Dwarf Initial-Final Mass Relation for Progenitor Stars from 0.85 to 7.5 M . *ApJ*, 866(1):21.

Curtis, G. (2019). Properties of gravitational waves from binary black holes in the local universe. Master's thesis, University College London.

de Avellar, M. G. B., Méndez, M., Altamirano, D., Sanna, A., and Zhang, G. (2016). Phase lags of quasi-periodic oscillations across source states in the low-mass X-ray binary 4U 1636-53. *MNRAS*, 461:79–92.

de Avellar, M. G. B., Méndez, M., Sanna, A., and Horvath, J. E. (2013). Time lags of the kilohertz quasi-periodic oscillations in the low-mass X-ray binaries 4U 1608-52 and 4U 1636-53. *MNRAS*, 433:3453–3463.

de Mink, S. E., Cantiello, M., Langer, N., Pols, O. R., Brott, I., and Yoon, S.-C. (2009). Rotational mixing in massive binaries. Detached short-period systems. *A&A*, 497:243–253.

de Mink, S. E. and Mandel, I. (2016a). Merging binary black holes formed through chemically homogeneous evolution in short-period stellar binaries. *MNRAS*, 458:2634–2647.

de Mink, S. E. and Mandel, I. (2016b). The chemically homogeneous evolutionary channel for binary black hole mergers: Rates and Properties of gravitational-wave events detectable by advanced LIGO. *MNRAS*.

Demorest, P. B., Pennucci, T., Ransom, S. M., Roberts, M. S. E., and Hessels, J. W. T. (2010). A two-solar-mass neutron star measured using Shapiro delay. *Nature*, 467:1081–1083.

Di Carlo, U. N., Giacobbo, N., Mapelli, M., Pasquato, M., Spera, M., Wang, L., and Haardt, F. (2019). Merging black holes in young star clusters. *MNRAS*, 487(2):2947–2960.

Di Carlo, U. N., Mapelli, M., Bouffanais, Y., Giacobbo, N., Santoliquido, F., Bressan, A., Spera, M., and Haardt, F. (2020). Binary black holes in the pair instability mass gap. *MNRAS*, 497(1):1043–1049.

Di Salvo, T., Méndez, M., and van der Klis, M. (2003). On the correlated spectral and timing properties of 4U 1636-53: An atoll source at high accretion rates. *A&A*, 406:177–192.

Dominik, M., Berti, E., O'Shaughnessy, R., Mandel, I., Belczynski, K., Fryer, C., Holz, D. E., Bulik, T., and Pannarale, F. (2015). Double Compact Objects III: Gravitational-wave Detection Rates. *ApJ*, 806:263.

Done, C. and Gierliński, M. (2003). Observing the effects of the event horizon in black holes. *MNRAS*, 342(4):1041–1055.

Done, C., Gierlinski, M., and Kubota, A. (2007). Modelling the behaviour of accretion flows in X-ray binaries. Everything you always wanted to know about accretion but were afraid to ask. *A&A*, 15:1–66.

Dotani, T., Inoue, H., Mitsuda, K., Nagase, F., Negoro, H., Ueda, Y., Makishima, K., Kubota, A., Ebisawa, K., and Tanaka, Y. (1997). ASCA Observation of Cygnus X-1 in the Soft State: Mass of the Compact Object. *ApJ*, 485(2):L87–L90.

du Buisson, L., Marchant, P., Podsiadlowski, P., Kobayashi, C., Abdalla, F. B., Taylor, P., Mandel, I., de Mink, S. E., Moriya, T. J., and Langer, N. (2020). Cosmic Rates of Black Hole Mergers and Pair-Instability Supernovae from Chemically Homogeneous Binary Evolution. *arXiv e-prints*, page arXiv:2002.11630.

du Buisson, L., Motta, S., and Fender, R. (2019). Mass and spin measurements for the neutron star 4U1608-52 through the relativistic precession model. *MNRAS*, 486(4):4485–4497.

du Buisson, L., Motta, S., and Fender, R. (2021). Very low-frequency oscillations from the 11 Hz pulsar in Terzan 5: frame dragging back on the table. *MNRAS*, 502(4):5472–5479.

Dunn, R. J. H., Fender, R. P., Körding, E. G., Belloni, T., and Cabanac, C. (2010). A global spectral study of black hole X-ray binaries. *MNRAS*, 403:61–82.

Duquennoy, A. and Mayor, M. (1991). Multiplicity among solar-type stars in the solar neighbourhood. II - Distribution of the orbital elements in an unbiased sample. *A&A*, 500:337–376.

Eddington, A. S. (1924). On the relation between the masses and luminosities of the stars. *MNRAS*, 84:308–332.

Eggleton, P. P. (1983). Aproximations to the radii of Roche lobes. *ApJ*, 268:368–369.

El-Badry, K., Rix, H.-W., and Weisz, D. R. (2018). An Empirical Measurement of the Initial-Final Mass Relation with Gaia White Dwarfs. *ApJ*, 860(2):L17.

Estabrook, F. B. (1985). Response functions of free mass gravitational wave antennas. *General Relativity and Gravitation*, 17(8):719–724.

Farmer, R., Renzo, M., de Mink, S. E., Marchant, P., and Justham, S. (2019). Mind the Gap: The Location of the Lower Edge of the Pair-instability Supernova Black Hole Mass Gap. *ApJ*, 887(1):53.

Farr, W. M., Stevenson, S., Miller, M. C., Mandel, I., Farr, B., and Vecchio, A. (2017). Distinguishing spin-aligned and isotropic black hole populations with gravitational waves. *Nature*, 548:426–429.

Ferraro, F. R., Dalessandro, E., Mucciarelli, A., Beccari, G., Rich, R. M., Origlia, L., Lanzoni, B., Rood, R. T., Valenti, E., Bellazzini, M., Ransom, S. M., and Cocozza, G. (2009). The cluster Terzan 5 as a remnant of a primordial building block of the Galactic bulge. *Nature*, 462(7272):483–486.

Ferraro, F. R., Massari, D., Dalessandro, E., Lanzoni, B., Origlia, L., Rich, R. M., and Mucciarelli, A. (2016). The Age of the Young Bulge-like Population in the Stellar System Terzan 5: Linking the Galactic Bulge to the High-z Universe. *ApJ*, 828(2):75.

Ferraro, F. R., Pallanca, C., Lanzoni, B., Crociati, C., Dalessandro, E., Origlia, L., Rich, R. M., Saracino, S., Mucciarelli, A., Valenti, E., Geisler, D., Mauro, F., Villanova, S., Moni Bidin, C., and Beccari, G. (2020). A new class of fossil fragments from the hierarchical assembly of the Galactic bulge. *arXiv e-prints*, page arXiv:2011.09966.

Forward, R. L. (1978). Wideband laser-interferometer gravitational-radiation experiment. *Phys. Rev. D*, 17(2):379–390.

Fowler, W. A. and Hoyle, F. (1964). Neutrino Processes and Pair Formation in Massive Stars and Supernovae. *ApJS*, 9:201.

Fragione, G. and Kocsis, B. (2018). Black Hole Mergers from an Evolving Population of Globular Clusters. *Phys. Rev. Lett.*, 121(16):161103.

Fraley, G. S. (1968). Supernovae Explosions Induced by Pair-Production Instability. *Ap&SS*, 2:96–114.

Frank, J., King, A., and Raine, D. J. (2002). *Accretion Power in Astrophysics: Third Edition*.

Frohmaier, C., Angus, C. R., Vincenzi, M., Sullivan, M., Smith, M., Nugent, P. E., Cenko,

S. B., Gal-Yam, A., Kulkarni, S. R., Law, N. M., and Quimby, R. M. (2021). From core collapse to superluminous: the rates of massive stellar explosions from the Palomar Transient Factory. *MNRAS*, 500(4):5142–5158.

Fryer, C. L. (1999). Mass limits for black hole formation. *The Astrophysical Journal*, 522(1):413–418.

Fryer, C. L., Woosley, S. E., and Heger, A. (2001). Pair-Instability Supernovae, Gravity Waves, and Gamma-Ray Transients. *ApJ*, 550(1):372–382.

Gaia Collaboration, Prusti, T., de Bruijne, J. H. J., Brown, A. G. A., and Vallenari, A. (2016). The Gaia mission. *A&A*, 595:A1.

Gaia Collaboration, Smart, R. L., Sarro, L. M., Rybizki, J., Reylé, C., Robin, A. C., Hambly, N. C., Abbas, U., Barstow, M. A., de Bruijne, J. H. J., Bucciarelli, B., Carrasco, J. M., Cooper, W. J., Hodgkin, S. T., Masana, E., Michalik, D., Sahlmann, J., Sozzetti, A., Brown, A. G. A., Vallenari, A., Prusti, T., Babusiaux, C., and Biermann, M. (2020). Gaia Early Data Release 3: The Gaia Catalogue of Nearby Stars. *arXiv e-prints*, page arXiv:2012.02061.

Gal-Yam, A., Mazzali, P., Ofek, E. O., Nugent, P. E., Kulkarni, S. R., Kasliwal, M. M., Quimby, R. M., Filippenko, A. V., Cenko, S. B., Chornock, R., Waldman, R., Kasen, D., Sullivan, M., Beshore, E. C., Drake, A. J., Thomas, R. C., Bloom, J. S., Poznanski, D., Miller, A. A., Foley, R. J., Silverman, J. M., Arcavi, I., Ellis, R. S., and Deng, J. (2009). Supernova 2007bi as a pair-instability explosion. *Nature*, 462(7273):624–627.

Galloway, D. K., Muno, M. P., Hartman, J. M., Psaltis, D., and Chakrabarty, D. (2008). Thermonuclear (Type I) X-Ray Bursts Observed by the Rossi X-Ray Timing Explorer. *ApJS*, 179:360–422.

Gentile Fusillo, N. P., Tremblay, P.-E., Gänsicke, B. T., Manser, C. J., Cunningham, T., Cukanovaite, E., Hollands, M., Marsh, T., Raddi, R., Jordan, S., Toonen, S., Geier, S., Barstow, M., and Cummings, J. D. (2019). A Gaia Data Release 2 catalogue of white dwarfs and a comparison with SDSS. *MNRAS*, 482(4):4570–4591.

Gerosa, D. and Berti, E. (2017). Are merging black holes born from stellar collapse or previous mergers? *Phys. Rev. D*, 95(12):124046.

Gierliński, M. and Done, C. (2002a). A comment on the colour-colour diagrams of low-mass X-ray binaries. *MNRAS*, 331:L47–L50.

Gierliński, M. and Done, C. (2002b). The X-ray spectrum of the atoll source 4U 1608-52. *MNRAS*, 337(4):1373–1380.

Gierliński, M., Zdziarski, A. A., Poutanen, J., Coppi, P. S., Ebisawa, K., and Johnson, W. N. (1999). Radiation mechanisms and geometry of Cygnus X-1 in the soft state. *MNRAS*, 309(2):496–512.

Gilfanov, M., Revnivtsev, M., and Molkov, S. (2003). Boundary layer, accretion disk and X-ray variability in the luminous LMXBs. *A&A*, 410:217–230.

Gomez, S., Berger, E., Nicholl, M., Blanchard, P. K., Villar, V. A., Patton, L., Chornock, R., Leja, J., Hosseinzadeh, G., and Cowperthwaite, P. S. (2019). SN 2016iet: The Pulsational or Pair Instability Explosion of a Low-metallicity Massive CO Core Embedded in a Dense Hydrogen-poor Circumstellar Medium. *ApJ*, 881(2):87.

Grevesse, N., Noels, A., and Sauval, A. J. (1996). Standard Abundances. In Holt, S. S. and Sonneborn, G., editors, *Cosmic Abundances*, volume 99 of *Astronomical Society of the Pacific Conference Series*, page 117.

Haardt, F. and Maraschi, L. (1993). X-Ray Spectra from Two-Phase Accretion Disks. *ApJ*, 413:507.

Hamann, W. R., Koesterke, L., and Wessolowski, U. (1995). Spectral analyses of the Galactic Wolf-Rayet stars: hydrogen-helium abundances and improved stellar parameters for the WN class. *A&A*, 299:151.

Hariharan, P. (2006). *Basics of interferometry [electronic resource]*. Ebook central. Elsevier Academic Press, Boston.

Hartman, Z. D. and Lepine, S. (2020). VizieR Online Data Catalog: SUPERWIDE: wide binaries in Gaia & SUPERBLINK (Hartman+, 2020). *VizieR Online Data Catalog*, page J/ApJS/247/66.

Hasinger, G. and van der Klis, M. (1989). Two patterns of correlated X-ray timing and spectral behaviour in low-mass X-ray binaries. *A&A*, 225:79–96.

Heger, A., Cumming, A., and Woosley, S. E. (2007). Millihertz Quasi-periodic Oscillations from Marginally Stable Nuclear Burning on an Accreting Neutron Star. *ApJ*, 665(2):1311–1320.

Heger, A., Fryer, C. L., Woosley, S. E., Langer, N., and Hartmann, D. H. (2003). How Massive Single Stars End Their Life. *ApJ*, 591(1):288–300.

Heger, A. and Langer, N. (2000). Presupernova Evolution of Rotating Massive Stars. II. Evolution of the Surface Properties. *ApJ*, 544:1016–1035.

Heger, A. and Woosley, S. E. (2002). The Nucleosynthetic Signature of Population III. *ApJ*, 567:532–543.

Heggie, D. and Hut, P. (2003). BOOK REVIEW: The Gravitational Million-Body Problem: A Multidisciplinary Approach to Star Cluster Dynamics. *Classical and Quantum Gravity*, 20(20):4504–4505.

Heggie, D. C. (1975). Binary evolution in stellar dynamics. *MNRAS*, 173:729–787.

Helmi, A., Babusiaux, C., Koppelman, H. H., Massari, D., Veljanoski, J., and Brown, A. G. A. (2018). The merger that led to the formation of the Milky Way's inner stellar halo and thick disk. *Nature*, 563(7729):85–88.

Herzig, K., El Eid, M. F., Fricke, K. J., and Langer, N. (1990). Theoretical light curves for exploding massive Wolf-Rayet stars. *AAP*, 233:462–473.

Hild, S., Chelkowski, S., and Freise, A. (2008). Pushing towards the ET sensitivity using 'conventional' technology. *arXiv e-prints*, page arXiv:0810.0604.

Hobbs, G., Lorimer, D. R., Lyne, A. G., and Kramer, M. (2005). A statistical study of 233 pulsar proper motions. *MNRAS*, 360:974–992.

Hobson, M. P., Efstathiou, G. P., and Lasenby, A. N. (2006). *General Relativity*. Cambridge University Press.

Homan, J., van der Klis, M., Fridriksson, J. K., Remillard, R. A., Wijnands, R., Méndez, M., Lin, D., Altamirano, D., Casella, P., Belloni, T. M., and Lewin, W. H. G. (2010). XTE J1701-462 and Its Implications for the Nature of Subclasses in Low-magnetic-field Neutron Star Low-mass X-ray Binaries. *ApJ*, 719(1):201–212.

Homan, J., Wijnands, R., van der Klis, M., Belloni, T., van Paradijs, J., Klein-Wolt, M., Fender, R., and Méndez, M. (2001). Correlated X-Ray Spectral and Timing Behavior of the Black Hole Candidate XTE J1550-564: A New Interpretation of Black Hole States. *ApJS*, 132:377–402.

Hong, J., Vesperini, E., Askar, A., Giersz, M., Szkudlarek, M., and Bulik, T. (2018). Binary black hole mergers from globular clusters: the impact of globular cluster properties. *MNRAS*, 480(4):5645–5656.

Horvath, J. E. and de Souza, R. A. (2017). The stifness of the supranuclear equation of state (once again). In *Journal of Physics Conference Series*, volume 861 of *Journal of Physics Conference Series*, page 012010.

Hoyle, F. (1953). On the Fragmentation of Gas Clouds Into Galaxies and Stars. *ApJ*, 118:513.

Hulse, R. A. and Taylor, J. H. (1975). Discovery of a pulsar in a binary system. *ApJL*, 195:L51–L53.

Hwang, H.-C., Ting, Y.-S., Schlaufman, K. C., Zakamska, N. L., and Wyse, R. F. G. (2020). The non-monotonic, strong metallicity dependence of the wide-binary fraction. *MNRAS*.

Hynes, R. I. (2010). Multiwavelength Observations of Accretion in Low-Mass X-ray Binary Systems. *arXiv e-prints*, page arXiv:1010.5770.

Iben, Icko, J. (1967). Stellar Evolution Within and off the Main Sequence. *ARA&A*, 5:571.

Iben, Icko, J. and Livio, M. (1993). Common Envelopes in Binary Star Evolution. *PASP*, 105:1373.

Igoshev, A. and Verbunt, F. (2018). Natal kicks of neutron stars. In *American Astronomical Society Meeting Abstracts #231*, volume 231 of *American Astronomical Society Meeting Abstracts*, page 132.03.

Ingram, A. and Done, C. (2010). A physical interpretation of the variability power spectral components in accreting neutron stars. *MNRAS*, 405:2447–2452.

Ingram, A. and Done, C. (2012a). Modelling variability in black hole binaries: linking simulations to observations. *MNRAS*, 419:2369–2378.

Ingram, A. and Done, C. (2012b). The effect of frame dragging on the iron Kα line in X-ray binaries. *MNRAS*, 427(2):934–947.

Ingram, A., Done, C., and Fragile, P. C. (2009). Low-frequency quasi-periodic oscillations spectra and Lense-Thirring precession. *MNRAS*, 397:L101–L105.

Ingram, A. and Motta, S. (2014). Solutions to the relativistic precession model. *MNRAS*, 444:2065–2070.

Ingram, A. and Motta, S. (2020). A review of quasi-periodic oscillations from black hole X-ray binaries: observation and theory. *arXiv e-prints*, page arXiv:2001.08758.

Ingram, A. and van der Klis, M. (2015). Phase-resolved spectroscopy of low-frequency quasi-periodic oscillations in GRS 1915+105. *MNRAS*, 446(4):3516–3525.

Ingram, A., van der Klis, M., Middleton, M., Altamirano, D., and Uttley, P. (2017). Tomographic reflection modelling of quasi-periodic oscillations in the black hole binary H 1743-322. *MNRAS*, 464(3):2979–2991.

Ingram, A., van der Klis, M., Middleton, M., Done, C., Altamirano, D., Heil, L., Uttley, P., and Axelsson, M. (2016). A quasi-periodic modulation of the iron line centroid energy in the black hole binary H1743-322. *MNRAS*, 461(2):1967–1980.

Jahoda, K., Markwardt, C. B., Radeva, Y., Rots, A. H., Stark, M. J., Swank, J. H., Strohmayer, T. E., and Zhang, W. (2006). Calibration of the Rossi X-Ray Timing Explorer Proportional Counter Array. *ApJS*, 163:401–423.

Jahoda, K., Swank, J. H., Giles, A. B., Stark, M. J., Strohmayer, T., Zhang, W., and Morgan, E. H. (1996). In-orbit performance and calibration of the Rossi X-ray Timing Explorer (RXTE) Proportional Counter Array (PCA). In Siegmund, O. H. and Gummin, M. A., editors, *EUV, X-Ray, and Gamma-Ray Instrumentation for Astronomy VII*, volume 2808 of *Proc. SPIE*, pages 59–70.

Janka, H.-T. (2012). Explosion Mechanisms of Core-Collapse Supernovae. *Annual Review of Nuclear and Particle Science*, 62:407–451.

Janka, H. T. (2013). Natal kicks of stellar mass black holes by asymmetric mass ejection in fallback supernovae. *MNRAS*, 434:1355–1361.

Joyce, S. R. G., Barstow, M. A., Casewell, S. L., Burleigh, M. R., Holberg, J. B., and Bond, H. E. (2018). Testing the white dwarf mass-radius relation and comparing optical and far-UV spectroscopic results with Gaia DR2, HST, and FUSE. *MNRAS*, 479(2):1612–1626.

Kankare, E., Efstathiou, A., Kotak, R., Kool, E. C., Kangas, T., O'Neill, D., Mattila, S., Vaisanen, P., Ramphul, R., Mogotsi, M., Ryder, S. D., Parker, S., Reynolds, T., Fraser, M., Pastorello, A., Cappellaro, E., Mazzali, P. A., Ochner, P., Tomasella, L., Turatto, M., Kotilainen, J., Kuncarayakti, H., Perez-Torres, M. A., Randriamanakoto, Z., Romero-Canizales, C., Berton, M., Cartier, R., Chen, T. W., Galbany, L., Gromadzki, M., Inserra, C., Maguire, K., Moran, S., Muller-Bravo, T. E., Nicholl, M., Reguitti, A., and Young, D. R. (2021). Core-collapse supernova subtypes in luminous infrared galaxies. *arXiv e-prints*, page arXiv:2102.13512.

Kasen, D., Woosley, S. E., and Heger, A. (2011). Pair Instability Supernovae: Light Curves, Spectra, and Shock Breakout. *ApJ*, 734(2):102.

Kato, S. (2001). Basic Properties of Thin-Disk Oscillations [1]. *PASJ*, 53(1):1–24.

Kato, S. and Fukue, J. (1980). Trapped Radial Oscillations of Gaseous Disks around a Black Hole. *PASJ*, 32:377.

Kato, S., Fukue, J., and Mineshige, S. (2008). *Black-Hole Accretion Disks — Towards a New Paradigm —*.

Kerr, R. P. (1963). Gravitational field of a spinning mass as an example of algebraically special metrics. *Phys. Rev. Lett.*, 11:237–238.

Kilic, M., Bergeron, P., Dame, K., Hambly, N. C., Rowell, N., and Crawford, C. L. (2019). The age of the Galactic stellar halo from Gaia white dwarfs. *MNRAS*, 482(1):965–979.

Kilic, M., Hermes, J. J., Córsico, A. H., Kosakowski, A., Brown, W. R., Antoniadis, J., Calcaferro, L. M., Gianninas, A., Althaus, L. G., and Green, M. J. (2018). A refined search for pulsations in white dwarf companions to millisecond pulsars. *MNRAS*, 479(1):1267–1272.

Kim, C., Kalogera, V., and Lorimer, D. R. (2003). The Probability Distribution of Binary Pulsar Coalescence Rates. I. Double Neutron Star Systems in the Galactic Field. *ApJ*, 584:985–995.

King, A. R., Frank, J., Kolb, U., and Ritter, H. (1997). Transients among Binaries with Evolved Low-Mass Companions. *ApJ*, 484(2):844–847.

King, A. R. and Ritter, H. (1998). The light curves of soft X-ray transients. *MNRAS*, 293(1):L42–L48.

Kobayashi, C., Umeda, H., Nomoto, K., Tominaga, N., and Ohkubo, T. (2006). Galactic Chemical Evolution: Carbon through Zinc. *ApJ*, 653:1145–1171.

Kobulnicky, H. A. and Fryer, C. L. (2007). A New Look at the Binary Characteristics of Massive Stars. *ApJ*, 670(1):747–765.

Köhler, K., Langer, N., de Koter, A., de Mink, S. E., Crowther, P. A., Evans, C. J., Gräfener, G., Sana, H., Sanyal, D., Schneider, F. R. N., and Vink, J. S. (2015). The evolution of rotating very massive stars with LMC composition. *A&A*, 573:A71.

Królak, A. and Patil, M. (2017). The First Detection of Gravitational Waves. *Universe*, 3(3):59.

Kroupa, P. (2001). On the variation of the initial mass function. *MNRAS*, 322:231–246.

Kruckow, M. U., Tauris, T. M., Langer, N., Szécsi, D., Marchant, P., and Podsiadlowski, P. (2016). Common-envelope ejection in massive binary stars. Implications for the progenitors of GW150914 and GW151226. *A&A*, 596:A58.

Langer, N. (1992). Helium enrichment in massive early type stars. *A&A*, 265:L17–L20.

Langer, N., Norman, C. A., de Koter, A., Vink, J. S., Cantiello, M., and Yoon, S. C. (2007). Pair creation supernovae at low and high redshift. *A&A*, 475(2):L19–L23.

Lanzoni, B., Ferraro, F. R., Dalessandro, E., Mucciarelli, A., Beccari, G., Miocchi, P., Bellazzini, M., Rich, R. M., Origlia, L., Valenti, E., Rood, R. T., and Ransom, S. M. (2010). New Density Profile and Structural Parameters of the Complex Stellar System Terzan 5. *ApJ*, 717(2):653–657.

Lasota, J.-P. (2001). The disc instability model of dwarf novae and low-mass X-ray binary transients. *New A Rev.*, 45(7):449–508.

Lasota, J.-P. (2016). *Black Hole Accretion Discs*, volume 440, page 1.

Levine, A. M., Bradt, H., Cui, W., Jernigan, J. G., Morgan, E. H., Remillard, R., Shirey,

R. E., and Smith, D. A. (1996). First Results from the All-Sky Monitor on the Rossi X-Ray Timing Explorer. *ApJL*, 469:L33.

Lewin, W. H. G., van Paradijs, J., and van der Klis, M. (1988). A review of quasi-periodic oscillations in low-mass X-ray binaries. *Space Sci. Rev.*, 46(3-4):273–377.

Lim, B., Rauw, G., Nazé, Y., Sung, H., Hwang, N., and Park, B.-G. (2019). Extended main sequence turn-off originating from a broad range of stellar rotational velocities. *Nature Astronomy*, 3:76–81.

Limongi, M. and Chieffi, A. (2018). Presupernova Evolution and Explosive Nucleosynthesis of Rotating Massive Stars in the Metallicity Range -3 $\leq$ [Fe/H] $\leq$ 0. *ApJS*, 237(1):13.

Lin, D., Remillard, R. A., and Homan, J. (2007). Evaluating Spectral Models and the X-Ray States of Neutron Star X-Ray Transients. *ApJ*, 667:1073–1086.

Lin, D., Remillard, R. A., and Homan, J. (2009). Spectral States of XTE J1701 - 462: Link Between Z and Atoll Sources. *ApJ*, 696:1257–1277.

Linares, M., Altamirano, D., Watts, A., van der Klis, M., Wijnands, R., Homan, J., Casella, P., Patruno, A., Armas-Padilla, M., Cavecchi, Y., Degenaar, N., Kalamkar, M., Kaur, R., Yang, Y., and Rea, N. (2010). Discovery of mHz QPOs and burst rate evolution in the active Terzan 5 neutron star transient. *The Astronomer's Telegram*, 2958:1.

Linares, M., Chakrabarty, D., and van der Klis, M. (2011). On the Cooling Tails of Thermonuclear X-ray Bursts: The IGR J17480-2446 Link. *ApJ*, 733(2):L17.

Linares, M., Shahbaz, T., and Casares, J. (2018). Peering into the Dark Side: Magnesium Lines Establish a Massive Neutron Star in PSR J2215+5135. *ApJ*, 859:54.

Lindegren, L., Perryman, M. A., Bastian, U., Dainty, J. C., Hog, E., van Leeuwen, F., Kovalevsky, J., Labeyrie, A., Loiseau, S., Mignard, F., Noordam, J. E., Le Poole, R. S., Thejll, P., and Vakili, F. (1994). GAIA: global astrometric interferometer for astrophysics. In Breckinridge, J. B., editor, *Amplitude and Intensity Spatial Interferometry II*, volume 2200 of *Society of Photo-Optical Instrumentation Engineers (SPIE) Conference Series*, pages 599–608.

Lipunov, V. M., Postnov, K. A., and Prokhorov, M. E. (1997). Formation and coalescence of relativistic binary stars: the effect of kick velocity. *MNRAS*, 288:245–259.

Lodato, G. and Facchini, S. (2013). Wave-like warp propagation in circumbinary discs - II. Application to KH 15D. *MNRAS*, 433:2157–2164.

Maccarone, T. J. and Coppi, P. S. (2003). Hysteresis in the light curves of soft X-ray transients. *MNRAS*, 338(1):189–196.

Machida, M. and Matsumoto, R. (2008). Excitation of Low-Frequency QPOs in Black-Hole Accretion Flows. *PASJ*, 60:613.

Mackey, A. D., Wilkinson, M. I., Davies, M. B., and Gilmore, G. F. (2007). The effect of stellar-mass black holes on the structural evolution of massive star clusters. *MNRAS*, 379(1):L40–L44.

Madau, P. and Dickinson, M. (2014). Cosmic Star-Formation History. *ARA&A*, 52:415–486.

Maeder, A. (1987). Evidences for a bifurcation in massive star evolution. The ON-blue stragglers. *A&A*, 178:159–169.

Maggiore, M. (2008). *Gravitational Waves Volume 1: Theory and Experiments*. Oxford University Press, Oxford, United Kingdom.

Malhan, K., Ibata, R. A., and Martin, N. F. (2018). Ghostly tributaries to the Milky Way: charting the halo's stellar streams with the Gaia DR2 catalogue. *MNRAS*, 481(3):3442–3455.

Mancuso, G. C., Altamirano, D., Méndez, M., Lyu, M., and Combi, J. A. (2021). Drifts of the marginally stable burning frequency in the X-ray binaries 4U 1608-52 and Aql X-1. *MNRAS*, 502(2):1856–1863.

Mandel, I. (2016). Estimates of black hole natal kick velocities from observations of low-mass X-ray binaries. *MNRAS*, 456:578–581.

Mandel, I., Haster, C.-J., Dominik, M., and Belczynski, K. (2015). Distinguishing types of compact-object binaries using the gravitational-wave signatures of their mergers. *MNRAS*, 450:L85–L89.

Mandel, I. and O'Shaughnessy, R. (2010). Compact binary coalescences in the band of ground-based gravitational-wave detectors. *Classical and Quantum Gravity*, 27(11):114007.

Mapelli, M., Spera, M., Montanari, E., Limongi, M., Chieffi, A., Giacobbo, N., Bressan, A., and Bouffanais, Y. (2020). Impact of the Rotation and Compactness of Progenitors on the Mass of Black Holes. *ApJ*, 888(2):76.

Marchant, P., Langer, N., Podsiadlowski, P., Tauris, T. M., de Mink, S., Mandel, I., and Moriya, T. J. (2017). Ultra-luminous X-ray sources and neutron-star-black-hole mergers from very massive close binaries at low metallicity. *A&A*, 604:A55.

Marchant, P., Langer, N., Podsiadlowski, P., Tauris, T. M., and Moriya, T. J. (2016). A new route towards merging massive black holes. *A&A*, 588:A50.

Marchant, P., Renzo, M., Farmer, R., Pappas, K. M. W., Taam, R. E., de Mink, S., and Kalogera, V. (2018). Pulsational pair-instability supernovae in very close binaries. *arXiv e-prints*, page arXiv:1810.13412.

Marchant, P., Renzo, M., Farmer, R., Pappas, K. M. W., Taam, R. E., de Mink, S. E., and Kalogera, V. (2019). Pulsational Pair-instability Supernovae in Very Close Binaries. *ApJ*, 882(1):36.

Marchetti, T. (2020). Gaia EDR3 in 6D: Searching for unbound stars in the Galaxy. *arXiv e-prints*, page arXiv:2012.02123.

Marchetti, T., Rossi, E. M., and Brown, A. G. A. (2019). Gaia DR2 in 6D: searching for the fastest stars in the Galaxy. *MNRAS*, 490(1):157–171.

Marchetti, T., Rossi, E. M., Kordopatis, G., Brown, A. G. A., Rimoldi, A., Starkenburg, E., Youakim, K., and Ashley, R. (2017). An artificial neural network to discover hypervelocity stars: candidates in Gaia DR1/TGAS. *MNRAS*, 470(2):1388–1403.

Marino, A. F., Milone, A. P., Casagrande, L., Przybilla, N., Balaguer-Núñez, L., Di

Criscienzo, M., Serenelli, A., and Vilardell, F. (2018a). Discovery of Extended Main Sequence Turnoffs in Galactic Open Clusters. *ApJ*, 863(2):L33.

Marino, A. F., Przybilla, N., Milone, A. P., Da Costa, G., D'Antona, F., Dotter, A., and Dupree, A. (2018b). Different Stellar Rotations in the Two Main Sequences of the Young Globular Cluster NGC 1818: The First Direct Spectroscopic Evidence. *AJ*, 156(3):116.

Marshall, F. E., Wijnands, R., and van der Klis, M. (1998). SAX J1808.4-3658 = XTE J1808-369. *IAUCIRC*, 6876.

Massari, D., Breddels, M. A., Helmi, A., Posti, L., Brown, A. G. A., and Tolstoy, E. (2018). Three-dimensional motions in the Sculptor dwarf galaxy as a glimpse of a new era. *Nature Astronomy*, 2:156–161.

Massari, D., Mucciarelli, A., Dalessand ro, E., Ferraro, F. R., Origlia, L., Lanzoni, B., Beccari, G., Rich, R. M., Valenti, E., and Ransom, S. M. (2012). High-resolution Reddening Map in the Direction of the Stellar System Terzan 5. *ApJ*, 755(2):L32.

Massari, D., Mucciarelli, A., Ferraro, F. R., Origlia, L., Rich, R. M., Lanzoni, B., Dalessand ro, E., Valenti, E., Ibata, R., Lovisi, L., Bellazzini, M., and Reitzel, D. (2014). Ceci N'est Pas a Globular Cluster: The Metallicity Distribution of the Stellar System Terzan 5. *ApJ*, 795(1):22.

McClintock, J. E., Narayan, R., and Steiner, J. F. (2014). Black Hole Spin via Continuum Fitting and the Role of Spin in Powering Transient Jets. *Space Science Reviews*, 183:295–322.

McConnell, M. L., Ryan, J. M., Collmar, W., Schönfelder, V., Steinle, H., Strong, A. W., Bloemen, H., Hermsen, W., Kuiper, L., Bennett, K., Phlips, B. F., and Ling, J. C. (2000). A High-Sensitivity Measurement of the MeV Gamma-Ray Spectrum of Cygnus X-1. *ApJ*, 543(2):928–937.

Medvedev, M. V. (2004). Boundary Layer Self-Similar Solution for the Hot Radiative Accretion onto a Rapidly Spinning Neutron Star. *ApJ*, 613(1):506–511.

Medvedev, M. V. and Narayan, R. (2001). Self-similar Hot Accretion Flow onto a Neutron Star. *ApJ*, 554(2):1255–1267.

Meingast, S. and Alves, J. (2019). Extended stellar systems in the solar neighborhood. I. The tidal tails of the Hyades. *A&A*, 621:L3.

Melis, C., Zuckerman, B., Dufour, P., Song, I., and Klein, B. (2018). The First Polluted White Dwarf from Gaia DR2: The Cool DAZ Gaia J1738-0826. *Research Notes of the American Astronomical Society*, 2(2):64.

Méndez, M., Altamirano, D., Belloni, T., and Sanna, A. (2013). The phase lags of high-frequency quasi-periodic oscillations in four black hole candidates. *MNRAS*, 435:2132–2140.

Merloni, A., Vietri, M., Stella, L., and Bini, D. (1999). On gravitomagnetic precession around black holes. *MNRAS*, 304:155–159.

Meynet, G. and Maeder, A. (2005). Stellar evolution with rotation. XI. Wolf-Rayet star populations at different metallicities. *A&A*, 429:581–598.

Michelson, A. A. and Morley, E. W. (1887). On the Relative Motion of the Earth and of the Luminiferous Ether. *Sidereal Messenger*, 6:306–310.

Middleditch, J. and Priedhorsky, W. C. (1986). Discovery of rapid quasi-periodic oscillations in Scorpius X-1. *ApJ*, 306:230–237.

Miller, J. M., Maitra, D., Cackett, E. M., Bhattacharyya, S., and Strohmayer, T. E. (2011). A Fast X-ray Disk Wind in the Transient Pulsar IGR J17480-2446 in Terzan 5. *ApJ*, 731(1):L7.

Miller, M. C., Lamb, F. K., Dittmann, A. J., Bogdanov, S., Arzoumanian, Z., Gendreau, K. C., Guillot, S., Harding, A. K., Ho, W. C. G., Lattimer, J. M., Ludlam, R. M., Mahmoodifar, S., Morsink, S. M., Ray, P. S., Strohmayer, T. E., Wood, K. S., Enoto, T., Foster, R., Okajima, T., Prigozhin, G., and Soong, Y. (2019). PSR J0030+0451 Mass and Radius from NICER Data and Implications for the Properties of Neutron Star Matter. *ApJ*, 887(1):L24.

Misner, C. W., Thorne, K. S., and Wheeler, J. A. (1973). *Gravity*. W. H. Freeman and Company, San Francisco.

Mitsuda, K., Inoue, H., Koyama, K., Makishima, K., Matsuoka, M., Ogawara, Y., Shibazaki, N., Suzuki, K., Tanaka, Y., and Hirano, T. (1984). Energy spectra of low-mass binary X-ray sources observed from Tenma. *PASJ*, 36:741–759.

Mitsuda, K., Inoue, H., Nakamura, N., and Tanaka, Y. (1989). Luminosity-related changes of the energy spectrum of X 1608-522. *PASJ*, 41:97–111.

Mokiem, M. R., de Koter, A., Vink, J. S., Puls, J., Evans, C. J., Smartt, S. J., Crowther, P. A., Herrero, A., Langer, N., Lennon, D. J., Najarro, F., and Villamariz, M. R. (2007). The empirical metallicity dependence of the mass-loss rate of O- and early B-type stars. *A&A*, 473:603–614.

Molteni, D., Sponholz, H., and Chakrabarti, S. K. (1996). Resonance Oscillation of Radiative Shock Waves in Accretion Disks around Compact Objects. *ApJ*, 457:805.

Moriya, T. J., Jiang, J.-a., Yasuda, N., Kokubo, M., Kawana, K., Maeda, K., Pan, Y.-C., Quimby, R. M., Suzuki, N., Takahashi, I., Tanaka, M., Tominaga, N., Nomoto, K., Cooke, J., Galbany, L., González-Gaitán, S., Lee, C.-H., and Pignata, G. (2021). Constraints on the Rate of Supernovae Lasting for More Than a Year from Subaru/Hyper Suprime-Cam. *ApJ*, 908(2):249.

Motta, S., D'Aì, A., Papitto, A., Riggio, A., Di Salvo, T., Burderi, L., Belloni, T., Stella, L., and Iaria, R. (2011). X-ray bursts and burst oscillations from the slowly spinning X-ray pulsar IGR J174802446 (Terzan 5). *Monthly Notices of the Royal Astronomical Society*, 414(2):1508–1516.

Motta, S., Homan, J., Muñoz Darias, T., Casella, P., Belloni, T. M., Hiemstra, B., and Méndez, M. (2012). Discovery of two simultaneous non-harmonically related quasi-periodic oscillations in the 2005 outburst of the black hole binary GRO J1655-40. *MNRAS*, 427:595–606.

Motta, S. E., Belloni, T. M., Stella, L., Muñoz-Darias, T., and Fender, R. (2014a). Precise mass and spin measurements for a stellar-mass black hole through X-ray timing: the case of GRO J1655-40. *MNRAS*, 437:2554–2565.

Motta, S. E., Franchini, A., Lodato, G., and Mastroserio, G. (2018). On the different flavours of Lense-Thirring precession around accreting stellar mass black holes. *MNRAS*, 473:431–439.

Motta, S. E., Muñoz-Darias, T., Sanna, A., Fender, R., Belloni, T., and Stella, L. (2014b). Black hole spin measurements through the relativistic precession model: XTE J1550-564. *MNRAS*, 439:L65–L69.

Motta, S. E., Rouco-Escorial, A., Kuulkers, E., Muñoz-Darias, T., and Sanna, A. (2017). Links between quasi-periodic oscillations and accretion states in neutron star low-mass X-ray binaries. *MNRAS*, 468:2311–2324.

Muñoz-Darias, T., Fender, R. P., Motta, S. E., and Belloni, T. M. (2014). Black hole-like hysteresis and accretion states in neutron star low-mass X-ray binaries. *MNRAS*, 443:3270–3283.

Muñoz-Darias, T., Motta, S., and Belloni, T. M. (2011). Fast variability as a tracer of accretion regimes in black hole transients. *MNRAS*, 410:679–684.

Mukherjee, A., Messenger, C., and Riles, K. (2018). Accretion-induced spin-wandering effects on the neutron star in Scorpius X-1: Implications for continuous gravitational wave searches. *Phys. Rev. D*, 97(4):043016.

Muno, M. P., Remillard, R. A., and Chakrabarty, D. (2002). How Do Z and Atoll X-Ray Binaries Differ? *ApJ*, 568(1):L35–L39.

Myeong, G. C., Vasiliev, E., Iorio, G., Evans, N. W., and Belokurov, V. (2019). Evidence for two early accretion events that built the Milky Way stellar halo. *MNRAS*, 488(1):1235–1247.

Naoz, S. (2016). The Eccentric Kozai-Lidov Effect and Its Applications. *ARA&A*, 54:441–489.

Narayan, R., Piran, T., and Shemi, A. (1991). Neutron star and black hole binaries in the Galaxy. *ApJL*, 379:L17–L20.

Neijssel, C. J., Vigna-Gómez, A., Stevenson, S., Barrett, J. W., Gaebel, S. M., Broekgaarden, F. S., de Mink, S. E., Szécsi, D., Vinciguerra, S., and Mandel, I. (2019). The effect of the metallicity-specific star formation history on double compact object mergers. *MNRAS*, 490(3):3740–3759.

Nelemans, G., Tauris, T. M., and van den Heuvel, E. P. J. (1999). Constraints on mass ejection in black hole formation derived from black hole X-ray binaries. *A&A*, 352:L87–L90.

Nicholl, M., Smartt, S. J., Jerkstrand, A., Inserra, C., McCrum, M., Kotak, R., Fraser, M., Wright, D., Chen, T. W., Smith, K., Young, D. R., Sim, S. A., Valenti, S., Howell, D. A., Bresolin, F., Kudritzki, R. P., Tonry, J. L., Huber, M. E., Rest, A., Pastorello, A., Tomasella, L., Cappellaro, E., Benetti, S., Mattila, S., Kankare, E., Kangas, T., Leloudas, G., Sollerman, J., Taddia, F., Berger, E., Chornock, R., Narayan, G., Stubbs, C. W., Foley, R. J., Lunnan, R., Soderberg, A., Sanders, N., Milisavljevic, D., Margutti, R., Kirshner, R. P., Elias-Rosa, N., Morales-Garoffolo, A., Taubenberger, S., Botticella, M. T., Gezari, S., Urata, Y., Rodney, S., Riess, A. G., Scolnic, D., Wood-Vasey, W. M., Burgett, W. S., Chambers, K., Flewelling, H. A., Magnier, E. A., Kaiser, N.,

Metcalfe, N., Morgan, J., Price, P. A., Sweeney, W., and Waters, C. (2013). Slowly fading super-luminous supernovae that are not pair-instability explosions. *Nature*, 502(7471):346–349.

Nitz, A. H., Dent, T., Davies, G. S., Kumar, S., Capano, C. D., Harry, I., Mozzon, S., Nuttall, L., Lundgren, A., and Tápai, M. (2019). 2-OGC: Open Gravitational-wave Catalog of binary mergers from analysis of public Advanced LIGO and Virgo data. *arXiv e-prints*, page arXiv:1910.05331.

Nomoto, K., Kobayashi, C., and Tominaga, N. (2013). Nucleosynthesis in Stars and the Chemical Enrichment of Galaxies. *ARA&A*, 51:457–509.

Novikov, I. D. and Thorne, K. S. (1973). Astrophysics of black holes. In *Black Holes (Les Astres Occlus)*, pages 343–450.

Nowak, M. A., Vaughan, B. A., Wilms, J., Dove, J. B., and Begelman, M. C. (1999). Rossi X-Ray Timing Explorer Observation of Cygnus X-1. II. Timing Analysis. *ApJ*, 510:874–891.

O'Neill, S. M., Reynolds, C. S., Miller, M. C., and Sorathia, K. A. (2011). Low-frequency Oscillations in Global Simulations of Black Hole Accretion. *ApJ*, 736(2):107.

Origlia, L., Massari, D., Rich, R. M., Mucciarelli, A., Ferraro, F. R., Dalessandro, E., and Lanzoni, B. (2013). The Terzan 5 Puzzle: Discovery of a Third, Metal-poor Component. *ApJ*, 779(1):L5.

Origlia, L., Rich, R. M., Ferraro, F. R., Lanzoni, B., Bellazzini, M., Dalessandro, E., Mucciarelli, A., Valenti, E., and Beccari, G. (2011). Spectroscopy Unveils the Complex Nature of Terzan 5. *ApJ*, 726(2):L20.

Orosz, J. A., McClintock, J. E., Narayan, R., Bailyn, C. D., Hartman, J. D., Macri, L., Liu, J., Pietsch, W., Remillard, R. A., Shporer, A., and Mazeh, T. (2007). A 15.65-solar-mass black hole in an eclipsing binary in the nearby spiral galaxy M 33. *Nature*, 449:872–875.

O'Shaughnessy, R. and Kim, C. (2010). Pulsar Binary Birthrates with Spin-opening Angle Correlations. *ApJ*, 715:230–241.

Ourique, G., Romero, A. D., Kepler, S. O., Koester, D., and Amaral, L. A. (2019). A study of cool white dwarfs in the Sloan Digital Sky Survey Data Release 12. *MNRAS*, 482(1):649–657.

Özel, F. and Freire, P. (2016). Masses, Radii, and the Equation of State of Neutron Stars. *ARA&A*, 54:401–440.

Paczynski, B. (1976). Common Envelope Binaries. In Eggleton, P., Mitton, S., and Whelan, J., editors, *Structure and Evolution of Close Binary Systems*, volume 73 of *IAU Symposium*, page 75.

Papitto, A., D'Aì, A., Motta, S., Riggio, A., Burderi, L., di Salvo, T., Belloni, T., and Iaria, R. (2011). The spin and orbit of the newly discovered pulsar IGR J17480-2446. *A&A*, 526:L3.

Patruno, A., Alpar, M. A., van der Klis, M., and van den Heuvel, E. P. J. (2012). The Peculiar Evolutionary History of IGR J17480-2446 in Terzan 5. *ApJ*, 752(1):33.

Pawar, D. D., Kalamkar, M., Altamirano, D., Linares, M., Shanthi, K., Strohmayer, T., Bhattacharya, D., and Klis, M. v. d. (2013). Discovery of twin khz quasi-periodic oscillations in the low-mass x-ray binary xte j1701â‌'407. *MNRAS*, 433(3):2436–2444.

Paxton, B., Bildsten, L., Dotter, A., Herwig, F., Lesaffre, P., and Timmes, F. (2011). Modules for Experiments in Stellar Astrophysics (MESA). *ApJS*, 192:3.

Paxton, B., Cantiello, M., Arras, P., Bildsten, L., Brown, E. F., Dotter, A., Mankovich, C., Montgomery, M. H., Stello, D., Timmes, F. X., and Townsend, R. (2013). Modules for Experiments in Stellar Astrophysics (MESA): Planets, Oscillations, Rotation, and Massive Stars. *ApJS*, 208:4.

Paxton, B., Marchant, P., Schwab, J., Bauer, E. B., Bildsten, L., Cantiello, M., Dessart, L., Farmer, R., Hu, H., Langer, N., Townsend, R. H. D., Townsley, D. M., and Timmes, F. X. (2015). Modules for Experiments in Stellar Astrophysics (MESA): Binaries, Pulsations, and Explosions. *ApJS*, 220:15.

Paxton, B., Schwab, J., Bauer, E. B., Bildsten, L., Blinnikov, S., Duffell, P., Farmer, R., Goldberg, J. A., Marchant, P., Sorokina, E., Thoul, A., Townsend, R. H. D., and Timmes, F. X. (2018). Modules for Experiments in Stellar Astrophysics (MESA): Convective Boundaries, Element Diffusion, and Massive Star Explosions. *ApJS*, 234(2):34.

Paxton, B., Smolec, R., Schwab, J., Gautschy, A., Bildsten, L., Cantiello, M., Dotter, A., Farmer, R., Goldberg, J. A., Jermyn, A. S., Kanbur, S. M., Marchant, P., Thoul, A., Townsend, R. H. D., Wolf, W. M., Zhang, M., and Timmes, F. X. (2019). Modules for Experiments in Stellar Astrophysics (MESA): Pulsating Variable Stars, Rotation, Convective Boundaries, and Energy Conservation. *ApJS*, 243(1):10.

Peille, P., Barret, D., and Uttley, P. (2015). The Spectral-timing Properties of Upper and Lower kHz QPOs. *ApJ*, 811:109.

Pelisoli, I., Bell, K. J., Kepler, S. O., and Koester, D. (2019). The sdA problem - III. New extremely low-mass white dwarfs and their precursors from Gaia astrometry. *MNRAS*, 482(3):3831–3842.

Perpinyà-Vallès, M., Rebassa-Mansergas, A., Gänsicke, B. T., Toonen, S., Hermes, J. J., Gentile Fusillo, N. P., and Tremblay, P. E. (2019). Discovery of the first resolved triple white dwarf. *MNRAS*, 483(1):901–907.

Peters, P. C. (1964). Gravitational Radiation and the Motion of Two Point Masses. *Physical Review*, 136:1224–1232.

Peters, P. C. and Mathews, J. (1963). Gravitational radiation from point masses in a keplerian orbit. *Phys. Rev.*, 131:435–440.

Phinney, E. S. (1991). The rate of neutron star binary mergers in the universe - Minimal predictions for gravity wave detectors. *ApJL*, 380:L17–L21.

Podsiadlowski, P. (2001). *Common-Envelope Evolution and Stellar Mergers*, volume 229 of *Astronomical Society of the Pacific Conference Series*, page 239.

Podsiadlowski, P. (2014). *The evolution of binary systems*, page 45–88. Canary Islands Winter School of Astrophysics. Cambridge University Press.

Pooley, D., Homan, J., Heinke, C., Linares, M., Altamirano, D., and Lewin, W. (2010).

Chandra Identification of the Transient in Terzan 5: Not the 2000 Transient. *The Astronomer's Telegram*, 2974:1.

Popham, R. and Sunyaev, R. (2001). Accretion Disk Boundary Layers around Neutron Stars: X-Ray Production in Low-Mass X-Ray Binaries. *ApJ*, 547(1):355–383.

Prestwich, A. H., Kilgard, R., Crowther, P. A., Carpano, S., Pollock, A. M. T., Zezas, A., Saar, S. H., Roberts, T. P., and Ward, M. J. (2007). The Orbital Period of the Wolf-Rayet Binary IC 10 X-1: Dynamic Evidence that the Compact Object Is a Black Hole. *ApJL*, 669:L21–L24.

Prialnik, D. (2010). *An Introduction to the Theory of Stellar Structure and Evolution*. Cambridge University Press, Cambridge, United Kingdom.

Price-Whelan, A. M., Nidever, D. L., Choi, Y., Schlafly, E. F., Morton, T., Koposov, S. E., and Belokurov, V. (2019). Discovery of a Disrupting Open Cluster Far into the Milky Way Halo: A Recent Star Formation Event in the Leading Arm of the Magellanic Stream? *ApJ*, 887(1):19.

Psaltis, D., Belloni, T., and van der Klis, M. (1999). Correlations in Quasi-periodic Oscillation and Noise Frequencies among Neutron Star and Black Hole X-Ray Binaries. *ApJ*, 520:262–270.

Rakavy, G. and Shaviv, G. (1967). Instabilities in Highly Evolved Stellar Models. *ApJ*, 148:803.

Reid, I. N. and Hawley, S. L. (2005). *New light on dark stars : red dwarfs, low-mass stars, brown dwarfs*. Springer-Verlag Berlin Heidelberg.

Repetto, S., Igoshev, A. P., and Nelemans, G. (2017). The Galactic distribution of X-ray binaries and its implications for compact object formation and natal kicks. *MNRAS*, 467:298–310.

Revnivtsev, M., Churazov, E., Gilfanov, M., and Sunyaev, R. (2001). New class of low frequency QPOs: Signature of nuclear burning or accretion disk instabilities? *A&A*, 372:138–144.

Revnivtsev, M., Sazonov, S., and Sunyaev, R. (2007). Origin of the Galactic Ridge X-Ray Emission. *Progress of Theoretical Physics Supplement*, 169:125–130.

Revnivtsev, M. G. and Gilfanov, M. R. (2006). Boundary layer emission and Z-track in the color-color diagram of luminous LMXBs. *A&A*, 453(1):253–259.

Riess, A. G., Casertano, S., Yuan, W., Macri, L., Bucciarelli, B., Lattanzi, M. G., MacKenty, J. W., Bowers, J. B., Zheng, W., Filippenko, A. V., Huang, C., and Anderson, R. I. (2018). Milky Way Cepheid Standards for Measuring Cosmic Distances and Application to Gaia DR2: Implications for the Hubble Constant. *ApJ*, 861(2):126.

Riggio, A., Burderi, L., Di Salvo, T., Papitto, A., Egron, E., Belloni, T., D'Ai', A., Iaria, R., Floris, M., Motta, S., Testa, V., and Menna, M. T. (2012). Sub-arcsecond position of the the transient 11-Hz X-ray pulsar in the Globular Cluster Terzan 5 derived from a Moon occultation observed by RXTE. *The Astronomer's Telegram*, 3892:1.

Riley, T. E., Watts, A. L., Bogdanov, S., Ray, P. S., Ludlam, R. M., Guillot, S., Arzoumanian, Z., Baker, C. L., Bilous, A. V., Chakrabarty, D., Gendreau, K. C.,

Harding, A. K., Ho, W. C. G., Lattimer, J. M., Morsink, S. M., and Strohmayer, T. E. (2019). A NICER View of PSR J0030+0451: Millisecond Pulsar Parameter Estimation. *ApJ*, 887(1):L21.

Rodriguez, C. L. and Antonini, F. (2018). A Triple Origin for the Heavy and Low-spin Binary Black Holes Detected by LIGO/VIRGO. *ApJ*, 863(1):7.

Rodriguez, C. L. and Loeb, A. (2018). Redshift Evolution of the Black Hole Merger Rate from Globular Clusters. *ApJ*, 866(1):L5.

Röser, S., Schilbach, E., and Goldman, B. (2019). Hyades tidal tails revealed by Gaia DR2. *A&A*, 621:L2.

Rothschild, R. E., Blanco, P. R., Gruber, D. E., Heindl, W. A., MacDonald, D. R., Marsden, D. C., Pelling, M. R., Wayne, L. R., and Hink, P. L. (1998). In-flight performance of the high energy x-ray timing experiment on the rossi x-ray timing explorer. *The Astrophysical Journal*, 496(1):538.

Ruiz-Lara, T., Gallart, C., Bernard, E. J., and Cassisi, S. (2020). The recurrent impact of the Sagittarius dwarf on the star formation history of the Milky Way. *Nature Astronomy*, 4:965–973.

Salaris, M. and Cassisi, S. (2005). *Evolution of Stars and Stellar Populations*. John Wiley Sons, Ltd.

Salpeter, E. E. (1955). The Luminosity Function and Stellar Evolution. *ApJ*, 121:161.

Sana, H., de Mink, S. E., de Koter, A., Langer, N., Evans, C. J., Gieles, M., Gosset, E., Izzard, R. G., Le Bouquin, J.-B., and Schneider, F. R. N. (2012). Binary Interaction Dominates the Evolution of Massive Stars. *Science*, 337:444.

Sander, A. A. C. and Vink, J. S. (2020). On the nature of massive helium star winds and Wolf-Rayet-type mass-loss. *MNRAS*, 499(1):873–892.

Sathyaprakash, B., Abernathy, M., Acernese, F., Ajith, P., Allen, B., Amaro-Seoane, P., Andersson, N., Aoudia, S., Arun, K., Astone, P., and et al. (2012). Scientific objectives of Einstein Telescope. *Classical and Quantum Gravity*, 29(12):124013.

Schuler, S. C., King, J. R., and The, L.-S. (2009). Stellar Nucleosynthesis in the Hyades Open Cluster. *ApJ*, 701(1):837–849.

Schutz, B. F. (1986). Determining the Hubble constant from gravitational wave observations. *Nature*, 323(6086):310–311.

Schutz, B. F. and Tinto, M. (1987). Antenna patterns of interferometric detectors of gravitational waves - I. Linearly polarized waves. *MNRAS*, 224:131–154.

Shakura, N. I. and Sunyaev, R. A. (1973). Black holes in binary systems. Observational appearance. *A&A*, 24:337–355.

Shaposhnikov, N. and Titarchuk, L. (2008). XTE J1650-500 - The Lightest Galactic Black Hole. In *AAS/High Energy Astrophysics Division #10*, volume 10 of *AAS/High Energy Astrophysics Division*, page 1.08.

Shen, K. J., Boubert, D., Gänsicke, B. T., Jha, S. W., Andrews, J. E., Chomiuk, L., Foley, R. J., Fraser, M., Gromadzki, M., Guillochon, J., Kotze, M. M., Maguire, K., Siebert,

M. R., Smith, N., Strader, J., Badenes, C., Kerzendorf, W. E., Koester, D., Kromer, M., Miles, B., Pakmor, R., Schwab, J., Toloza, O., Toonen, S., Townsley, D. M., and Williams, B. J. (2018). Three Hypervelocity White Dwarfs in Gaia DR2: Evidence for Dynamically Driven Double-degenerate Double-detonation Type Ia Supernovae. *ApJ*, 865(1):15.

Sibgatullin, N. R. and Sunyaev, R. A. (2000). Energy Release During Disk Accretion onto a Rapidly Rotating Neutron Star. *Astronomy Letters*, 26:699–724.

Silsbee, K. and Tremaine, S. (2017). Lidov-Kozai Cycles with Gravitational Radiation: Merging Black Holes in Isolated Triple Systems. *ApJ*, 836(1):39.

Sobolewska, M. A. and Życki, P. T. (2006). Spectral and Fourier analyses of X-ray quasi-periodic oscillations in accreting black holes. *MNRAS*, 370:405–414.

Song, H. F., Meynet, G., Maeder, A., Ekström, S., and Eggenberger, P. (2016). Massive star evolution in close binaries. Conditions for homogeneous chemical evolution. *A&A*, 585:A120.

Soubiran, C., Cantat-Gaudin, T., Romero-Gómez, M., Casamiquela, L., Jordi, C., Vallenari, A., Antoja, T., Balaguer-Núñez, L., Bossini, D., Bragaglia, A., Carrera, R., Castro-Ginard, A., Figueras, F., Heiter, U., Katz, D., Krone-Martins, A., Le Campion, J. F., Moitinho, A., and Sordo, R. (2018). Open cluster kinematics with Gaia DR2. *A&A*, 619:A155.

Spera, M. and Mapelli, M. (2017). Very massive stars, pair-instability supernovae and intermediate-mass black holes with the sevn code. *MNRAS*, 470(4):4739–4749.

Spera, M., Mapelli, M., Giacobbo, N., Trani, A. A., Bressan, A., and Costa, G. (2019). Merging black hole binaries with the SEVN code. *MNRAS*, 485(1):889–907.

Stefanov, I. Z. (2014). Confronting models for the high-frequency QPOs with Lense-Thirring precession. *MNRAS*, 444:2178–2185.

Stella, L. and Vietri, M. (1998). Lense-Thirring Precession and Quasi-periodic Oscillations in Low-Mass X-Ray Binaries. *ApJL*, 492:L59–L62.

Stella, L. and Vietri, M. (1999). kHz Quasiperiodic Oscillations in Low-Mass X-Ray Binaries as Probes of General Relativity in the Strong-Field Regime. *Physical Review Letters*, 82:17–20.

Stella, L., Vietri, M., and Morsink, S. M. (1999). Correlations in the Quasi-periodic Oscillation Frequencies of Low-Mass X-Ray Binaries and the Relativistic Precession Model. *ApJL*, 524:L63–L66.

Stevenson, S., Ohme, F., and Fairhurst, S. (2015). Distinguishing Compact Binary Population Synthesis Models Using Gravitational Wave Observations of Coalescing Binary Black Holes. *ApJ*, 810:58.

Stevenson, S., Sampson, M., Powell, J., Vigna-Gómez, A., Neijssel, C. J., Szécsi, D., and Mandel, I. (2019). The Impact of Pair-instability Mass Loss on the Binary Black Hole Mass Distribution. *ApJ*, 882(2):121.

Stiller, R. A., Littlefield, C., Garnavich, P., Wood, C., Hambsch, F.-J., and Myers, G.

(2018). High-time-resolution Photometry of AR Scorpii: Confirmation of the White Dwarf's Spin-down. *AJ*, 156(4):150.

Strohmayer, T. E. (2001). Discovery of a 450 HZ Quasi-periodic Oscillation from the Microquasar GRO J1655-40 with the Rossi X-Ray Timing Explorer. *ApJL*, 552:L49–L53.

Strohmayer, T. E. and Markwardt, C. B. (2010). EXO 1745-248 is an 11 Hz Eclipsing Pulsar. *The Astronomer's Telegram*, 2929:1.

Strohmayer, T. E., Markwardt, C. B., Pereira, D., and Smith, E. A. (2010). A Refined Orbital Solution and the Transient Pulsar in Terzan 5 is Not Eclipsing. *The Astronomer's Telegram*, 2946:1.

Sunyaev, R. A. and Truemper, J. (1979). Hard X-ray spectrum of CYG X-1. *Nature*, 279:506–508.

Syunyaev, R. A. and Shakura, N. I. (1986). Disk Accretion onto a Weak Field Neutron Star - Boundary Layer Disk Luminosity Ratio. *Soviet Astronomy Letters*, 12:117–120.

Szécsi, D., Langer, N., Yoon, S.-C., Sanyal, D., de Mink, S., Evans, C. J., and Dermine, T. (2015). Low-metallicity massive single stars with rotation. Evolutionary models applicable to I Zwicky 18. *A&A*, 581:A15.

Taam, R. E. and Sandquist, E. L. (2000). Common Envelope Evolution of Massive Binary Stars. *ARA&A*, 38:113–141.

Tagger, M. and Pellat, R. (1999). An accretion-ejection instability in magnetized disks. *A&A*, 349:1003–1016.

Taylor, P. and Kobayashi, C. (2014). Seeding black holes in cosmological simulations. *MNRAS*, 442:2751–2767.

Taylor, P. and Kobayashi, C. (2015a). Quantifying AGN-driven metal-enhanced outflows in chemodynamical simulations. *MNRAS*, 452:L59–L63.

Taylor, P. and Kobayashi, C. (2015b). The effects of AGN feedback on present-day galaxy properties in cosmological simulations. *MNRAS*, 448:1835–1846.

Taylor, P. and Kobayashi, C. (2016). Time evolution of galaxy scaling relations in cosmological simulations. *MNRAS*, 463:2465–2479.

Taylor, P. and Kobayashi, C. (2017). The metallicity and elemental abundance gradients of simulated galaxies and their environmental dependence. *MNRAS*, 471:3856–3870.

Terreran, G., Pumo, M. L., Chen, T. W., Moriya, T. J., Taddia, F., Dessart, L., Zampieri, L., Smartt, S. J., Benetti, S., Inserra, C., Cappellaro, E., Nicholl, M., Fraser, M., Wyrzykowski, Ł., Udalski, A., Howell, D. A., McCully, C., Valenti, S., Dimitriadis, G., Maguire, K., Sullivan, M., Smith, K. W., Yaron, O., Young, D. R., Anderson, J. P., Della Valle, M., Elias-Rosa, N., Gal-Yam, A., Jerkstrand, A., Kankare, E., Pastorello, A., Sollerman, J., Turatto, M., Kostrzewa-Rutkowska, Z., Kozłowski, S., Mróz, P., Pawlak, M., Pietrukowicz, P., Poleski, R., Skowron, D., Skowron, J., Soszyński, I., Szymański, M. K., and Ulaczyk, K. (2017). Hydrogen-rich supernovae beyond the neutrino-driven core-collapse paradigm. *Nature Astronomy*, 1:713–720.

Thorne, K. S. (1995). Gravitational Waves. In Kolb, E. W. and Peccei, R. D., editors, *Particle and Nuclear Astrophysics and Cosmology in the Next Millenium*, page 160.

Thorne, K. S. and Price, R. H. (1975). Cygnus X-1: an interpretation of the spectrum and its variability. *ApJ*, 195:L101–L105.

Titarchuk, L. and Hua, X.-M. (1995). A Comparison of Thermal Comptonization Models. *ApJ*, 452:226.

Toffano, M., Mapelli, M., Giacobbo, N., Artale, M. C., and Ghirlanda, G. (2019). The host galaxies of double compact objects across cosmic time. *MNRAS*, 489(4):4622–4631.

Torrealba, G., Belokurov, V., Koposov, S. E., Li, T. S., Walker, M. G., Sanders, J. L., Geringer-Sameth, A., Zucker, D. B., Kuehn, K., Evans, N. W., and Dehnen, W. (2019). The hidden giant: discovery of an enormous Galactic dwarf satellite in Gaia DR2. *MNRAS*, 488(2):2743–2766.

Tremblay, P.-E., Fontaine, G., Fusillo, N. P. G., Dunlap, B. H., Gänsicke, B. T., Hollands, M. A., Hermes, J. J., Marsh, T. R., Cukanovaite, E., and Cunningham, T. (2019). Core crystallization and pile-up in the cooling sequence of evolving white dwarfs. *Nature*, 565(7738):202–205.

van der Klis, M. (1989a). Fourier techniques in X-ray timing. In Ögelman, H. and van den Heuvel, E. P. J., editors, *NATO Advanced Science Institutes (ASI) Series C*, volume 262 of *NATO Advanced Science Institutes (ASI) Series C*, page 27.

van der Klis, M. (1989b). Quasi-periodic oscillations and noise in low-mass X-ray binaries. *Annual Reviews*, 27:517–553.

van der Klis, M. (2000). Millisecond Oscillations in X-ray Binaries. *Annual Reviews*, 38:717–760.

van der Klis, M. (2006). Overview of QPOs in neutron-star low-mass X-ray binaries. *Advances in Space Research*, 38:2675–2679.

van der Klis, M. (2006). *Rapid X-ray variability*, page 39–112. Cambridge Astrophysics. Cambridge University Press.

van der Klis, M., Jansen, F., van Paradijs, J., Lewin, W. H. G., van den Heuvel, E. P. J., Trumper, J. E., and Szatjno, M. (1985). Intensity-dependent quasi-periodic oscillations in the X-ray flux of GX5 - 1. *Nature*, 316:225–230.

van der Klis, M., Swank, J. H., Zhang, W., Jahoda, K., Morgan, E. H., Lewin, W. H. G., Vaughan, B., and van Paradijs, J. (1996). Discovery of Submillisecond Quasi-periodic Oscillations in the X-Ray Flux of Scorpius X-1. *ApJL*, 469:L1.

van Doesburgh, M. and van der Klis, M. (2017). Testing the relativistic precession model using low-frequency and kHz quasi-periodic oscillations in neutron star low-mass X-ray binaries with known spin. *MNRAS*, 465:3581–3606.

van Paradijs, J. (1996). On the Accretion Instability in Soft X-Ray Transients. *ApJ*, 464:L139.

van Straaten, S., van der Klis, M., Kuulkers, E., and Méndez, M. (2001). An Atlas of Burst Oscillations and Spectral Properties in 4U 1728-34. *ApJ*, 551:907–920.

Venumadhav, T., Zackay, B., Roulet, J., Dai, L., and Zaldarriaga, M. (2019). New Binary Black Hole Mergers in the Second Observing Run of Advanced LIGO and Advanced Virgo. *arXiv e-prints*, page arXiv:1904.07214.

Vigna-Gómez, A., Justham, S., Mandel, I., de Mink, S. E., and Podsiadlowski, P. (2019). Massive Stellar Mergers as Precursors of Hydrogen-rich Pulsational Pair Instability Supernovae. *ApJ*, 876(2):L29.

Vink, J. S. and de Koter, A. (2005). On the metallicity dependence of Wolf-Rayet winds. *A&A*, 442:587–596.

Vink, J. S., de Koter, A., and Lamers, H. J. G. L. M. (2001). Mass-loss predictions for O and B stars as a function of metallicity. *A&A*, 369:574–588.

von Weizsäcker, C. F. (1937). Über elementumwandlungen in innern der sterne i. *Physikalische Zeitschrift*, 38:176—-191.

von Weizsäcker, C. F. (1938). Über elementumwandlungen in innern der sterne ii. *Physikalische Zeitschrift*, 39:633—-646.

Voss, R. and Tauris, T. M. (2003). Galactic distribution of merging neutron stars and black holes - prospects for short gamma-ray burst progenitors and LIGO/VIRGO. *MNRAS*, 342:1169–1184.

Wagoner, R. V. (1999). Relativistic diskoseismology. *Phys. Rep.*, 311:259–269.

Wagoner, R. V., Silbergleit, A. S., and Ortega-Rodríguez, M. (2001). "Stable" Quasi-periodic Oscillations and Black Hole Properties from Diskoseismology. *ApJL*, 559:L25–L28.

Wang, Z.-Y., Huang, C.-Y., Wang, D.-X., and Wang, J.-Z. (2012). A model of low-frequency quasi-periodic oscillations in black hole X-ray binaries. *Research in Astronomy and Astrophysics*, 12(6):661–670.

Weisberg, J. M., Nice, D. J., and Taylor, J. H. (2010). Timing Measurements of the Relativistic Binary Pulsar PSR B1913+16. *ApJ*, 722:1030–1034.

Wijnands, R. and van der Klis, M. (1999). The Broadband Power Spectra of X-Ray Binaries. *ApJ*, 514:939–944.

Woosley, S. E. (2017). Pulsational Pair-instability Supernovae. *ApJ*, 836:244.

Woosley, S. E. (2019). The Evolution of Massive Helium Stars, Including Mass Loss. *ApJ*, 878(1):49.

Woosley, S. E., Blinnikov, S., and Heger, A. (2007). Pulsational pair instability as an explanation for the most luminous supernovae. *Nature*, 450(7168):390–392.

Woosley, S. E. and Heger, A. (2006). The Progenitor Stars of Gamma-Ray Bursts. *ApJ*, 637:914–921.

Woosley, S. E., Heger, A., and Weaver, T. A. (2002). The evolution and explosion of massive stars. *Reviews of Modern Physics*, 74(4):1015–1071.

Xu, S., Su, K. Y. L., Rogers, L. K., Bonsor, A., Olofsson, J., Veras, D., van Lieshout, R., Dufour, P., Green, E. M., Schlawin, E., Farihi, J., Wilson, T. G., Wilson, D. J., and Gänsicke, B. T. (2018). Infrared Variability of Two Dusty White Dwarfs. *ApJ*, 866(2):108.

Yoon, S.-C. and Langer, N. (2005). Evolution of rapidly rotating metal-poor massive stars towards gamma-ray bursts. *A&A*, 443:643–648.

Yoon, S.-C., Langer, N., and Norman, C. (2006). Single star progenitors of long gamma-ray bursts. I. Model grids and redshift dependent GRB rate. *A&A*, 460:199–208.

Yusof, N., Hirschi, R., Meynet, G., Crowther, P. A., Ekström, S., Frischknecht, U., Georgy, C., Abu Kassim, H., and Schnurr, O. (2013). Evolution and fate of very massive stars. *MNRAS*, 433(2):1114–1132.

Zevin, M., Pankow, C., Rodriguez, C. L., Sampson, L., Chase, E., Kalogera, V., and Rasio, F. A. (2017). Constraining Formation Models of Binary Black Holes with Gravitational-wave Observations. *ApJ*, 846:82.

Ziegler, J. and Freese, K. (2020). Filling the Black Hole Mass Gap: Avoiding Pair Instability in Massive Stars through Addition of Non-Nuclear Energy. *arXiv e-prints*, page arXiv:2010.00254.

Notes